



저작자표시-비영리-변경금지 2.0 대한민국

이용자는 아래의 조건을 따르는 경우에 한하여 자유롭게

- 이 저작물을 복제, 배포, 전송, 전시, 공연 및 방송할 수 있습니다.

다음과 같은 조건을 따라야 합니다:



저작자표시. 귀하는 원저작자를 표시하여야 합니다.



비영리. 귀하는 이 저작물을 영리 목적으로 이용할 수 없습니다.



변경금지. 귀하는 이 저작물을 개작, 변형 또는 가공할 수 없습니다.

- 귀하는, 이 저작물의 재이용이나 배포의 경우, 이 저작물에 적용된 이용허락조건을 명확하게 나타내어야 합니다.
- 저작권자로부터 별도의 허가를 받으면 이러한 조건들은 적용되지 않습니다.

저작권법에 따른 이용자의 권리는 위의 내용에 의하여 영향을 받지 않습니다.

이것은 [이용허락규약\(Legal Code\)](#)을 이해하기 쉽게 요약한 것입니다.

[Disclaimer](#)

공학박사 학위논문

# Study on the Manganese based Water Oxidation Catalyst

망간 기반의 물 산화 촉매에 관한 연구

2016년 8월

서울대학교 대학원

재료공학부

진 경 석

## Abstract

# Study on the Manganese based Water Oxidation Catalyst

Kyoungsuk Jin

Department of Materials Science and Engineering

The Graduate School

Seoul National University

Hydrogen energy is considered as the most promising alternative energy resources, due to its high energy density and environmentally friendly nature. Historically, hydrogen production has been mainly progressed by gas reforming process, which requires high pressure and high temperature and produces CO<sub>2</sub> and other pollutants. Recently, electrochemical hydrogen production has drawn great attention because byproduct of the reaction is only oxygen gas. To operate overall electrochemical water splitting reaction, anodic oxygen evolution reaction (OER) is considered as the rate determining step. Four electrons and four proton involved reaction kinetics results in relatively large overpotential values, compared to cathodic hydrogen evolution reaction. For the decades a lot of research efforts have been dedicated to develop robust and efficient water oxidation catalyst.

On the other hand, in nature, there exist water oxidizing complex of which active site is consist of manganese and calcium elements. On the contrary to the fact that noble metal based catalysts, IrO<sub>2</sub>, RuO<sub>2</sub> materials are used in industry, nature chose to use earth abundant manganese and calcium to oxidize water. Moreover,

surprisingly, catalytic efficiency of  $Mn_4Ca$  cluster in photosystem II, is superior to previously reported synthetic catalysts. Such an exceptional performance of the biological system has inspired to study manganese based catalysts.

However, unfortunately, manganese based water oxidation catalysts have suffered from the serious activity degradation problem under neutral condition. Although many researchers have tried to address this issue, fundamental resolution is not suggested yet. In this thesis, we report efficient and robust manganese based water oxidation catalysts. From the our designed manganese based catalysts, we believe that long lasting issue in Mn catalysts is completely resolved.

In chapter 2, we discovered new crystal structure, manganese phosphate compound ( $Mn_3(PO_4)_2 \cdot 3H_2O$ ) as water oxidation catalyst. Due to the bulky phosphate groups, highly distorted crystal structure are generated. Computational analysis clearly revealed that phosphate ligations in structure could make relatively longer Mn-O bonding and more distorted geometry, compared to previously reported Mn-based oxides. Unique structural flexibility can stabilize Jahn-Teller distorted Mn(III) and thus facilitate Mn(II) oxidation, as verified by electron paramagnetic resonance spectroscopy.

In chapter 3, as an another strategy to stabilize Mn(III) species on the catalyst surface, we developed nanosized manganese based water oxidation catalysts. Sub 10 nm sized manganese oxide nanoparticles were synthesized via hot injection method. The surface treatment and ambient heat treatment process activate manganese oxide nanoparticles which results in high catalytic efficiency under neutral pH. Catalytic performance of manganese oxide nanoparticles are the one of the best record among the that of first-row transition metal based catalysts.

In chapter 4, From the various *in-situ* analysis and electrokinetic study, we demonstrated the detailed oxygen evolving catalytic cycle of manganese oxide

nanoparticles, which is totally different from that of bulk Mn materials. Proton coupled electron transfer occurs before and during water oxidation catalysis and thus high valent Mn(IV)=O species can participate in the rate determining step for oxygen evolution.

In chapter 5, We developed Ni-decorated Mn<sub>3</sub>O<sub>4</sub> nanoparticles as new water oxidation catalysts. In this work, we newly discovered that under ambient annealing process, atomic nickel diffusion phenomena occurs at the metal oxide interface. With our methodology surface specific heteroatom doping can be possible. Ni-decorated Mn<sub>3</sub>O<sub>4</sub> nanoparticles exhibit outstanding performance under neutral and basic condition. Interestingly, we discovered that during water oxidation catalysis, unique Mn status is generated on the catalyst surface. From the EPR analysis, we verified low-spin Mn(IV) species are formed, which has never been reported before. Computation study also supported that atomically doped Ni atom induced distorted Mn geometry in Mn<sub>3</sub>O<sub>4</sub> nanoparticles structure and thus stabilize low Mn(IV) species.

In conclusion, we discovered various manganese based water oxidation catalysts. Our designed catalysts could overcome the issues in manganese catalysts and finally achieved excellent performance for oxygen evolution catalysis.

**Keywords: Manganese oxide, Water Oxidation, Oxygen Evolution Reaction, Nanocatalysts, Electrochemical study, Reaction Intermediate, Hybrid Structure**

**Student Number: 2010-22773**

# Contents

---

List of Tables .....	x
----------------------	---

List of Figures .....	xiii
-----------------------	------

---

<b>Chapter 1 Introduction</b> .....	1
1.1 The necessity for the development of future energy resources	1
1.2 Electrochemical hydrogen production: Water electrolysis .....	3
1.3 Water splitting Catalysts .....	7
1.3.1. Hydrogen evolution reaction (HER) .....	8
1.3.1.1. Genral description for HER .....	8
1.3.1.2. Experimental parameter in electrochemical reaction...	12
1.3.1.3. Various HER catalysts.....	17
1.3.1.4. Characterization methods for electrocatalysts .....	31
1.3.2. Oxygen evolution reaction (OER).....	33
1.3.2.1. Water splitting and OER.....	33
1.3.2.2. Natural photosynthetic complex.....	37
1.3.2.3 Mn <sub>4</sub> Ca cluster for water oxidation .....	39
1.3.2.3.1. Atomic structural analysis of PS II active center...	40
1.3.2.3.2. Electronic structural analysis for PS II active center	43
1.3.2.4 Bio-inspired Mn based water oxidation catalysts.....	49

1.3.2.4.1. Fundamental issue .....	49
1.3.2.4.2. The descriptors for Mn based electrocatalysts.....	52
1.3.2.4.3. Limitation for catalysis under neutral pH.....	54
1.3.2.4.4. Recent discovery in Mn based catalyts .....	61
1.3.2.5. Extended solid state OER catalyts .....	71
1.3.2.5.1. Noble metal based OER electrocatalyts.....	71
1.3.2.5.2. Transition metal based catalyts .....	72
1.4. Scope of Thesis .....	86
1.5. Concluding Remarks .....	88

## **Chapter 2 Hydrated Manganese(II) Phosphate ( $\text{Mn}_3(\text{PO}_4)_2 \cdot 3\text{H}_2\text{O}$ ) as Water Oxidation Catalyst .....**

2.1 Introduction .....	90
2.2 Experimental Methods .....	94
2.2.1 Materials .....	94
2.2.2 Synthesis procedure.....	94
2.2.3 Powder X-ray diffraction.....	95
2.2.4 ICP/MS & TGA analysis .....	95
2.2.5. Rietveld analysis.....	96
2.2.6. Scanning electron microscopy (SEM) analysis .....	96
2.2.7. Transmission electron microscopy (TEM) analysis .....	97
2.2.8. Brunauer–Emmett–Teller (BET) method .....	97
2.2.9. Cyclic Voltammetry (CV) .....	97
2.2.10. Gas Chromatography (GC) .....	99

2.2.11. Electron paramagnetic resonance (EPR) spectroscopy .....	100
2.2.12. DFT calculation.....	102
2.3 Results and Discussions .....	103
2.3.1 Basic characterization of $\text{Mn}_3(\text{PO}_4)_2 \cdot 3\text{H}_2\text{O}$ structure.....	103
2.3.2 Electrochemical analysis of $\text{Mn}_3(\text{PO}_4)_2 \cdot 3\text{H}_2\text{O}$ .....	115
2.3.3 Mechanistic studies of $\text{Mn}_3(\text{PO}_4)_2 \cdot 3\text{H}_2\text{O}$ .....	126
2.4. Concluding Remarks .....	135

---

**Chapter 3 Monodisperse Manganese Oxide Nanocrystals  
with High Activity for Water Oxidation Catalysis .....** 136

3.1 Introduction.....	136
3.2 Experimental Methods.....	139
3.2.1. Synthesis and Materials .....	139
3.2.2. Synthetic procedures for sub 10 nm sized monodisperse manganese oxide nanoparticles.....	139
3.2.3 Synthetic procedures for sub 15, 20 nm sized monodisperse manganese oxide nanoparticles .....	140
3.2.4 Purification details.....	143
3.2.5 Surface modification of MnO nanocrystals .....	143
3.2.5.1 $\text{BF}_4^-$ functionalized MnO nanocrystals.....	143
3.2.5.2 Ammonia treated sample by spin coating.....	144
3.2.6. Powder X-ray Diffraction .....	146
3.2.7. Scanning Electron Microscopy (SEM) Analysis .....	146

3.2.8. Transmission Electron Microscopy (TEM) Analysis.....	146
3.2.9. Fourier Transform Infrared Spectroscopy (FT-IR) Analysis..	146
3.2.10. X-ray Photon (XPS) Spectroscopy .....	147
3.2.11. Electrochemical Methods .....	148
3.2.12 EPR Spectroscopy .....	148
3.2.13 Basic EPR Theory.....	149
3.3 Results and Discussions .....	152
3.3.1. Monodisperse manganese (II) oxide nanocrystals .....	152
3.3.2. Electrochemical characterization.....	154
3.3.2.1 Effect of duration time for surface treatment.....	154
3.3.2.2. Electrochemical analysis on partially oxidized MnO NPs	164
3.3.3. Spectroscopic analysis: Inspection of Mn valency .....	176
3.3.4. Electrokinetic study of MnO NPs.....	180
3.4. Concluding Remarks.....	184

## **Chapter 4. Mechanistic Investigation of Electrocatalytic Water**

### **Oxidation by Uniform 10 nm sized MnO Nanoparticles 185**

4.1. Introduction .....	185
4.2. Results and Discussions .....	191
4.2.1. Thickness dependent activity of MnO nanoparticles .....	191
4.2.2 Theory of Oxygen Evolution reaction (OER) Mechanism .....	195
4.2.3. Electrokinetics in MnO Nanoparticles.....	199
4.2.4. <i>In-situ</i> spectroscopy analysis .....	203
4.2.5. Proposed Water Oxidation Mechanism.....	212

4.3. Concluding Remarks.....	214
------------------------------	-----

---

## **Chapter 5. Ni-hybridized Manganese Oxide (Mn<sub>3</sub>O<sub>4</sub>)**

<b>Nanoparticles .....</b>	<b>215</b>
5.1. Introduction .....	215
5.2. Materials and Synthesis procedure .....	218
5.2.1. Synthesis of Manganese (II) Oxide Nanoparticles.....	218
5.2.2. Fabrication of NiO <sub>x</sub> /Mn <sub>3</sub> O <sub>4</sub> .....	219
5.3. Results and Discussions .....	221
5.3.1. Structural Characterization.....	221
5.3.2. Electrochemical characterization .....	225
5.3.3. Electronic structure analysis : Resting state .....	230
5.3.3. Electronic structure analysis: During Water Oxidation Catalysis	234
5.3.3.1. In-situ XANES & UV-Vis analysis .....	234
5.3.3.2. EPR analysis. ....	234
5.3.3.3. Interpretation of EPR results .....	237
5.4. Concluding Remarks .....	242

---

<b>Chapter 6. Conclusion .....</b>	<b>243</b>
------------------------------------	------------

---

**References** ..... 245

---

**국문 초록** ..... 260

---

## List of Tables

<b>Table 1.1.</b>	Various manufacturers of electrolyzer production.....	39
<b>Table 1.2.</b>	Tafel slope and exchange current for previously reported various hydrogen evolution catalysts. Loading method and electrolyte used are described as well .....	25
<b>Table 1.3</b>	Tafel slope, turnover frequency(TOF), and exchange current values for the previously reported binary metals catalysts. Loading method and electrolyte used are described. ....	29
<b>Table 1.4</b>	Tafel slope and exchange current values of previously reported carbon based HER catalysts. Loading method and electrolyte used are described. ....	30
<b>Table 1.5.</b>	Selection of experimental values of Tafel slope, overpotential, and onset potential for oxygen evolution on various electrocatalysts and electrodes. ....	70
<b>Table 1.6.</b>	Selection of experimental values of Tafel slope, overpotential and Onset potential for oxygen evolution on various electrocatalysts and electrodes. Preparation Method and Electrolyte used are described.	85

---

**Table 2.1.** Crystal structures of manganese based oxide and phosphate compounds. It showed that almost all manganese oxide compounds display higher symmetry than manganese phosphate compounds. (All data were referred from JCPDS Card.)..... 107

**Table 2.2.** Bond lengths between manganese and neighboring oxygen atoms in  $\text{Mn}_3(\text{PO}_4)_2 \cdot 3\text{H}_2\text{O}$ . Average Mn-O bond distance is 2.215 Å. JCPDS Card.)..... 111

**Table 2.3.** Mn-Mn distance in  $\text{Mn}_3(\text{PO}_4)_2 \cdot 3\text{H}_2\text{O}$ . Distance values between edge-sharing manganese atoms and corner-sharing manganese atoms were obtained. Average Mn-Mn bond distance was 3.412 Å. Generally, corner sharing manganese atoms had larger Mn-Mn distances than edge sharing ones. .... 112

**Table 2.3.** The TOF values of the various manganese oxide catalysts that have been reported and of our catalyst, commercial MnO, and MnO<sub>2</sub>, which were used in this study for water oxidation catalysis. TOF values ( $\text{s}^{-1}$  per Mn,  $\mu\text{mol}/\text{m}^2 \text{ s}$ ) were calculated based on the oxygen evolution rates divided by the mole number of Mn atoms and total surface area of the catalysts. These values are indexed in the second and fourth columns, respectively. The BET values of the catalysts and the experimental conditions are summarized in the third and

fourth columns, respectively. .... 122

---

**Table 3.1.** Comparison of onset potential depending on the ammonia treatment time and fourth columns, respectively. The BET values of the catalysts and the experimental conditions are summarized in the third and fourth columns, respectively. .... 162

**Table 3.2.** Comparison of OER activity for various water oxidation catalysts. .... 170

**Table 3.3.** The TOF values of the various manganese oxide catalysts that have been reported by others and of our catalyst, partially oxidized MnO NCs. The detailed experimental conditions for photo and electrochemical catalysis are summarized in the third column. .... 162

---

**Table 5.1.** Water oxidation efficiency comparison of various OER catalysts ..... 229

## List of Figures

- Figure 1.1.** Various electrolyzer system for water splitting reaction. (a) Alkaline electrolyzer, (b) PEM electrolyzer, (c) Solid oxide electrolyzer 6
- Figure 1.2.** Schematic of the current to potential curve of water splitting reaction ..... 9
- Figure 1.3.** Experimentally measured exchange current,  $\log(J_0)$ , for hydrogen evolution over different metal surfaces plotted as a function of the calculated hydrogen chemisorption energy per atom. .... 15
- Figure 1.4.** Experimentally measured exchange current,  $\log(J_0)$ , for hydrogen evolution over different catalyst plotted as a function of the calculated the free energy for hydrogen adsorption. Data are collected from the previous literature (Table 1.2 ~ 4). .... 16
- Figure 1.5.** Structure and electrochemical property of Pt<sub>3</sub>Ni nanoframe (a) Schematic illustrations and corresponding TEM images of the samples obtained at four representative stages during the transformation process from polyhedral to nanoframes. (b) Comparison of HER activities for Pt/C, Pt/Ni(OH)<sub>2</sub>/C, Pt<sub>3</sub>Ni nanoframes/C, and Pt<sub>3</sub>Ni frames/Ni(OH)<sub>2</sub>/C in alkaline electrolyte. 18

<b>Figure 1.6.</b>	Scheme for overall water splitting in photosystem. ....	34
<b>Figure 1.7.</b>	(a) Atomic structure of the Mn cluster in S <sub>1</sub> state by XFEL. Roman numerals indicate Mn-O, Ca-O, Mn-water, and Ca-water distances(Å) in the Mn cluster. (b) Comparison between the earlier XRD structure and the later XFEL structure of the Mn cluster in S <sub>1</sub> state. ....	45
<b>Figure 1.8.</b>	The Kok cycle with spectroscopically consistent structures of the Mn cluster and their spin states. ....	46
<b>Figure 1.9.</b>	Proposed water channels to and from the Mn cluster in S <sub>2</sub> -S <sub>3</sub> transition. ....	47
<b>Figure 1.10.</b>	Structural model for all S <sub>i</sub> states of the Mn cluster: atomic structure of the Mn cluster, Mn-Mn distances (Å) of optimized geometries, the nature of magnetic couplings(AF for antiferromagnetic coupling and F for ferromagnetic coupling), and total spin numbers respectively. (c) Proposed S <sub>3</sub> intermediate states upon S <sub>2</sub> -S <sub>3</sub> transition. The loss of the Asp61/W1 hydrogen bond with subsequent low-barrier water insertion <i>via</i> the Asp61 channel and rearrangement is involved. ....	48
<b>Figure 1.11.</b>	Electrochemical activity of various manganese oxide catalysts under (a) pH 7 and (b) pH 13. ....	50
<b>Figure 1.12.</b>	(a) Schematic illustration of a current density ( <i>j</i> ) vs potential ( <i>U</i> ) curve for a pristine δ-MnO <sub>2</sub> electrode under neutral pH conditions.	

The surface-associated intermediate  $\text{Mn}^{3+}$  species are rapidly consumed by charge disproportionation to form  $\text{Mn}^{2+}$  and  $\text{Mn}^{4+}$ , resulting in no net charges passing across the electrode. .... 56

**Figure 1.13.** Pair distribution functions of manganese atoms (a) in pristine  $\text{MnO}_2$  (blue) and in reduced manganese oxide as Mn(II) (black) and Mn(III) (red); (b) in pristine  $\text{Mn}_3(\text{PO}_4)_2 \cdot 3\text{H}_2\text{O}$  (black) and in oxidized manganese phosphate (red), in which all Mn(II) atoms were intentionally oxidized to Mn(III); and (c) in pristine MnO (black) and in oxidized manganese oxide (red) (d) The pressure on the cell of each Mn compound when Mn was reduced or oxidized to the 3+ state. It is noted that the pressure is unrealistically large because all the Mn atoms change the charge state. .... 57

**Figure 1.14.** Schematic representation of crystalline structure (a) and cyclic voltammetry curves of  $\text{Mn}_3(\text{PO}_4)_2 \cdot 3\text{H}_2\text{O}$  and activity comparison with conventional Mn oxide compounds under neutral pH. ... 60

**Figure 1.15.** HR-TEM images of inactive crystalline MnO(left) and active  $\text{MnO}_x$ (right) after ceric ammonium nitrate treatment ..... 64

**Figure 1.16.** TEM Image (a) and cyclic voltammetry curves of 10 nm sized monodisperse manganese oxide nanoparticles and activity comparison with other transition metal based catalysts. (b) (scale bar : 100nm, inset : 5nm)..... 65

**Figure 1.17.** (a) Synthesis of bio-inspired Mn based electrocatalyst. Curved lines in structures schematically represent 2-pyridyl groups. (Inset) A recent structure of the OEC from crystallographic studies is shown. OAc/AcO, acetoxy group; Me, methyl; Bu, butyl (b) Cyclic voltammograms of 3 in (a) (solid trace, DMA solution) and 4 in (a) (dashed trace, DMF solution) with 0.1 M n Bu<sub>4</sub>NPF<sub>6</sub>. (c) The redox potentials of the [MMn<sub>3</sub>O<sub>2</sub>] complexes are correlated with the Lewis acidity of the redox-inactive metal(M : Na, Sr, Ca, Zn, Y). .... 66

**Figure 1.18.** (a), (b), (c) Proposed Mn<sub>4</sub>Ca cluster derived from polarized Mn EXAFS in relation to the putative ligands obtained from the 3.0 Å resolution x-ray crystal structure. The spheres represent Mn (red), Ca (green), and the bridging oxygen ligand atoms (gray). The assignment of ligands is tentative because it is based on the electron density of the Mn<sub>4</sub>Ca cluster, and its immediate environment may be altered by x-ray damage. (d) High-resolution structural models for the Mn<sub>4</sub>Ca cluster in PSII from polarized EXAFS. The Mn<sub>4</sub>Ca models I, II, and III are shown on the right..... 67

**Figure 1.19.** (a) X-ray diffraction pattern of s-MnO<sub>x</sub> (black) and i-MnO<sub>x</sub> (red). Reflections are labeled by squares for β- MnO<sub>2</sub>, by circles for γ - MnO<sub>2</sub>, by triangles for the layered MnO<sub>2</sub> phase. (b) X-ray absorption spectra of s-MnO<sub>x</sub> (black) and i-MnO<sub>x</sub> (red) deposited on electrodes before and after catalysis. (Mn(IV) ions are presented as spheres in magenta, Mn(III) ions in dark purple, and oxygen as red spheres.)..... 69

**Figure 1.20.** (a) SEM image of the electrodeposited catalyst after  $30\text{C}/\text{cm}^2$  were passed in 0.1 M KPi electrolyte at pH 7.0, containing 0.5 mM  $\text{Co}^{2+}$ . (b) Tafel plot (black circles),  $\eta = (V_{\text{appl}} - iR) - E(\text{pH } 7)$  (where  $V_{\text{appl}}$  is the applied potential), of a catalyst film on ITO in 0.1 M KPi electrolyte pH 7.0, corrected for the  $iR$  drop of the solution. pH data were converted into a Tafel plot (red circles),  $h = (V_{\text{appl}} + 0.059\Delta\text{pH} - iR) - E(\text{pH } 7)$ , assuming Nernstian behavior and correcting for the  $iR$  drop of the solution. The pH = 5 and pH = 8 data points are indicated by arrows. (c) Current density dependence on pH in 0.1 M KPi electrolyte. The potential was set at 1.24 V (versus NHE) with no  $iR$  compensation. (d) CVs scans of a Ni borate catalyst film at pH values of 7.82, 8.30, 8.68, 8.88, 9.16, 9.42, 9.72, and 9.98 in. going from left to right, respectively. The inset shows a linear fit for the 8.7–10.0 pH region, with a slope of 96 mV/pH unit. The CVs were taken at scan rates of 50 mV/s. (e) Tafel plot,  $\eta = (V_{\text{appl}} - iR - E^0)$ , of a Ni- $\text{B}_i$  catalyst film operated in 0.2 M  $\text{B}_i$ , pH 9.2 where  $\eta$  is the overpotential,  $iR$  accounts for the uncompensated solution resistance, and  $E^0$  is the thermodynamic potential for water oxidation at this pH (0.69 V vs. NHE)..... 74

**Figure 2.1.** Thermogravimetric analysis (TGA) of  $\text{Mn}_3(\text{PO}_4)_2 \cdot 3\text{H}_2\text{O}$ . The first drop of weight showed evaporation of  $\text{H}_2\text{O}$  molecules attached on the surface. Sequential weight drops of  $\text{Mn}_3(\text{PO}_4)_2 \cdot 3\text{H}_2\text{O}$  indicated that

H<sub>2</sub>O molecules were intercalated in Mn<sub>3</sub>(PO<sub>4</sub>)<sub>2</sub>·3H<sub>2</sub>O structure. With the total weight loss (13.198 %) during TGA analysis, except that generated by surface water molecules, we could draw that three H<sub>2</sub>O were embedded in manganese phosphate structure. And we also obtained from the ICP-MS result and EDS analysis that the ratio of manganese and phosphate was 3:2. .... 108

**Figure 2.2.** Comparison between XRD pattern of our Mn<sub>3</sub>(PO<sub>4</sub>)<sub>2</sub>·3H<sub>2</sub>O and previously reported JCPDS pattern of Mn<sub>3</sub>(PO<sub>4</sub>)<sub>2</sub>·3H<sub>2</sub>O. The JCPDS card data was significantly different from our data in terms of peak positions and peak intensity. .... 109

**Figure 2.3.** Schematic representation of crystalline Mn<sub>3</sub>(PO<sub>4</sub>)<sub>2</sub>·3H<sub>2</sub>O. (a. b) Coordination and arrangement of each manganese atom. Larger spheres denote Mn atoms, and smaller spheres denote phosphate atoms. (c) Mn(2) atoms are connected to each other by edge O-O sharing. Mn(2) and Mn(3) atoms are bridged by edge O-O<sub>w</sub> sharing, and Mn(2) atoms are linked to Mn(4) atoms by O<sub>w</sub> vertex sharing. (O<sub>w</sub> : Oxygen atom in a water molecule) (d) Bonding character of Mn(5) and Mn(6). The Mn(5) atoms share two oxygen atoms with each other whereas the Mn(6) atom does not share any atoms with other manganese atoms. (e) Spherical cluster around the P(1) site, with a radius of 4.5 Å illustrating the asymmetrical arrangement of the manganese atoms. 110

**Figure 2.4.** (a, b) Crystal structure of [Mn<sub>4</sub>O<sub>10</sub>(H<sub>2</sub>O)<sub>2</sub>]<sub>2</sub> sheet composed of Mn(1),

Mn(2), Mn(3), and Mn(4). Mn(5) and Mn(6) were omitted for clarity. (c) Chemical environment around water (1) and water (2) molecules. Water (1) were ligated to both Mn(2) and Mn(3) atoms, and water (2) were ligated to Mn(1) and Mn(4) atoms. (d) Chemical environment around water (3) and water (4). In the case of water (3), no chemical bond existed around water (3), while water (4) were solely ligated to Mn(6) atom. (e) Chemical environment around water (5) and water (6). Water (5) were ligated together with Mn(2) and Mn(4) atoms. Water (6) were only ligated to Mn(3) atoms. (f) Chemical structure of  $[\text{Mn}_4\text{O}_{10}(\text{H}_2\text{O})_2]_2$  unit cell. (g) Chemical structure of  $\text{Mn}_2\text{O}_8$  dimer involving two Mn(5) atoms. .... 113

**Figure 2.5.** Characterization of  $\text{Mn}_3(\text{PO}_4)_2 \cdot 3\text{H}_2\text{O}$ . (a, b) SEM images and (c) TEM image of a [001], [010]-oriented  $\text{Mn}_3(\text{PO}_4)_2 \cdot 3\text{H}_2\text{O}$  sheet and SAED patterns (inset). (d) Rietveld-refined XRD patterns of  $\text{Mn}_3(\text{PO}_4)_2 \cdot 3\text{H}_2\text{O}$ .  $R_{\text{wp}} = 1.05\%$ ,  $R_p = 1.22\%$ ,  $R_{\text{exp}} = 0.59\%$ , and  $\chi^2 = 1.79$ ..... 114

**Figure 2.6.** Electrochemical characterization of  $\text{Mn}_3(\text{PO}_4)_2 \cdot 3\text{H}_2\text{O}$ , MnO, and  $\text{MnO}_2$ . (a) Polarization-corrected cyclic voltammetry (CV) curves and (b) Tafel plots for  $\text{Mn}_3(\text{PO}_4)_2 \cdot 3\text{H}_2\text{O}$ , MnO, and  $\text{MnO}_2$  spin-coated on the FTO substrate in which the current value was normalized to the weight and surface area of the catalysts, respectively ..... 118

**Figure 2.7.** The amount of oxygen evolved by  $\text{Mn}_3(\text{PO}_4)_2 \cdot 3\text{H}_2\text{O}$ , MnO, and  $\text{MnO}_2$  with a  $\text{Ru}^{2+}(\text{bpy})_3\text{-S}_2\text{O}_8^{2-}$  system, as recorded by gas chromatography (black, red, and blue). The amount of evolved oxygen was normalized

to the total Mn atoms and surface area in the solution. The turnover frequency numbers of the compounds were estimated from the amount of oxygen gas evolved during the initial 10 min of photolysis for each compounds..... 119

**Figure 2.8.** FE-SEM images of (a) bulk MnO and (b) MnO<sub>2</sub>. (c) The XRD patterns demonstrate that each material has monophasic features and that there are no secondary phases (scale bar: 10 μm)..... 120

**Figure 2.9.** Cyclic voltammetry curves for five catalysts before polarization correction : Mn<sub>3</sub>(PO<sub>4</sub>)<sub>2</sub>·3H<sub>2</sub>O (red), nano MnO (pink), Mn<sub>3</sub>O<sub>4</sub> (blue), Mn<sub>2</sub>O<sub>3</sub> (dark yellow), and MnO<sub>2</sub> (black) Catalyst loaded working electrode were scanned at the rate of 10 mV sec<sup>-1</sup> in 0.5 M phosphate buffer solution at applied potentials ranging from 0.7 V to 1.5 V. 123

**Figure 2.10.** (a) Catalytic current profile obtained upon constant potential (1.4 V vs NHE) electrolysis under pH 7. As shown in the figure, considerable catalytic current was maintained after 2 hours of electrolysis. (b) Cyclic Voltammetry curves of Mn<sub>3</sub>(PO<sub>4</sub>)<sub>2</sub>·3H<sub>2</sub>O, showing the 1<sup>st</sup>, 5<sup>th</sup>, 10<sup>th</sup>, 20<sup>th</sup>, 50<sup>th</sup>, and 100<sup>th</sup> cycles. All cyclic voltammetry curves were obtained in N<sub>2</sub> saturated 0.5 M Na-Pi buffer at a scan rate of 10 mV sec<sup>-1</sup>. 124

**Figure 2.11.** Stability of Mn<sub>3</sub>(PO<sub>4</sub>)<sub>2</sub>·3H<sub>2</sub>O during the water oxidation reaction. To evaluate the stability of Mn<sub>3</sub>(PO<sub>4</sub>)<sub>2</sub>·3H<sub>2</sub>O, bulk electrolysis analysis was performed at (a) 1.28 V and (c) 1.5 V. After 30 min of electrolysis, the catalysts were collected and analyzed. As shown in the SAED patterns, the single-crystalline feature of Mn<sub>3</sub>(PO<sub>4</sub>)<sub>2</sub>·3H<sub>2</sub>O was

maintained at both (b) 1.28 V and (d) 1.5 V (scale bar: 200 nm).125

**Figure 2.12.** EPR analysis of  $\text{Mn}_3(\text{PO}_4)_2 \cdot 3\text{H}_2\text{O}$ , showing the valence change of Mn. (a) Perpendicular mode and (b) Parallel mode X-band CW-EPR spectra of  $\text{Mn}_3(\text{PO}_4)_2 \cdot 3\text{H}_2\text{O}$  varying electrolysis potentials with constant bulk electrolysis time of 1 hr..... 131

**Figure 2.13.** Parallel mode CW-EPR Spectra of  $\text{Mn}_3(\text{PO}_4)_2 \cdot 3\text{H}_2\text{O}$  at three different potentials, 1.0 V (blue), 1.28 V (black), 1.40 V (red) respectively. When the stabilizing agent, pyrophosphate was not used during the preparation of EPR samples,  $\text{Mn}^{\text{III}}$  hyperfine splitting was not observed but only broad signal arising from oxygen were detected. .... 132

**Figure 2.14.** The pair distribution functions of manganese atoms (a) in pristine  $\text{MnO}_2$  (blue) and reduced manganese oxide as  $\text{Mn}(\text{II})$  (black) and  $\text{Mn}(\text{III})$  (red); (b) in pristine  $\text{Mn}_3(\text{PO}_4)_2 \cdot 3\text{H}_2\text{O}$  (black) and oxidized manganese phosphate (red) in which all  $\text{Mn}^{\text{II}}$  atoms were intentionally oxidized to  $\text{Mn}^{\text{III}}$ ; and (c) in pristine  $\text{MnO}$  (black) and oxidized manganese oxide (red). The pair distribution function near 2 Å in  $\text{Mn}_3(\text{PO}_4)_2 \cdot 3\text{H}_2\text{O}$  indicates that the Mn-O bonds originated from phosphate groups. In contrast to  $\text{MnO}_2$ , the split of the pair distribution function from black to red in  $\text{Mn}_3(\text{PO}_4)_2 \cdot 3\text{H}_2\text{O}$  and  $\text{MnO}$  indicates the J-T distortion. (d) The pressure on the cell of each Mn compound when Mn was reduced or oxidized to the 3+ state..... 133

**Figure 2.15.** Computational results for the oxidation process of  $\text{Mn}_3(\text{PO}_4)_2 \cdot 3\text{H}_2\text{O}$ . Unit cell structure when (a) Mn atoms remain in the 2+ oxidation state and (b) all of the manganese atoms inside the crystal are oxidized to

Mn(III). When Mn(2) atom is oxidized to Mn(III), a hydrogen atom (green) is transferred from w1 to w3, resulting in auto-ionization of 2H<sub>2</sub>O into OH<sup>-</sup> and H<sub>3</sub>O<sup>+</sup> near Mn(2). (c, d). Pair distribution functions of Mn atoms in pristine Mn<sub>3</sub>(PO<sub>4</sub>)<sub>2</sub>·3H<sub>2</sub>O and oxidized Mn<sub>3</sub>(PO<sub>4</sub>)<sub>2</sub>·3H<sub>2</sub>O in the 3+ state. (c) The Mn-O bonding is indicated in the diagram, and the oxygen atoms in these bonds originate from the phosphate groups. Compared to the pristine state, the oxidized state exhibits two different bond lengths, one of which one is shorter and the other longer than the pristine state bond length, indicating successful and stable J-T distortion in the oxidized Mn<sub>3</sub>(PO<sub>4</sub>)<sub>2</sub>·3H<sub>2</sub>O. (d) The oxygen atoms in the bonds originate from the water molecules (Ow) or hydroxyl ions. The splitting of the Mn-O bonding peak in oxidized Mn<sub>3</sub>(PO<sub>4</sub>)<sub>2</sub>·3H<sub>2</sub>O confirms the presence of hydroxyl ions, and it also indicates successful J-T distortion around Mn(III). ..... 134

**Figure 3.1.** Scheme for synthesizing manganese (II) oxide nanoparticles by hot injection method. .... 142

**Figure 3.2.** Schematic for ammonia treatment methods ..... 145

**Figure 3.3.** Scheme for the elimination of the degeneracy problem of the  $\alpha$  and  $\beta$  electron spin states by applied magnetic field. .... 151

**Figure 3.4.** TEM image of 10 nm sized MnO nanoparticles Scale : 100 nm, inset: 5 nm ..... 153

- Figure 3.5.** SEM images of MnO nanoparticles on the FTO substrate. Sub 10 nm sized MnO nanoparticles are well assembled after deposition on the FTO substrate..... 157
- Figure 3.6.** X-ray diffraction results of as-prepared and partially oxidized MnO nano crystals. As clearly shown in the Figure 3.6, partially oxidized MnO NCs have MnO and Mn<sub>3</sub>O<sub>4</sub> mixture phases ..... 158
- Figure 3.7.** Fourier transform infrared (FT-IR) spectra of as-prepared, and partially oxidized MnO NCs. As shown in the figure, characteristic peak of alkyl chain around 2800 cm<sup>-1</sup> was almost disappeared after surface treatment. Specifically, The vibrations at 2,922 cm<sup>-1</sup> and 2,852 cm<sup>-1</sup> are asym (C–H) and sym (C–H) features. This result indicates that long organic chain on the synthesized MnO surface was successfully eliminated by ammonia treatment. .... 159
- Figure 3.8.** X-ray photo-electron spectroscopy of different duration ammonia treated MnO in the Mn 2p region. All the XPS spectra were calibrated to C 1s at 285.0 eV. As shown in the figure, peak positions were positively shifted as ammonia treatment time gets longer. ...160
- Figure 3.9.** Comparison of water oxidizing performance for MnO nanocrystals depending on the duration of ammonia treated MnO electrodes (as-synthesized, 30 minutes, 1 hour, 2 hours, 4 hours, 8 hours and 24 hours). 1 hour treated MnO crystal films showed the lowest onset potential at

1.18V (vs. NHE), while as-synthesized MnO film displayed the lowest catalytic activity. .... 161

**Figure 3.10.** Activity trend depending on the ammonia treatment time. More than 3 times of experiments were performed in each conditions. .... 163

**Figure 3.11.** (a) HR-TEM image of the synthesized, monodisperse 8 nm MnO particles. (scale bar : 100 nm) Inset shows a high resolution image of the MnO particles. (scale bar : 5 nm). (b) Polarization-corrected curves for Mn(III)-decorated MnO (red), Co-Pi film (pink), MnO<sub>x</sub> film (brown), fully oxidized MnO (green) and as-prepared MnO nanoparticles (blue)..... 167

**Figure 3.12.** Polarization corrected curves of partially oxidized MnO NCs (black) and conventional Mn-oxide nano-compounds, Mn<sub>2</sub>O<sub>3</sub> (blue), MnO<sub>2</sub> (brown), and Mn<sub>3</sub>O<sub>4</sub> (green). Catalytic current value is normalized based on the (a) loading amount and (b) surface area of each catalysts. Surface area of each catalysts was obtained by BET analysis. (partially oxidized MnO NCs: 28.08 m<sup>2</sup> /g, nano Mn<sub>2</sub>O<sub>3</sub> : 25.43 m<sup>2</sup> /g, nano Mn<sub>3</sub>O<sub>4</sub>: 52.76 m<sup>2</sup> /g and MnO<sub>2</sub> : 14.61 m<sup>2</sup> /g)..... 168

**Figure 3.13.** TEM images of various sized MnO NCs; (a) 10 nm, (b) 15 nm, (c) 20 nm and (d) ~60-80 nm MnO NCs. (scale bar : 50 nm) (e) CV curves for various sized partially oxidized MnO NCs (10 nm (black), 15 nm (red), 20 nm (blue), ~60-80 nm (green)) and other conventional Mn-Oxide nano compounds (Mn<sub>2</sub>O<sub>3</sub> (purple), commercial bulk MnO

(gray), MnO<sub>2</sub>(brown), and Mn<sub>3</sub>O<sub>4</sub>(pink)). f. Tafel plots of various sized partially oxidized MnO NCs and other conventional Mn-oxide nano compounds..... 169

**Figure 3.14.** Measurement of evolved O<sub>2</sub> molecules and catalytic stability test. (a) The amount of evolved O<sub>2</sub> molecules measured by experimental amount (red line) and the theoretical amount of evolved O<sub>2</sub> (blue line) during bulk electrolysis. The theoretical amount of O<sub>2</sub> molecules was plotted assuming a Faradaic efficiency of 100%. b. XPS analysis of partially oxidized MnO NCs. even after 1 h of electrolysis, there was no peak shift in Mn 2p region, which indicates the high stability of partially oxidized MnO NCs. .... 173

**Figure 3.15.** OER polarization curves of partially oxidized MnO NCs on FTO under 50 cycles of accelerated stability test. (a) Chronoamperometry analysis of partially oxidized MnO NCs.(b) ..... 175

**Figure 3.16.** Change in the Mn oxidation state during surface treatment (a, b). Comparison of the XANES data collected from the as-prepared (black), Mn(III)-decorated (Light blue) and fully oxidized MnO (red) with other Mn-oxide compounds. (c) Parallel mode X-band CW-EPR spectra (Inset: perpendicular mode CW-EPR spectra) demonstrating Mn<sup>II</sup> oxidation to a higher oxidation state, Mn<sup>III</sup>, which results in a mixed valency. .... 179

**Figure 3.17.** (a) Cyclic voltammetry curves and (b) Tafel plot of partially oxidized MnO NCs under neutral pH conditions, Inset figure indicates that partially oxidized MnO NCs follows Nernst behavior under near neutral condition. .... 183

---

**Figure 4.1.** Characterization of MnO NPs film. (a) TEM image of synthesized MnO NPs and Plane (b) and cross sectional (c~e) SEM image of MnO NPs films on FTO substrate. .... 193

**Figure 4.2.** Electrochemical analysis of MnO NPs films. Polarization corrected cyclic voltammetric curves (a), Tafel plot near the onset potentials (b), pH dependency at neutral pH range (c), buffer concentration dependency (d), and summary table for resultant reaction order (e) of various thickness MnO NPs film. .... 194

**Figure 4.3.** Comparison of redox characteristics for MnO NPs and bulk manganese oxide compounds. (a) pH dependent redox peak shift of MnO NPs and (b) comparison of redox behaviour between bulk Mn<sub>3</sub>O<sub>4</sub> and MnO compounds and MnO NPs..... 202

**Figure 4.4.** Mn valency change during water oxidation catalysis. Parallel mode X-band CW-EPR spectra (a) (Inset: perpendicular mode CW-EPR spectra), and peak to peak EPR intensity (b). Mn K-edge XANES spectra (c) and average Mn oxidation state demonstrating electro-oxidation of

manganese to higher valency : Initial state (red), 0.4 V (green), 1.1 V (blue), 1.3 V (cyan) vs. NHE..... 208

**Figure 4.5.** *In-situ* UV-Vis spectra of MnO NPs. (a) difference spectra depending on applied potentials. (b) difference spectra of bulk MnO (c, d) Potential dependences of the current density (solid line) and difference absorbance at 400 and 600 nm for MnO NPs. .... 209

**Figure 4.6.** *In-situ* UV-Vis spectra. Difference spectra of (a) MnO NPs in organic electrolytes at various applied potentials: 0.8 V (black), 0.9 V (red), 1.0 V (green), 1.1 V (blue) vs NHE and (b) bulk MnO compounds in phosphate on applied potential: 0.8 V (black), 0.9 V (red), 1.0 V (green), 1.1V (cyan), 1.2V (magenta), 1.3 V (yellow), 1.4 V (dark yellow), 1.5 V (blue) vs NHE 210

**Figure 4.7.** *In-situ* Raman spectra of MnO NPs. All the potential dependent spectra are collected during bulk electrolysis at designed potentials..... 209

**Figure 4.8.** Proposed water oxidation mechanism of conventional Mn catalyst (top) and monodisperse 10 nm sized MnO nano-catalyst. (bottom) Blue and red dotted rectangle indicates quasi-equilibrium and rate determining step, respectively ..... 213

---

**Figure 5.1.** (a) Schematic illustration of Mn<sub>3</sub>O<sub>4</sub>/NiO<sub>x</sub> structure. (b, c) Morphology of NiO<sub>x</sub> and Mn<sub>3</sub>O<sub>4</sub> nanoparticles. (d) ESB/SEM cross images of Mn<sub>3</sub>O<sub>4</sub>/NiO<sub>x</sub> which shows that Mn<sub>3</sub>O<sub>4</sub> and NiO<sub>x</sub> catalysts are stacked in

form of bi-layer structure. .... 220

**Figure 5.2.** Structural characterization: (a)  $\text{Mn}_3\text{O}_4$  Nanoparticles, (b) scheme for fabrication (c) Cross-sectional TEM image, (d,e) Select area electron diffraction image (f,g) O K-edge, Mn and Ni  $L_{2,3}$  edge EELS spectra of Ni- $\text{Mn}_3\text{O}_4/\text{NiO}$  structure ..... 223

**Figure 5.3.** TEM images of (a) Ni-decorated  $\text{Mn}_3\text{O}_4$  nanoparticles and (b) pristine  $\text{Mn}_3\text{O}_4$  nanoparticles. EELS spectra (c) and relative EELS intensity comparison(d,e), XAS spectra, and proposed electronic structure of Ni-decorated  $\text{Mn}_3\text{O}_4$  nanoparticles and pristine  $\text{Mn}_3\text{O}_4$  nanoparticles 224

**Figure 5.4.** Electrochemical characterization. (a) Polarization-corrected curves for  $\text{Mn}_3\text{O}_4/\text{NiO}$ , partially oxidized MnO NPs (green),  $\text{CoO}_x$  film (brown), (b)  $\text{NiO}/\text{Mn}_3\text{O}_4$ ,  $\text{Mn}_3\text{O}_4$  NPs (red), and  $\text{NiO}_x$  films (blue) under near neutral (c) and basic condition. Inset shows Tafel plot of  $\text{Mn}_3\text{O}_4/\text{NiO}$ ,  $\text{Mn}_3\text{O}_4$  NPs and  $\text{NiO}_x$  films. .... 227

**Figure 5.5.** Sustainability test for OER electrocatalysts in neutral condition. Controlled – potential was held constant for 40,000 sec. Continuous potential cycling test was also performed (inset). .... 228

**Figure 5.6.** (a,b) *Ex-situ* XANES Mn K-edge spectra and (c) Average Mn oxidation state of  $\text{Mn}_3\text{O}_4/\text{NiO}$ ,  $\text{Mn}_3\text{O}_4$  NPs, partially oxidized MnO NPs, and reference Mn oxide compounds. (d) Comparison of XPS spectra ( $\text{Mn}_3\text{O}_4/\text{NiO}$ ) for resting state and after OER test in neutral and basic

conditions. .... 233

**Figure 5.7.** *In-situ* XAS spectra (a) and enlarged pre-edge region (b) of Ni-decorated  $Mn_3O_4$  nanoparticles. Potential dependent perpendicular (c) and parallel mode (d) EPR spectra of Ni-decorated  $Mn_3O_4$  nanoparticles.... 236

**Figure 5.8.** Simulation of EPR data (perpendicular mode :left, parallel mode: right) of initial state and catalytic active state of Ni-decorated  $Mn_3O_4$  nanoparticles. Inset displays the calculated EPR simulation parameters. .... 240

**Figure 5.9.** Proposed electronic structure for catalytic active state of Ni-decorated  $Mn_3O_4$  nanoparticles..... 241

# Chapter 1. Introduction

## 1.1. The necessity for the development of future energy resources

Development of sustainable energy source is an urgent issue in the future because the amount of energy consumption have been increasing tremendously. The world energy consumption rate is projected to double from 13.5 TW in 2001 to 27 TW by 2050 and to triple to 43 TW by 2100.<sup>[1]</sup> At present, energy source, such as coal and oil, can provide sufficient amount of energy to humankind. However, renewable and sustainable energy source must be developed for our future because present energy sources have several disadvantages. Carbon dioxide gas is emitted when coal and oil are burned because their main component, carbon, combines with oxygen in the air. 1 kg of coal emits 2.31 kg of CO<sub>2</sub> and 1 gallon of gasoline emits 8.9 kg of CO<sub>2</sub><sup>[2]</sup>. Because high CO<sub>2</sub> concentration accompany high average temperature of the earth,<sup>[4]</sup> CO<sub>2</sub> emission should be inhibited. In addition to this, severe energy depletion will occur unless renewable and sustainable energy is developed because deposits of fossil fuel are limited. So many researchers have been trying to develop sustainable energy source, such as solar, wind, biomass, biofuel, geothermal and hydrogen energy.

Among the various types of sustainable energy, hydrogen is the most common element that can be used as an energy source for fuel cells. Hydrogen is an ideal fuel source because when it is used, by-products are water, heat and electricity

without CO<sub>2</sub> emission. Hydrogen is also non-toxic while nuclear energy, coal, and gasoline are all either toxic or found in hazardous environment. Moreover, hydrogen energy is very efficient fuel source than traditional sources of energy. It has high energy density of 142 kJ/g while gasoline has energy density of 46 kJ/g and natural gas has energy density of 47.2 kJ/g.<sup>[3]</sup> Unlike non-renewable sources of energy, hydrogen energy can be produced on demand.

## **1.2. Electrochemical hydrogen production: Water electrolysis**

Among the various candidates for alternative energy resources, hydrogen is regarded as one of the best promising ones, due to its high energy density and environmentally friendly nature. However, currently most of hydrogen production has been processed by gas reforming process, which is not eco-friendly. Specifically, more than 96% of total hydrogen amount is produced through gas reforming and about 4% of total hydrogen is produced by water electrolysis. Gas reforming method inevitably generates undesired products, such as carbon dioxide (CO<sub>2</sub>) and also requires high temperature and high pressure to operate.

Recently, electrochemical water oxidation has drawn great attention to produce hydrogen. One of the strong point of this method is that water electrolysis only produces molecular hydrogen and oxygen without any by-products. Thus, we can say that electrochemical water splitting is the genuine clean methodology to produce hydrogen sources. In order to commercially use hydrogen as main energy resources, mass production should be realized. Therefore, developments of electrolyzers have been made for low-cost and high efficient water splitting to generate hydrogen. There are representative types of commercial available electrolyzer. (Table 1.1)

<b>Manufacturer</b>	<b>Technology</b>	<b>Rated production(Nm<sup>3</sup>/h)</b>	<b>Efficiency (%)</b>	<b>Location</b>
AccaGen	Alkaline	1-100	52.8-72.7	Switzerland
Avalence	Alkaline	0.4-4.6	65.2-70.8	USA
Erredue	Alkaline	0.6-21.3	59-69.8	Italy
Giner	PEM	3.7	65.5	USA
Statoil	Alkaline	10-500	82.3	Norway
Hydrogenics	Alkaline	10-60	65.5-68.1	Canada
Hydrogenics	PEM	1	49.2	Canada
H2 Logic	Alkaline	0.66-42.62	64.9-70.8	Denmark
Proton Onsite	PEM	0.27-30	48.5-61	USA
ELT	alkaline	3-330	76.9-82.3	Germany

**Table 1.1** Various manufacturers of electrolyzer production

In this section, we will introduce more detailed information for the each electrolyzers. First of all, the alkaline electrolyzer is a type of electrolyzer consisting of two separate electrodes operating in a liquid alkaline electrolyte. (Figure 1.1 (a)).<sup>[4]</sup> The alkaline electrolyzer is safe to use and its life span reaches up to 15 years.<sup>[5]</sup> In addition to this, operating efficiency is estimated to about 50~82%. These days, the alkaline electrolyzer has been used for industrial application due to the outlined advantages. Detailed condition of alkaline electrolyzer is depicted in Figure 1 (a). Membrane should be inserted in the cell to separate the 2 electrodes. Assembled electrolyzer is dipped in concentrated KOH solution (25~30 wt%) to maximize its ionic conductivity and operating temperature is about 65 °C to 100°C.<sup>[6]</sup>

Secondly, the Proton Exchange Membrane (PEM) electrolyzer is an water electrolysis device, adopting proton conduction concept by using polymer membrane as an electrolyte.<sup>[7]</sup> In PEM electrolyzers, a thin polymeric membrane has a cross-linked structure, which is stable in an acidic solution due to the presence of functional groups of the sulfonic acid. The functional groups are also responsible for the proton conducting ability of the materials through an ion exchange mechanism.<sup>[8]</sup> The most commonly used membrane for PEM electrolyzer is the Nafion. Detailed condition of the PEM electrolyzer is depicted in Figure 1.1 (b).

Thirdly, solid oxide electrolyzer operates water splitting reaction, mediated at a high temperature of 600 °C ~ 900 °C. Water splitting using the solid oxide electrolyzer is more efficient than that using the alkaline and the PEM electrolyzer.<sup>[9]</sup> Detailed condition of the PEM electrolyzer is depicted in Figure 1.1 (c).

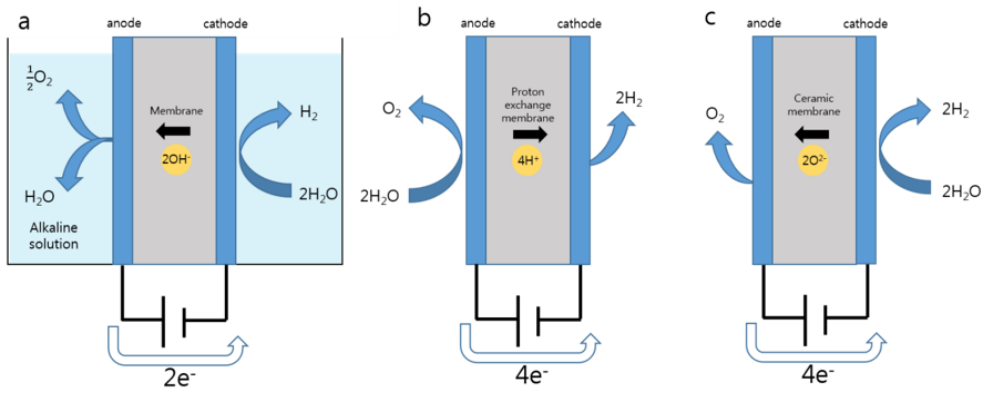


**Figure 1.1** Various electrolyzer system for water splitting reaction. (a) Alkaline electrolyzer, (b) PEM electrolyzer, (c) Solid oxide electrolyzer

### **1.3 Water splitting Catalysts**

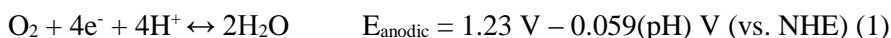
As stated above section, water electrolysis is composed of separate half cell reaction, hydrogen evolution reaction (HER) and oxygen evolution reaction (OER). Thermodynamically, water splitting reaction can be initiated after 1.23 V vs. RHE. However, due to the kinetic issue, conductivity, and charge transport limitation over the electrode, certain amount of overpotential is essentially needed. For the several decades, a numerous researches have been dedicated to discover efficient and robust water splitting catalysts. Because water splitting is subdivided into two halfcell reaction, study for the catalysts is also separately investigated. Hereafter, we will review on the recent discovery of HER and OER catalysts, respectively.

### 1.3.1. Hydrogen evolution catalysts.

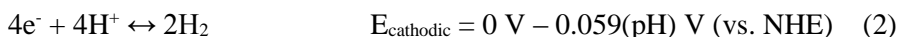
#### 1.3.1.1. General description for HER

Overall water splitting reaction can be expressed as follows.

i) Water oxidation reaction (Oxidation reaction)



ii) Hydrogen evolution reaction (Reduction reaction)



It can be easily deduced that thermodynamic potential of water splitting is  $E_{\text{cell}}^{\circ} = 1.23\text{V}$  vs. NHE at pH 0, calculated by subtracting (2) from (1). Due to the kinetic issue, additional potential, namely overpotential is required to initiate the net reaction. In the view of overall reaction, if current of  $i_c$  flows at the cathode, same current  $i_a$  must flow at the anode to complete the circuit. Thus, overall overpotential for water splitting is obtained by summation of overpotential in both electrodes. Figure 1.2 displays general current versus potential curve for water splitting reaction. Red line and blue line indicates oxidation and reduction reaction of water electrolysis, respectively. The overpotential at the cathode and anode is written  $\eta_c$  and  $\eta_a$ , respectively. Therefore, total applied potential,  $E_{\text{appl}}$  is as follows:

$$E_{\text{appl}} = 1.23\text{V} + \eta_c + \eta_a \quad (3)$$

For the practical application, it is needed to reduce overpotentials. Electrocatalyst for water splitting can reduce the overpotential required for electrolysis of water.

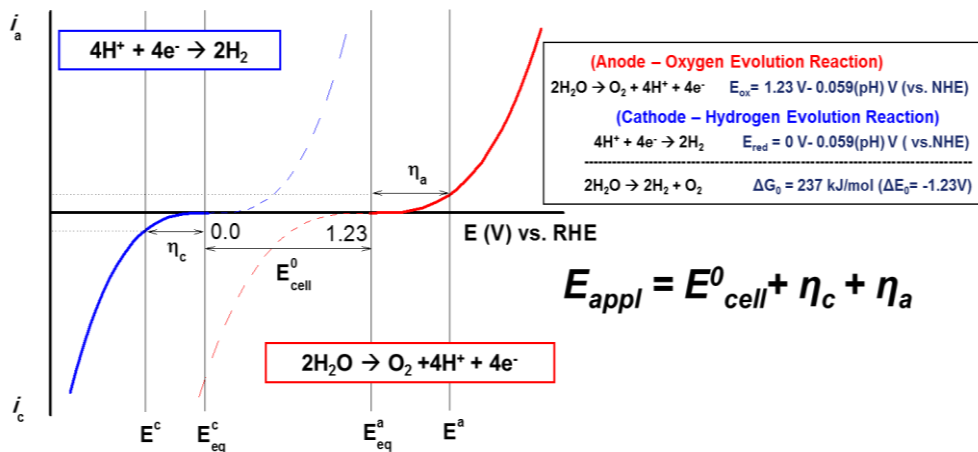
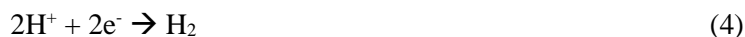


**Figure 1.2** Schematic of the current to potential curve of water splitting reaction

The hydrogen evolution reaction can be written as follow:



Thermodynamic potential at standard condition, pH 0 is 0 V vs. NHE and the potential is dependent on pH ( $E = 0 \text{ V} - 0.059(\text{pH})$  vs NHE). Following representative reaction equations have been suggested as mechanism for hydrogen evolution reaction.



where  $\text{H}_{\text{ads}}$  is the adsorbed hydrogen atom on the surface. Firstly, equation 5 is a proton discharge step (the Volmer reaction), and equation 6 is a desorption step (the Heyrovsky reaction), and eq. (7) is a recombination step (the Tafel reaction). From equation 6 or equation 7, hydrogen molecules are generated. Therefore, we can think two distinct pathways for HER by combination of equation 5~7.

A combination of equation 5, 7 is known as Volmer-Tafel mechanism. In this mechanism, protons from the solution are discharged on the surface, forming adsorbed hydrogen atoms ( $\text{H}_{\text{ads}}$ ). Then, two adjacent adsorbed hydrogen atoms can be combined to form molecular hydrogen (equation 7).

The combination of eq. (5) and (6) step is known as the Volmer-Heyrovsky mechanism. A proton from electrolyte solution is discharged on the catalyst surface to form an adsorbed hydrogen atom. This step is followed by combination with another proton and electron to form molecular hydrogen.

Candidate for HER catalyst include i) noble metals such as Pt, Pd, and Ru as well as ii) transition metal oxide, and iii) carbon based compounds. Since Pt catalysts have long been studied as HER catalysts, HER mechanism mediated by Pt is well described, as follows.



### 1.3.1.2. Experimental parameter in electrochemical reaction

Catalytic activity can be estimated with following experimental parameters; the exchange current density and the bonding energy of hydrogen adsorbed to the catalyst.<sup>[10]</sup> The exchange current is the forward and backward rate when equation 4 is in equilibrium. The ability of a given catalyst is usually evaluated by the exchange current density value because catalytic rate is proportional to exchange current value. The exchange current density ( $J_0$ ) is defined as the one at zero overpotential.<sup>[11]</sup> Normally, catalytic effect is clearly manifested from improving the rate of charge transfer at the interface between the electrode and electrolyte or from lowering the activation energy barrier for a chemical reaction and experimentally expressed by  $J_0$ . The higher  $J_0$  indicates that electron transfer or the adsorption/desorption of protons at the electrode/electrolyte occur more easily with a lower kinetic barrier.

The chemisorption of hydrogen at the catalyst is also the indicator for the ability of catalytic activity for HER.  $\Delta G_{H^*}$ , the free energy of the adsorbed stated calculated as:<sup>[12]</sup>

$$\Delta G_{H^*} = \Delta E_H + \Delta E_{ZPE} - T\Delta S_H \quad (12)$$

where,  $\Delta E_H$  is the hydrogen chemisorption energy,  $\Delta E_{ZPE}$  is the difference in zero point energy between the adsorbed and the gas phase, T is the temperature, and the  $\Delta S_H$  is the entropy of  $H_2$  in the gas phase at standard conditions. The chemisorption energy of hydrogen is also dependent on the surface coverage of the adsorbates.

Theoretically, it is expected that moderate binding energy to adsorbate is required to make efficient catalytic activity. As shown in Figure 1.3, this trend makes so called volcano shape. The volcano plot is usually displayed by catalytic activity versus activity descriptor. In case of HER catalysis, the volcano shape can be described by the exchange current density versus the metal – hydrogen bond strength (Figure 1.3) or the exchange current density versus the calculated the free energy for hydrogen adsorption (Figure 1.4). In the figure, Pt, Pd, and Ru catalysts, noble metal based catalysts are located on the top of the volcano curve. Their moderate binding energy is known to lead good catalytic performance. The overpotential can be understood as the additional energy required to overcome the kinetic barriers. Overpotential is related to the logarithm of the current density as described by the Tafel law <sup>[13]</sup>

$$\eta = A \ln (J/J_0) \quad (13)$$

where parameters  $\eta$  is the overpotential,  $A$  is the “Tafel slope”,  $J$  is the current density,  $J_0$  is “the exchange current density”. The exchange current density includes the activity of the catalyst on the electrode and Tafel slope indicates the mechanism of the water splitting reaction on the electrode. The Tafel slope is also defined to be a measure of the potential increase required to increase the resultant current density by one order of magnitude. The Tafel slope is an inherent property of the catalyst that is determined by the rate-limiting step. Therefore, the value of the Tafel slope should be mechanism dependent and is also related to the adsorbed hydrogen coverage ( $\theta_H$ ) on the surface of electrode.<sup>[14]</sup> For instance, if the recombination of

adsorbed hydrogen (the Tafel reaction) is the rate-determining step for the HER and if the coverage is very high ( $\theta_{\text{H}} \approx 1$ ), the measured Tafel slope is expected as 40 mV/decade. In addition, if the electrochemical desorption step (the Heyrovsky reaction) is the rate-determining step, a Tafel slope of 40 ~ 118 mV/decade is expected and exact value is dependent on the value of  $\theta_{\text{H}}$  (0 ~ 1).

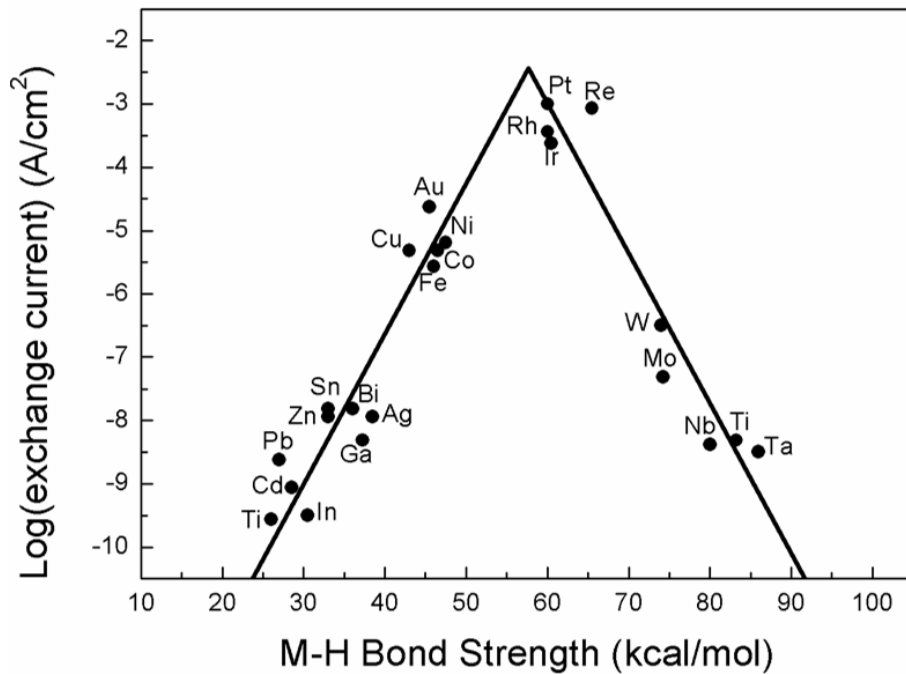


**Figure 1.3.** Experimentally measured exchange current,  $\log(J_0)$ , for hydrogen evolution over different metal surfaces plotted as a function of the calculated hydrogen chemisorption energy per atom.

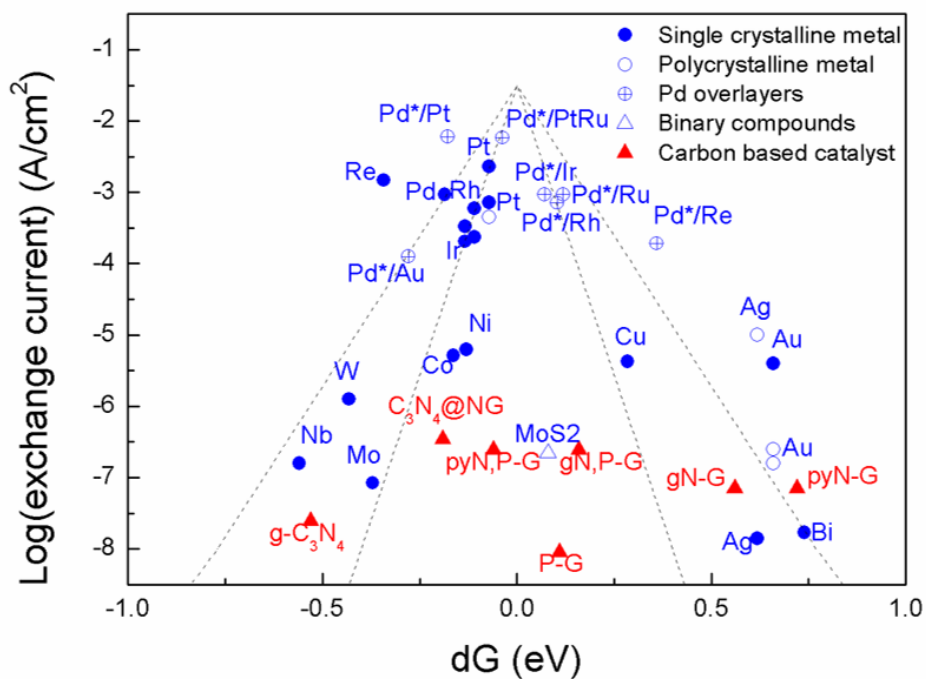


**Figure 1.4.** Experimentally measured exchange current,  $\log(J_0)$ , for hydrogen evolution over different catalyst plotted as a function of the calculated the free energy for hydrogen adsorption. Data are collected from the previous literature (Table 1.2 ~ 4).

### 1.3.1.3. Various HER catalysts

Traditionally, pure metals (Pt, Pd, Ni, etc.),<sup>[15]</sup> metal composites/alloys (Ni–Mo, Ni–Co, Ni–Mo–Cd, etc.),<sup>[16]</sup> and compounds including nonmetallic elements (RuO<sub>2</sub>, Sr<sub>x</sub>NbO<sub>3</sub>, Mo<sub>3</sub>S<sub>4</sub>, etc.)<sup>[17]</sup> have been used for HER catalysts.

Many researches in HER have been made for HER of metal based elements or metal as HER electrocatalysts since a few decades. Among metal based catalysts, Pt, Pd, and Ru are near the top of the volcano curve, showing highly catalytic activity for HER. Their binding energy to hydrogen is neither too strong nor too weak, which leads to the good catalytic behavior. Table 1.2 are the selection of experimental values of exchange current for the hydrogen evolution on metals and metal oxides. Recent progress has been concentrated on the incorporation of noble metal nanoparticle in earth-abundant elements rather than usage of full noble metals only. Notwithstanding, there has been a report about a highly active and durable class of electrocatalysts by exploiting the structural evolution of Pt-Ni bimetallic nanocrystals (Figure 1.5).<sup>[18]</sup> Table 1.2 ~ 1.4 are the selection of experimental values of exchange current for the hydrogen evolution on metals, metal oxides, bimetallic compounds, and other types of catalysts, respectively. Recently, binary and bimetallic catalysts also have been attracting attention in renewable energy technologies due to the low cost and high stability, but their insufficient activity compared to the pure metallic catalysts is still a challenging issue.

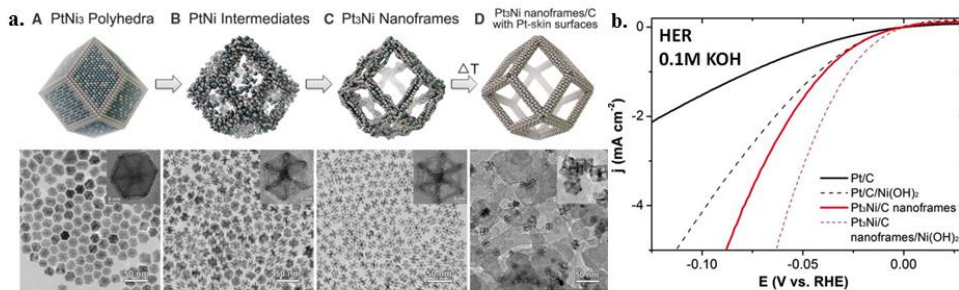


**Figure 1.5.** Structure and electrochemical property of Pt<sub>3</sub>Ni nanoframe (a) Schematic illustrations and corresponding TEM images of the samples obtained at four representative stages during the transformation process from polyhedral to nanoframes. (b) Comparison of HER activities for Pt/C, Pt/Ni(OH)<sub>2</sub>/C, Pt<sub>3</sub>Ni nanoframes/C, and Pt<sub>3</sub>Ni frames/Ni(OH)<sub>2</sub>/C in alkaline electrolyte. <sup>[18]</sup>

Catalysts	Loading method	Electrolyte	Activity		Ref. (Year)
			Tafel Slope (mV/dec)	Exchange current $-\log(j_0)$ (A/cm <sup>2</sup> )	
Ni/Si-micro wire	Electro deposition	KHP, K <sub>2</sub> SO <sub>4</sub> , KOH (pH 4.5)	N/A	N/A	[19](2011)
Ni-Mo/Si-micro wire	Electro deposition	KHP, K <sub>2</sub> SO <sub>4</sub> , KOH (pH 4.5)	N/A	N/A	[19](2011)
Ag	Ag wire	H <sub>2</sub> SO <sub>4</sub> , K <sub>3</sub> PO <sub>4</sub>	N/A	7.9	[20](1967)
		0.1M H <sub>2</sub> SO <sub>4</sub>	N/A	7.9	[21](1967)
		1M H <sub>2</sub> SO <sub>4</sub>	N/A	7.8(+) 11.0(-)	[22](1970)
		1M H <sub>2</sub> SO <sub>4</sub>	N/A	7.9	[23](1968)
		0.1M HCl 0.4M HCl	(58±2) (57±2)	5.82~6.77 5.11~5.96	[24](1957)
Al	Chemipolished	N/A	N/A	8.0	[25](1957)
	Al wire	0.5M H <sub>2</sub> SO <sub>4</sub>	114	7.7	[26](1968)
Au	Pure Au	0.5M H <sub>2</sub> SO <sub>4</sub>	N/A	5.9	[27](1967)
		0.1M HCl	85	6.7	[28](1957)
		0.1M HCl	118	6.3	[29](1955)
Bi	Pure Bi	0.45M H <sub>2</sub> SO <sub>4</sub>	N/A	10.4	[30](1964)

		1M H <sub>2</sub> SO <sub>4</sub>	N/A	7.8(+) 10.0(-)	[31](1969)
		0.5M H <sub>2</sub> SO <sub>4</sub>	N/A	10.8	[32](1970)
		0.1M HClO <sub>4</sub>	N/A	8.1	[33](1961)
Cd	Cd wire	1M H <sub>2</sub> SO <sub>4</sub>	N/A	11.6	[34](1970)
		0.25M H <sub>2</sub> SO <sub>4</sub>	135±12	10.8	[35](1964)
Co	Pure Co	0.5M H <sub>2</sub> SO <sub>4</sub>	N/A	5.3	[36](1963)
		0.05M H <sub>2</sub> SO <sub>4</sub>	N/A	5.6	[37](1970)
		1M H <sub>2</sub> SO <sub>4</sub>	N/A	5.2	[38](1946)
Cr	Pure Cr	0.5M H <sub>2</sub> SO <sub>4</sub>	126	6.5	[39](1969)
		0.01M HCl	116	7.25	[28](1957)
		0.5M H <sub>2</sub> SO <sub>4</sub>	N/A	7.4	[40](1968)
Cu	Pure Cu	0.5M H <sub>2</sub> SO <sub>4</sub>	N/A	7.8	[41](1966)
		0.5M H <sub>2</sub> SO <sub>4</sub>	N/A	7.9	[42](1969)
		0.5M H <sub>2</sub> SO <sub>4</sub>	120	7.7	[43](1965)
		0.5M H <sub>2</sub> SO <sub>4</sub>	N/A	7.9	[44](1970)
Fe	Pure Fe	0.5M H <sub>2</sub> SO <sub>4</sub>	N/A	5.1	[27](1967)
		0.5M H <sub>2</sub> SO <sub>4</sub>	120	5.6	[43](1965)
		0.01M HCl	118	6.29	[28](1957)
		1M H <sub>2</sub> SO <sub>4</sub>	N/A	6.0	[38](1946)
		1M H <sub>2</sub> SO <sub>4</sub>	N/A	5.9	[45](1956)
Ga	Dropped Pure Ga	1M H <sub>2</sub> SO <sub>4</sub>	N/A	8.4(+) 10.8(-)	[31](1969)

		0.5M H <sub>2</sub> SO <sub>4</sub>	N/A	10.4	[46](1969)
		0.5M H <sub>2</sub> SO <sub>4</sub>	N/A	10.1	[47](1965)
		0.1M HClO <sub>4</sub>	2.63±0.10	9.9	[48](1966)
Hg	Dropped Pure Hg	7.5M HClO <sub>4</sub>	483	12.2	[49](1969)
		0.5M H <sub>2</sub> SO <sub>4</sub>	N/A	12.5	[50](1934)
		0.125M H <sub>2</sub> SO <sub>4</sub>	N/A	12.1	[51](1944)
		0.1M HCl	113±1	12.3	[52](1949)
		0.05M H <sub>2</sub> SO <sub>4</sub>	N/A	12.6	[53](1965)
In	Pure In	0.1M HClO <sub>4</sub>	120	11.9	[54](1964)
		0.5M H <sub>2</sub> SO <sub>4</sub>	N/A	9.4(+) 11.0(-)	[55](1970)
		0.1M HClO <sub>4</sub>	120	11.2	[56](1965)
		1M H <sub>2</sub> SO <sub>4</sub>	N/A	9.7	[57](1965)
Ir	Pure Ir	0.5M H <sub>2</sub> SO <sub>4</sub>	N/A	3.4	[27](1967)
		0.5M H <sub>2</sub> SO <sub>4</sub>	N/A	3.7	[53](1965)
Mn	Pure Mn	0.05M H <sub>2</sub> SO <sub>4</sub>	N/A	10.9	[58](1962)
Mo	Pure Mo	0.1M HCl	92±12	7.3	[28](1957)
Nb	Pure Nb	0.5M H <sub>2</sub> SO <sub>4</sub>	N/A	8.4	[59](1965)
Ni	Ni wire	0.25M H <sub>2</sub> SO <sub>4</sub>	124±10	5.2	[35](1964)
		0.5M H <sub>2</sub> SO <sub>4</sub>	N/A	5.25	[60](1965)
		0.5M H <sub>2</sub> SO <sub>4</sub>	N/A	5.3	[27](1967)

		0.05M H <sub>2</sub> SO <sub>4</sub>	N/A	5.15	[37](1970)
		1M HClO <sub>4</sub>	125	5.3	[61](1964)
Os	Pure Os	1M HCl	124	4.1	[62](1970)
Pb	Pure Pb	0.25M H <sub>2</sub> SO <sub>4</sub>	125±14	11.3	[35](1964)
		0.01-1M HCl	N/A	11.5	[63](1970)
Pd	Pure Pd	0.1M H <sub>2</sub> SO <sub>4</sub>	N/A	3.0	[53](1965)
		1M H <sub>2</sub> SO <sub>4</sub>	N/A	3.2	[64](1961)
		0.1M HCl	55	3.3	[28](1957)
		0.1M HCl	110±5	2.8	[65](1960)
		0.5M H <sub>2</sub> SO <sub>4</sub>	N/A	3.1	[27](1967)
Re	Pure Re	1M H <sub>2</sub> SO <sub>4</sub>	N/A	3.0	[66](1950)
Rh	Pure Rh	0.5M H <sub>2</sub> SO <sub>4</sub>	N/A	3.6	[53](1965)
		0.25M H <sub>2</sub> SO <sub>4</sub>	28±2	3.2	[35](1964)
		0.01M HCl	55	3.8	[28](1957)
		0.5M H <sub>2</sub> SO <sub>4</sub>	N/A	3.5	[27](1967)
Ru	Pure Ru	1M HCl	117	4.2	[62](1970)
Sb	Pure Sb	0.5M H <sub>2</sub> SO <sub>4</sub>	N/A	8.1	[67](1969)
		1M H <sub>2</sub> SO <sub>4</sub>	N/A	5.1(+), 7.8(-)	[31](1969)
		1M H <sub>2</sub> SO <sub>4</sub>	N/A	9.0	[68](1957)
		1M H <sub>2</sub> SO <sub>4</sub>	N/A	9.3	[38](1946)
		1M HClO <sub>4</sub>	170	5.7	[61](1964)
Sn	Pure Sn	1M H <sub>2</sub> SO <sub>4</sub>	N/A	7.8(+), 9.8(-)	[31](1969)

		1M H <sub>2</sub> SO <sub>4</sub>	N/A	10.5	[69](1956)
		1M H <sub>2</sub> SO <sub>4</sub>	N/A	9.3	[38](1946)
		1M HCl	N/A	10.2	[53](1965)
Ta	Pure Ta	0.5M H <sub>2</sub> SO <sub>4</sub>	N/A	8.5	[59](1965)
		1M HClO <sub>4</sub>	N/A	8.6	[70](1969)
Te	Pure Te	1M HClO <sub>4</sub>	48	11	[61](1964)
Ti	Pure Ti	1M H <sub>2</sub> SO <sub>4</sub>	N/A	8.2	[71](1962)
		pH2.2 H <sub>2</sub> SO <sub>4</sub>	150	8.3	[72](1970)
		0.5M NaCl	150	8.5	[73](1954)
Tl	Pure Tl	0.1M HClO <sub>4</sub>	N/A	9.5(+), 11.7(-)	[74](1970)
		0.8M H <sub>2</sub> SO <sub>4</sub>	N/A	11.1	[75](1951)
		1M HCl	85	9.8	[76](1948)
Zn	Pure Zn	1M H <sub>2</sub> SO <sub>4</sub>	N/A	10.5	[77](1957)
		1M H <sub>2</sub> SO <sub>4</sub>	N/A	10.6	[78](1970)
		0.5M HCl	N/A	10.6	[79](1969)
		1M HCl	N/A	10.0	[80](1963)
Pt	Pure Pt	0.05M H <sub>2</sub> SO <sub>4</sub>	(26±3)	N/A	[81](1952)
		H <sub>2</sub> SO <sub>4</sub> Buffer (pH 0.5)	(26)	N/A	[82](1954)
		(pH 0.9)	(30)		
		(pH 1.4)	(30)		
		(pH 1.9)	(30)		
		(pH 1.95)	(30)		

		(pH 2.0)	(35)		
		(pH 2.25)	(35)		
		(pH 2.35)	(29)		
		(pH 2.7)			
		NaHCO <sub>3</sub>			
		Buffer	(138)		
		(pH 8.2)	(116)		
		(pH 9.4)	(126)		
		(pH 9.6)	(125)		
		(pH 10.4)	(127)		
		(pH 10.9)	(128)		
		(pH 11.2)			
		NaOH	(126)		
		buffer			
		(pH 12.1)			
	Pure Pt	1M H <sub>2</sub> SO <sub>4</sub>	(25.5±0.5)	2.82(P <sub>H2</sub> =1.0atm) 3.15(P <sub>H2</sub> =0.46atm) 3.40(P <sub>H2</sub> =0.31atm) 3.56(P <sub>H2</sub> =0.24atm) 3.95(P <sub>H2</sub> =0.14atm) 4.23(P <sub>H2</sub> =0.05atm)	[ <sup>183</sup> ](1959)
	Pure Pt	Prepared in H <sub>2</sub> 0.1M HCl 1.0M HCl 1.5M HCl	28±2 30±22 29±1	3.45±0.45 2.95±0.55 2.85±0.65	[ <sup>24</sup> ](1957)

W	W wire	0.1M HCl	60±3	5.96~5.35	[24](1957)
Ni	Ni foil	1M NaOH	(115)	5.70	[84](1998)
TiO <sub>2</sub> -Bi <sub>2</sub> O <sub>3</sub> NPs/ Bi-doped TiO <sub>2</sub> NPs/ SnO <sub>2</sub> - Bi <sub>2</sub> O <sub>3</sub> / IrO <sub>2</sub> - Ta <sub>2</sub> O <sub>5</sub> /Ti	Sequential Coating with heat treatment	50mM NaCl	N/A	N/A	[85](2012)
RuO <sub>2</sub> - IrO <sub>2</sub> /Ti	Chemical Deposition	1M HClO <sub>4</sub>	40	N/A	[86](1994)

\*KHP : Potassium Hydrogen phthalate

**Table 1.2.** Tafel slope and exchange current for previously reported various hydrogen evolution catalysts. Loading method and electrolyte used are described as well.

Catalyst/ Substrate (adhesive)	Loading method	Electrolyte	Activity			Ref. (Year)
			Tafel Slope (mV/dec)	TOFs (S <sup>-1</sup> )	Exchange current -log(j <sub>0</sub> ) (A/cm <sup>2</sup> )	
MoS <sub>2</sub> NSs/GC (Nafion)	Mechanical activation	0.5M H <sub>2</sub> SO <sub>4</sub>	(68)	0.08(potential x)	4.41	<sup>[94]</sup> (2013)
MoS <sub>x</sub> /Ti-n <sup>+</sup> p-Si	Electro deposition	1.0M HClO <sub>4</sub>	(39)	N/A	N/A	<sup>[95]</sup> (2012)
MoS <sub>x</sub> /GC (2<x<3)	Wet- Chemical- Synthesis Drop casting	0.5M H <sub>2</sub> SO <sub>4</sub>	(50)	0.3(at 200mV)	N/A	<sup>[96]</sup> (2012)
Mo <sub>2</sub> C/CNT-Gr	Modified Urea-glass route	0.5M H <sub>2</sub> SO <sub>4</sub>	(58)	N/A	4.21	<sup>[97]</sup> (2014)
Mo <sub>2</sub> C/CNT (Nafion)	Carburization	0.1M HClO <sub>4</sub>	(65.3±3.1)	N/A	4.85	<sup>[98]</sup> (2013)
MoS <sub>2</sub> /Mo/n <sup>+</sup> p-Si	Sputtering & Sulphidization	1M HClO <sub>4</sub>	112.23( 103.84)	N/A	5.77	<sup>[99]</sup> (2013)
Undoped MoS <sub>x</sub> /Act-C-	Electro deposition	1M HClO <sub>4</sub>	(38.4)	N/A	5.97	<sup>[100]</sup> (2013)

Paper						
1T-MoS <sub>2</sub> /GC	Electrochemical Exfoliation	0.5M H <sub>2</sub> SO <sub>4</sub>	43.5±2.5(40)	N/A	N/A	<sup>[188]</sup> (2013)
MoS <sub>3</sub> /GC	Drop or Spray casting	1M H <sub>2</sub> SO <sub>4</sub>	(41) (54)	N/A	7.70 6.20	<sup>[1101]</sup> (2012)
MoS <sub>3</sub> -MWCNT/GC	Drop or Spray casting	1M H <sub>2</sub> SO <sub>4</sub>	(41) (42)	N/A	7.10 6.89	<sup>[1101]</sup> (2012)
MoS <sub>x</sub> /GC (2<x<3)	Electrodeposition	1M H <sub>2</sub> SO <sub>4</sub>	(40.5)	0.8(at 220mV)	6.89	<sup>[1102]</sup> (2011)
WS <sub>2</sub> -NSs/GC	Electrochemical Exfoliation	0.5M H <sub>2</sub> SO <sub>4</sub>	60(55)	175(at 288mV)	4.70	<sup>[189]</sup> (2013)
MoS <sub>2</sub> -NPs/Au	PVD & Sulphidization	pH 0.24 H <sub>2</sub> SO <sub>4</sub>	(57.5±2.5)	0.02	6.70±0.19	<sup>[1103]</sup> (2007)
1T-MoS <sub>2</sub> -NSs/Graphite	CVD	0.5M H <sub>2</sub> SO <sub>4</sub>	54(43)	N/A	N/A	<sup>[1104]</sup> (2013)
[Mo <sub>3</sub> S <sub>4</sub> ] <sup>4+</sup> /HOPG (Nafion)	Drop casting	0.5M H <sub>2</sub> SO <sub>4</sub>	(120)	0.07	6.66	<sup>[1105]</sup> (2008)
MoS <sub>2</sub> /RGO	Solvother	0.5M	(41)	N/A	N/A	<sup>[1106]</sup> (2011)

	mal Synthesis	H <sub>2</sub> SO <sub>4</sub>				
$\alpha$ -MoS <sub>2.7</sub> /NPG	Chemical plating	0.5M H <sub>2</sub> SO <sub>4</sub>	(41)	N/A	N/A	<sup>[107]</sup> (2014)
[Mo <sub>3</sub> S <sub>13</sub> ] <sup>2-</sup> /GP	Drop casting	0.5M H <sub>2</sub> SO <sub>4</sub>	(40)	3(at 200mV)	N/A	<sup>[87]</sup> (2014)
MoO <sub>3</sub> -MoS <sub>2</sub> NWs/FTO	HWCVD & Sulphidiza tion	0.5M H <sub>2</sub> SO <sub>4</sub>	(55±5)	4(at 272mV)	N/A	<sup>[108]</sup> (2011)
Mesoporous DG MoS <sub>2</sub> /FTO	Electrode position & Sulphidiza tion	0.5M H <sub>2</sub> SO <sub>4</sub>	(50)	N/A	6.16	<sup>[109]</sup> (2012)
WC/Graphite (Nafion)	Carburizat ion	100mM H <sub>2</sub> SO <sub>4</sub> 100mM Na <sub>3</sub> PO <sub>4</sub>	N/A	N/A	N/A	<sup>[90]</sup> (2009)
Co-S/FTO	Electrode position	1.0M K <sub>3</sub> PO <sub>4</sub>	(93)	0.017(at 187 mV)	3.59	<sup>[93]</sup> (2013)
NiMoN <sub>x</sub> /C	Reducing precursor	0.1M HClO <sub>4</sub>	(35.9)	N/A	0.24	<sup>[110]</sup> (2012)
Li-MoS <sub>2</sub> /CFP	Electroche mical exfoliatio	0.5M H <sub>2</sub> SO <sub>4</sub>	(62)	0.1	0.167	<sup>[111]</sup> (2014)

	n					
CoSe <sub>2</sub> /CFP	Drop casting & Selenization	0.5M H <sub>2</sub> SO <sub>4</sub>	(42.1)	N/A	0.0049±0.0014	<sup>[91]</sup> (2014)
Co <sub>0.6</sub> Mo <sub>1.4</sub> N <sub>2</sub> /G C	Nitration & Drop casting	0.1M HClO <sub>4</sub>	N/A	N/A	0.23	<sup>[92]</sup> (2013)
Ni <sub>74</sub> Mo <sub>16</sub> P <sub>10</sub> /Cu Ni <sub>74</sub> Mo <sub>16</sub> P <sub>10</sub> /Cu Ni <sub>86</sub> Mo <sub>12</sub> P <sub>2</sub> /Cu Ni <sub>71</sub> Mo <sub>27</sub> P <sub>2</sub> /Cu Ni <sub>73</sub> P <sub>27</sub> /Cu Ni <sub>89</sub> Mo <sub>11</sub> /Cu Ni <sub>50</sub> Mo <sub>45</sub> P <sub>5</sub> /Cu Ni <sub>92</sub> P <sub>8</sub> /Cu	Electro deposition	1M NaOH	(97) (103) (112) (89) (109) (180) (74) (57)	N/A	0.05 0.12 1.29 3.10 0.07 12.7 1.98 0.24	<sup>[84]</sup> (1998)

\*NS : Nano Sheet \*NP : Nano particles \*GC : Glassy Carbon \*Act-C-Paper : Activated Carbon paper \*α : Amorphous catalyst \*NPG : Dealloyed nanoporous gold \*GP : Graphite paper \*HWCVD : Hot-wire chemical vapor deposition \*DG : Double Gyroid \*g- : Graphitic \*NG : N-Graphene \*CFP : Carbon Fiber Paper

**Table 1.3** Tafel slope, turnover frequency(TOF), and exchange current values for the previously reported binary metals catalysts. Loading method and electrolyte used are described.

Catalyst/Substrate (adhesive)	Loading method	Electrolyte	Activity			Ref. (Year)
			Tafel Slope (mV/dec)	TOF s (S <sup>-1</sup> )	Exchange current -log(j <sub>0</sub> ) (A/cm <sup>2</sup> )	
Monolayer graphene	CVD grown graphene	1M HClO <sub>4</sub>	(75)	N/A	7.57	[114](2013)
N doped Gr	Annealing mixed precursors	0.5M H <sub>2</sub> SO <sub>4</sub> 0.1M KOH	(116) (143)	N/A	7.15 9.93	[116](2014)
P doped Gr	Annealing mixed precursors	0.5M H <sub>2</sub> SO <sub>4</sub> 0.1M KOH	(133) (159)	N/A	8.05 10.79	[116](2014)
N,P doped Gr	Annealing mixed precursors	0.5M H <sub>2</sub> SO <sub>4</sub> 0.1M KOH	(91) (145)	N/A	6.62 9.40	[116](2014)
g-C <sub>3</sub> N <sub>4</sub> @NG/GC (Nafion)	Exfoliation & Polycondensation	0.5M H <sub>2</sub> SO <sub>4</sub>	(51.5)	N/A	6.46	[117](2014)

**Table 1.4.** Tafel slope and exchange current values of previously reported carbon based HER catalysts. Loading method and electrolyte used are described.

#### 1.3.1.4. Characterization methods for electrocatalysts

Electro-catalytic activity for each catalysts is investigated with cyclic voltammetry (CV) methods. Generally, also in this thesis, electrochemical measurements are performed in a three-electrode system, consisting of the working electrode, the counter electrode, and the reference electrode. Pt electrode or HOPG electrode is used for counter electrode and Ag/AgCl/KCl electrode or saturated Calomel electrode is used as the reference electrode. In order to compare the activity with other catalysts easily, potential should be selected and unified. In this thesis, we used Normal Hydrogen electrode (NHE) and Reversible hydrogen electrode (RHE). Each reference electrodes should be carefully calibrated in an aqueous solution with high purity H<sub>2</sub> saturation at room temperature. The RHE scale can be varied between -0.197 V and -0.266 V vs. the Ag/AgCl/KCl reference electrode depending on the concentration of KCl.<sup>[118]</sup> Since the potential difference between Ag/AgCl and RHE is also dependent on other experimental conditions, such as electrolyte pH, temperature, and so on, the potential should be carefully measured before each set of measurement and it is better to conduct same experiments several times to check the reproducibility.

Various conducting substrate have been used as working electrode. Representative examples are fluorine doped tin oxide, indium tin oxide, glassy carbon, highly oriented pyrolytic graphite (HOPG), carbon paper, nickel foam, and so on. Moreover, loading of catalyst materials on the working electrode are also

important process. Spin coating method or dropcasting of catalyst ink or screen printing of catalyst paste are the representative preparation methods. Conventionally, catalyst powder was mixed with 1~10 wt % of Nafion, a carbon black, and proper solvent to make ink. And mixing with organic binder, carbon black and N-methylpyrrolidone(NMP) solution makes catalyst paste. Prepared working electrode was stored at 100 ~ 110 °C for drying.

## **1.3.2. Oxygen evolution reaction (OER)**

### **1.3.2.1. Water splitting and OER**

Water electrolysis to generate hydrogen and oxygen molecules is an environmentally friendly energy conversion method.<sup>[119, 120]</sup> In nature, there is water oxidizing complex, existing in photosystem of plant. In the photosystem, there are two separate subunits, photosystem I and photosystem II. In the photosystem II, the water is oxidized into oxygen, which is catalyzed by  $Mn_4CaO_5$  cluster.<sup>[121]</sup>

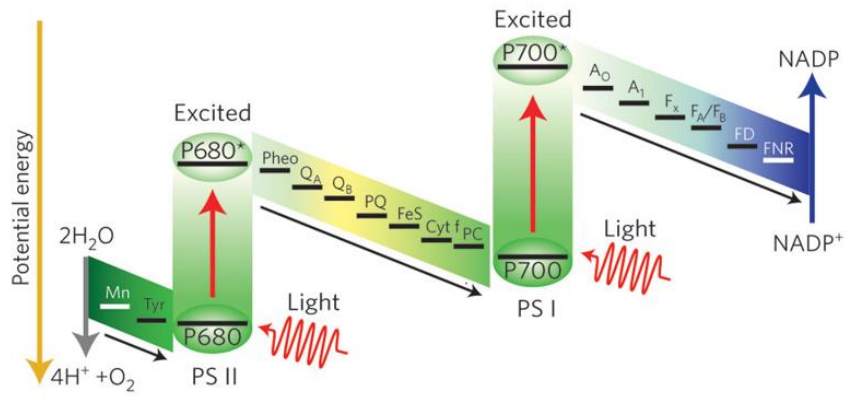


**Figure 1.6.** Scheme for overall water splitting in photosystem.

As shown in Figure 1.6, the electrons arisen from the water oxidation are transferred via several steps and then excited using visible light at two reaction centers, P700 and P680.<sup>[121-122]</sup> These electrons and surrounding hydrogen ions are incorporated with the  $\text{NADP}^+$  (Nicotin amide adenine dinucleotide phosphate), and consequently reduced form of  $\text{NADP}^+$ ,  $\text{NADPH}$ , are formed.<sup>[122-123]</sup> The reducing power  $\text{NADPH}$  was used for making glyceraldehyde 3-phosphate which is used as immediate nutrient in plant.<sup>[124]</sup> Therefore, we can understand natural photosystem as two separate half cell reaction, water oxidation and  $\text{NADP}$  reduction reaction, respectively. Inspired by biological complex, artificial water splitting is categorized into two redox reactions, as well. At the anodic part, water is oxidized into oxygen molecules, and at the cathode, the protons reduced into hydrogen using the electrons from the anode.<sup>[123]</sup> This reaction can be summarized into the above described overall water splitting equations (1) and (2).

The anode half reaction, oxygen evolution reaction (OER) has been regarded as a major bottleneck in the overall water splitting process due to the slow transfer rate of four electrons and the high activation energy barrier for O-O bond formation. In this chapter, artificial water splitting system, specifically OER process and OER catalysts will be discussed. Regarding OER catalysts, most researches are basically progressed by inspiration from the photosystem II. Intensive researches have focused on developing photo/electro catalysts for overall water splitting.<sup>[124, 125]</sup> First, in case of photocatalysts, electrons and holes are generated by light at the conduction band and valence band of the catalysts, respectively.<sup>[126]</sup> The electrons at

the conduction band and the holes at the valence band are used for hydrogen and oxygen production respectively. Using the photocatalysts, water can be converted into hydrogen and oxygen molecules with only visible lights without any additional voltage. Historically, Since Fujishima group used  $\text{TiO}_2$  as photocatalysts for water splitting for the first time in 1970s,<sup>[124]</sup> many photocatalysts for cathodic and anodic reaction have been developed. However, even after using photocatalysts, the catalytic performance of the catalysts was not good enough due to the intrinsic kinetic barrier.<sup>[125]</sup> This phenomenon is originated from the nature of water splitting reaction that requires multi-step reactions which involve multi electron and holes.<sup>[123]</sup> To enhance the efficiency, many researches have designed the combination of electrocatalysts and semiconductor for both anodic and cathodic reaction. Indeed, there have been numerous studies to find the electrocatalysts and incorporate them with the photoanode/photocathode materials to lower the activation energy and promote the efficiency of water splitting reaction.<sup>[127]</sup>

### 1.3.2.2. Natural photosynthetic complex

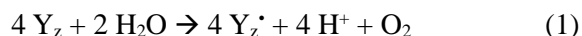
There exist unexceptionally efficient water oxidizing catalyst in biological systems, such as algae, plants, and cyanobacteria.  $Mn_4CaO_5$  cluster, reaction center in photosystem II (PS II), can mediate the oxygen evolution reaction with low overpotentials ( $\eta$  : 160mV) and high turnover frequencies ( $\sim 10^3 s^{-1}$  per Mn atom), which have not been achieved so far with any synthetic catalysts. Four manganese and one calcium atoms are asymmetrically structured by the specific coordination with surrounding peptides such as histidine and aspartic acid. Each four Mn atoms undergo successive changes in oxidation state, taking part in a so-called Kok cycle. A number of research efforts have been dedicated to develop manganese based catalysts to mimic biological complex. Unfortunately, however, apparent activity gap exist between biological enzyme and synthetic Mn catalysts, and the reasons underlying the differences in ability are not fully clarified. Therefore, fundamentally it is required to understand the structure detailed catalytic cycle of  $Mn_4CaO_5$  cluster in PS II. Several spectroscopic analysis, such as XRD, XAS, and RIXS analysis have been adopted to obtain the structural information in each step in kok cycle.

This chapter will be described as follows. Firstly, we focused on the structural uniqueness of the  $Mn_4Ca$  cluster in PS II. Recent discovery of the electronic and magnetic structural information for each steps in kok cycle and proposed water oxidizing steps were summarized. Secondly, we overviewed the

various Mn based electrocatalysts under neutral and basic conditions. Critical arguments about the factors which affect the performance of Mn based electrocatalysts and the associated scientific issues will be introduced as well.

### 1.3.2.3 Mn<sub>4</sub>Ca cluster for water oxidation

Water oxidizing complex (WOC) in PS II catalyzes water oxidation reaction with an oxidant of redox-active tyrosine residue (Tyr161, Y<sub>z</sub>), oxidized by light absorption from P680 reaction center. The actual net reaction equation for oxygen evolving reaction is written as equation (1).



Four electrons transfer from the Mn cluster to Y<sub>z</sub> is accompanied with four deprotonating to thylakoid lumen during water oxidation. In 1970, Kok *et al.* suggested a linear four step mechanism of natural water oxidation called Kok cycle comprised of five intermediate S<sub>i</sub>(i = 0-4) states where subscript i denotes the number of oxidizing equivalents stored for oxygen evolution. After four oxidizing equivalents are accumulated subsequently, the S<sub>4</sub> state can release a dioxygen molecule and spontaneously decays to the most reduced S<sub>0</sub> state. Under dark adaption condition, S<sub>0</sub> state is gradually oxidized to dark stable S<sub>1</sub> state.

Interestingly, WOC in PS II exhibit superior catalytic performance to synthetic catalysts. According to previous study, turnover frequency value is around 25,000 mmol/Mn mol and overpotential is around 160mV at pH 6.5, which has never been achieved by manmade catalysts. In order to mimic the unprecedented efficiency, fundamental challenge is to understand the atomic and electronic structural change of the Mn cluster during Kok cycle. In this section, we will summarize a detailed structural analysis of each S<sub>i</sub> state which has been studied over four decades.

### 1.3.2.3.1. Atomic structural analysis of PS II active center

The dark-stable  $S_1$  state is considered as a starting point for structural analysis because the structure of  $S_1$  state can be detected by X-ray crystallographic methods. Although several studies on crystallization of  $S_1$  state have been reported since 2001, the structural information of  $S_1$  state could not be identified until 2011 due to the resolution limit of analytical instruments. Finally, in 2011, for the first time, Umena *et al.* succeeded to assign the detailed atomic structure of  $S_1$  state with a 1.9 Å resolved X-ray diffraction technique. At this resolution, the structure of the Mn cluster can be described clearly because the electron density of each atom in the Mn cluster was individually separated. They revealed the Mn cluster had a distorted cubane structure, consist of three distinct manganese atoms and 1 calcium atoms with oxo-bridges, with a dangling another manganese atom. In addition, 4 water ligands bound to the calcium atom and the dangling manganese atom and the surrounding environments of the Mn cluster were identified. Interestingly, O5 has a relatively long Mn-O distance compared to other bonding in the cluster, which implies that O5 could be moved easier than other atoms due to weaker bonding strength and thus O5 would play an important role in natural water oxidation.

After crystal structure of Mn cluster was suggested by 1.9 Å resolution XRD analysis, there have been debates about the position of O5 atom. Whereas the XRD result suggest that position of O5 is the midpoint of Mn1 and Mn4, different analysis were obtained by EXAFS and DFT calculation method that O5 should be

more closer to Mn4 than Mn1. This discrepancy is originated by X-ray radiation damage to the Mn cluster, which results in partial reduction of manganese, elongation of atomic distance, and destruction of the Mn cluster. According to the related works on the X-ray damage to the Mn complex, around 25% of manganese was reduced under the XRD of 1.9 Å resolution condition and the S<sub>1</sub> state could be reduced to S<sub>0</sub> state and even to pre-S<sub>0</sub> states like S<sub>-1</sub>, S<sub>-2</sub>, and S<sub>-3</sub> states. Recently, in 2015, Suga *et al.* reported ‘radiation-damage-free’ S<sub>1</sub> structure at a 1.95 Å resolution by using femtosecond X-ray free electron laser(XFEL), which could collect diffraction pattern before the radiation damage. Contrast to the previous XRD structure, the XFEL position of O5 was closer to Mn4 than Mn1, which is well matched with the previous EXAFS and DFT analysis.

The S<sub>2</sub> state, one electron oxidized state from the S<sub>1</sub>, has been investigated by using EPR, EXAFS, and DFT analysis. Interestingly, two distinctive species are identified which exhibit a multiline EPR signal at  $g = 2$  under room temperature and a signal at  $g \geq 4.1$  under lower temperature. Furthermore, it is revealed that the two EPR signals interconvert reversibly each other by changing the temperature or illumination condition, indicating the S<sub>2</sub> state has two interconvertible spin states with total spin numbers of  $S = 1/2$  for the multiline EPR signal at  $g = 2$  and  $S = 5/2$  for the EPR signal at  $g \geq 4.1$  respectively. The structural uniqueness of S<sub>2</sub> state is also verified from the EXAFS studies and DFT calculations. Specifically, open cubane structure with  $S = 1/2$  is constructed as O5 move toward Mn4 site if Mn4(III) is oxidized to Mn4(IV) under light illumination. On the other hand, when Mn1(III)

is oxidized to Mn1(IV), closed cubane structure with  $S = 5/2$  is expected as O5 move toward Mn1. Such a unique inter-convertibility of  $S_2$  state makes complicated to understand Kok cycle.

It should be noted that detailed mechanism of Kok cycle could be entirely changed depending on which  $S_2$  states would be participated in the next  $S_2$ - $S_3$  transition where a water substrates is inserted and subsequently O-O bond formation occurs. There have been two representative studies about the mechanisms of  $S_2$ - $S_3$  transition, which are a quantum mechanics/molecular mechanics(QM/MM) based work by Guidoni *et al.* and a DFT based work by Siegbahn. Guidoni *et al.* Firstly, Guidoni *et al* suggested the closed cubane  $S_2$  structure would be participated in the transition and W3 bound to Ca atom would shift to occupy the uncoordinated site of Mn4 following the oxidation of Mn4(III) to Mn4(IV). On the other hand, Siegbahn proposed the open cubane  $S_2$  structure would be involved and a new water molecule outside the Mn cluster would enter the empty coordination site of Mn1 following the oxidation Mn1(III) to Mn1(IV). Up to now, it is not clear which one is the active structure for the next state. Therefore, the following O-O bond formation and the subsequent  $S_3$  and  $S_4$  states are still controversial. Nevertheless, the  $S_3$  state comprised of all the six-coordinated Mn(IV) with the total spin number  $S = 3$  was verified by recent EPR works and the clues of the O-O bond formation has been discovered by substrate exchange experiments using ammonia and methanol.

### 1.3.2.3.2. Electronic structural analysis for PS II active center

Generally, the geometric structure is closely related with the spin state of metal components, originated from inter-magnetic coupling. Thus, resolution of electronic structure in Mn<sub>4</sub>Ca cluster, specifically Mn valency change in Kok cycle is essentially demanding task. In this regard, electron paramagnetic resonance (EPR) spectroscopy has been adopted to investigate the spin state of the cluster. In terms of total spin number, the S<sub>i</sub> states can be classified into “resting-like states(S<sub>0</sub>, S<sub>1</sub>, and open cubane S<sub>2</sub>)” with low total spin numbers and “active-like states(closed cubane S<sub>2</sub>, S<sub>3</sub>, and S<sub>4</sub>) with high total spin numbers, which indicates the strong correlation between the catalytic reactivity and the spin state of the Mn cluster.

As a pioneering work, Pantazis et al have focused on unraveling the electronic structure of the cluster by EPR analysis and DFT calculations. For instance, a closed structure in active like states would adopt a high spin state because a ferromagnetic coupling of metal-oxo-metal bonding is normally preferred when the bonding angle became close to 90°. So, it is expected that the active-like states of the Mn cluster, where the water insertion and the O-O bond formation occurs, favor high spin states. In this respect, they emphasized the role of inter-convertible S<sub>2</sub> state, which is key step for dramatic change from low spin to high spin state accompanying the formation of closed cubane structure. Additionally substrate substitution experiments using ammonia and methanol supported such hypothesis and implied a new water inserting pathway including Mn<sub>4</sub> and the Asp61 residue. Combined

together, Pantazis et al proposed a new  $S_2$ - $S_3$  transition model: i) deprotonation of W1, ii) hydrogen bond formation between W2 and O5 iii) nucleophilic attack of another water molecule to Mn4 iv) successive rearrangement of the atomic structure. Regarding  $S_3$  states, Two possible intermediates with total spin number  $S = 6$  and 3 were suggested based on the DFT calculations. However, up to now, EPR signals corresponding to the  $S_3$  intermediates have not been detected yet.

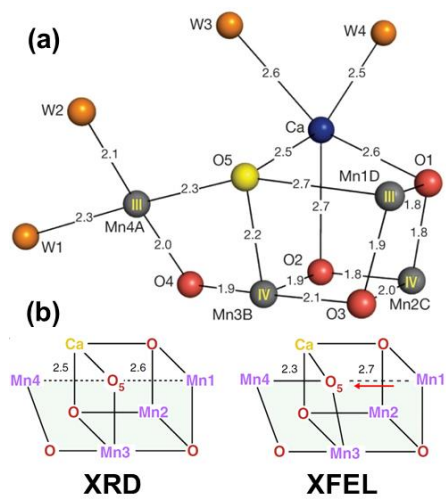


**Figure 1.7.** (a) Atomic structure of the Mn cluster in S<sub>1</sub> state by XFEL. Roman numerals indicate Mn-O, Ca-O, Mn-water, and Ca-water distances(Å) in the Mn cluster. (b) Comparison between the earlier XRD structure and the later XFEL structure of the Mn cluster in S<sub>1</sub> state.

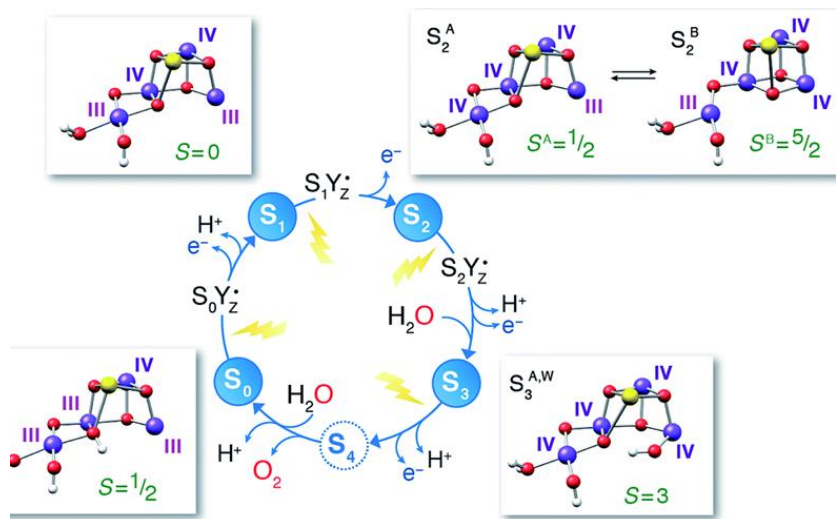


**Figure 1.8.** The Kok cycle with spectroscopically consistent structures of the Mn cluster and their spin states.

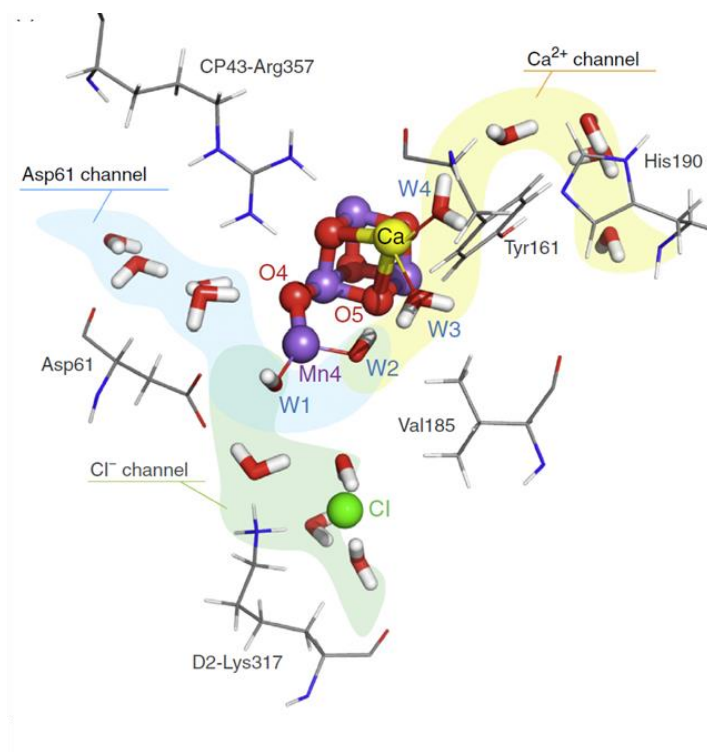


**Figure 1.9.** Proposed water channels to and from the Mn cluster in S<sub>2</sub>-S<sub>3</sub> transition.

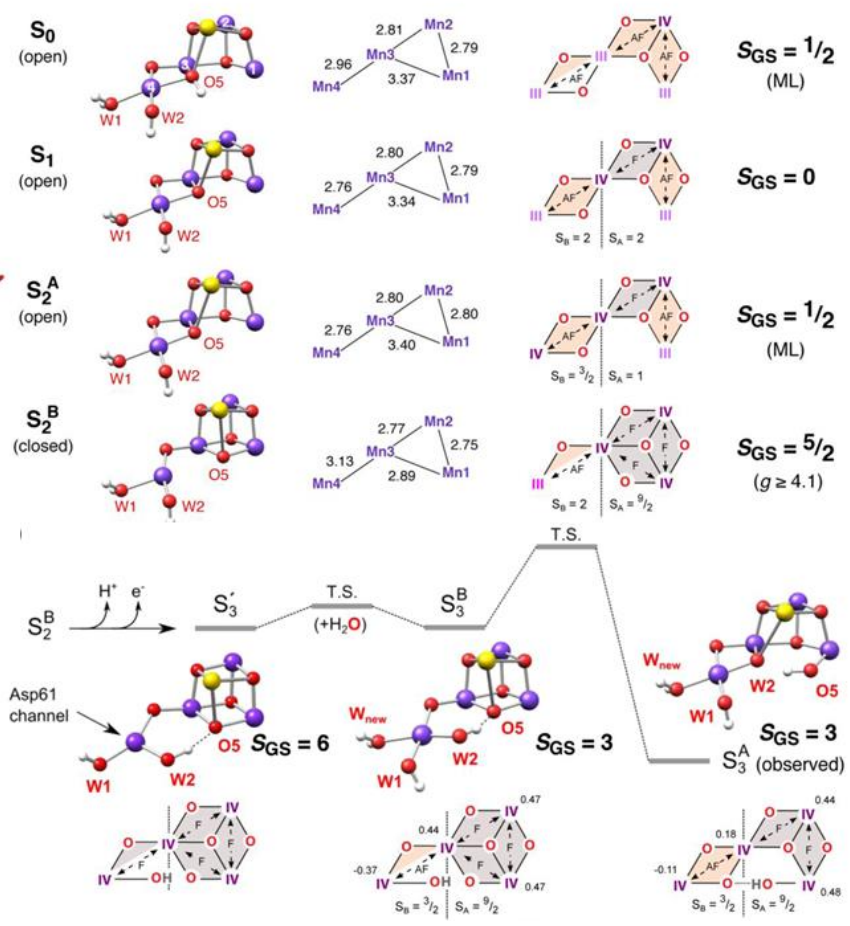


**Figure 1.10.** Structural model for all  $S_i$  states of the Mn cluster: atomic structure of the Mn cluster, Mn-Mn distances(Å) of optimized geometries, the nature of magnetic couplings(AF for antiferromagnetic coupling and F for ferromagnetic coupling), and total spin numbers respectively. (c) Proposed  $S_3$  intermediate states upon  $S_2$ - $S_3$  transition. The loss of the Asp61/W1 hydrogen bond with subsequent low-barrier water insertion *via* the Asp61 channel and rearrangement is involved.

### **1.3.2.4. Bio-inspired Mn based water oxidation catalysts**

#### **1.3.2.4.1. Fundamental issue: Inferior activity at neutral condition**

The extraordinary water oxidizing performance of the cubical  $\text{Mn}_4\text{CaO}_5$  cluster has continuously inspired researchers to develop Mn based oxygen evolving catalysts. <sup>[129-134]</sup> Representatively, asymmetric cubical structure, proton coupled electron transfer, and mixed valency, are considered as primary factors for outstanding activity of the cluster. In addition, non-toxic and earth abundant nature and intrinsic facile redox capability of manganese are also attractive property for the OER application. <sup>[135]</sup> Therefore, for several decades, discovery of bio-mimetic water oxidizing catalysts have been intensely progressed to replace noble metal such as Ir, Ru based commercial catalysts.

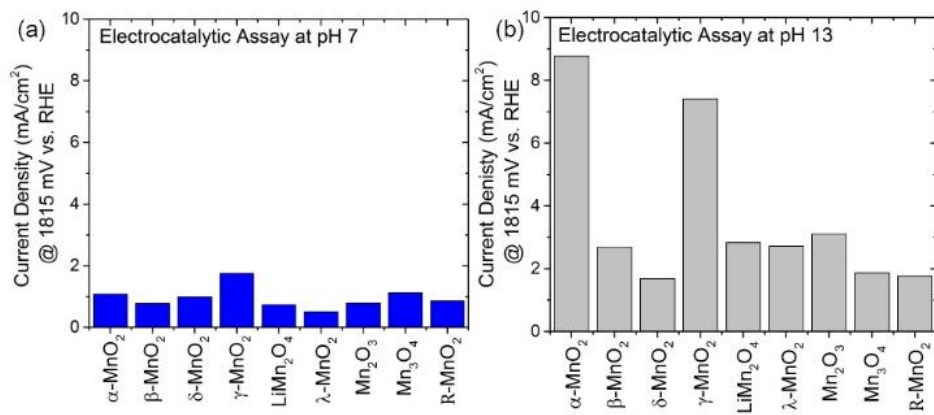


**Figure 1.11.** Electrochemical activity of various manganese oxide catalysts under (a) pH 7 and (b) pH 13

However, contrary to the expectation, catalytic activity for oxygen evolution reaction is just moderate compared to other first row transition metal based catalysts. Specifically, under neutral pH, severe activity degradation were observed. According to recently reported benchmarking paper, all the conventional manganese oxide compounds such as  $\text{Mn}_2\text{O}_3$ ,  $\text{MnO}_2$ ,  $\text{Mn}_3\text{O}_4$  exhibit inferior activity compared to the activity at pH 13 (Figure 1.11). Compared to the fact that well-known catalysts, amorphous cobalt phosphate or nickel borate materials only requires around 400mV overpotentials to reach  $1\text{mA}/\text{cm}^2$ , more than 600mV of overpotential are needed to operate water oxidation process by Mn catalysts. For a long time, it has been main issue in Mn based OER catalysts and still remains as an unresolved problem. In the following section, we will focus on the review the discussions for activity descriptor of Mn catalysts and recent discovery in Mn based OER catalysts.

#### 1.3.2.4.2. The descriptors for OER activity in Mn based electrocatalysts

For the decades, a lot of researches have been attempted to find out the activity descriptor of Mn based catalyts. Firstly, it has been verified that the local structure is strongly correlated to catalytic activity. Dismuke group investigated the water oxidation activity of several representative manganese oxides,  $Mn_3O_4$ ,  $Mn_2O_3$ , and various  $MnO_2$  polymorphs.<sup>[136]</sup> In this study, they discovered that catalysts which possess longer average Mn-O distances in edge sharing octahedra exhibit higher catalytic performance. The manganese oxides with longer average Mn-Mn distance indicate that oxygen atoms are weakly bonded to manganese. Moreover, it was discovered that the order for OER activity ( $Mn_2O_3 > Mn_3O_4 \gg$  polymorphs of  $MnO_2$ ) is well matched with the portion of Mn(III) as well.

The Dau and Strasser group also emphasized the atomic structure of manganese through comparison between two different nanostructures, layered and cross-linked manganese oxides.<sup>[137]</sup> Layered  $MnO_x$  exhibits higher intrinsic onset activity than cross-linked  $MnO_x$  owing to electrochemical accessibility. The layered structure has higher accessibility for water molecules and buffer species through interlayer compared to cross-linked  $MnO_x$ . Because tunnel structure in the cross-linked structure is not suitable size for passing the large molecules. This structural difference results in a larger number of active sites for layered  $MnO_x$  than cross-linked  $MnO_x$ . However, unlike inherent onset activity, Tafel analysis indicated that layered  $MnO_x$  exhibits poor electrochemical activity compared to cross-linked  $MnO_x$ .

Layered  $\text{MnO}_x$  is composed of edge-shared (di- $\mu$ -oxo)  $\text{MnO}_6$  with few defect sites. In cross-linked  $\text{MnO}_x$ , more defect sites are driven by mixed structure, edge-shared and corner-shared (mono- $\mu$ -oxo)  $\text{MnO}_6$  octahedral. These defect sites resulting in di- $\mu_2$ -oxo structure are highly related to OER activity, so layered  $\text{MnO}_x$  (109 mV/dec) has low Tafel slope (high electrochemical activity) compared to cross-linked  $\text{MnO}_x$  (151 mV/dec).

Suib group studied the structure-activity relationship of nanostructured  $\text{MnO}_2$  ( $\alpha$ ,  $\beta$  and  $\delta$ - $\text{MnO}_2$ ) and amorphous  $\text{MnO}_x$ .<sup>[138]</sup> The OER activity of analyzed manganese oxides is attributed to the di- $\mu_2$ -oxo structure in the edge-shared  $\text{MnO}_6$  octahedral. Suitable tunnel size and large surface area are also required for moderate catalytic performance. Because these structural factors lead to high reachability of water molecules and other reactants. Additionally, Low charge transfer resistance examined by electrochemical impedance spectroscopy (EIS) enhances OER efficiency.

### 1.3.2.4.3. Limitation for catalysis under neutral pH

As stated above section, manganese based electrocatalysts have inherent hindrance for water oxidation under neutral condition. This undesired phenomena has relevance with Mn redox process during catalysis. As shown in Figure 1.12, when  $\text{Mn}^{3+}$  species which adopt  $t^3_{2g}e^1_g$  d orbital configuration is generated under catalytic reaction, there exist two possible reaction pathways; i) J-T distortion and ii) Charge disproportionation. In case of conventional Mn oxide compounds, unfortunately, rigid and highly symmetric  $\text{MnO}_6$  octahedrons hamper Jahn-Teller (J-T) distortion of Mn enters. Instead, charge disproportionation reaction, which makes  $\text{Mn}^{3+}$  split into  $\text{Mn}^{2+}$  and  $\text{Mn}^{4+}$  is proceeded. The suppressed redox kinetics sequentially leads to inferior catalytic performance. Theoretically, instability of  $\text{Mn}^{3+}$  intermediates in conventional manganese oxide were demonstrated via computation analysis. Figure 1.13 displays pair distribution function of  $\text{MnO}_2$ , and MnO compounds when manganese atoms were intentionally oxidized to  $\text{Mn}^{3+}$  state. As expected, J-T distortion is barely observed in reduced  $\text{MnO}_2$  case. Moreover, although J-T distortion is proceeded to some extent in oxidized MnO structure, high inner pressure makes Mn(III) in MnO unstable, as shown in Figure 1.13d. In addition, in case of  $\text{Mn}^{3+}$  containing Mn oxide compounds, such as  $\text{Mn}_2\text{O}_3$ , it was verified that facile valency change is difficult to occur due to the high reorganizational energy associated with  $\text{Mn}^{3+}$  oxidation. Similar phenomena was reported in the Ni(III)-Bi catalysts. Non-anodized  $\text{Ni}^{3+}$ -Bi catalysts have properties inferior (Tafel slope: 100

mV/dec) to those of their anodized counterparts because of the reorganization energy required to oxidize J-T distorted  $\text{Ni}^{3+}$  to non-distorted  $\text{Ni}^{4+}$ . The Nocera group interrogated mechanism for electrodeposited manganese oxide ( $\text{MnO}_x$ ) through electrokinetic analysis. <sup>[139]</sup> Combined Tafel analysis and proton dependence in the electrokinetic rate law, two competing mechanisms were revealed. In basic condition, one-proton and one-electron PCET prior to rate determining step dominates. But, in acidic condition, CD of Mn(III) predominates.

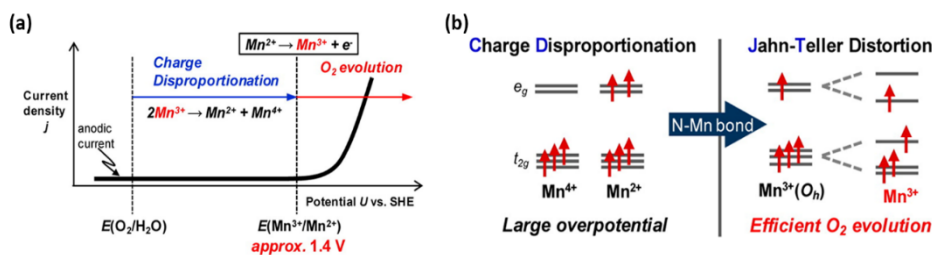


**Figure 1.12.** (a) Schematic illustration of a current density ( $j$ ) vs potential ( $U$ ) curve for a pristine  $\delta$ - $\text{MnO}_2$  electrode under neutral pH conditions. The surface-associated intermediate  $\text{Mn}^{3+}$  species are rapidly consumed by charge disproportionation to form  $\text{Mn}^{2+}$  and  $\text{Mn}^{4+}$ , resulting in no net charges passing across the electrode.

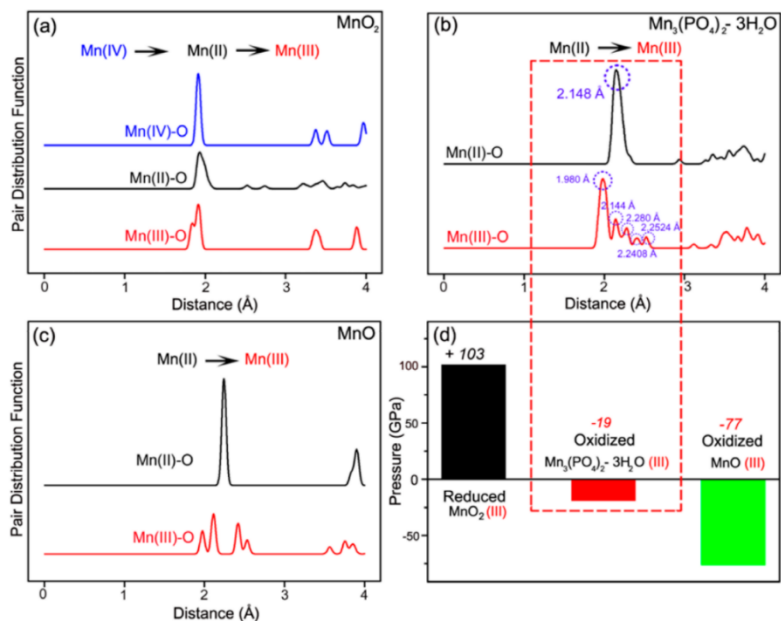


**Figure 1.13.** Pair distribution functions of manganese atoms (a) in pristine MnO<sub>2</sub> (blue) and in reduced manganese oxide as Mn(II) (black) and Mn(III) (red); (b) in pristine Mn<sub>3</sub>(PO<sub>4</sub>)<sub>2</sub>·3H<sub>2</sub>O (black) and in oxidized manganese phosphate (red), in which all Mn(II) atoms were intentionally oxidized to Mn(III); and (c) in pristine MnO (black) and in oxidized manganese oxide (red) (d) The pressure on the cell of each Mn compound when Mn was reduced or oxidized to the 3+ state. It is noted that the pressure is unrealistically large because all the Mn atoms change the charge state.

Therefore, the fundamental challenge is how to flexibly change the valence state of Mn atoms with ease and stabilize reaction intermediates in a crystal structure during oxygen evolution at neutral pH. Recently, Nakamura group examined CD effect of MnO<sub>2</sub> nanoparticles in wide range of pH (4~13) performed *In-situ* Uv-vis spectroscopy.<sup>[140]</sup> The spectral change related to Mn(III) species as surface intermediate was observed with accompanying increase of anodic current for water oxidation. Ligand exchange method with poly-(allylamine hydrochloride) (PAH) was tried to prevent Mn(III) intermediate from CD process.<sup>[141]</sup> N-Mn bonds formed by the ligand exchange broke the symmetric structure of MnO<sub>6</sub> with Mn(III) and effectively inhibited CD process. This effect reduced an onset potential about ~500 mV for MnO<sub>2</sub> nanoparticles at pH 8.

Recently, our group reported several phosphor containing manganese compounds as water oxidizing catalysts. Firstly, Mn<sub>3</sub>(PO<sub>4</sub>)<sub>2</sub>·3H<sub>2</sub>O, new crystal structure was synthesized by wet precipitation method. Compared to previously reported Mn based crystalline catalysts, Mn<sub>3</sub>(PO<sub>4</sub>)<sub>2</sub>·3H<sub>2</sub>O has highly distorted structure, triclinic with possessing three water molecules inside of the unit cell. Six different manganese sites in one unit cell can be seen in Figure 1.14a. Bulky phosphate polyhedron induces a less-ordered Mn arrangement in Mn<sub>3</sub>(PO<sub>4</sub>)<sub>2</sub>·3H<sub>2</sub>O structure, which results in improved catalytic activity compared to conventional Mn oxide compounds (Figure 1.14b). Computational analysis, displayed in Figure 1.13, indicated that the structural flexibility in Mn<sub>3</sub>(PO<sub>4</sub>)<sub>2</sub>·3H<sub>2</sub>O could stabilize the Jahn–Teller-distorted Mn(III) and thus facilitate Mn(II) oxidation as well. Nam group also

studied a pyrophosphate based Mn compound,  $\text{Li}_2\text{MnP}_2\text{O}_7$  for water oxidation catalysis. Influence of oxidation state of Mn and asymmetric Mn geometry on water oxidation catalysis was verified using  $\text{Li}_2\text{MnP}_2\text{O}_7$  and its derivatives. Indeed, outlined researches Mn(III) portion and asymmetric arrangement of Mn atoms which can be seen in the WOC, enhance catalytic water oxidation reaction.

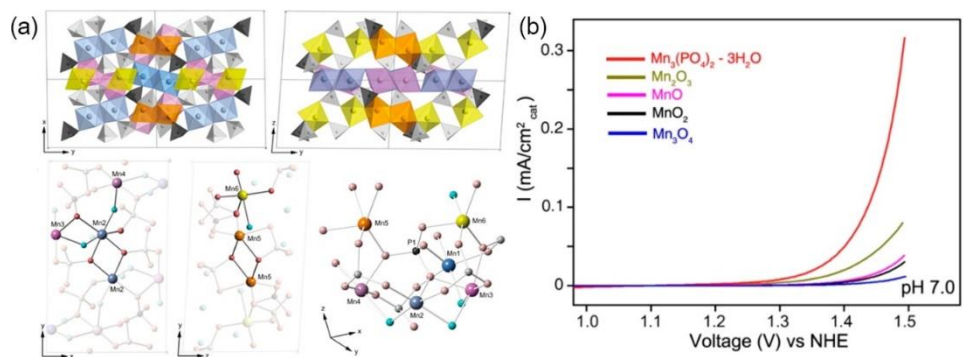


**Figure 1.14.** Schematic representation of crystalline structure (a) and cyclic voltammetry curves of  $\text{Mn}_3(\text{PO}_4)_2 \cdot 3\text{H}_2\text{O}$  and activity comparison with conventional Mn oxide compounds under neutral pH. (b)

#### 1.3.2.4.4. Recent discovery in Mn based catalysts

Aformentioned, mixed Mn valency ( $Mn^{3+/4+}$ ) is the one of the unique properties in  $Mn_4Ca$  cluster. Theoretically, Navrotsky et.al verified the effect of mixed valence state on the OER performance during oxidation and reduction stage. Due to the no huge structure changes with closely balanced equilibrium of two mixed valence, it is more advantageous to redox process. It was also experimentally demonstrated with four different manganese compounds;  $CaMnO$ ,  $Mn_2O_3$ ,  $MnO_2$  and  $Mn_3O_4$ . Among the candidates, mixed valent  $CaMnO$  ( $Mn^{3+}$  and  $Mn^{4+}$ ) showed the highest catalytic activities and efficient electron transfer capability.

In order to realize the mixed valent state, recently amorphorized structure has been intensely studied. Driess group synthesized amorphous  $MnO_x$  structure using chemical oxidants, ceric ammonium nitrate(CAN) (Figure 1.15). They claimed that enhanced activity compared to initial crystalline  $MnO$  should be attributed to the change in mean oxidation states from + 2 to about + 2.5 after CAN treatment and insisted the amorphorized structure, resembles the  $Mn_4CaO_5$  cluster in nature [10]. In their following report, by changing atmosphere (air, nitrogen, and vacuum) they synthesized various kinds of manganese based catalyst, bixbyite ( $Mn_2O_3$ ), hausmannite( $Mn_3O_4$ ), and manganosite ( $MnO$ ) and found an exceptionally high activity of  $Mn_2O_3$ .<sup>[142]</sup>

Dau and Jaramillo group realized mix valent catalysts using electrodeposition method.<sup>[143]</sup> From the XANES and XPS analysis, existence of

mixed valency was verified and good activity for water oxidation was reported. By analyzing EXAFS and XANES, the average oxidation state of manganese in the active  $\text{MnO}_x$  film was determined to be +3.8, differing from +4.0 in inactive film<sup>[144]</sup>. And in their subsequent research with Strasser group, the structural designs of s- $\text{MnO}_x$  and i- $\text{MnO}_x$  kept nearly unchanged during oxygen evolution reaction, but the oxidation state of manganese increased from 3.5 to 3.9-4. Mn-based catalysts, s- $\text{MnO}_x$  and i- $\text{MnO}_x$  were synthesized by chemical symproportionation and impregnation respectively. The former has similar structure to  $\delta$ - $\text{MnO}_2$  that is analogous to layered architecture and the latter shows combination of 3D cross-linked  $\beta$ - and defective  $\gamma$ - $\text{MnO}_2$ . By analyzing electrochemical and electrokinetic characterization, they found that there exists a fundamental difference in catalytic performance between cross-linked and layered structures.

Recently, Nam group reported nanosized manganese oxide catalysts, displaying outstanding catalytic activity under neutral condition. As shown in Figure 1.16, sub 10 nm sized monodisperse MnO nanoparticles showed unexpectedly high catalytic performance compared to well-known catalysts, Co-Pi and  $\text{MnO}_x$ . Additionally, they synthesized various nanosized manganese oxide,  $\text{Mn}_5\text{O}_8$ ,  $\text{Mn}_3\text{O}_4$ ,  $\text{Mn}_2\text{O}_3$  and found out that nanosized manganese oxide showed similar catalytic activity regardless of phase and superior to their bulk counterparts. It was demonstrated that the stability of  $\text{Mn}^{3+}$  intermediates could be significantly improved on nanosized oxide surface, during catalysis.

Agapie group has synthesized  $[\text{Mn}_3\text{CaO}_4]^{6+}$  core structure which is almost

identical to that of the WOC in nature by using a trinucleating ligand.<sup>[136c]</sup> This was the first work that mimics the local Mn geometry of the WOC nearly perfect.(Figure 1.18)<sup>[145]</sup> Moreover, using the  $[\text{Mn}_3\text{CaO}_4]^{6+}$  core structure, they further synthesized  $\text{Mn}_3\text{M}(\mu_4\text{-O})(\mu_2\text{-O})(\text{M} = \text{Ca}^{2+}, \text{Sr}^{2+}, \text{Na}^+, \text{Zn}^{2+}, \text{Y}^{3+})$  to understand the role of redox-inactive metals on water oxidation catalysis.<sup>[146]</sup> By comparing their catalysts, they found that redox inactive metals (M) can modulate the redox potential of Mn atoms.<sup>[146]</sup> From this result, they make a conclusion that Ca ions might change the redox potential of Mn atoms in the WOC, and consequently enhances the catalytic ability of the WOC.<sup>[146]</sup> (Figure 1.17)

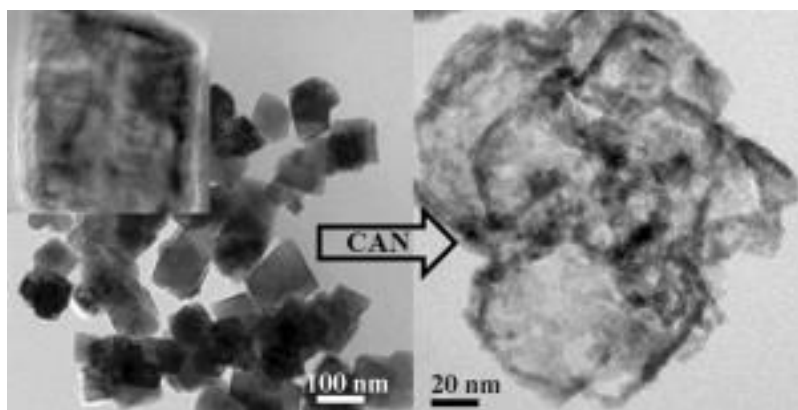


**Figure 1.15.** HR-TEM images of inactive crystalline MnO(left) and active MnO<sub>x</sub>(right) after ceric ammonium nitrate(CAN) treatment.

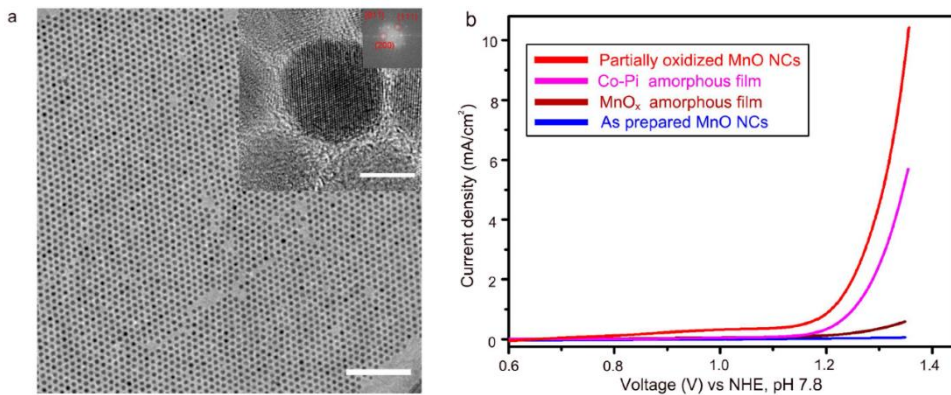


**Figure 1.16.** TEM Image (a) and cyclic voltammometry curves of 10 nm sized monodisperse manganese oxide nanoparticles and activity comparison with other transition metal based catalysts. (b) (scale bar : 100nm, inset : 5nm)

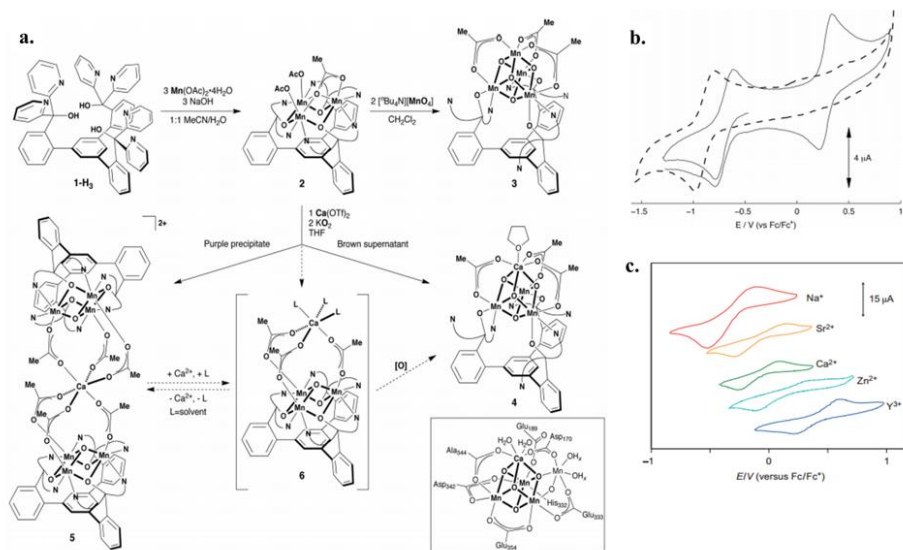


**Figure 1.17.** (a) Synthesis of bio-inspired Mn based electrocatalyst. Curved lines in structures schematically represent 2-pyridyl groups. (Inset) A recent structure of the OEC from crystallographic studies is shown. OAc/AcO, acetoxy group; Me, methyl; Bu, butyl (b) Cyclic voltammograms of 3 in (a) (solid trace, DMA solution) and 4 in (a) (dashed trace, DMF solution) with 0.1 M n Bu<sub>4</sub>NPF<sub>6</sub>. (c) The redox potentials of the [MMn<sub>3</sub>O<sub>2</sub>] complexes are correlated with the Lewis acidity of the redox-inactive metal (M : Na, Sr, Ca, Zn, Y).

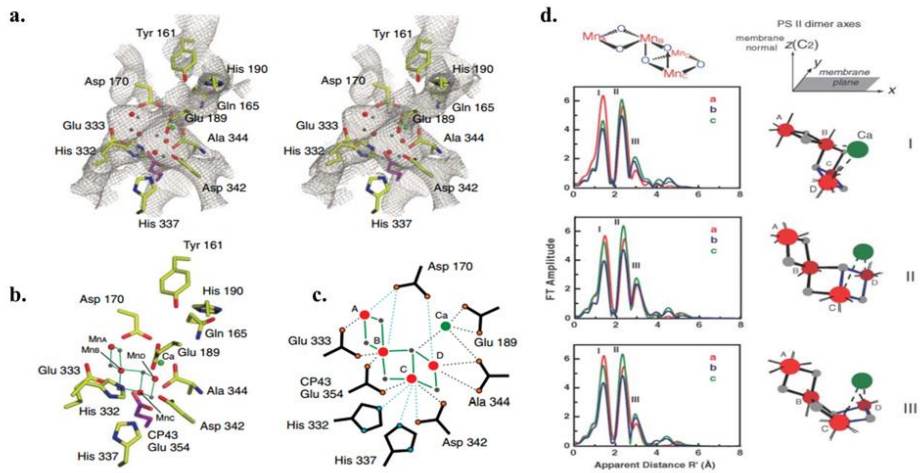


**Figure 1.18.** (a), (b), (c) Proposed Mn<sub>4</sub>Ca cluster derived from polarized Mn EXAFS in relation to the putative ligands obtained from the 3.0 Å resolution x-ray crystal structure. The spheres represent Mn (red), Ca (green), and the bridging oxygen ligand atoms (gray). The assignment of ligands is tentative because it is based on the electron density of the Mn<sub>4</sub>Ca cluster, and its immediate environment may be altered by x-ray damage. (d) High-resolution structural models for the Mn<sub>4</sub>Ca cluster in PSII from polarized EXAFS. The Mn<sub>4</sub>Ca models I, II, and III are shown on the right.

Jaramillo group made an hypothesis that the observed OER activity is more attributed to Mn(III,IV) oxide rather than Mn(II,III,IV) oxide. When the potential was increased to about 1.8V vs RHE, related to OER, about 80% of the catalytic film was oxidized and formed a mixed Mn(III,IV) oxide<sup>[147]</sup>. Also MnO<sub>x</sub>/Au-GC composite made by adding Au to MnO<sub>x</sub> showed an surprisingly high enhancement in catalytic performance compared to the pure MnO<sub>x</sub> catalysts reported before.<sup>[147]</sup>

On the other hand, there also have been intense attempts to improve the catalytic activity under neutral pH. As stated above, instability of Mn<sup>3+</sup> species due to suppressed J-T distortion is regarded as the main reason for the activity degradation. Previously, Nakamura group demonstrated that controlling the disproportionation and comproportionation efficiencies of Mn(III) ions is an important factor to make water oxidation efficient at neutral pH. δ-MnO<sub>2</sub> which shows layered structure was coated on fluorine-doped tin oxide using spray deposition method to fabricate manganese oxide electrodes. These electrodes showed catalytic activity towards water oxidation at pH from 4 to 13. By comparing tendency in the onset potential of water oxidation current at various pH, Mn(III) ions were demonstrated as the precursor of water oxidation. Table 1 shows the experimental values of activity-related terms and also the preparation methods of Mn-based catalysts and electrolytes used for analysis are listed for indirect comparison.

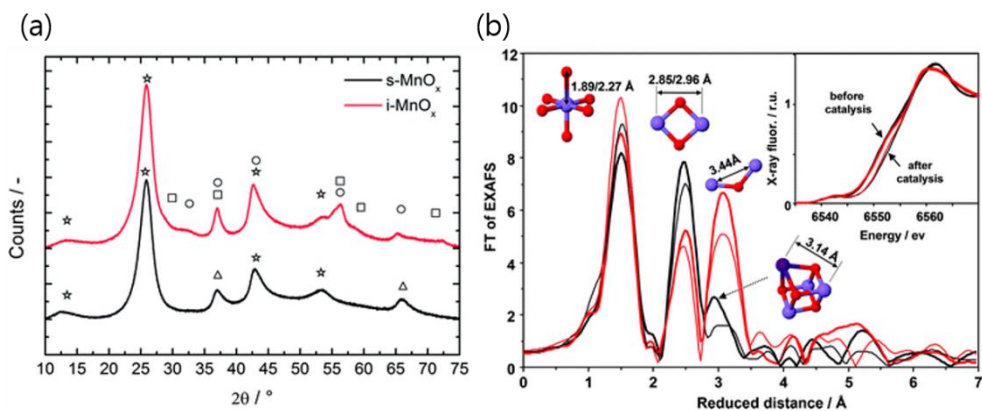


**Figure 1.19.** (a) X-ray diffraction pattern of s-MnO<sub>x</sub> (black) and i-MnO<sub>x</sub> (red). Reflections are labeled by squares for  $\beta$ -MnO<sub>2</sub>, by circles for  $\gamma$ -MnO<sub>2</sub>, by triangles for the layered MnO<sub>2</sub> phase. (b) X-ray absorption spectra of s-MnO<sub>x</sub> (black) and i-MnO<sub>x</sub> (red) deposited on electrodes before and after catalysis. (Mn(IV) ions are presented as spheres in magenta, Mn(III) ions in dark purple, and oxygen as red spheres.)

**Table 1.5.** Selection of experimental values of Tafel slope, overpotential, and onset potential for oxygen evolution on various electrocatalysts and electrodes.

Catalyst/ Substrate	Preparation Method	Electrolyte	Tafel slope (mV/dec)	Overpotential
MnO <sub>x</sub>	Corrosion method	0.1M Na-Pi at pH 7	120	N/A
MnO <sub>x</sub> films /FTO	Electro-deposition	0.1M Na-Pi at pH 7	76	0.5 mA/cm <sup>2</sup> @565 mV
Mn <sub>3</sub> (PO <sub>4</sub> ) <sub>2</sub> - 3H <sub>2</sub> O /FTO	Drop casting	0.5M Na-Pi at pH 7	120	0.316 mA/cm <sup>2</sup> @680 mV
Mn <sub>2</sub> O <sub>3</sub> NP /FTO	Drop casting	0.5M Na-Pi at pH 7	120	0.08 mA/cm <sup>2</sup> @680 mV
Li <sub>2</sub> MnP <sub>2</sub> O <sub>7</sub> /FTO	Drop casting	0.5M Na-Pi	120	5 A/g@680 mV
Mn <sub>2</sub> O <sub>8</sub> /FT O	Drop casting	0.3M Na-Pi at pH 7.8	78.7	5 mA/cm <sup>2</sup> @580 mV
MnO <sub>x</sub> /Au-Si <sub>3</sub> N <sub>4</sub>	Electro-deposition	0.1M KOH	N/A	N/A
Activated MnO <sub>x</sub> /FTO	Electro-deposition	0.1M Na-Pi at pH 7	74	N/A
As- deposited MnO <sub>x</sub> /FTO	Electro-deposition	0.1M Na-Pi at pH 7	123	N/A
MnO <sub>x</sub> /Au-GC	Sputtering	0.1M KOH	N/A	0.09 mA/cm <sup>2</sup> @300 mV
γ-MnOOH /Au	Electro-deposition	0.5 M H <sub>2</sub> SO <sub>4</sub>	N/A	N/A
α-Mn <sub>2</sub> O <sub>3</sub>	Electro-deposition	0.1 M KOH	N/A	1mA/cm <sup>2</sup> @300 mV
MnO/GC	Atomic layer deposition	0.1M KOH	N/A	0.4mA/cm <sup>2</sup> @300 mV
MnOOH /Pt(111)	Electro-deposition	0.1M KOH/LiOH	N/A	N/A
MnO <sub>x</sub>	Spin coating	1 M KOH	49	0.002mA/cm <sup>2</sup> @300 mV
β-MnO <sub>2</sub>	screen-printed	1M NaOH		10 mA/cm <sup>2</sup> @500 mV

### **1.3.2.5. Extended solid state OER catalysts**

#### **1.3.2.5.1. Noble metal based OER electrocatalysts**

Since many interrupting factors are existing that hinder the oxygen evolution reaction (OER) during water-electrolysis, many groups of scientist have focused to find the most efficient catalysts which has superior catalytic activities. The first trial was done by the use of noble metal based compounds as the catalysts. Typically, ruthenium (Ru),<sup>[148]</sup> iridium (Ir), and platinum (Pt)<sup>[149]</sup> were chosen for investigating its catalytic activity in various conditions<sup>[150]</sup>. Due to its unique electronic structure such as the fully filled d-bands that gives no interference of Fermi level, electrons have more freedom to alternate its chemical behaviors during the reaction. Therefore, the noble metal based catalysts have high catalytic activities compared to other types of catalysts. For example, IrO<sub>x</sub> exhibits 1 mA/cm<sup>2</sup> of OER current with the only 200mV of overpotential (1.43 V vs RHE) and small Tafel slope value of 40 mV/dec. RuO<sub>2</sub> anodes reaches 1 mA/cm<sup>2</sup> at the applied potential value of 1.36 V vs RHE and has also small Tafel slope of 40 mV/dec.<sup>[151]</sup> Trasatti group demonstrated that an optimized metal-oxygen bond strength in RuO<sub>2</sub> and IrO<sub>x</sub> resulted in their high OER catalyticactivity.<sup>[152]</sup> Moreover, Norskov and Rossmeisl group theoretically explained the high activity of RuO<sub>2</sub> based on the difference between the binding energy of O\* and OH\* which is assumed as rate-limiting step in the overall water oxidation process.<sup>[153]</sup> Using DFT calculation, RuO<sub>2</sub> exhibits the minimum difference among the various transition metal based OER catalyst,

confirming their theoretical origin of high activity.<sup>[154]</sup> Noble metal based OER catalysts has moderate stability.<sup>[155]</sup> their long-term stability and high catalytic activity, noble metal based OER electrocatalysts have been recognized as promising anode materials for overall water oxidation systems.<sup>[156]</sup>

However, a problem does exist in using noble metal based catalysts. The cost of the material itself is extremely high due to its scarcity from earth (average prices/oz, Ru = \$151.96/oz., Pt= \$1035.62/oz. and Ir = \$476.15/oz.) so that it is very hard to use these materials as the general supply of energy. According to US department of energy (DOE), hydrogen production from water electrolysis is currently \$2.50/kg. This price is still more expensive than electricity which is only \$35/kWh. Therefore, noble metal catalysts which has immoderate price cannot be the next alternative in producing high efficiency of energy with lower price of the water electrolysis. Thus, an investigation for the different types of catalyst materials had to be carefully considered.

#### **1.3.2.5.2. Transition metal (Co, Ni, Cu, and Fe) based catalysts**

Precious metal oxides, such as RuO<sub>2</sub> and IrO<sub>2</sub>, exhibit superb OER catalytic activity; however, their high price remains as an unavoidable weakness. Therefore, the development of efficient, durable, and inexpensive alternative catalysts is needed. In this regard, intensive researches have focused on developing transition metal based OER electrocatalysts.<sup>[157]</sup> Meyer group introduced copper based electro-

catalysts which have high catalytic activities in alkali phosphate buffer condition<sup>[158]</sup>. In 2012, they also reported the Cu-peptide molecular catalyst with well-defined OER mechanism<sup>[159]</sup>. They verified the oxidation state change of copper initially from Cu(II) to Cu(III) and the intermediate state of Cu(IV) occurs with the formation of peroxide. It showed a high stability during the measurement. In this result, they pointed out the important key to oxidize water is either by the fluent transfer of oxygen atom to water molecule or with intermolecular O-O coupling. The overpotential was about 0.52V at pH 11 which is relatively high value, but its impressive catalytic stability along with the high turnover frequency, 33 s<sup>-1</sup> exhibited a new path for transition metal based electrocatalyst for water oxidation. Nocera groups employed amorphous inorganic films containing Co atoms and phosphate anions.<sup>[160]</sup> The films were prepared by electro-deposition of Co -Pi films onto ITO substrate using phosphate buffer with Co(II) ions. Interestingly, the Co -Pi catalyst is formed *in situ* and operates water oxidation with moderate overpotential value (~430 mV) in neutral water under ambient conditions.<sup>[161]</sup> Moreover, the Co-Pi films have self-repairing characteristics that the films are continuously deposited on the ITO substrate during the OER.<sup>[162]</sup> (Figure 1.19) Similar with Co-Pi films, they also presented Ni based amorphous films by electrodeposition method.<sup>[163]</sup> Instead of Co(II) ions and phosphate buffer, they used Ni(II) ions and borate buffer to make the films. Interestingly, the Ni-Bi catalyst is also formed *in situ* and catalyzes the water oxidation reaction under the overpotential value of ~620 mV at pH 9.2.<sup>[163]</sup>

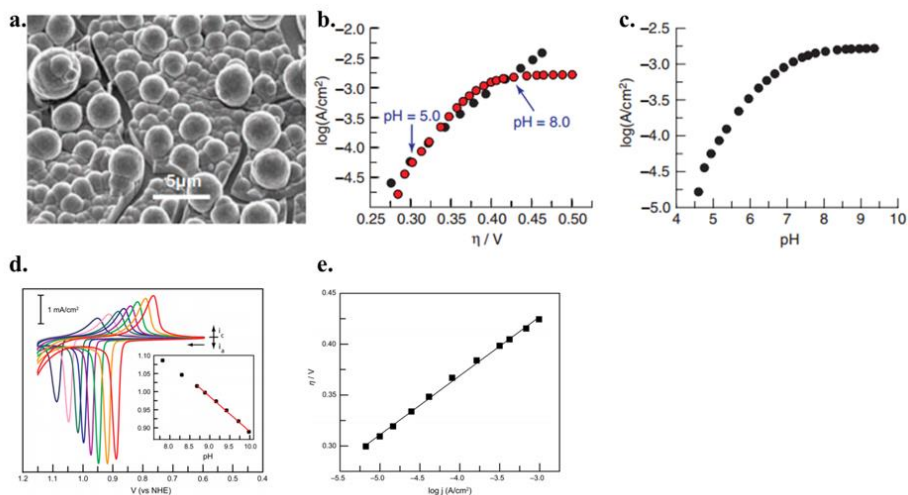


**Figure 1.20.** (a) SEM image of the electrodeposited catalyst after  $30\text{C}/\text{cm}^2$  were passed in  $0.1\text{ M KPi}$  electrolyte at  $\text{pH } 7.0$ , containing  $0.5\text{ mM Co}^{2+}$ . (b) Tafel plot (black circles),  $\eta = (V_{\text{appl}} - iR) - E(\text{pH } 7)$  (where  $V_{\text{appl}}$  is the applied potential), of a catalyst film on ITO in  $0.1\text{ M KPi}$  electrolyte  $\text{pH } 7.0$ , corrected for the  $iR$  drop of the solution.  $\text{pH}$  data were converted into a Tafel plot (red circles),  $h = (V_{\text{appl}} + 0.059\Delta\text{pH} - iR) - E(\text{pH } 7)$ , assuming Nernstian behavior and correcting for the  $iR$  drop of the solution. The  $\text{pH} = 5$  and  $\text{pH} = 8$  data points are indicated by arrows. (c) Current density dependence on  $\text{pH}$  in  $0.1\text{ M KPi}$  electrolyte. The potential was set at  $1.24\text{ V}$  (versus NHE) with no  $iR$  compensation. (d) CVs scans of a Ni borate catalyst film at  $\text{pH}$  values of  $7.82, 8.30, 8.68, 8.88, 9.16, 9.42, 9.72$ , and  $9.98$  in. going from left to right, respectively. The inset shows a linear fit for the  $8.7\text{--}10.0\text{ pH}$  region, with a slope of  $96\text{ mV}/\text{pH}$  unit. The CVs were taken at scan rates of  $50\text{ mV}/\text{s}$ . (e) Tafel plot,  $\eta = (V_{\text{appl}} - iR - E^0)$ , of a Ni-Bi catalyst film operated in  $0.2\text{ M Bi}$ ,  $\text{pH } 9.2$  where  $\eta$  is the overpotential,  $iR$  accounts for the uncompensated solution resistance, and  $E^0$  is the thermodynamic potential for water oxidation at this  $\text{pH}$  ( $0.69\text{ V}$  vs. NHE).

Inspired from the high catalytic activities of Co, Ni based amorphous films, Berlinguette group has recently developed amorphous  $\text{Fe}_{100-y-z}\text{Co}_y\text{Ni}_z\text{O}_x$  films. They have utilized the photochemical metal-organic deposition method to make the amorphous films under low-temperature. This method can produce amorphous metal oxide films where metals are distributed homogeneously in the films. Surprisingly, the catalytic ability of  $\text{Fe}_{100-y-z}\text{Co}_y\text{Ni}_z\text{O}_x$  films is similar to that of  $\text{IrO}_x$  catalysts under only basic condition. Moreover, Other than amorphous metal oxide films, Hongjie Dai group synthesized the ultrathin, layered Ni-Fe based double hydroxide plates onto mildly oxidized CNT. In this case, the Ni-Fe plates and CNT were utilized as the OER catalysts and working electrodes, respectively. This system is found to be highly catalytic active which is comparable to conventional Ir based electrocatalysts under basic conditions.

In order to systemically understand and compare the catalytic abilities of transition metal oxide electrocatalysts, Jaramillo groups synthesized various Co, Fe, Ni based electrocatalysts, synthesized by electrodeposition. The overpotential values of the catalysts where current density of the catalysts reached at the  $10 \text{ mA/cm}^2$  were measured for comparison. Under alkaline condition, it was observed that these catalysts can operate OER catalysis under moderate overpotential value between 350 mV and 430 mV.<sup>[164]</sup>

As another route, many researches have been developed for the transition metal complexes which are comprised of transition metal and surrounding organic ligands.<sup>[165,166]</sup> The organic ligands were used to systemically arrange the transition

metals and stabilize the local structure and the valency state of the metals.<sup>[132c, 132d]</sup> Due to the high controllability of the organic ligands, a lot of transition metal complexes, including mononuclear, binuclear, and multinuclear complexes, were developed and their catalytic abilities were evaluated.<sup>[165]</sup> Additionally, the complexes have been used as platforms for understanding the role of local structure of transition metal and surrounding ligands on OER catalysis.<sup>[165]</sup> However, most of the complexes have difficulty in mass-production compared to transition metal based oxide films because the synthesis of organic ligands and complexes is not facile.<sup>[165]</sup> In this respect, ease of synthesis of surrounding organic ligands can be another breakthrough for commercializing the transition metal complexes for OER catalysis.

Catalyst /Substrate	Loading Method	Electrolyte	Activity		
			Tafel slope (mV/dec)	Overpotential	Onset potential (V vs. RHE)
RuO <sub>2</sub>	Electrodeposition	0.1M HClO <sub>4</sub> (pH 1.3)	40	N/A	1.36
IrO <sub>2</sub>	Thermal decomposition	1M H <sub>2</sub> SO <sub>4</sub>	40	N/A	1.44
Ir/C	N/A	1M KOH	40	10 mA/cm <sup>2</sup> @280 mV	N/A
RuO <sub>2</sub>	N/A	0.1M KOH	N/A	10 A/g@298 mV	N/A
IrO <sub>2</sub>	N/A	0.1M KOH	N/A	10 A/g@288 mV	N/A
IrO <sub>x</sub>	electrodeposition	1M NaOH	N/A	10 mA/cm <sup>2</sup> @325 mV	N/A
hematite(Fe <sub>2</sub> O <sub>3</sub> )/FTO	Annealing of amorphous FeO <sub>x</sub>	0.1M KOH	40	0.5 mA/cm <sup>2</sup> @470 mV	1.62

LaNiO <sub>3</sub> electrode	co- precipitati on	1M NaOH	43	N/A	1.38
LaCoO <sub>3</sub> electrode	High-T solid-state reactions	1M NaOH	70	N/A	N/A
LaMnO <sub>3</sub> electrode	High-T solid-state reactions	1M NaOH	126	N/A	N/A
SrVO <sub>3</sub> electrode	High-T solid-state reactions	1M NaOH	235	N/A	N/A
LaVO <sub>3</sub> electrode	High-T solid-state reactions	1M NaOH	175	N/A	N/A
Co <sub>3</sub> O <sub>4</sub> /metal	thermal decompos ition	1M KOH	45	N/A	1.4
Co <sub>3</sub> O <sub>4</sub> /metal	electropho terical deposition	1M KOH	41	100 mA/cm <sup>2</sup> @494 mV	N/A
[(TGG <sup>4+</sup> )Cu <sup>II</sup> - OH <sub>2</sub> ] <sup>2+</sup> /GC	Peptide- metal Self Assembly	0.25M phosphate buffer pH11	N/A	N/A	1.75
NiFe- LDH/CNT	Hummers' s method,	1M KOH	31	10 mA/cm <sup>2</sup> @240	N/A

	Solvothermal treatment			mV	
NiFe-LDH/CNT	Hummers' method, Solvothermal treatment	0.1M KOH	35	10 mA/cm <sup>2</sup> @300 mV	N/A
NiFe-LDH NP /GC	Hummers' method, Solvothermal treatment	1M KOH	N/A	5 mA/cm <sup>2</sup> @290 mV	N/A
Mn <sub>3</sub> O <sub>4</sub> /CoSe <sub>2</sub>	simple polyol reduction route	0.1M KOH	49	10 mA/cm <sup>2</sup> @450 mV	N/A
core-ring NiCo <sub>2</sub> O <sub>4</sub> electrode	hydroxide decomposition method	1 M KOH	54	100 mA/cm <sup>2</sup> @315 mV	N/A
NiCo <sub>2</sub> O <sub>4</sub> electrode	electrophoretic deposition	1M KOH	59	100 mA/cm <sup>2</sup> @438 mV	N/A
NiCo <sub>2</sub> O <sub>4</sub> electrode	acetyl-acetate	4M NaOH	N/A	100 mA/cm <sup>2</sup> @300	N/A

	sol-gel route			mV	
$\text{Mn}_3(\text{PO}_4)_2 \cdot 3\text{H}_2\text{O}$ NP/FTO	Drop casting	0.5 M sodium phosphate electrolyte at pH 7	120	0.316 mA/cm <sup>2</sup> @680 mV	N/A
$\text{Mn}_2\text{O}_3$ NP/FTO	Drop casting	0.5 M sodium phosphate electrolyte at pH 7	120	0.08 mA/cm <sup>2</sup> @680 mV	N/A
$\text{LiMnP}_2\text{O}_7/\text{FTO}$	Drop casting	0.5 M sodium phosphate buffer (pH 7.0)	120	5 A/g@680 mV	N/A
$\text{Li}_{1.5}\text{MnP}_2\text{O}_7/\text{FTO}$	Drop casting	0.5 M sodium phosphate buffer (pH 7.0)	120	4 A/g@680 mV	N/A
$\text{Li}_{1.7}\text{MnP}_2\text{O}_7/\text{FTO}$	Drop casting	0.5 M sodium phosphate buffer (pH	120	2.8 A/g@680 mV	N/A

		7.0)			
Li <sub>2</sub> MnP <sub>2</sub> O <sub>7</sub> /FTO	Drop casting	0.5 M sodium phosphate buffer (pH 7.0)	120	2 A/g@680 mV	N/A
amor-FeO <sub>x</sub> /FTO	photochemical metal-organic deposition	0.1M KOH	40	0.5 mA/cm <sup>2</sup> @400 mV	1.55
amor-CoO <sub>x</sub> /FTO	photochemical metal-organic deposition	0.1M KOH	42	N/A	1.44
amor-NiO <sub>x</sub> /FTO	photochemical metal-organic deposition	0.1M KOH	73	N/A	1.42
amor-FeCoO <sub>x</sub> /FTO	photochemical metal-organic deposition	0.1M KOH	33	0.5 mA/cm <sup>2</sup> @250 mV	1.41

amor- FeNiO <sub>x</sub> /FTO	photoche mical metal- organic deposition	0.1M KOH	24	0.5 mA/cm <sup>2</sup> @250 mV	1.44
amor- FeCoNiO <sub>x</sub> /FT O	photoche mical metal- organic deposition	0.1M KOH	31	0.5 mA/cm <sup>2</sup> @250 mV	1.42
amor- CoP <sub>2</sub> /FTO	electrodep osition	0.1M potassium phosphate electrolyte	60	N/A	1.51
amor- NiB <sub>2</sub> /FTO	electrodep osition	0.1M potassium borate pH 9.2	58	1 mA/cm <sup>2</sup> @425 mV	1.53
amor- MnO <sub>x</sub> /FTO	electrodep osition	0.1M phosphate buffer	76	0.5 mA/cm <sup>2</sup> @565 mV or 1 mA/cm <sup>2</sup> @590 mV	1.59
Fe <sub>100</sub> O <sub>x</sub> /FTO	photoche mical metal-	0.1 M KOH	40	0.5 mA/cm <sup>2</sup> @380 mV, 1	1.55

	organic deposition			mA/cm <sup>2</sup> @410 mV	
Fe <sub>36</sub> Co <sub>64</sub> O <sub>x</sub> /FTO	photochemical metal-organic deposition	0.1 M KOH	40	0.5 mA/cm <sup>2</sup> @250 mV, 1 mA/cm <sup>2</sup> @270 mV	1.43
Co <sub>100</sub> O <sub>x</sub> /FTO	photochemical metal-organic deposition	0.1 M KOH	42	0.5 mA/cm <sup>2</sup> @260 mV, 1 mA/cm <sup>2</sup> @270 mV	1.44
Fe <sub>40</sub> Ni <sub>60</sub> O <sub>x</sub> /FTO	photochemical metal-organic deposition	0.1 M KOH	34	0.5 mA/cm <sup>2</sup> @230 mV, 1 mA/cm <sup>2</sup> @250 mV	1.42
Ni <sub>100</sub> O <sub>x</sub> /FTO	photochemical metal-organic deposition	0.1 M KOH	73	0.5 mA/cm <sup>2</sup> @250 mV, 1 mA/cm <sup>2</sup> @280 mV	1.42
Co <sub>41</sub> Ni <sub>59</sub> O <sub>x</sub> /FTO	photochemical metal-organic	0.1 M KOH	73	0.5 mA/cm <sup>2</sup> @270 mV, 1 mA/cm <sup>2</sup> @300	1.42

	deposition			mV	
$\text{Fe}_{39}\text{Co}_{39}\text{Ni}_{22}\text{O}_x/\text{FTO}$	photochemical metal-organic deposition	0.1 M KOH	40	0.5 mA/cm <sup>2</sup> @250 mV, 1 mA/cm <sup>2</sup> @280 mV	1.42
NiFe Oxide/GC	electrodeposition	1M KOH	N/A	5 mA/cm <sup>2</sup> @420 mV	N/A
$\text{Ni}_{1-x}\text{Cu}_x\text{Co}_2\text{O}_4/\text{Ni}$	thermal decomposition	5M KOH	45~62	100 mA/cm <sup>2</sup> @410 mV	N/A
$\text{NiCu}_{2-y}\text{Co}_y\text{O}_4/\text{Ni}$	thermal decomposition	5M KOH	60~64	100 mA/cm <sup>2</sup> @450 mV	N/A
$\text{NiFeO}_x/\text{GC}$	electrodeposition	1M NaOH	N/A	10 mA/cm <sup>2</sup> @351 mV	N/A
$\text{CoFeO}_x/\text{GC}$	electrodeposition	1M NaOH	N/A	10 mA/cm <sup>2</sup> @362 mV	N/A
$\text{NiCoO}_x/\text{GC}$	electrodeposition	1M NaOH	N/A	10 mA/cm <sup>2</sup> @377 mV	N/A
$\text{CoO}_x/\text{GC}$	electrodeposition	1M NaOH	N/A	10 mA/cm <sup>2</sup> @392 mV	N/A

NiLaO <sub>x</sub> /GC	electrodeposition	1M NaOH	N/A	10 mA/cm <sup>2</sup> @410 mV	N/A
NiCuO <sub>x</sub> /GC	electrodeposition	1M NaOH	N/A	10 mA/cm <sup>2</sup> @412 mV	N/A
CoO <sub>x</sub> /CoPi/GC	electrodeposition	1M NaOH	N/A	10 mA/cm <sup>2</sup> @423 mV	N/A
NiO <sub>x</sub> /GC	electrodeposition	1M NaOH	N/A	10 mA/cm <sup>2</sup> @424 mV	N/A
NiCeO <sub>x</sub> /GC	Electrodeposition	1M NaOH	N/A	10 mA/cm <sup>2</sup> @433 mV	N/A

\*LDH : Layered double hydroxide \*CNT : Carbon Nano Tube \*GC : Glassy Carbon

**Table 1.5.** Selection of experimental values of Tafel slope, overpotential and Onset potential for oxygen evolution on various electrocatalysts and electrodes. Preparation Method and Electrolyte used are described.

## 1.4. Scope of Thesis

While exceptional water oxidizing performance of photosystem II, continue to inspire to develop manganese based catalysts, still activity of Mn catalysts is quite low. Such large activity discrepancy between biological system and synthetic catalysts should be resolved. In this study, we have attempted to develop efficient and robust manganese based water oxidation catalysts in the following chapters.

Chapter 2 investigates new water oxidation catalysts,  $\text{Mn}_3(\text{PO}_4)_2 \cdot 3\text{H}_2\text{O}$  catalysts. Insertion of bulky phosphate group makes local structure distorted. We verified that if structural flexibility is sufficiently granted, catalytic activity could be largely improved. Computation results also demonstrated that reaction intermediates, Mn(III) species are stabilized in distorted  $\text{Mn}_3(\text{PO}_4)_2 \cdot 3\text{H}_2\text{O}$  structure. To gauge the activity of the Mn catalysts, we newly suggested two standards, J-T distortion and inner pressure.

Chapter 3 investigates the partially oxidized manganese oxide nanoparticles. Via thermal decomposition method, monodisperse 10 nm sized manganese oxide nanoparticles were synthesized. After surface treatment and mild annealing process, highly active manganese catalysts could be prepared. In neutral condition, our partially oxidized manganese oxide nanoparticles exhibit outstanding activity.

Chapter 4 investigates the detailed mechanism of manganese oxide

nanoparticles. We found out that nanosized manganese oxide catalysts always display superior activity to bulk counterparts. In this chapter, we compared water oxidizing mechanism of nanoparticles and bulk compounds. Various *in-situ* spectroscopic analysis were performed to check the change of Mn status. Finally, it was successfully demonstrated that while  $\text{Mn(II)} \rightarrow \text{Mn(III)}$  reaction is rate determining step for bulk manganese oxide compounds,  $\text{Mn(III)}$  is stable generated by proton coupled electron transfer on nanoparticle surface.

Chapter 5 investigates Ni- $\text{Mn}_3\text{O}_4/\text{NiO}$  hybrid structures. In order to partially oxidize manganese atoms in oxide structure, nickel elements which is more electro-negative than manganese are doped in  $\text{Mn}_3\text{O}_4$ . In this study, it was verified that only in mild annealing condition, nickel or nickel oxide cluster can be diffused in to manganese oxide structure, more than 600nm distance. HR-TEM EELS analysis demonstrated existence of nickel on the  $\text{Mn}_3\text{O}_4$  structure. Ni decorated  $\text{Mn}_3\text{O}_4$  nanoparticles exhibit more improved catalytic activity than pristine  $\text{Mn}_3\text{O}_4$  nanoparticles. More importantly, during water oxidation catalysis, unique Mn high valent status was discovered. Low spin  $\text{Mn(IV)}$  species could be characterized by EPR analysis. Computation study, XANES and SQUID analysis also supported existence of low spin  $\text{Mn(IV)}$ ,  $S=1/2$  species. It is first demonstration and discovery of low spin  $\text{Mn(IV)}$  oxo species in inorganic materials.

## 1.5. Concluding Remarks

Hydrogen energy is considered as ultimate alternative energy resources to cope with the modern energy crisis. In order to construct electrochemical water splitting scheme, it is highly required to develop efficient and robust catalysts. Up to now, development of an earth-abundant catalyst that operates at neutral pH with a low overpotential is still a challenging issue.

The  $Mn_4Ca$  cluster, existing in natural photosystem II exhibit outstanding oxygen evolving performance. Via Kok cycle, composed of four sequential Mn redox states, four electron and four proton transfer reaction is efficiently mediated in WOC. Various spectroscopic analysis and computation study have been attempted to reveal the exact structure and accurate water oxidizing process in WOC. Moreover, inspired by  $Mn_4Ca$  cluster, development of efficient Mn catalysts have been investigated for the decades. However, contrary to expectation, significant activity discrepancy still exist between synthetic catalysts and natural WOC under neutral pH. It is expected that adopting unique properties of WOC, mixed valency, proton-coupled electron transfer, and structural flexibility, is the possible resolutions to realize efficient Mn based water oxidation catalysts. While precious metal oxides, such as  $RuO_2$ , and  $IrO_2$ , exhibit outstanding OER catalytic activity, their high price remains an unavoidable weakness. Therefore, the development of efficient, durable, and inexpensive alternative catalysts is demanding.

In this thesis, we have attempted to develop efficient and robust manganese

based water oxidation catalysts. Three catalysts,  $\text{Mn}_3(\text{PO}_4)_2 \cdot 3\text{H}_2\text{O}$ , MnO nanoparticles, and Ni-decorated  $\text{Mn}_3\text{O}_4$  nanoparticles have newly developed. With various spectroscopic analysis and electrochemical measurement, detailed mechanism was verified. We are sure that long lasting problem in Mn based catalysts under neutral condition is completely resolved in our Mn catalyst systems.

## **Chapter 2. Hydrated Manganese(II) Phosphate ( $\text{Mn}_3(\text{PO}_4)_2 \cdot 3\text{H}_2\text{O}$ ) as Water Oxidation Catalyst**

### **2.1. Introduction**

Splitting water into hydrogen and oxygen is a promising pathway for solar energy conversion and storage systems. The oxygen evolution reaction (OER) has been regarded as a major bottleneck in the overall water splitting process due to the slow transfer rate of the four electrons involved and the high activation energy barrier for O–O bond formation. In nature, there is a water oxidation complex (WOC) in photosystem II (PSII) composed of the earth-abundant elements, Mn and Ca. The WOC in PSII, in the form of a cubical  $\text{CaMn}_4\text{O}_5$  cluster, efficiently catalyzes water oxidation under neutral conditions with an extremely low overpotential value ( $\sim 160$  mV) and a high turnover frequency (TOF) number ( $\sim 25\,000$   $\text{mmolO}_2 \text{ mol}^{-1} \text{ Mn s}^{-1}$ ). Recently, X-ray analysis of the PSII structure at a resolution of  $1.9 \text{ \AA}$  provided detailed structural information about the cubical  $\text{Mn}_4\text{CaO}_5$  cluster stabilized by a surrounding peptide ligand. Four Mn atoms are oxo-bridged in asymmetric positions and undergo successive changes in oxidation state, taking part in a so-called Kok cycle. It has also been suggested that O–O bond formation occurs at specific sites in

the  $\text{Mn}_4\text{CaO}_5$  cluster. The unique capabilities of the cubical  $\text{Mn}_4\text{CaO}_5$  cluster have inspired the design of Mn-based catalysts for the OER. For example, the geometry of oxo-bridged Mn atoms has been synthetically controlled by designer organic ligands.  $[\text{Mn}_4\text{O}_4\text{L}_6]^+$  ( $\text{L} = (\text{MeOPh})_2\text{PO}_2$ ) or  $[\text{Mn}_4\text{O}_4\text{L}_6]^+$ -Nafion systems have been demonstrated as efficient water oxidation catalysts. Recently, the Agapie group developed a  $[\text{Mn}_3\text{CaO}_4]^{6+}$  core structure that was almost identical to that of the WOC in nature using trinucleating ligands. Moreover, using the  $[\text{Mn}_3\text{CaO}_4]^{6+}$  core structure, they further synthesized  $\text{Mn}_3\text{M}(\mu_4\text{-O})(\mu_2\text{-O})$  ( $\text{M} = \text{Ca}^{2+}, \text{Sr}^{2+}, \text{Na}^+, \text{Zn}^{2+}$ , and  $\text{Y}^{3+}$ ) to understand the role of redox-inactive metals in water oxidation catalysis.

As another route, various crystalline manganese oxide polymorphs and amorphous  $\text{MnO}_x$  have been investigated as water oxidation catalysts. Previous studies have reported that, among the various Mn oxide candidates, the materials whose structure and Mn valency were similar to those of the  $\text{Mn}_4\text{CaO}_5$  cluster showed high activity. For example, the Dismukes group mimicked the  $[\text{Mn}_4\text{O}_4]$  core units in the  $\text{Mn}_4\text{CaO}_5$  cluster by removing the Li ions from  $\text{LiMn}_2\text{O}_4$  Li ion battery cathode materials. Interestingly, the catalytically inactive  $\text{LiMn}_2\text{O}_4$  materials converted into active  $\lambda\text{-MnO}_2$ , which has a  $[\text{Mn}_4\text{O}_4]$  core unit. They assumed that the  $[\text{Mn}_4\text{O}_4]$  core unit in the  $\lambda\text{-MnO}_2$  was the origin of its high catalytic activity. Recently, our group also found that a higher Mn(III) content in the OER catalysts can boost catalytic activity by increasing the degree of distortion in the Mn polyhedron. Moreover, the Driess group developed amorphous  $\text{MnO}_x$  nanoparticles whose local structures and Mn atom valence states resembled those of the  $\text{Mn}_4\text{CaO}_5$  cluster. They

synthesized active, amorphous  $\text{MnO}_x$  ( $1 < x < 2$ ) particles by oxidizing inactive, crystalline MnO nanoparticles using Ce(IV) oxidants.

Moreover, the Dau group developed a new electrodeposition method to produce active  $\text{MnO}_x$  films that exhibited much higher activities than conventionally electrodeposited Mn oxide films. Using X-ray adsorption spectroscopy (XAS) analysis, they found that the newly developed electrodeposited amorphous  $\text{MnO}_x$  films had mixed valency (III/IV) and a disordered Mn geometry, which are recognized as important properties of the  $\text{Mn}_4\text{CaO}_5$  cluster. The Jaramillo group also found that active manganese oxide catalysts contained Mn(III) and Mn(IV) atoms, which are major components of the  $\text{Mn}_4\text{CaO}_5$  cluster.<sup>38</sup> While Mn oxide compounds generally exhibit moderate catalytic abilities under basic conditions, their activity is significantly degraded at neutral pH. There have been several reports investigating the possible origin of the degradation mechanism of Mn oxide compounds under neutral pH. For example, the Nakamura group reported that the instability of the Mn(III) ions in the rigid and highly symmetric  $\text{MnO}_6$  octahedron can decrease the activity of  $\text{MnO}_2$  under neutral pH using electrochemical and spectroscopic analyses. On the basis of theoretical approaches, they enhanced the catalytic ability by coordinating amide groups to the  $\text{MnO}_2$  surface. They suggested that Mn–N bonds lower the symmetry of Mn octahedra and consequently Mn(III) can be stabilized in the octahedra under neutral pH. From the viewpoint of the degradation mechanism presented by the Nakamura group, the high catalytic activities of certain Mn oxide materials under neutral conditions might originate from their crystal structures,

which can stabilize Mn(III) ions effectively.

MnO<sub>x</sub> films can stabilize the Mn(III) ion and enhance OER catalysis. Moreover, the Dismukes group recently found that initially Mn(III) containing crystalline oxides displayed higher catalytic activities than Mn(IV)-based oxides.<sup>41</sup> Therefore, it can be predicted that the catalysts that stabilize the Mn(III) state with ease during the OER at neutral pH may possess high activity under neutral conditions. Herein, we synthesized a new water oxidation catalyst, Mn<sub>3</sub>(PO<sub>4</sub>)<sub>2</sub>·3H<sub>2</sub>O, and identified its crystal structure and OER catalytic activity under neutral conditions. While transition metal phosphate compounds have been widely investigated as cathode materials for Li ion batteries, there has been no attempt to study the OER catalytic performance of phosphate containing Mn-based crystals. We verified that the bulky phosphate polyhedron induces a less-ordered Mn geometry in Mn<sub>3</sub>(PO<sub>4</sub>)<sub>2</sub>·3H<sub>2</sub>O, whose structure is similar to that of catalytic active Mn(III)-containing materials. Computational analysis revealed that distinctive structural features of Mn<sub>3</sub>(PO<sub>4</sub>)<sub>2</sub>·3H<sub>2</sub>O could successfully stabilize Mn(III) during water oxidation, leading to superior catalytic activity under neutral conditions.

## 2.2 Experimental Methods

### 2.2.1 Materials

MnCl<sub>2</sub>·4H<sub>2</sub>O (99%), HEPES (2-(2-hydroxyethyl)-1-piperazinyl)Ethanesulfonic acid (99 %), KH<sub>2</sub>PO<sub>4</sub> (99 %), Na<sub>4</sub>P<sub>2</sub>O<sub>7</sub> (95 %), PVDF(Polyvinylidene difluoride, average M<sub>w</sub> ~530,000, pellets), Nafion 117 solution (5 wt % in aliphatic alcohols and water), NMP(1-Methyl-2-pyrrolidinone, 99.5 %) solution, Na<sub>2</sub>S<sub>2</sub>O<sub>8</sub> powder (>98 %), Ru(bpy)<sub>3</sub>·6H<sub>2</sub>O (Tris(2,2'-bipyridyl) dichloro-ruthenium(II) hexahydrate) (99.95 % trace metal basis), MnO<sub>2</sub> (99.99 %), MnO (99.99%), Na<sub>2</sub>HPO<sub>4</sub>·7H<sub>2</sub>O (ACS reagent, 98.0-102.0 %), Isopropyl alcohol (99.7 %), NaOH (98.0 %), and NaH<sub>2</sub>PO<sub>4</sub>·2H<sub>2</sub>O (99.0 %) were purchased from Sigma Aldrich and used as received without further purification. Fluorine doped Tin-Oxide coated glass (FTO, TEC-8) which has 15 Ω sq<sup>-1</sup> surface resistivity was obtained as pre-cut by 1.0 cm × 1.5 cm glass pieces from Pilkington Company.

### 2.2.2 Synthesis procedure

Manganese (II) phosphate hydrate was synthesized by adding 40 ml of 1.0 mM KH<sub>2</sub>PO<sub>4</sub> in HEPES (1.85 mM, pH 7.4) to 40 mL of 1.0 mM MnCl<sub>2</sub>·4H<sub>2</sub>O solution at 37°C. The mixed solution slowly became turbid, indicating the formation of manganese (II) phosphate hydrate. After 3 h, the precipitate was centrifuged and

washed three times with deionized (DI) water. Collected particles were then lyophilized before characterization.

### **2.2.3 Powder X-ray diffraction**

Powder X-ray diffraction (XRD) was carried out on a D-8 Advance X-ray diffractometer with Cu K $\alpha$  radiation ( $\lambda=1.54056\text{\AA}$ ). For the measurement, precipitated  $\text{Mn}_3(\text{PO}_4)_2 \cdot 3\text{H}_2\text{O}$  powder was collected and lyophilized at least 2 days. The lyophilized powder was loaded on Si holder, retrofitted in X-ray diffractometer. XRD patterns were recorded in a range of  $5 \sim 100^\circ$  with a step of  $0.02^\circ$  and a velocity of  $0.02^\circ/16$  s. Obtained XRD patterns were compared with previously reported JDPDS cards.

### **2.2.4 ICP/MS & TGA analysis**

Inductively Coupled Plasma-Mass Spectrometer (ICP/MS, 720-ES, Varian) measurement was conducted to determine the exact chemical composition of  $\text{Mn}_3(\text{PO}_4)_2 \cdot 3\text{H}_2\text{O}$ .

Thermo Gravimetric analysis (TGA) was performed on the lyophilized  $\text{Mn}_3(\text{PO}_4)_2 \cdot 3\text{H}_2\text{O}$  powder described above. 2.177 mg of the samples were loaded to Thermo gravimetric analyzer(Q-5000 IR, TA instrument, USA) and its weight loss measured in a range of  $25\sim 500^\circ\text{C}$  with  $5^\circ\text{C min}^{-1}$

### **2.2.5. Rietveld analysis**

The crystal structure of switzerite was obtained from American Mineralogist Crystal Structure Database (AMCSD). The presumed crystal structure of the  $\text{Mn}_3(\text{PO}_4)_2 \cdot 3\text{H}_2\text{O}$  was drawn with CrystalMaker (CrystalMaker Software) based on its atom coordination information. The maximum bond length between manganese atom and oxygen atom was set to 2.5 Å. Local structure around the P(1) site was visualized by defining the spherical cluster around the P(1) site at the radius of 4.5 Å. The final structure of  $\text{Mn}_3(\text{PO}_4)_2 \cdot 3\text{H}_2\text{O}$  was refined by Rietveld refinement using TOPAS Academic.

### **2.2.6. Scanning electron microscopy(SEM) analysis**

The morphology of synthesized  $\text{Mn}_3(\text{PO}_4)_2 \cdot 3\text{H}_2\text{O}$  was characterized with a high resolution scanning electron microscope (Supra 55VP, Carl Zeiss, Germany). The samples were investigated right after the electrochemical measurements or formation of  $\text{Mn}_3(\text{PO}_4)_2 \cdot 3\text{H}_2\text{O}$  flower like plates on FTO glasses. The samples were rinsed gently with deionized water at least 3 times and dried with nitrogen gas. Pt coating was done by Pt Sputter Coater (BAL-TEC/SCD 005) because  $\text{Mn}_3(\text{PO}_4)_2 \cdot 3\text{H}_2\text{O}$  particles were not conductive enough. Images were taken with an acceleration

voltage of 2 kV, and EDX spectra with a 15 kV. Sample positions coincided with the illuminated area.

### **2.2.7. Transmission electron microscopy (TEM) analysis**

TEM images and selected area electron diffraction (SAED) patterns were obtained using a high resolution transmission electron microscope (JEM-3000F, JEOL, Japan) with an acceleration voltage of 300 kV. The TEM samples were collected from FTO glass right after the catalyst formation or electrochemical measurement, and dispersed in ethanol by sonication about 1 min. About 10  $\mu\text{l}$  of dispersed  $\text{Mn}_3(\text{PO}_4)_2 \cdot 3\text{H}_2\text{O}$  were dropped on the TEM grid and dried in an oven.

### **2.2.8. Brunauer–Emmett–Teller (BET) method**

Brunauer-Emmett-Teller (BET) analysis was conducted on the lyophilized  $\text{Mn}_3(\text{PO}_4)_2 \cdot 3\text{H}_2\text{O}$  powder. 0.5070 g of the sample was loaded to BET analyzer (Physisorption Analyzer, micromeritics, USA) under  $\text{N}_2$  adsorption environment.

### **2.2.9. Cyclic Voltammetry (CV)**

All electrochemical experiments were conducted under a three-electrode

electrochemical cell system. A BASi Ag/AgCl/KCl<sub>sat</sub> reference electrode and a Pt foil (2 cm × 2 cm × 0.1 mm, 99.997% purity, Alfa Aesar) were used as a reference electrode and a counter electrode, respectively. Electrochemical tests were carried out at ambient temperature using a potentiostat system (CHI 600D, CH Instruments). Electrode potential was converted to the NHE scale, using the following equation:  $E(\text{NHE}) = E(\text{Ag/AgCl}) + 0.197 \text{ V}$ . Additionally, overpotential values were calculated by the difference between the iR corrected potential ( $V = V_{\text{applied}} - iR$ ) and the thermodynamic point of water oxidation at a specified pH. The electrolyte was phosphate buffer with 500mM buffer strength under the pH 7. The electrolyte was degassed by bubbling with high-purity nitrogen (99.999 %) for at least 1 hour prior to the start of each experiment and stirred vigorously during the measurement to prevent the mass transport problem..

The preparation procedure of the working electrodes containing our catalysts can be found as follows. Firstly, 5 mg of catalyst powder was dispersed in 1 ml of water mixed solvent with 100  $\mu\text{l}$  of neutralized Nafion solution. Then the mixture was sonicated for at least 30 min to make homogeneous ink. Next, 50  $\mu\text{l}$  of the catalyst solution was dropped onto the FTO substrate and spin-coating was performed at 3000 rpm for 30sec. Finally, prepared working electrode was dried at 80 °C oven before CV measurement. The working electrode was cycled at least 3 times with the potential stepped from 0.7 V to 1.5 V without pause at a scan rate of 10  $\text{mV sec}^{-1}$  before all electrochemical data were recorded. Prior to every electrochemical experiment, the solution resistance was measured in the electrolysis

bath. All the data were iR-compensated.

### **2.2.10. Gas Chromatography (GC)**

The photo-oxidation reactions for O<sub>2</sub> evolution were conducted in an outer-irradiation-type quartz reactor (120 ml) with a closed circulating gas system at ambient temperature. The UV light source was a 450 W high-pressure mercury lamp maintaining a distance of 15 cm between the reactor and the lamp. The lamp was surrounded by a circulating cooling water jacket. In the quartz reactor, 6 mg of Mn<sub>3</sub>(PO<sub>4</sub>)<sub>2</sub>·3H<sub>2</sub>O, solid [Ru(bpy)<sub>3</sub>]Cl<sub>2</sub>, and Na<sub>2</sub>S<sub>2</sub>O<sub>8</sub> (final concentrations 1.5 mM [Ru(bpy)<sub>3</sub>]Cl<sub>2</sub> and 12.5 mM Na<sub>2</sub>S<sub>2</sub>O<sub>8</sub> in the sample solution) were dispersed together in a 25 ml phosphate buffer (100 mM, pH 7). The solution was stirred and sonicated at least 30 minutes respectively to allow complete dispersion. During the stirring and the sonication, the reactor was covered with aluminum foil to prevent irradiation of light. After the reactor connected with the closed gas circulation system inside, the solution was purged with high-purity Ar gas (99.999 %) for 30 minutes before irradiation. The amount of evolved O<sub>2</sub> was recorded every 5 minutes via gas chromatography (DS6200, Donam, Korea). Additionally, the control experiment was also carried out, wherein no [Ru(bpy)<sub>3</sub>]Cl<sub>2</sub> was contained in the reactor. The TOF number was calculated and compared with other manganese based catalysts.

### 2.2.11. Electron paramagnetic resonance (EPR) spectroscopy

All EPR measurements were carried out at KBSI, Western Seoul Center, Korea Basic Science Institute, University-Industry Cooperation Building, 150 Bukahyun-ro, Seodaemun-gu Seoul, 120-140, Korea. Electron paramagnetic resonance (EPR) was performed using a Bruker EMX/Plus spectrometer equipped with a dual mode cavity (ER 4116DM). Low temperatures were achieved and controlled using a liquid He quartz cryostat (Oxford Instruments ESR900) with an temperature and gas flow controller (Oxford Instruments ITC503). The experimental conditions are as follows. Microwave frequency 9.64 GHz (perpendicular mode), 9.4 GHz (parallel mode), modulation amplitude 10G, modulation frequency 100 kHz microwave power 0.94 mW (perpendicular mode), 5.0 mW (parallel mode) temperature 5.7K. 10 scans were added for each spectrum.

All the  $\text{Mn}_3(\text{PO}_4)_2 \cdot 3\text{H}_2\text{O}$  samples were loaded on FTO glass (1.5 cm  $\times$  2.5 cm) in the form of carbon paste. In order to obtain carbon paste, we mixed  $\text{Mn}_3(\text{PO}_4)_2 \cdot 3\text{H}_2\text{O}$ , PVDF, carbon in the ratio of 8:1:1 (weight ratio), and then 100  $\mu\text{l}$  NMP solution was dropped on the mixture. The paste was loaded on the FTO substrate carefully by blade and dried in the 80  $^\circ\text{C}$  oven. To eliminate residual  $\text{Mn}^{\text{III}}$  ion on the surface of  $\text{Mn}_3(\text{PO}_4)_2 \cdot 3\text{H}_2\text{O}$ , the paste-loaded FTO glass was dipped in 20 mM pyrophosphate solution at least 30 minutes and gently rinsed with deionized water prior to bulk electrolysis.

The bulk electrolysis was conducted using a cyclic voltammetry system (CHI 760D, CH Instruments, Inc.) under pH 7, 500 mM sodium phosphate buffer solution. Designed potentials were applied to each sample for 30 minutes, respectively. After the bulk electrolysis, the samples were rinsed gently by deionized water and transferred to an EPR tube by blade under Ar (99.999 %) atmosphere as promptly as possible. The EPR tube was frozen and stored at 77K in liquid nitrogen immediately.

### 2.2.12. DFT calculation

The first-principles density functional theory (DFT) calculations were performed with GGA+U functional using the Vienna *Ab-initio* simulation package (VASP) code. Electron-ion interactions were approximated by the projected augmented wave (PAW) method. The effective  $U$  parameter of 4.0 eV was used for Mn d orbitals. The cutoff energy for plane-wave basis set was consistently chosen to be 800 eV, and the k-space was sampled by a  $2 \times 2 \times 2$  regular mesh. Atomic positions and lattice parameters were relaxed until the force and stress were reduced below  $0.02 \text{ eV } \text{\AA}^{-1}$  and 2 kbar. The atomic charges were estimated by the Bader analysis for pristine  $\text{Mn}_3(\text{PO}_4)_2 \cdot 3\text{H}_2\text{O}$ , oxidized Mn phosphate,  $\beta\text{-MnO}_2$ , and reduced Mn oxide.

## 2.3 Results and Discussions

### 2.3.1 Basic characterization of $\text{Mn}_3(\text{PO}_4)_2 \cdot 3\text{H}_2\text{O}$ structure

In order to newly developed manganese phosphate based materials, various spectroscopic analysis were performed. Firstly, inductively coupled plasma–mass spectrometry (ICP) measurements and thermogravimetric analysis (TGA) revealed that the ratio of manganese atoms to phosphorus atoms in the manganese(II) phosphate hydrate crystal was 3:2 and that three water molecules were embedded per unit cell inside the crystal structure (Figure 2.1). X-ray diffraction (XRD) analysis confirmed that the crystal structure of synthesized manganese phosphate is  $\text{Mn}_3(\text{PO}_4)_2 \cdot 3\text{H}_2\text{O}$ . In this study, we discovered a new crystal,  $\text{Mn}_3(\text{PO}_4)_2 \cdot 3\text{H}_2\text{O}$ , whose crystal structure has never been identified completely. First, we tried to match our diffraction pattern with the available crystal structures in the Inorganic Crystal Structure Database (ICSD), but the existing JCPDS data did not provide a match. Among the available data, the most similar pattern comes from JCPDS card No. 00-003-0426 (quality mark: low precision (O)) for poorly crystalline  $\text{Mn}_3(\text{PO}_4)_2 \cdot 3\text{H}_2\text{O}$  (Figure 2.2 and Table 2.1). However, there is no crystallographic information available, such as the lattice parameter, atom coordination, Z-factor and plane index. Therefore, we determined the accurate crystal structure of  $\text{Mn}_3(\text{PO}_4)_2 \cdot 3\text{H}_2\text{O}$  by performing Rietveld refinement analysis and density-functional theory (DFT) calculations, and we compared simulated diffraction data with the experimental data (Figure 2.5d).

To computationally determine the crystal structure of  $\text{Mn}_3(\text{PO}_4)_2 \cdot 3\text{H}_2\text{O}$ , we focused on the crystal structure of switzerite ( $\text{Mn}_3(\text{PO}_4)_2 \cdot 7\text{H}_2\text{O}$ ), which had been determined previously.<sup>69</sup> Since the position of H atoms or orientation of water molecules were not well resolved in experiment, we annealed the initial switzerite structure at 300 K during 3 ps using the first-principles molecular dynamics (MD) simulation subsequently relaxed the structure at 0 K, obtaining the theoretical lattice parameters and atomic positions at equilibrium. According to the previous study, switzerite can transform to metaswitzerite ( $\text{Mn}_3(\text{PO}_4)_2 \cdot x\text{H}_2\text{O}$ ,  $3 < x < 4$ ) by expelling some water molecules and condensing the neutral layers along  $c$  in the framework structure.<sup>69</sup> The transformation is topotactic; only a minor change in atomic position occurs during dehydration.<sup>69</sup> Thus, in our first attempt to determine the structure, we assumed that the crystal structure of  $\text{Mn}_3(\text{PO}_4)_2 \cdot 3\text{H}_2\text{O}$  can be derived in a topotactic manner by removing four water molecules from switzerite. From the TGA analysis, we knew that there should be three water molecules per  $\text{Mn}_3(\text{PO}_4)_2$ .

Starting from the switzerite structure, we first removed three water molecules per formula unit in various combinations consistent with the structural information provided in previous study. These structures were then fully relaxed using density functional theory (DFT) methods and the lowest-energy structure was chosen as the metaswitzerite. We then removed one additional water molecule per formula unit in every possible way and relaxed the structure again. The most stable structure was regarded as the theoretical structure of  $\text{Mn}_3(\text{PO}_4)_2 \cdot 3\text{H}_2\text{O}$ , which is triclinic, P1, with  $a = 8.640(3) \text{ \AA}$ ,  $b = 13.354(8) \text{ \AA}$ ,  $c = 8.455(1) \text{ \AA}$ ,  $\alpha = 86.50(1)^\circ$

$\beta = 105.12(5)^\circ$   $\gamma = 90.14(3)^\circ$  and  $Z = 4$ . All of the peaks obtained experimentally can be matched with those obtained from the simulated crystal structure

Close observation of the newly identified  $\text{Mn}_3(\text{PO}_4)_2 \cdot 3\text{H}_2\text{O}$  crystals allows us to distinguish six different manganese sites in one unit cell (Figure 2.3). As shown in Figure 2.3, the surrounding geometry of each manganese is symmetrically broken because  $\text{Mn}_3(\text{PO}_4)_2 \cdot 3\text{H}_2\text{O}$  has triclinic crystal systems with the lowest symmetry. For example, Mn(1), Mn(2), Mn(3) and Mn(4) have distorted octahedral coordination, whereas Mn(5) and Mn(6) have distorted trigonal bipyramidal (TBP) geometry (Figure 2.3).

Water molecules are also positioned differently inside one unit cell ( $[\text{Mn}_3(\text{PO}_4)_2 \cdot 3\text{H}_2\text{O}]_4$ ,  $Z = 4$ ). Of the 12 water molecules in each unit cell, eight water molecules (water 1) participate in bridging two manganese atoms in a Mn(1, 2, 3 and 4) sheet. Two water molecules (water 2) are bound to Mn(6). The other two water molecules (water 3) stay between two sheets of Mn(1, 2, 3 and 4) without forming any coordinated bonds (Figure 2.4).

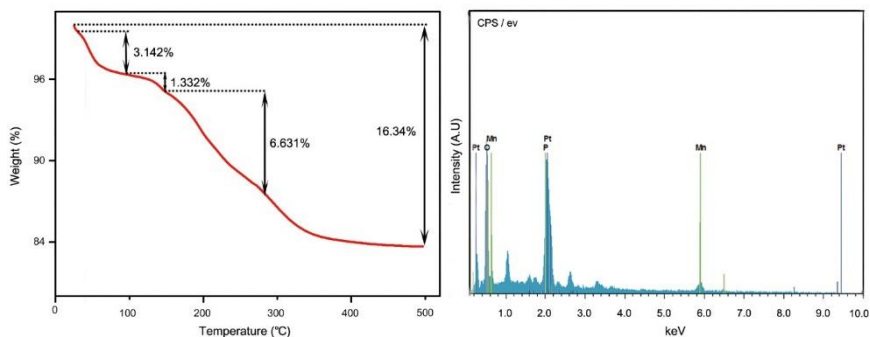
The asymmetric geometry of each manganese atom can be observed clearly by displaying the local structure around the P(1) position (Figure 2.3e). We measured the distances between manganese atoms in the simulated crystal structure. The shortest distance is 3.348 Å, between Mn(2) and Mn(3), and the longest one is 6.408 Å, between Mn(3) and Mn(5) in the local structure around the P(1) position. The average Mn-Mn distance is 3.411 Å, and the average Mn-O distance is 2.215

Å, which is much longer than the distances reported previously for Mn oxide-based compounds.<sup>70</sup> (Table 2.2 and Table 2.3). In PSII, the Mn<sub>4</sub>CaO<sub>5</sub> cluster also has an asymmetric geometry, distorted chair form and different distances between the four manganese atoms. In the cluster, the shortest distance is 2.8 Å, and the longest is 5.4 Å.<sup>19</sup>

Mn<sub>3</sub>(PO<sub>4</sub>)<sub>2</sub>·3H<sub>2</sub>O crystals prefer to grow in sheet-like structures under our experimental conditions. When the fluorine-doped tin oxide (FTO) glass is dipped during the synthesis of Mn<sub>3</sub>(PO<sub>4</sub>)<sub>2</sub>·3H<sub>2</sub>O, the sheets that can be found in bulk solution are assembled into a flower-like morphology, as shown in Figure 2.5a,b. High-resolution transmission electron microscopy (HRTEM) and selective area electron diffraction (SAED) analysis reveal that the two axes in the rectangular sheet are aligned in the [001] and [010] directions (Figure 2.5c and Figure 2.5c inset).

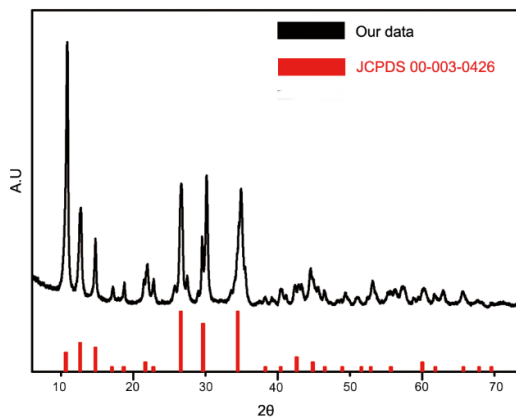
Oxide compound	System	Phosphate compound	System
<b>MnO</b>	Cubic (Fm3m)	<b>Mn<sub>2</sub>P<sub>2</sub>O<sub>7</sub></b>	Monoclinic(C2/m)
<b>Mn<sub>2</sub>O<sub>3</sub></b>	Orthorhombic (P bca)	<b>Mn<sub>3</sub>(PO<sub>4</sub>)<sub>2</sub></b>	Monoclinic(P2 <sub>1</sub> /a)
<b>MnOOH</b>	Monoclinic (B2 <sub>1</sub> /d)	<b>MnP<sub>4</sub>O<sub>11</sub></b>	Triclinic (P1) <sup>-</sup>
<b>Mn<sub>3</sub>O<sub>4</sub></b>	Tetragonal (I 4 <sub>1</sub> /amd)	<b>Mn<sub>2</sub>P<sub>4</sub>O<sub>12</sub></b>	Monoclinic (C2/c)
<b>MnO<sub>2</sub></b>	Tetragonal (P4 <sub>2</sub> /mmm)	<b>Mn<sub>3</sub>(PO<sub>4</sub>)<sub>2</sub></b>	Monoclinic (C2 <sub>1</sub> /c)
<b>MnFe<sub>2</sub>O<sub>4</sub></b>	Tetragonal (P4 <sub>2</sub> /nnm)	<b>Mn(PO<sub>3</sub>)<sub>3</sub></b>	Orthorhombic (Pnaa)
<b>CoMnO</b>	Cubic, Tetragonal (I4 <sub>1</sub> /amd)	<b>Mn<sub>3</sub>(PO<sub>4</sub>)<sub>2</sub> - 3H<sub>2</sub>O</b>	Triclinic (Our work)

**Table 2. 4** Crystal structures of manganese based oxide and phosphate compounds. It showed that almost all manganese oxide compounds display higher symmetry than manganese phosphate compounds. (All data were referred from JCPDS Card.)



	<b>Atomic weight</b>	<b>Solution concentration</b>	<b>Molar ratio</b>
<b>Mn</b>	54.938	6.92	3
<b>P</b>	30.974	2.49	1,92

**Figure 2.1.** Thermogravimetric analysis (TGA) of  $\text{Mn}_3(\text{PO}_4)_2 \cdot 3\text{H}_2\text{O}$ . The first drop of weight showed evaporation of  $\text{H}_2\text{O}$  molecules attached on the surface. Sequential weight drops of  $\text{Mn}_3(\text{PO}_4)_2 \cdot 3\text{H}_2\text{O}$  indicated that  $\text{H}_2\text{O}$  molecules were intercalated in  $\text{Mn}_3(\text{PO}_4)_2 \cdot 3\text{H}_2\text{O}$  structure. With the total weight loss (13.198 %) during TGA analysis, except that generated by surface water molecules, we could draw that three  $\text{H}_2\text{O}$  were embedded in manganese phosphate structure. And we also obtained from the ICP-MS result and EDS analysis that the ratio of manganese and phosphate was 3:2. Based on these results, we concluded that chemical formula of our catalyst was  $\text{Mn}_3(\text{PO}_4)_2 \cdot 3\text{H}_2\text{O}$ .



JCPDS 00-003-0426	Comments
Experimental Reference	The Dow Chemical Company, Midland, Michigan, USA. <i>Private Communication</i>
Chemical Formula	$\text{Mn}_3(\text{PO}_4)_2 \cdot 3\text{H}_2\text{O}$
Empirical Formula	$\text{H}_6\text{Mn}_3\text{O}_{11}\text{P}_2$
Weight %	H1.48 Mn40.32 O43.05 P15.15
Atomic %	H27.27 Mn13.64 O50.00 P9.09
Physical Information	None
Crystal Information	None (Molecular weight = 408.8)
Structure Data	None (Centrosymmetric)

**Figure 2.2.** Comparison between XRD pattern of our  $\text{Mn}_3(\text{PO}_4)_2 \cdot 3\text{H}_2\text{O}$  and previously reported JCPDS pattern of  $\text{Mn}_3(\text{PO}_4)_2 \cdot 3\text{H}_2\text{O}$ . The JCPDS card data was significantly different from our data in terms of peak positions and peak intensity.

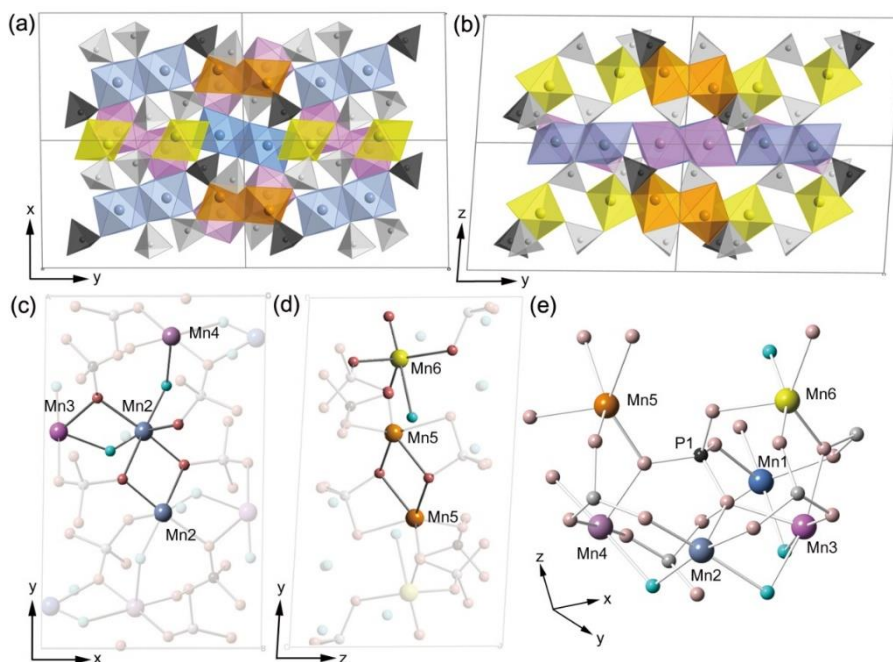


**Figure 2.3.** Schematic representation of crystalline  $\text{Mn}_3(\text{PO}_4)_2 \cdot 3\text{H}_2\text{O}$ . (a. b) Coordination and arrangement of each manganese atom. Larger spheres denote Mn atoms, and smaller spheres denote phosphate atoms. (c) Mn(2) atoms are connected to each other by edge O-O sharing. Mn(2) and Mn(3) atoms are bridged by edge O- $\text{O}_w$  sharing, and Mn(2) atoms are linked to Mn(4) atoms by  $\text{O}_w$  vertex sharing. ( $\text{O}_w$  : Oxygen atom in a water molecule) (d) Bonding character of Mn(5) and Mn(6). The Mn(5) atoms share two oxygen atoms with each other whereas the Mn(6) atom does not share any atoms with other manganese atoms. (e) Spherical cluster around the P(1) site, with a radius of 4.5 Å illustrating the asymmetrical arrangement of the manganese atoms.

Mn1	Mn2	Mn3	Mn4	Mn5	Mn6
2.210 Å	2.286 Å	2.163 Å	2.259 Å	2.214 Å	2.177 Å
2.145 Å	2.173 Å	2.286 Å	2.281 Å	2.208 Å	2.104 Å
2.119 Å	2.359 Å	2.262 Å	2.147 Å	2.316 Å	2.108 Å
2.317 Å	2.240 Å	2.218 Å	2.171 Å	2.120 Å	2.135 Å
2.139 Å	2.117 Å	2.264 Å	2.215 Å	2.121 Å	2.442 Å
2.468 Å	2.164 Å	2.175 Å	2.180 Å		

**Table 2.5.** Bond lengths between manganese and neighboring oxygen atoms in  $\text{Mn}_3(\text{PO}_4)_2 \cdot 3\text{H}_2\text{O}$ . Average Mn-O bond distance is 2.215 Å.

	Mn1	Mn2	Mn3	Mn4	Mn5
Edge	3.259 Å	3.348 Å	3.348 Å	3.398 Å	3.526 Å
Sharing	3.398 Å	3.208 Å	3.295 Å	3.337 Å	
Corner	3.664 Å	3.718 Å	3.664 Å	3.718 Å	3.609 Å
Sharing				3.609 Å	

**Table 2.3.** Mn-Mn distance in  $\text{Mn}_3(\text{PO}_4)_2 \cdot 3\text{H}_2\text{O}$ . Distance values between edge-sharing manganese atoms and corner-sharing manganese atoms were obtained. Average Mn-Mn bond distance was 3.412 Å. Generally, corner sharing manganese atoms had larger Mn-Mn distances than edge sharing ones.

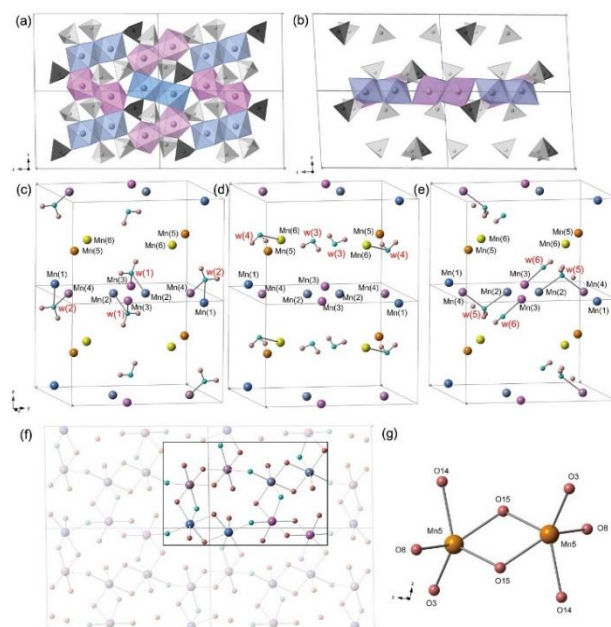


**Figure 2.4.** (a, b) Crystal structure of  $[\text{Mn}_4\text{O}_{10}(\text{H}_2\text{O})_2]_2$  sheet composed of Mn(1), Mn(2), Mn(3), and Mn(4). Mn(5) and Mn(6) were omitted for clarity. (c) Chemical environment around water (1) and water (2) molecules. Water (1) were ligated to both Mn(2) and Mn(3) atoms, and water (2) were ligated to Mn(1) and Mn(4) atoms. (d) Chemical environment around water (3) and water (4). In the case of water (3), no chemical bond existed around water (3), while water (4) were solely ligated to Mn(6) atom. (e) Chemical environment around water (5) and water (6). Water (5) were ligated together with Mn(2) and Mn(4) atoms. Water (6) were only ligated to Mn(3) atoms. (f) Chemical structure of  $[\text{Mn}_4\text{O}_{10}(\text{H}_2\text{O})_2]_2$  unit cell. (g) Chemical structure of  $\text{Mn}_2\text{O}_8$  dimer involving two Mn(5) atoms.

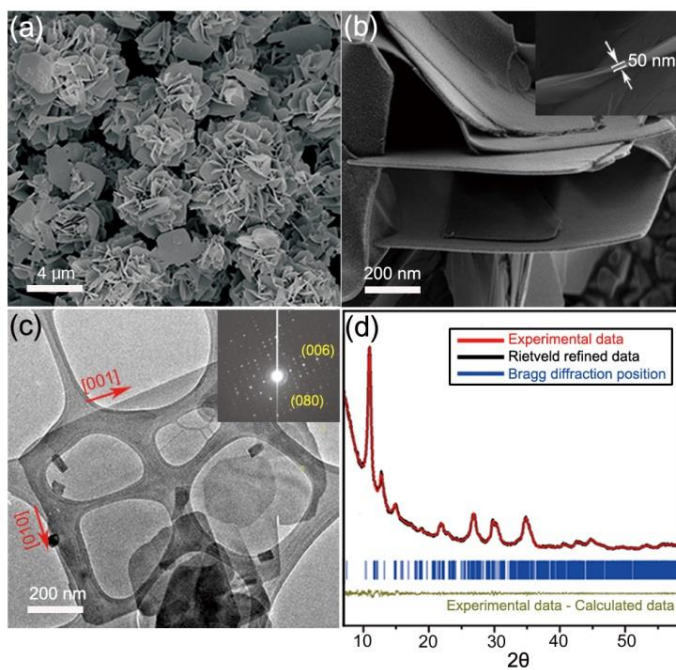


**Figure 2.5.** Characterization of  $\text{Mn}_3(\text{PO}_4)_2 \cdot 3\text{H}_2\text{O}$ . (a, b) SEM images and (c) TEM image of a [001], [010]-oriented  $\text{Mn}_3(\text{PO}_4)_2 \cdot 3\text{H}_2\text{O}$  sheet and SAED patterns (inset). (d) Rietveld-refined XRD patterns of  $\text{Mn}_3(\text{PO}_4)_2 \cdot 3\text{H}_2\text{O}$ .  $R_{\text{wp}} = 1.05\%$ ,  $R_{\text{p}} = 1.22\%$ ,  $R_{\text{exp}} = 0.59\%$ , and  $\chi^2 = 1.79$ .

### 2.3.2 Electrochemical analysis of $\text{Mn}_3(\text{PO}_4)_2 \cdot 3\text{H}_2\text{O}$

The water oxidation catalytic characteristics of  $\text{Mn}_3(\text{PO}_4)_2 \cdot 3\text{H}_2\text{O}$  were evaluated by cyclic voltammetry in 0.5 M sodium phosphate electrolyte at pH 7. (Figure 2.6)  $\text{Mn}_3(\text{PO}_4)_2 \cdot 3\text{H}_2\text{O}$  was deposited on the FTO substrate using previously reported method. The current value was normalized to the total weight or surface area of the catalyst on the working electrode. The OER activity curves were obtained by averaging the currents from the forward and reverse CV scans. (for raw CV curves before polarization correction, see Figure 2.9) Potentiostatic electrolysis of  $\text{Mn}_3(\text{PO}_4)_2 \cdot 3\text{H}_2\text{O}$  yield a current value similar to the averaged one (Figure 2.10). We expected that the average current value could be a reasonable approximation of the true steady-state current. As shown in Figure 2.6a, the oxygen evolution ability of  $\text{Mn}_3(\text{PO}_4)_2 \cdot 3\text{H}_2\text{O}$  was higher than that of commercial MnO (99.99%) and  $\text{MnO}_2$  (99.99%). The MnO and  $\text{MnO}_2$  had monophasic features with high crystallinity (Figure 2.8). The current of  $\text{Mn}_3(\text{PO}_4)_2 \cdot 3\text{H}_2\text{O}$  was  $5.2 \text{ A g}^{-1}$  whereas that of MnO and  $\text{MnO}_2$  was both below  $1 \text{ A g}^{-1}$  at the overpotential value of 680 mV (Figure 2.6a). Even after normalization by the surface area of each catalyst, the OER current of  $\text{Mn}_3(\text{PO}_4)_2 \cdot 3\text{H}_2\text{O}$  ( $0.146 \text{ mA cm}^{-2}_{\text{cat}}$ ) was still much higher than that of MnO ( $0.063 \text{ mA cm}^{-2}_{\text{cat}}$ ) and  $\text{MnO}_2$  ( $0.037 \text{ mA cm}^{-2}_{\text{cat}}$ ). The Tafel plot of each catalyst was obtained from polarization- corrected CV curves. The exchange current value of  $\text{Mn}_3(\text{PO}_4)_2 \cdot 3\text{H}_2\text{O}$  was 3 times larger than that of MnO and  $\text{MnO}_2$  (Figure 2.6b). The Tafel slopes of  $\text{Mn}_3(\text{PO}_4)_2 \cdot 3\text{H}_2\text{O}$ , MnO, and  $\text{MnO}_2$  were shown to be around 120

mV/dec. It might be resulted from the existence of limitation on electron transport through the catalyst due to its low conductivity as observed similarly in poorly conductive metal oxide materials. We are still investigating the catalytic performance of the carbon involved cell to improve its electrical conductivity.

In order to check the stability of the  $\text{Mn}_3(\text{PO}_4)_2 \cdot 3\text{H}_2\text{O}$ , we performed continuous potential cycling between 0.7 V and 1.5 V (vs NHE). As shown in Figure 2.10, the cyclic voltammetry currents of  $\text{Mn}_3(\text{PO}_4)_2 \cdot 3\text{H}_2\text{O}$  remained nearly constant even after 100 cycles, indicating high catalytic durability of  $\text{Mn}_3(\text{PO}_4)_2 \cdot 3\text{H}_2\text{O}$ . HR-TEM analysis was performed to examine the phase stability of the  $\text{Mn}_3(\text{PO}_4)_2 \cdot 3\text{H}_2\text{O}$  under OER condition. The single-crystalline feature of  $\text{Mn}_3(\text{PO}_4)_2 \cdot 3\text{H}_2\text{O}$  was stably maintained after 30 min of bulk electrolysis at 1.5 V. (Figure 2.11)

We also used gas chromatography to confirm the ability of  $\text{Mn}_3(\text{PO}_4)_2 \cdot 3\text{H}_2\text{O}$  to act as a photochemical oxygen-evolving catalyst. After 30 min of illumination, 13.8  $\mu\text{mol}$  of oxygen was formed for every mole of manganese in the crystal center. A negligible amount of oxygen was detected without the use of the photosensitizer  $\text{Ru}^{2+}(\text{bpy})_3$  (Figure 2.7). The turnover frequency (TOF) of the manganese phosphate catalyst was  $3.05 \times 10^{-5} \text{S}^{-1}/\text{Mn mol}$ . We also tested same experiments with reference materials,  $\text{MnO}$ , and  $\text{MnO}_2$  as photochemical oxygen-evolving catalysts (Figure 2.7). Based on the amount of  $\text{O}_2$  gas evolved during the initial 10 min of photolysis for each compound, the TOFs of the compounds were estimated. The TOF of  $\text{Mn}_3(\text{PO}_4)_2 \cdot 3\text{H}_2\text{O}$  was  $0.024 \mu\text{mol m}^{-2} \text{s}^{-1}$ , which is higher than the TOF of  $\text{MnO}$  or  $\text{MnO}_2$  ( $0.0084 \mu\text{mol m}^{-2} \text{s}^{-1}$  and  $0.0077 \mu\text{mol m}^{-2} \text{s}^{-1}$ ,

respectively). Moreover, the TOF of  $\text{Mn}_3(\text{PO}_4)_2 \cdot 3\text{H}_2\text{O}$  ( $0.024 \mu\text{mol m}^{-2} \text{s}^{-1}$ ) is higher than previously reported TOF values of Mn-oxide catalysts ( $0.0055 - 0.017 \mu\text{mol m}^{-2} \text{s}^{-1}$ ). In addition, the TOFs of the commercial MnO and  $\text{MnO}_2$  used in this study were  $0.0084 \mu\text{mol m}^{-2} \text{s}^{-1}$  and  $0.0074 \mu\text{mol m}^{-2} \text{s}^{-1}$ , respectively, in agreement with previously reported values for  $\text{MnO}_2$  ( $0.0055 - 0.017 \mu\text{mol m}^{-2} \text{s}^{-1}$ ). For comparison, the previously reported TOF values for other manganese compounds are summarized in Table 2.4.

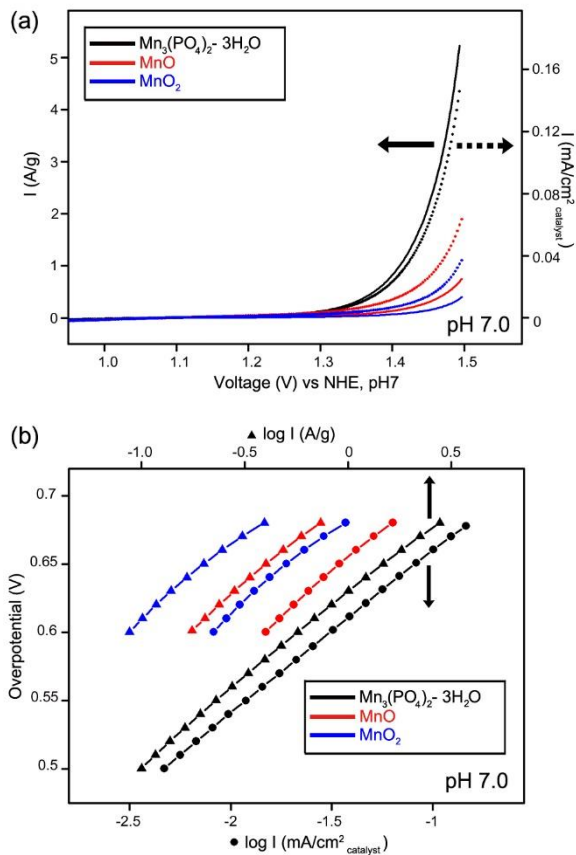


**Figure 2.6.** Electrochemical characterization of  $\text{Mn}_3(\text{PO}_4)_2 \cdot 3\text{H}_2\text{O}$ ,  $\text{MnO}$ , and  $\text{MnO}_2$ . (a) Polarization-corrected cyclic voltammetry (CV) curves and (b) Tafel plots for  $\text{Mn}_3(\text{PO}_4)_2 \cdot 3\text{H}_2\text{O}$ ,  $\text{MnO}$ , and  $\text{MnO}_2$  spin-coated on the FTO substrate in which the current value was normalized to the weight and surface area of the catalysts, respectively.

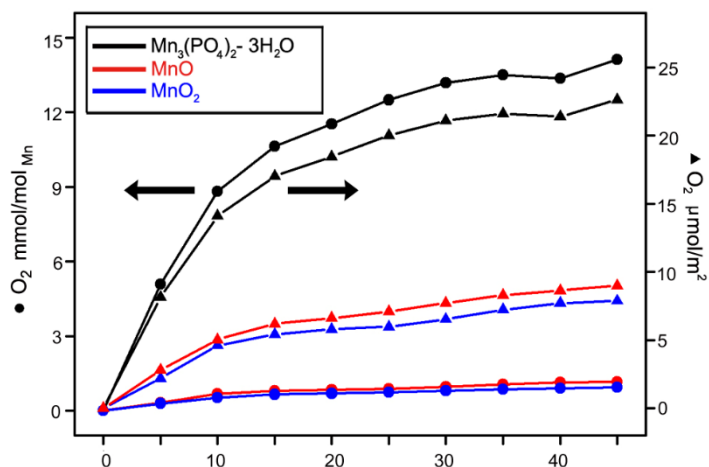


**Figure 2.7.** The amount of oxygen evolved by  $\text{Mn}_3(\text{PO}_4)_2 \cdot 3\text{H}_2\text{O}$ ,  $\text{MnO}$ , and  $\text{MnO}_2$  with a  $\text{Ru}^{2+}(\text{bpy})_3\text{-S}_2\text{O}_8^{2-}$  system, as recorded by gas chromatography (black, red, and blue). The amount of evolved oxygen was normalized to the total Mn atoms and surface area in the solution. The turnover frequency numbers of the compounds were estimated from the amount of oxygen gas evolved during the initial 10 min of photolysis for each compounds.

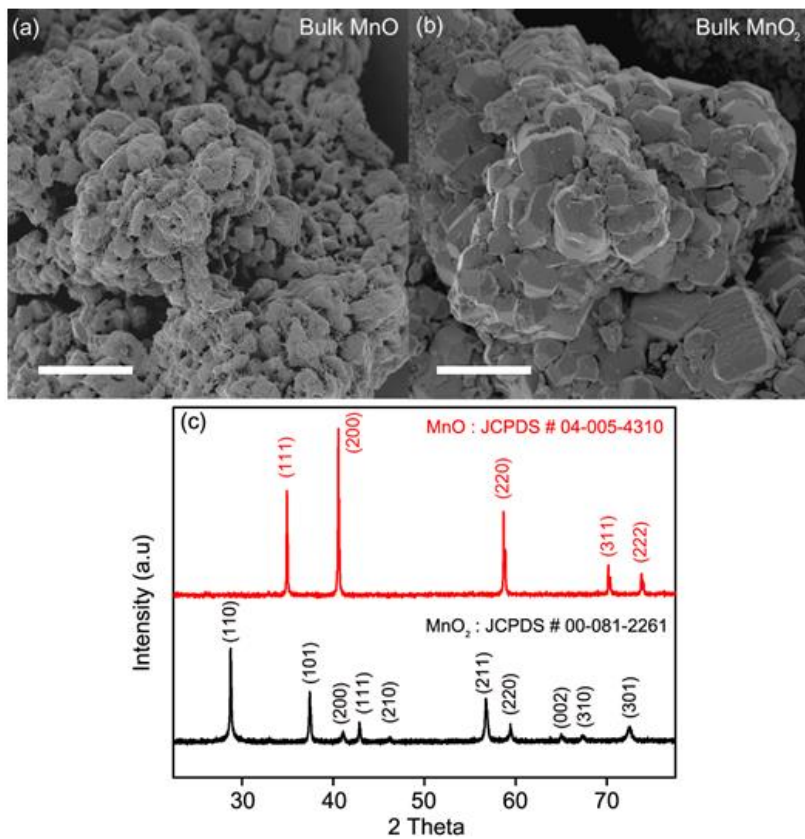


**Figure 2.8.** FE-SEM images of (a) bulk MnO and (b) MnO<sub>2</sub>. (c) The XRD patterns demonstrate that each material has monophasic features and that there are no secondary phases (scale bar: 10 μm)

<b>Catalyst</b>	<b>TOF ( s<sup>-1</sup> per Mn )</b>	<b>BET (m<sup>2</sup> per g)</b>	<b>TOF ( μmol/m<sup>2</sup> )</b>	<b>Experimental Condition</b>
λ-MnO <sub>2</sub> (LT)	3.0 X 10 <sup>-5</sup>	20.0	0.017	
CaMn <sub>2</sub> O <sub>4</sub>	3.2 X 10 <sup>-4</sup>	303	0.0098	Ru(bpy) <sub>3</sub> Cl <sub>2</sub> - [Co(NH <sub>3</sub> ) <sub>5</sub> Cl]Cl <sub>2</sub> , Acetate buffer ( pH 4 )
MnO <sub>2</sub> colloid	2.5 X 10 <sup>-5</sup>	40	0.0072	
α- MnO <sub>2</sub> nanotube	3.5 X 10 <sup>-5</sup>	25.1	0.016	Ru(bpy) <sub>3</sub> Cl <sub>2</sub> - Na <sub>2</sub> S <sub>2</sub> O <sub>8</sub> , No buffer (Initial pH 7)
α- MnO <sub>2</sub> nanowire	5.9 X 10 <sup>-5</sup>	47.9	0.014	Ru(bpy) <sub>3</sub> Cl <sub>2</sub> - Na <sub>2</sub> S <sub>2</sub> O <sub>8</sub> , No buffer (Initial pH 7)
β- MnO <sub>2</sub> nanowire	2.0 X 10 <sup>-5</sup>	14.9	0.015	Ru(bpy) <sub>3</sub> Cl <sub>2</sub> - Na <sub>2</sub> S <sub>2</sub> O <sub>8</sub> , No buffer (Initial pH 7)
Bulk α- MnO <sub>2</sub>	1.0 X 10 <sup>-5</sup>	20.8	0.0055	Ru(bpy) <sub>3</sub> Cl <sub>2</sub> - Na <sub>2</sub> S <sub>2</sub> O <sub>8</sub> , No buffer (Initial pH 7)
Our catalyst	1.5 X 10 <sup>-5</sup>	4.58	0.024	Ru(bpy) <sub>3</sub> Cl <sub>2</sub> - Na <sub>2</sub> S <sub>2</sub> O <sub>8</sub> , 0.1 M Na- Pi buffer ( pH 7 )

MnO <sub>2</sub> (commercial)	1.1 X 10 <sup>-6</sup>	1.48	0.0077	
MnO (Commercial)	8.8 X 10 <sup>-7</sup>	1.69	0.0084	

**Table 2.6.** The TOF values of the various manganese oxide catalysts that have been reported and of our catalyst, commercial MnO, and MnO<sub>2</sub>, which were used in this study for water oxidation catalysis. TOF values (s<sup>-1</sup> per Mn, μmol/m<sup>2</sup> s ) were calculated based on the oxygen evolution rates divided by the mole number of Mn atoms and total surface area of the catalysts. These values are indexed in the second and fourth columns, respectively. The BET values of the catalysts and the experimental conditions are summarized in the third and fourth columns, respectively.

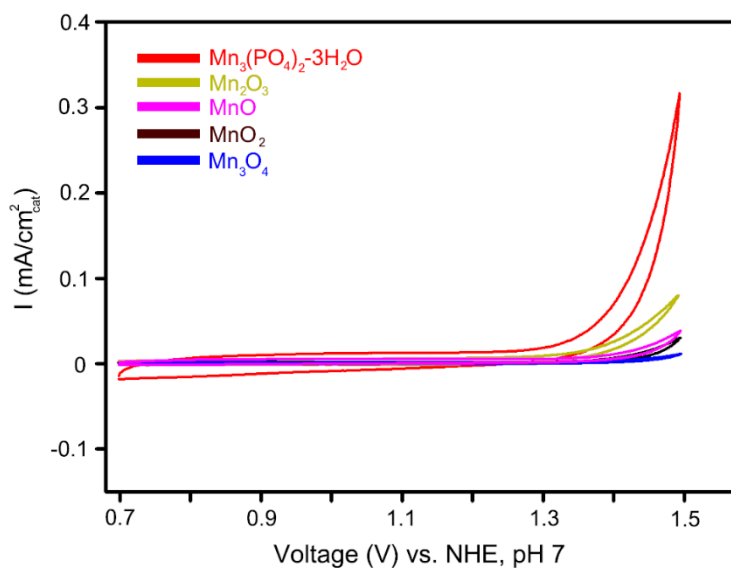


**Figure 2.9.** Cyclic voltammetry curves for five catalysts before polarization correction :  $\text{Mn}_3(\text{PO}_4)_2 \cdot 3\text{H}_2\text{O}$  (red), nano  $\text{MnO}$  (pink),  $\text{Mn}_3\text{O}_4$  (blue),  $\text{Mn}_2\text{O}_3$  (dark yellow), and  $\text{MnO}_2$  (black) Catalyst loaded working electrode were scanned at the rate of  $10 \text{ mV sec}^{-1}$  in 0.5 M phosphate buffer solution at applied potentials ranging from 0.7 V to 1.5 V.

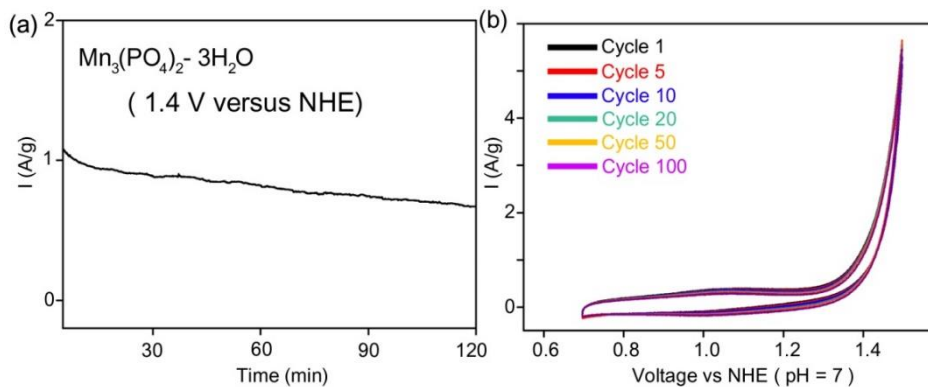


**Figure 2.10** (a) Catalytic current profile obtained upon constant potential (1.4 V vs NHE) electrolysis under pH 7. As shown in the figure, considerable catalytic current was maintained after 2 hours of electrolysis. (b) Cyclic Voltammetry curves of  $\text{Mn}_3(\text{PO}_4)_2 \cdot 3\text{H}_2\text{O}$ , showing the 1<sup>st</sup>, 5<sup>th</sup>, 10<sup>th</sup>, 20<sup>th</sup>, 50<sup>th</sup>, and 100<sup>th</sup> cycles. All cyclic voltammetry curves were obtained in  $\text{N}_2$  saturated 0.5 M Na-Pi buffer at a scan rate of  $10 \text{ mV sec}^{-1}$ .

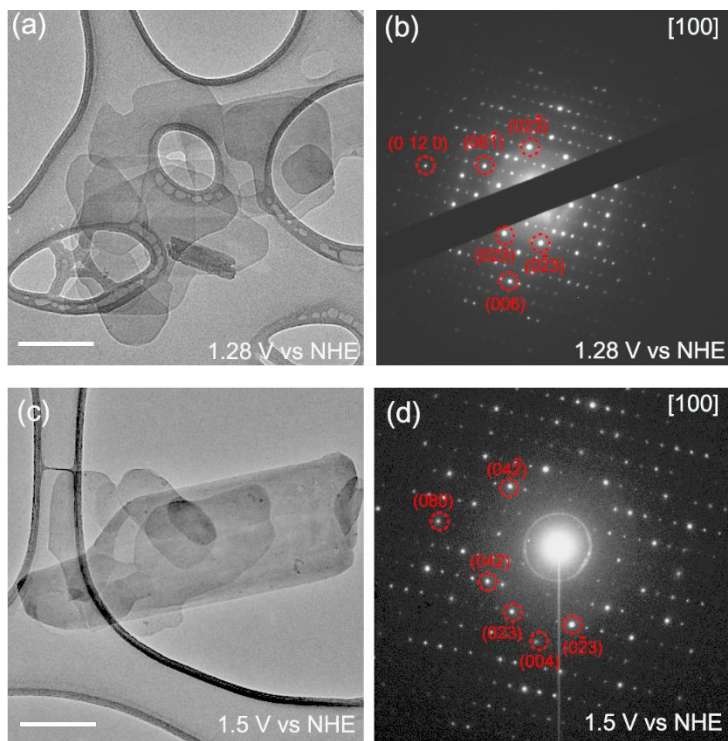


**Figure 2. 11.** Stability of  $\text{Mn}_3(\text{PO}_4)_2 \cdot 3\text{H}_2\text{O}$  during the water oxidation reaction. To evaluate the stability of  $\text{Mn}_3(\text{PO}_4)_2 \cdot 3\text{H}_2\text{O}$ , bulk electrolysis analysis was performed at (a) 1.28 V and (c) 1.5 V. After 30 min of electrolysis, the catalysts were collected and analyzed. As shown in the SAED patterns, the single-crystalline feature of  $\text{Mn}_3(\text{PO}_4)_2 \cdot 3\text{H}_2\text{O}$  was maintained at both (b) 1.28 V and (d) 1.5 V (scale bar: 200 nm).

### 2.3.3 Mechanistic studies of $\text{Mn}_3(\text{PO}_4)_2 \cdot 3\text{H}_2\text{O}$

The electron paramagnetic resonance (EPR) spectroscopy was utilized to investigate the manganese oxidation state of the  $\text{Mn}_3(\text{PO}_4)_2 \cdot 3\text{H}_2\text{O}$ . Three potentials (1.0 V, 1.28 V and 1.40 V) were selected to investigate the effect of changing potential on the manganese oxidation state during the catalytic cycle. The perpendicular mode continuous-wave EPR (CW-EPR) spectra of  $\text{Mn}_3(\text{PO}_4)_2 \cdot 3\text{H}_2\text{O}$  at three different applied potentials are shown in Figure 2.12a. The EPR spectrum of as-prepared  $\text{Mn}_3(\text{PO}_4)_2 \cdot 3\text{H}_2\text{O}$  exhibits a characteristic  $S = 5/2$ ,  $\text{Mn}^{\text{II}}$  signal, at  $g \sim 2$  with a six-line  $^{55}\text{Mn}$  ( $I = 5/2$ , 100% abundance) hyperfine splitting. Up to the electrolysis potential of 1.4 V, EPR spectra feature of  $\text{Mn}^{\text{II}}$  was maintained irrespective of applied potential values. We tried to detect other manganese oxidation state,  $\text{Mn}^{\text{III}}$ , with parallel polarization EPR using previous method, but only observed a broad peak arising most likely from oxygen due to the fast decaying nature of  $\text{Mn}^{\text{III}}$  (Figure 2.13). We then prepared the samples in pyrophosphate solution, which has been shown to effectively ligate to  $\text{Mn}^{\text{III}}$  ions before decaying and also known as redox-inert agent. Figure 2.12b presents the parallel-mode CW-EPR at different applied potentials. The well-resolved six-line  $S = 2$ ,  $\text{Mn}^{\text{III}}$  signal which cannot be detected from as-prepared  $\text{Mn}_3(\text{PO}_4)_2 \cdot 3\text{H}_2\text{O}$  powder, with hyperfine coupling of  $\sim 42$  G centered at  $g_{\text{eff}} \sim 8.2$ , appeared. This result shows the existence of  $\text{Mn}^{\text{III}}$  species on the surface of  $\text{Mn}_3(\text{PO}_4)_2 \cdot 3\text{H}_2\text{O}$  under OER condition.

To obtain a microscopic understanding of the improved catalytic activity of manganese phosphate, we performed DFT calculations and determined how much J-T distortion is induced for the  $\text{Mn}^{\text{III}}$  configuration, which is an important criterion for the stability of the  $\text{Mn}^{\text{III}}$  state. First, we selected  $\beta\text{-MnO}_2$ , which is composed of the highly symmetric  $\text{MnO}_6$  octahedron. According to a recently proposed mechanism<sup>57</sup>, the surface oxidation state of  $\beta\text{-MnO}_2$  is spontaneously reduced to  $\text{Mn}^{\text{II}}$  by electron injection from  $\text{H}_2\text{O}$  and then electro-oxidized into  $\text{Mn}^{\text{III}}$  when an electric potential of  $\sim 1.5$  V with respect to NHE is applied. Thus, we first negatively charged  $\beta\text{-MnO}_2$  by adding a number of electrons to enforce the  $\text{Mn}^{\text{II}}$  state in  $\beta\text{-MnO}_2$  ( $\text{Mn}^{\text{IV}} \rightarrow \text{Mn}^{\text{II}}$ ) and then oxidized this negatively charged  $\beta\text{-MnO}_2$  to form  $\text{Mn}^{\text{III}}$  ( $\text{Mn}^{\text{II}} \rightarrow \text{Mn}^{\text{III}}$ ). The pair distribution function shows that the average distance of Mn-O is  $1.916\text{\AA}$ , which splits into  $1.840$  and  $1.916\text{\AA}$  as a result of oxidation of  $\text{Mn}^{\text{II}}$  to  $\text{Mn}^{\text{III}}$  (Figure 2.14a). This small splitting indicates that the J-T distortion is significantly hindered.

However, the rate-limiting step in the catalytic cycle of  $\text{Mn}_3(\text{PO}_4)_2 \cdot 3\text{H}_2\text{O}$  is not yet fully resolved. Nevertheless, the transition from  $\text{Mn}^{\text{II}}$  to  $\text{Mn}^{\text{III}}$  is likely an important step, as in other  $\text{Mn}^{\text{II}}$ -based OER catalysts. In fact, the existence of  $\text{Mn}^{\text{III}}$  during the catalytic cycle was confirmed by EPR. For theoretical investigation, therefore, we positively charged  $\text{Mn}_3(\text{PO}_4)_2 \cdot 3\text{H}_2\text{O}$  by reducing a number of electrons such that all the Mn atoms were converted from  $\text{Mn}^{\text{II}}$  to  $\text{Mn}^{\text{III}}$ . The resulting pair distribution function of Mn-O in Figure 2.14b demonstrates that the Mn-O bond

lengths are split into various values of 1.980-2.524 Å upon full oxidation, clearly demonstrating significant J-T distortion in the Mn<sup>III</sup> octahedra of up to 0.5 Å.

We also performed similar calculations for MnO, which has the same resting Mn valency. The Mn<sup>II</sup>-O bond length (2.240 Å on average) splits into 2.090 and 2.440 Å in the Mn<sup>III</sup> configuration, indicating a degree of J-T distortion similar to that observed for Mn<sub>3</sub>(PO<sub>4</sub>)<sub>2</sub>·3H<sub>2</sub>O.

As another standard to gauge the stability of Mn<sup>III</sup>, we examined the average pressure when all the Mn atoms were in the Mn<sup>III</sup> configuration (Figure 2.14 d). A large value of pressure implies a tendency for the lattice to be distorted and destabilized when Mn<sup>III</sup> atoms are abundant. As shown in Figure 2.14 d, the magnitude of pressure follows the order MnO<sub>2</sub> > MnO > Mn<sub>3</sub>(PO<sub>4</sub>)<sub>2</sub>·3H<sub>2</sub>O. Interestingly, the catalytic activity exactly follows the reverse order. Therefore, in combination with the above analysis of the J-T distortion, we conclude that the structural flexibility that stabilizes the Mn<sup>III</sup> state is the key property underlying the high catalytic activity of Mn<sub>3</sub>(PO<sub>4</sub>)<sub>2</sub>·3H<sub>2</sub>O.

Our computation shows another interesting phenomenon during the Mn oxidation. Among six different Mn sites, Mn(2) is oxidized through the coupled reaction with both adsorbed (w1) and freely intercalated (w3) water molecules. As shown in Figure 2.15a,b, H<sub>2</sub>O (w1) originally coordinated around Mn(2) in pristine state spontaneously dissociates into OH<sup>-</sup> and H<sup>+</sup> when Mn(2) is oxidized in the 3+ state. The dissociated proton (H<sub>1</sub>) migrates to the adjacent free water molecule (w3), forming H<sub>3</sub>O<sup>+</sup>. Moreover, bonding length between Mn(2) and OH<sup>-</sup> ligand was

shorter compared to Mn-O bonding length in the pristine state. The shorter Mn(III)-OH<sup>-</sup> bond makes the Mn(III) state more stable via attractive Coulomb interaction between Mn(III) and OH<sup>-</sup> (Figure 2.15d).

We also explored the role of the phosphate anion in the context of the electrophilicity of Mn. According to previous studies, the insertion of electron-withdrawing groups around the transition metal can increase the electrophilicity of the metal-oxo group and promote the formation of O-O bonds via stronger Lewis acid (metal-oxo) – base (water) reactions. Indeed, it is well known that the strong P-O bond in the phosphate anion can induce strong polarization of oxygen ions and increase the electrophilicity of a transition metal around the phosphate group.

To determine whether the phosphate groups in Mn<sub>3</sub>(PO<sub>4</sub>)<sub>2</sub>-3H<sub>2</sub>O increase the electrophilicity of Mn, the Bader charge of the Mn atoms in Mn<sub>3</sub>(PO<sub>4</sub>)<sub>2</sub>-3H<sub>2</sub>O was calculated in the unit of electron charge  $e$  ( $>0$ ). We chose MnO as a reference, because the Mn in MnO has the same valency and oxygen counter anion. Compared to the Bader charge of MnO (1.542  $e$ ), Mn<sub>3</sub>(PO<sub>4</sub>)<sub>2</sub>-3H<sub>2</sub>O has a larger value of 1.639  $e$ , indicating increased Mn electrophilicity in Mn<sub>3</sub>(PO<sub>4</sub>)<sub>2</sub>-3H<sub>2</sub>O. Experimentally, this increased electrophilicity was also confirmed by comparing the Mn 2p peak values of MnO and Mn<sub>3</sub>(PO<sub>4</sub>)<sub>2</sub>-3H<sub>2</sub>O by X-ray photon spectroscopy (XPS). The Mn 2p peak value of Mn<sub>3</sub>(PO<sub>4</sub>)<sub>2</sub>-3H<sub>2</sub>O is 641.25 eV which is 1.05 eV higher than the value of MnO (640.2 eV). Thus, the experimental data and calculations indicate that the phosphate anion in Mn<sub>3</sub>(PO<sub>4</sub>)<sub>2</sub>-3H<sub>2</sub>O indeed increases the Lewis acidity of the manganese atom. Therefore, we believe that Mn-oxo groups in Mn<sub>3</sub>(PO<sub>4</sub>)<sub>2</sub>-3H<sub>2</sub>O

promote the nucleophilic attack of  $\text{H}_2\text{O}$ , and thus facilitate the formation of O-O bonds through stronger Lewis acid-base interactions.

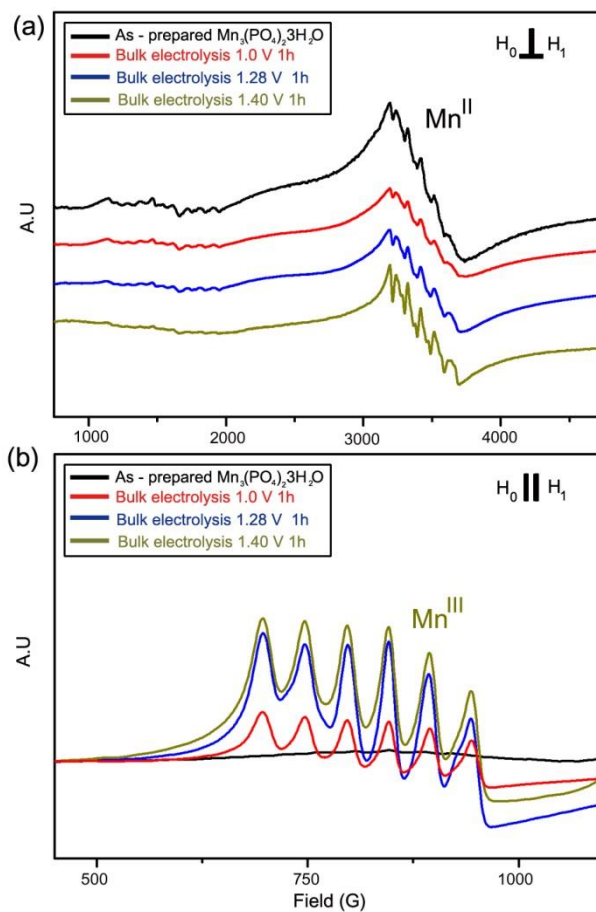


**Figure 2.12.** EPR analysis of  $\text{Mn}_3(\text{PO}_4)_2 \cdot 3\text{H}_2\text{O}$ , showing the valence change of Mn. (a) Perpendicular mode and (b) Parallel mode X-band CW-EPR spectra of  $\text{Mn}_3(\text{PO}_4)_2 \cdot 3\text{H}_2\text{O}$  varying electrolysis potentials with constant bulk electrolysis time of 1 hr.

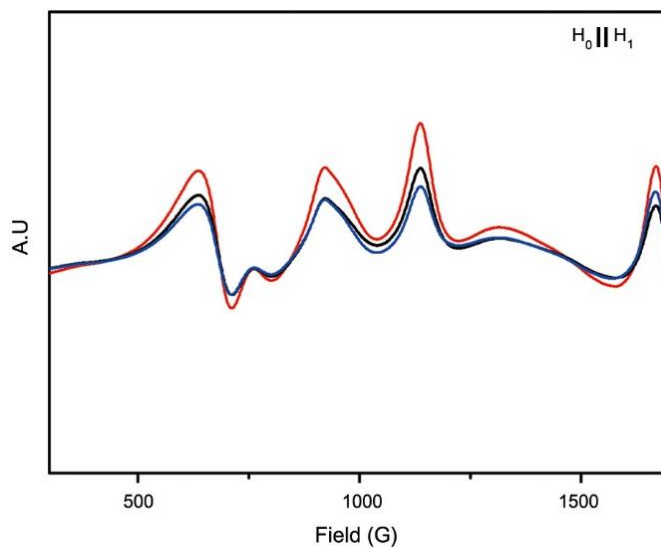


**Figure 2.13.** Parallel mode CW-EPR Spectra of  $\text{Mn}_3(\text{PO}_4)_2 \cdot 3\text{H}_2\text{O}$  at three different potentials, 1.0 V (blue), 1.28 V (black), 1.40 V (red) respectively. When the stabilizing agent, pyrophosphate was not used during the preparation of EPR samples,  $\text{Mn}^{\text{III}}$  hyperfine splitting was not observed but only broad signal arising from oxygen were detected.

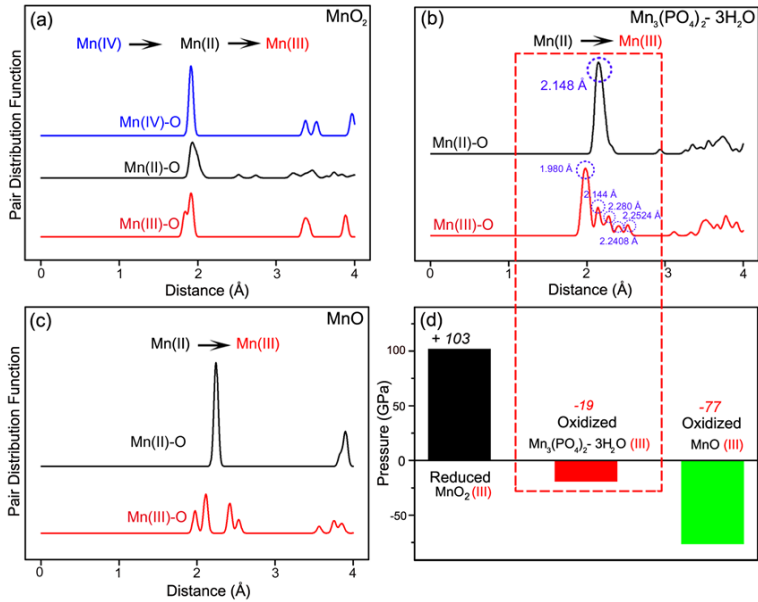


**Figure 2.14.** The pair distribution functions of manganese atoms (a) in pristine  $\text{MnO}_2$  (blue) and reduced manganese oxide as  $\text{Mn(II)}$  (black) and  $\text{Mn(III)}$  (red); (b) in pristine  $\text{Mn}_3(\text{PO}_4)_2 \cdot 3\text{H}_2\text{O}$  (black) and oxidized manganese phosphate (red) in which all  $\text{Mn}^{\text{II}}$  atoms were intentionally oxidized to  $\text{Mn}^{\text{III}}$ ; and (c) in pristine  $\text{MnO}$  (black) and oxidized manganese oxide (red). The pair distribution function near  $2 \text{ \AA}$  in  $\text{Mn}_3(\text{PO}_4)_2 \cdot 3\text{H}_2\text{O}$  indicates that the Mn-O bonds originated from phosphate groups. In contrast to  $\text{MnO}_2$ , the split of the pair distribution function from black to red in  $\text{Mn}_3(\text{PO}_4)_2 \cdot 3\text{H}_2\text{O}$  and  $\text{MnO}$  indicates the J-T distortion. (d) The pressure on the cell of each Mn compound when Mn was reduced or oxidized to the 3+ state.

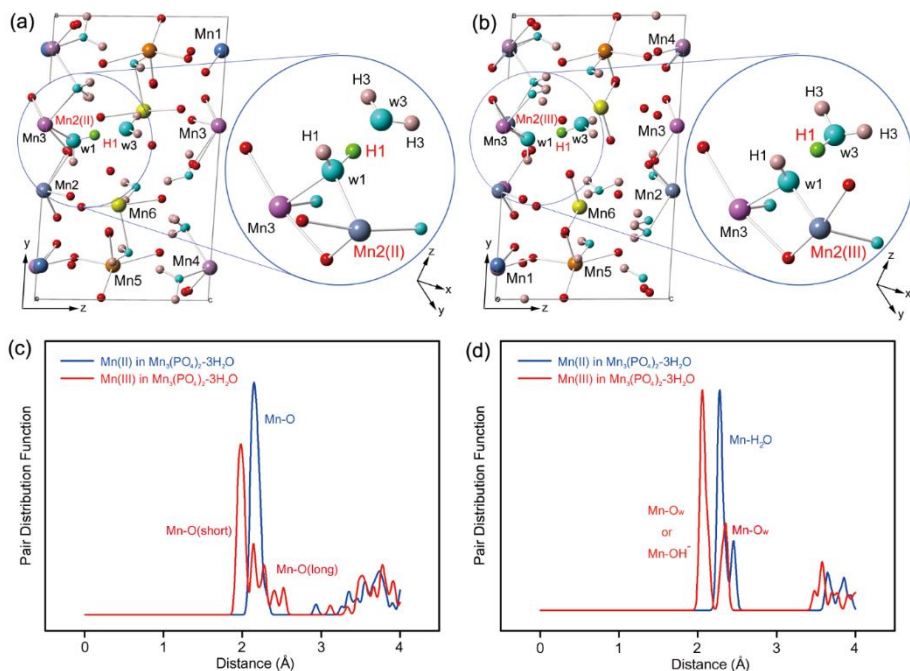


**Figure 2.15.** Computational results for the oxidation process of  $\text{Mn}_3(\text{PO}_4)_2 \cdot 3\text{H}_2\text{O}$ . Unit cell structure when (a) Mn atoms remain in the 2+ oxidation state and (b) all of the manganese atoms inside the crystal are oxidized to Mn(III). When Mn(2) atom is oxidized to Mn(III), a hydrogen atom (green) is transferred from w1 to w3, resulting in auto-ionization of  $2\text{H}_2\text{O}$  into  $\text{OH}^-$  and  $\text{H}_3\text{O}^+$  near Mn(2). (c, d). Pair distribution functions of Mn atoms in pristine  $\text{Mn}_3(\text{PO}_4)_2 \cdot 3\text{H}_2\text{O}$  and oxidized  $\text{Mn}_3(\text{PO}_4)_2 \cdot 3\text{H}_2\text{O}$  in the 3+ state. (c) The Mn-O bonding is indicated in the diagram, and the oxygen atoms in these bonds originate from the phosphate groups. Compared to the pristine state, the oxidized state exhibits two different bond lengths, one of which one is shorter and the other longer than the pristine state bond length, indicating successful and stable J-T distortion in the oxidized  $\text{Mn}_3(\text{PO}_4)_2 \cdot 3\text{H}_2\text{O}$ . (d) The oxygen atoms in the bonds originate from the water molecules (Ow) or hydroxyl ions. The splitting of the Mn-O bonding peak in oxidized  $\text{Mn}_3(\text{PO}_4)_2 \cdot 3\text{H}_2\text{O}$  confirms the presence of hydroxyl ions, and it also indicates successful J-T distortion around Mn(III).

## 2.4. Concluding Remarks.

In conclusion, we presented a new crystalline phase,  $\text{Mn}_3(\text{PO}_4)_2 \cdot 3\text{H}_2\text{O}$ , that is generated by an environmentally benign process and acts as an efficient OER catalyst. On the basis of XRD analysis and DFT calculations, we found that Mn atoms have an asymmetric geometry in the crystal and display a distorted crystal field with phosphate groups and water molecules.  $\text{Mn}_3(\text{PO}_4)_2 \cdot 3\text{H}_2\text{O}$  exhibits superior catalytic performance at neutral pH. DFT theoretical calculations verified the experimental observation that Mn(II) atoms can be easily oxidized into Mn(III) intermediate species through J–T distortion, which is stabilized by its structural nature, the distorted and flexible crystal field around the Mn atoms, and the water molecules inside the crystal. We expect that the discovery of this new  $\text{Mn}_3(\text{PO}_4)_2 \cdot 3\text{H}_2\text{O}$  crystal and the relationship between its structural features and catalytic performance will provide insights useful for the development of divalent Mn-based catalysts.

# **Chapter 3. Monodisperse Manganese Oxide Nanocrystals with High Activity for Water Oxidation Catalysis**

## **3.1. Introduction**

Development of cost-effective and robust catalysts has been a demanding challenge to solving the current energy crisis. Water splitting is regarded as a promising step towards environmentally sustainable energy schemes because electrolysis produces only hydrogen and oxygen, without any by-products. Within the overall water splitting process, the oxygen evolution reaction (OER), an anodic half cell reaction that generates an oxygen molecule from two water molecules, generally requires extremely high overpotential due to its slow reaction kinetics. Although Ir- and Ru-based precious metal catalysts display moderate catalytic activity for OER, their scarcity and poor stability limit their commercial application. However, a highly efficient oxygen evolving complex (OEC) exists in nature within photosystem II (PS II), with a core structure composed only of non-precious components, calcium and manganese ( $\text{Mn}_4\text{CaO}_5$  cluster). The mixed Mn valency and presence of the redox-inactive Ca are known to be key factors for facilitating the Mn redox reaction during the OER.

Inspired by the exceptional efficiency of this biological system, many research groups have attempted to mimic the OEC structure. Demonstration of calcium manganese compounds such as  $\text{CaMn}_2\text{O}_4 \cdot 4\text{H}_2\text{O}$ , which has improved water oxidation catalysis, represents a bio-inspired effort to mimic  $\text{Mn}_4\text{Ca}$  clusters. In the previous literature, Mn with mixed valency was reported to affect the Mn redox equilibria. While typical Mn-oxide compounds, such as  $\text{MnO}_2$  and  $\text{Mn}_2\text{O}_3$ , have limited redox capabilities in each phase, mixed-valence Mn compounds ( $\text{MnO}_x$  and  $\text{CaMn}_2\text{O}_4 \cdot 4\text{H}_2\text{O}$ ) allow for a more flexible Mn oxidation state in a single structure without severe structural deformations.

Despite these systematic approaches, however, the main challenge associated with manganese oxide catalysis is the degraded activity under near neutral conditions. This dramatic change in the manganese oxide compounds originates from the instability of the Mn (III) species during the OER process.

In this study, we discovered a new Mn-based catalyst that efficiently performs water oxidation under neutral conditions. We investigated the nanoscale effects on water oxidation catalysis and revealed a superior activity for monodisperse MnO nanoparticles. An  $\text{NH}_4\text{OH}$  surface treatment induced the partial oxidation of Mn (II) to generate Mn (III) species on the MnO surface. More importantly, the ammonia-treated MnO nanoparticles exhibited the highest catalytic activity amongst reported first row transition metal-based inorganic catalysts. Monodisperse MnO nanoparticles were prepared via hot injection with a slight modification from previously reported literature. Figure 3.4a show that the synthesized nanoparticles

have a pure, single crystalline MnO phase and are monodisperse at sub 10 nm. High resolution TEM (HR-TEM) (Figure 3.4) shows the lattice fringes of the MnO (110) planes (2.54 Å) and (200) plane (2.2 Å), which matches the XRD results.

## 3.2 Experimental Methods

### 3.2.1 Synthesis and Materials

Manganese acetate dehydrate ( $\text{Mn}(\text{CH}_3\text{COO})_3 \cdot 2\text{H}_2\text{O}$ , 97%), Myristic acid ( $\text{CH}_3(\text{CH}_2)_{12}\text{COOH}$ ,  $\geq 99\%$ ), Decanol ( $\text{CH}_3(\text{CH}_2)_9\text{OH}$ ,  $\geq 99\%$ ), Octadecene ( $\text{CH}_3(\text{CH}_2)_{15}\text{CH}=\text{CH}_2$ , 90%), Ammonia hydroxide solution (ACS reagent, 28.0-30.0%  $\text{NH}_3$  basis), Potassium iodide (KI,  $\geq 99\%$ ), Potassium chloride (KCl,  $\geq 99\%$ ), Potassium bromide (KBr,  $\geq 99\%$ ), Nitrosonium tetrafluoroborate ( $\text{NOBF}_4$ , 95%), Dimethylformamide (DMF,  $\geq 99.8\%$ ), Toluene ( $\text{C}_6\text{H}_5\text{CH}_3$ ,  $\geq 99.9\%$ ),  $\text{Na}_2\text{HPO}_4 \cdot 7\text{H}_2\text{O}$  (ACS reagent, 98.0-102.0%) and  $\text{NaH}_2\text{PO}_4 \cdot 2\text{H}_2\text{O}$  (99.0%) were purchased from Sigma Aldrich and used without additional purification. Fluorine doped Tin-Oxide coated glass (FTO, TEC-8) which has  $15\Omega/\text{sq}$  surface resistivity was obtained as pre-cut by  $1.0\text{ cm} \times 1.5\text{ cm}$  glass pieces from Pilkington Company.

### 3.2.2 Synthetic procedures for sub 10 nm sized monodisperse manganese oxide nanoparticles

Monodisperse manganese oxide nanoparticles were synthesized by hot injection method, well-known thermal decomposition methods. To prepare monodispersed sub 10 nm sized MnO nanoparticles, first step was to make two different mixture in two reaction pots: i) 1 mmol of  $\text{Mn}(\text{ac})_3$  and 2 mmol of myristic

acid into 20mL of octadecene and ii) 3mmol of decanol into 1mL of octadecene. Each reaction pots were degassed at 110°C for 2 hours with vigorous stirring. It should be noted that during this step, air gas should be completely removed. After 2 hours degassing, one reaction pot which contains the carboxylate mixture was heated above 295°C under argon atmosphere. When it reached to 295°C, the mixture of decanol was injected rapidly into the caboxyl solution. At this time the burst nucleation, essential step for monodisperse nanoparticles occurs along with high supersaturation . Reaction mixture maintained at 295°C 1h. As the manganese oxide nanoparticles grow, color of solution was changed from clear yellow to brown. The dark brown solution was then cooled to room temperature and 10 mL of acetone and toluene was added and centrifuged to obtain MnO precipitates. After repeating this purification step, it re-dispersed in non-polar solvents such as hexane or cyclohexane.

### **3.2.3 Synthetic procedures for sub 15, 20 nm sized monodisperse manganese oxide nanoparticles**

Various size of MnO nanoparticles could be obtained via controlling holding time at 295 °C. As another route, size control is possible by alteration of the ratios of myristic acid. To obtain 15nm MnO nanoparticles, the ratio of chemicals remained same but changed the aging duration to 2hour. 20nm MnO nanoparticles were synthesized with higher molar ratio of myristic acid with 1-hour aging duration.

Others synthetic procedures including purification were stayed same.

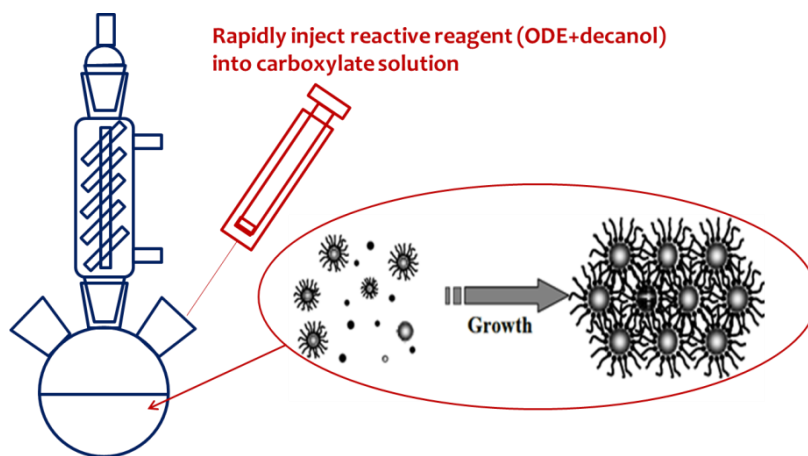


**Figure 3.1.** Scheme for synthesizing manganese (II) oxide nanoparticles by hot injection method.

### **3.2.4 Purification details**

Firstly, 1:1:1 ratio of the as synthesized solution, acetone and toluene was mixed and centrifuged to obtain MnO precipitates. After repeating this purification step, it was re-dispersed in nonpolar solvents such as hexane or cyclohexane. For the convenience, when volume ratio of the initial dark brown MnO solution to hexane is 10, we call its concentration 1C. For example, if we wash 100  $\mu$ L of dark brown MnO solution and disperse it in 10  $\mu$  L of hexane, we define concentration of final solution as 1C. Washing 200  $\mu$  L of MnO solution and dispersion in 10  $\mu$  L of hexane: 2C.

### **3.2.5 Surface modification of MnO nanocrystals**

#### **3.2.5.1 BF<sub>4</sub><sup>-</sup> functionalized MnO nanocrystals**

Functionalization of BF<sub>4</sub><sup>-</sup> ligands on the surface of manganese oxide nanocrystals were followed from previous study.<sup>3</sup> Firstly, purified MnO solution was dispersed in 5 mL hexane solution. (~5 mg/mL) And then the MnO solution was mixed with 0.01M of NOBF<sub>4</sub> dissolved in dimethylformamid (DMF) at room temperature and shaken gently for 10 minutes until phase separation finished. When brownish color of MnO nanoparticles transfer to DMF phase 1:1 volume ratio of acetone and toluene was added for further purification. After purification, BF<sub>4</sub><sup>-</sup>-capped MnO nanocrystals could be dispersed in polar solvents, such as DMF,

ethanol, and methanol.

### **3.2.5.2 Ammonia treated sample by spin coating**

One drop of as-synthesized MnO nanoparticles was spread on cleaned FTO glass substrates and then spin-coated at room temperature for several minutes. After full dry, it was dipped into 10 mL of ammonia hydroxide solution. After certain amount of time, the substrate was rinsed thoroughly with deionized water and dried at 50°C.(Figure 3.2)

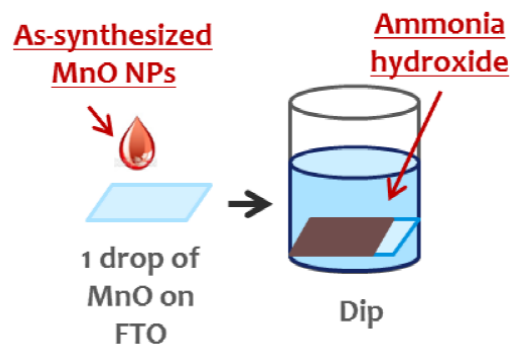


**Figure 3.2.** Schematic for ammonia treatment methods

### **3.2.6. Powder X-ray Diffraction**

Powder X-ray diffraction (XRD) was carried out on a D-8 Advance X-ray diffractometer with Cu K $\alpha$  radiation ( $\lambda=1.54056\text{\AA}$ ). The sample was prepared by drying MnO nanoparticles by freeze dryer more than 1 day. The lyophilized MnO powder was loaded on Si holder, retrofitted in X-ray diffractometer. XRD patterns were recorded in a range of  $5 \sim 70^\circ$  with a step of  $0.02^\circ$  and a velocity of  $0.02^\circ/4$  s. Obtained XRD patterns were compared with previously reported JDPDS cards.

### **3.2.7. Scanning Electron Microscopy (SEM) Analysis**

The MnO nanocrystals loaded on the FTO substrate was characterized with scanning electron microscope (Supra 55VP, Carl Zeiss, Germany). The samples were examined before the electrochemical measurements. Silver paste was placed on the edge of FTO substrate and carbon tape to make an electron path during the imaging. Images were taken with an acceleration voltage of 2kV.

### **3.2.8. Transmission Electron Microscopy (TEM) Analysis**

TEM images and selected area electron diffraction (SAED) patterns were obtained using a high resolution transmission electron microscope (JEM-3000F,

JEOL, Japan) with an acceleration voltage of 300 kV. To compare manganese oxidation state, three different conditions of samples were prepared. An as-synthesized MnO nanoparticle used as it was and to observe the changed oxidation state, the TEM samples were collected from FTO glass right after electrochemical measurement with dispersion in hexane. About 5  $\mu\text{L}$  of dispersed MnO were dropped on the TEM grid and dried at room temperature.

### **3.2.9. Fourier Transform Infrared Spectroscopy (FT-IR) Analysis**

FT-IR spectra were obtained using a FT-IR Spectrophotometer (Nicolet 6700, USA). As-synthesized MnO nanoparticle powder and ammonia treated MnO nanoparticle powder were sampled in form of KBr pellet. Two samples were scanned under air with resolution of 4 at  $600\text{cm}^{-1}$  to  $4000\text{cm}^{-1}$  wavelength. Total 32 cycles of scans were applied.

### **3.2.10. X-ray Photon (XPS) Spectroscopy**

The oxidation state of manganese was observed by using Al  $K\alpha$  1486.6eV x-rays (XPS, PHI 5000 VersaProbe). High resolution spectra of C-1s, Mn-2p and Mn-3s were collected with three different ammonia treated MnO thin film samples on FTO substrate: as-synthesized MnO, 1 hour ammonia treated and 24 hours ammonia treated. Due to ununiformed of the film the area at the edge of the samples

were selected for all samples. Initially carbon was calibrated with 285.5 eV line position. During runs, a pass energy of 23.5 eV, an energy step of 0.1 eV and a time of 20 ms per step were used.

### **3.2.11. Electrochemical Methods**

All electrochemical experiments were conducted under a three-electrode electrochemical cell system. Ag/AgCl/KCl<sub>sat</sub> reference electrode (BASi) and a Pt foil were used as a reference electrode and a counter electrode, respectively. Electrochemical tests were carried out at ambient temperature ( $21 \pm 1^\circ\text{C}$ ) using a potentiostat system (CHI 600D, CH Instruments). Electrode potential was converted to the NHE scale, using the following equation:  $E(\text{NHE}) = E(\text{Ag}/\text{AgCl}) + 0.197 \text{ V}$ . Additionally, overpotential values were calculated by the difference between the iR corrected potential ( $V = V_{\text{applied}} - iR$ ) and the thermodynamic point of water oxidation at a specified pH. During the measurement, the cycle from 0.0 V to 1.3 V was repeated at least four times per run with scan rate of 10 mV/sec. All the data were iR-compensated before the run. For stability test, CV results was recorded with scan rate of 100mV/sec.

### **3.2.12 EPR Spectroscopy**

All EPR measurements in this study were performed at Western Seoul Center, Korea Basic Science Institute, Seoul, South Korea. Electron paramagnetic resonance (EPR) was measured by Bruker EMX/Plus spectrometer equipped with a dual mode cavity (ER 4116DM). To obtain each spectrum result, microwave frequency 9.64 GHz (perpendicular mode), 9.4 GHz (parallel mode), modulation amplitude 10G, modulation frequency 100 kHz microwave power 0.94 mW (perpendicular mode), 5.0 mW (parallel mode) were applied at 5.7 K. 10 scans were repeated at each spectrum. To observe the changed oxidation state of manganese during electrochemical measurement, the bulk electrolysis with cyclic voltammetry system (CHI 760C, CH Instruments, Inc.) was applied under pH 7 phosphate buffer solution for 30 minutes respectively. After termination of electrolysis at each potentials, the samples were collected with blade as soon as possible and then transferred in to an EPR tube under Ar (99.999%) environment. The EPR tube was then frozen at 77K in liquid nitrogen.

### **3.2.13 Basic EPR Theory**

Generally, Electron Paramagnetic Resonance (EPR) analysis was conducted to get the detailed information of metal activesites. Specifically, it is very useful characterization tools in catalysis field, because EPR results can provide electronic structural information at resting/intermediate states. Theoretically, EPR spectrum is expressed with the spin Hamiltonian, as follows. (Figure 3.3.)

$$H = \beta \mathbf{B} \cdot \mathbf{g} \cdot \mathbf{S} + \mathbf{S} \cdot \mathbf{D} \cdot \mathbf{S} + \mathbf{S} \cdot \mathbf{A} \cdot \mathbf{I}$$

Where,  $\beta$  is Bohr magneton,  $\mathbf{g}$  is electron Zeeman tensor,  $\mathbf{D}$  is zero-field splitting tensor,  $\mathbf{A}$  is Nuclear hyperfine tensor,  $\mathbf{S}$  is electronic spin, and  $\mathbf{I}$  is nuclear spin operators. In EPR spectra electron information for Zeeman interaction, Hyperfine and superhyperfine interactions (electron spin / nuclear spin interaction), and spin-spin interaction (zero field splitting) are included.<sup>61</sup> Among these terms, the left term that relates external magnetic field is the only part which is magnetic field dependent.

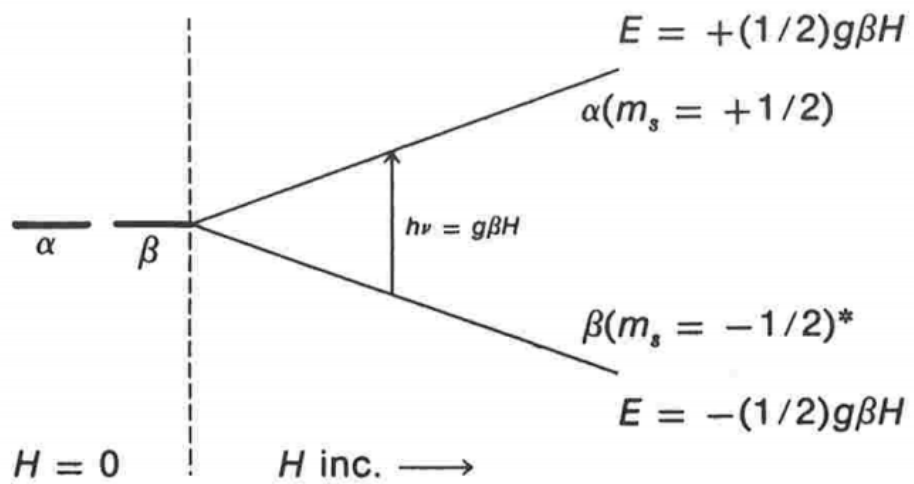


**Figure 3.3.** Scheme for the elimination of the degeneracy problem of the  $\alpha$  and  $\beta$  electron spin states by applied magnetic field.

### **3.3 Results and Discussions**

#### **3.3.1. Monodisperse sub 10 nm sized manganese (II) oxide nanocrystals**

Sub 10 nm sized monodisperse MnO nanoparticles were synthesized with modified hot injection method (Figure 3.4). 10 nm MnO nanoparticles were synthesized with small amount of surfactant which was 2 mmol of myristic acid. According to the previous study, size of nanoparticles was controlled by nucleation and growth mechanism. Referred to this concept, minimized solubility with shorten aging time were applied on MnO nanoparticles to synthesize smaller sized nanoparticles with prohibiting further growth of particles.

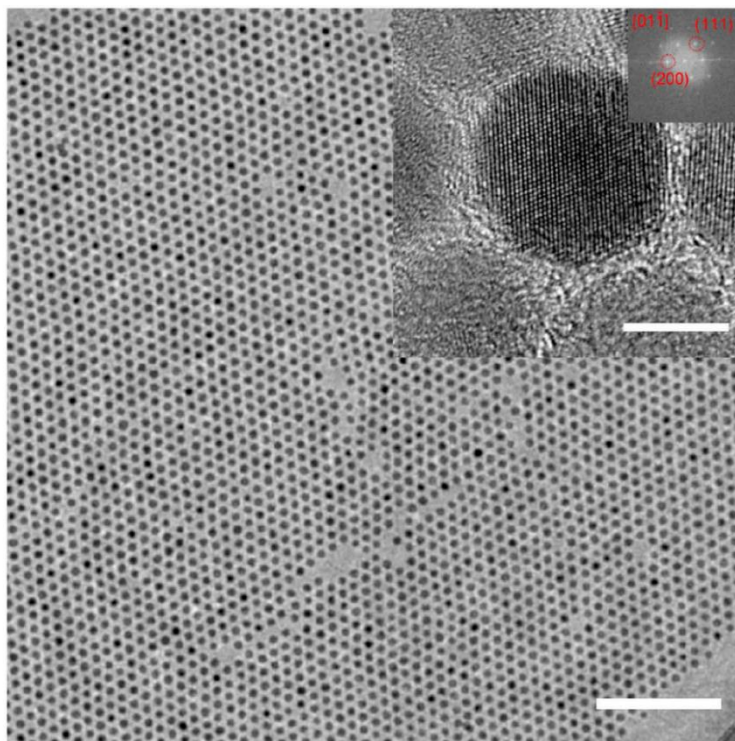


**Figure 3.4.** TEM image of 10 nm sized MnO nanoparticles.

Scale : 100 nm, inset: 5 nm

### **3.3.2. Electrochemical characterization**

#### **3.3.2.1 Effect of duration time for surface treatment**

In order to adopt our MnO nanocrystals to electrochemical water splitting reaction, it is required to deposit particles on the working electrode. In this study, we used fluorine doped tin oxide (FTO) glass conducting substrates as working electrode. Electrode preparation procedures are as follows. Firstly, purified manganese oxide nanoparticles are loaded on the FTO substrates by spin coating method. As shown in Figure 3.5, 10 nm sized manganese oxide nanocrystals are well arrayed on the substrates.

Since as synthesized MnO nanocrystals are not conductive due to the surrounding organic ligand, myristic acid, surface treatment process is needed for electrochemical application. In this study, we used ammonia solution to remove organic ligand. To confirm the elimination of organic ligands on the surface of MnO nanocrystals, FT-IR analysis were conducted on ammonia treated MnO powder and as-synthesized MnO powder. Figure 3.7 reveals that the intensity of carboxyl group at  $1400\text{ cm}^{-1}$  which is the attaching bond of myristic acid on the surface of MnO surface were almost disappeared and alkyl group at  $2900\text{ cm}^{-1}$  that are outer bond of myristic acid were also diminished at ammonia treated MnO film.

XPS results also supports that organic ligand could be removed by surface treatment. Disappearance of characteristic peaks for carboxyl group at 530eV was

confirmed. (Figure 3.6). Compared to the oxide peak at 528eV region with carboxyl group at 530eV range, the apparent reduced intensity were observed.

It is important to understand phase transformation by surface treatment. Figure 3.6 shows the phase change of MnO crystal structure along with ammonia treatment by XRD analysis. As-synthesized MnO sample showed three apparent representative MnO peaks at (111), (200) and (220) planes. However, as MnO treated with ammonia solution, it changed the crystal structure from pure MnO the mixtured MnO and Mn<sub>3</sub>O<sub>4</sub>. Broadening were occurred at all sharp MnO peaks and additionally many small peaks of Mn<sub>3</sub>O<sub>4</sub> were appeared. Mn<sub>3</sub>O<sub>4</sub> peaks from (111), (100), (004), (220), (105) and (224) were shown. XPS analysis was further conducted to check the surface status of manganese. As shown in figure 3.8, all the samples have two main peaks which are assigned to be Mn 2p<sub>3/2</sub> and its satellite peaks, respectively. After ammonia treatment was done, it can be observed that two distinct Mn 2p peak positions were shifted to more positive direction without entire phase change. It is originated from the partial oxidation of the Mn<sup>2+</sup> on the surface.

With verification of eliminated organic ligands on the surface of MnO nanoparticles and the crystal structure changes from pure MnO to mixed MnO and Mn<sub>3</sub>O<sub>4</sub> structure, the optimization of ammonia treatment were obtained with cyclic voltammogram measurements (0 minute/ 30 minutes/ 1 hour/ 2 hours/ 4 hours/ 8 hours and 24 hours). Among the various conditions, 1 hour ammonia treated MnO film showed the best results with the lowest onset potential at 1.18V(vs NHE) at 0.5mV/cm<sup>2</sup>. Table 3.1 and figure 3.9, 3.10 shows the onset potential variation with

error bar. 24 hours sample had the worst catalytic effect compared to seven other different samples.

Combined with electrochemical a with XRD, XPS, and FT-IR results, we demonstrated that pure MnO and pure Mn<sub>3</sub>O<sub>4</sub> phases gave slight negative effect on MnO as the electrocatalyst in neutral pH. Only 1h ammonia treatment is the optimal condition for catalytic application. It is clear that surface treatment by ammonia not only removed undised the organic ligands, but also changed the surface status to mixed valence, Mn(II) / Mn(III).

As next step, we annealed 1h ammonia treated MnO nanocrystals at 250 °C to enhance the adhesion of particles to substrate. To distinguish the surface-treated MnO particles from previously reported MnO particles, we refer to the 1h treated nanocrystals as “Partially oxidized MnO NCs”. XRD result indicated that partially oxidized MnO NCs have Mn<sub>3</sub>O<sub>4</sub> /MnO mixed phases, which was also revealed with HR-TEM analysis.

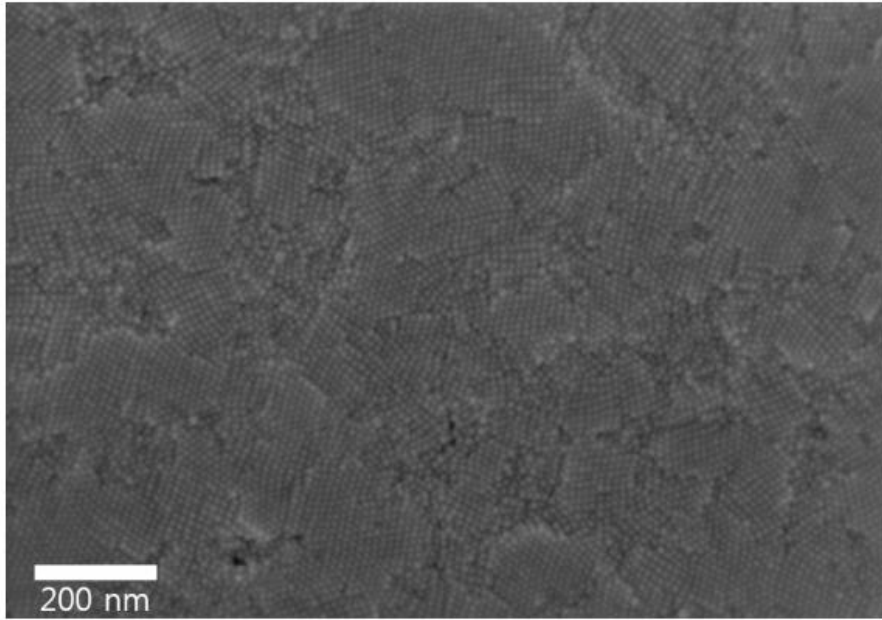


**Figure 3.5.** SEM images of MnO nanoparticles on the FTO substrate. Sub 10 nm sized MnO nanoparticles are well assembled after deposition on the FTO substrate.

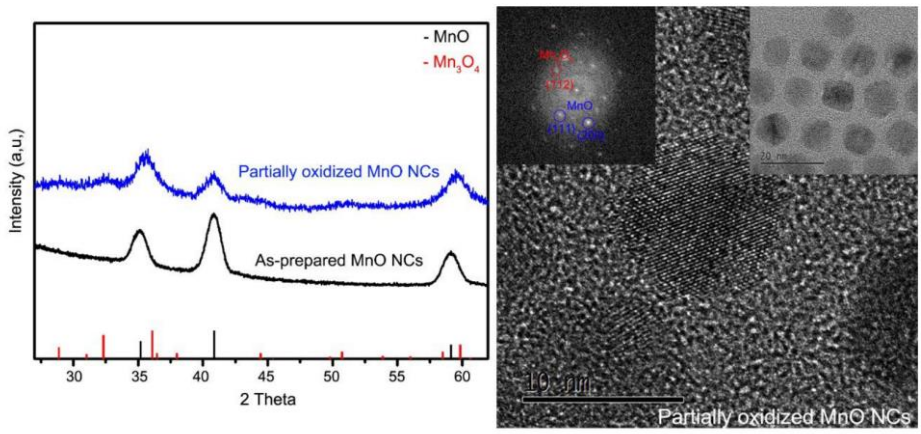


**Figure 3.6.** X-ray diffraction results of as-prepared and partially oxidized MnO nano crystals. As clearly shown in the Figure 3.5, partially oxidized MnO NCs have MnO and Mn<sub>3</sub>O<sub>4</sub> mixture phases

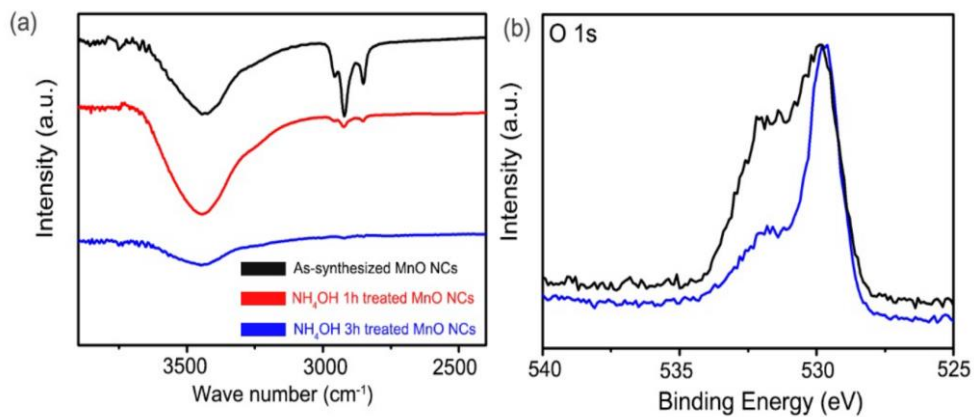


**Figure 3.7.** Fourier transform infrared (FT-IR) spectra of as-prepared, and partially oxidized MnO NCs. As shown in the figure, characteristic peak of alkyl chain around  $2800\text{ cm}^{-1}$  was almost disappeared after surface treatment. Specifically, The vibrations at  $2,922\text{ cm}^{-1}$  and  $2,852\text{ cm}^{-1}$  are asym (C–H) and sym (C–H) features. This result indicates that long organic chain on the synthesized MnO surface was successfully eliminated by ammonia treatment.

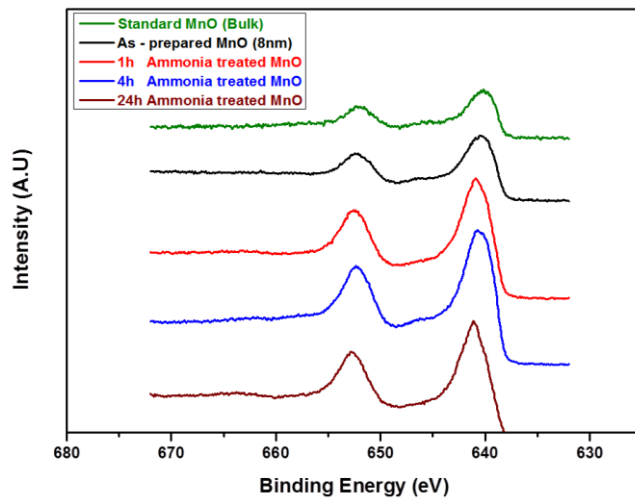


**Figure 3.8.** X-ray photo-electron spectroscopy of different duration ammonia treated MnO in the Mn 2p region. All the XPS spectra were calibrated to C 1s at 285.0 eV. As shown in the figure, peak positions were positively shifted as ammonia treatment time gets longer.

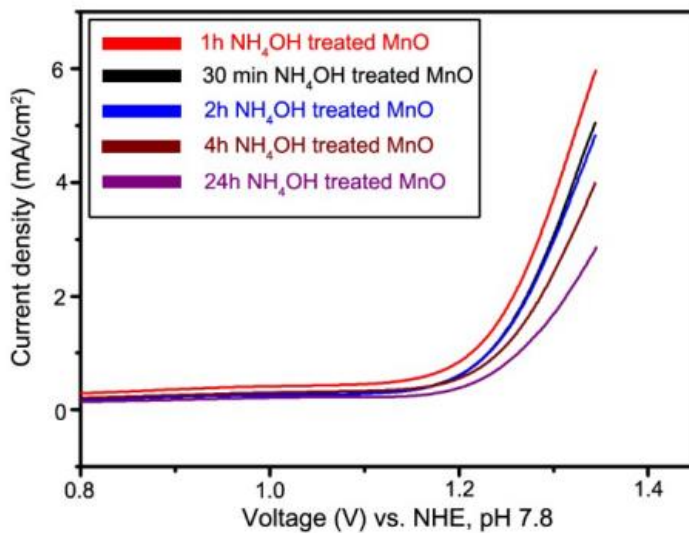


**Figure 3.9.** Comparison of water oxidizing performance for MnO nanocrystals depending on the duration of ammonia treated MnO electrodes (as-synthesized, 30 minutes, 1 hour, 2 hours, 4 hours, 8 hours and 24 hours). 1 hour treated MnO crystal films showed the lowest onset potential at 1.18V (vs. NHE), while as-synthesized MnO film displayed the lowest catalytic activity.

**Table 3.1** Comparison of onset potential depending on the ammonia treatment time

<b>Ammonia treatment (hr)</b>	<b>0.5</b>	<b>1</b>	<b>2</b>	<b>4</b>	<b>8</b>	<b>24</b>
Onset Potential (V vs NHE)	1.20	1.17	1.21	1.22	1.23	1.24

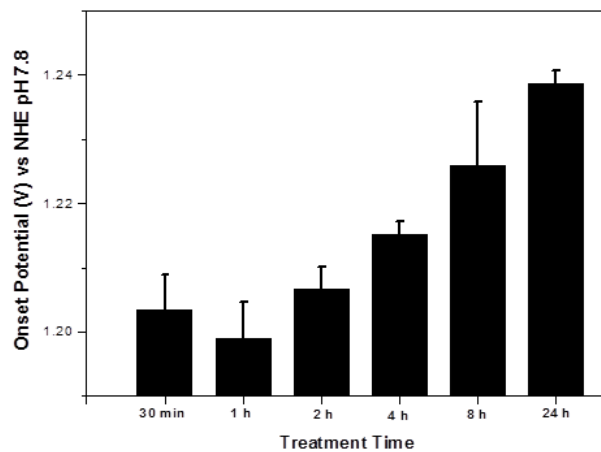


**Figure 3.10.** Activity trend depending on the ammonia treatment time. More than 3 times of experiments were performed in each condition.

### 3.3.2.2. Electrochemical analysis on partially oxidized MnO NPs

The water oxidation catalytic performance of the partially oxidized MnO nanoparticles was appraised via cyclic voltammetry (CV). All of the electrochemical measurements were performed at pH 7.8 in a 300 mM phosphate buffer solution. As shown in Figure 3.11b, a fairly low current and high onset potential were observed for the as-prepared MnO nanoparticles. This phenomenon was caused by the organic capping ligand around the MnO particles acting as an insulating barrier that blocked electron flow during the OER reaction. We then varied the NH<sub>4</sub>OH treatment time to optimize the surface treatment conditions. Figure 3.9 showed that MnO treated with NH<sub>4</sub>OH for 1 h exhibited the highest catalytic performance as mentioned in previous section.

We synthesized well-known catalyst materials to quantitatively evaluate their catalytic activity. Representative amorphous metal oxide materials, Co-oxide and Mn-oxide films, were prepared via electrodeposition,<sup>24,25</sup> and their catalytic activity was compared to the partially oxidized MnO nanocrystals. As shown in Figure 3.11b, the overpotential values at a current of 5 mAcm<sup>-2</sup> were 530 mV for partially oxidized MnO nanocrystals but 600 and 700 mV for the CoO<sub>x</sub> (Co-Pi) and MnO<sub>x</sub>, respectively.<sup>26,27</sup>

In addition, various Mn-oxide nanocatalysts (MnO<sub>2</sub>, Mn<sub>3</sub>O<sub>4</sub>, and Mn<sub>2</sub>O<sub>3</sub>) were synthesized using previously reported methods for direct comparisons.<sup>28</sup> XRD and SEM analyses were conducted to identify the phase and morphology of each

compound. Each Mn-oxide catalyst was mixed with a Nafion solution and loaded onto the FTO glass substrate via spin-coating. As expected from the previous literature, the Mn-oxide catalysts displayed inferior catalytic activities under near neutral conditions (Figure 3.13). A Tafel analysis was conducted and revealed that the exchange current density for the partially oxidized MnO nanocrystals was much higher than for the conventional Mn-oxide nanocatalysts. The Tafel slope was  $\sim 78$  mVdec<sup>-1</sup> for the partially oxidized MnO nanocrystals and 120 mVdec<sup>-1</sup> for the other Mn-oxide compounds (MnO, Mn<sub>3</sub>O<sub>4</sub>, Mn<sub>2</sub>O<sub>3</sub>, and MnO<sub>2</sub>). The catalytic activity and measurement conditions for each catalytic compound are summarized in Table 2.

We also displayed electrochemical data using other metric systems with respect to the loading amount (mass activity) and surface area because each catalyst was prepared on the working electrode in a different way (Figure 3.12). The catalyst surface area on the electrode was calculated by multiplying the catalyst weight on the electrode and BET value. For all metric systems, we concluded that the partially oxidized MnO nanocrystals had superior catalytic activity to the previously reported first row transition metal based catalysts.

As an effort to obtain deeper insight of the nano-size effect, we investigated the size dependency of partially oxidized MnO NCs on the water oxidation catalysis. We have prepared various sized MnO NCs and evaluated their catalytic activity. In this study, 10, 15, 20, and  $\sim 60$ -80 nm sized MnO NCs (Fig. 3.13a-d) have been synthesized via hot injection method. As shown in Fig. 3.13e, 10 nm particles exhibited the highest OER performance. From the Tafel analysis, almost same Tafel

slope was obtained and only difference are the onset potential and exchange current values (Fig. 3.13f). Considering the onset potential is normally determined by intrinsic material properties, it can be inferred that a change in surface structure of the MnO particles occurred depending on their size, which affects the Mn redox reaction.

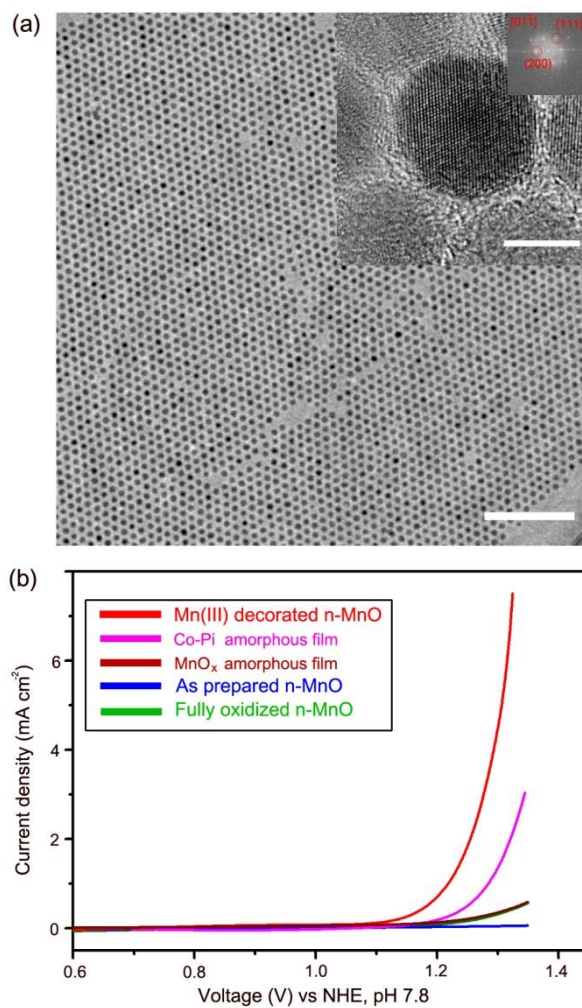


**Figure 3.11.** (a) HR-TEM image of the synthesized, monodisperse 8 nm MnO particles. (scale bar : 100 nm) Inset shows a high resolution image of the MnO particles. (scale bar : 5 nm). (b) Polarization-corrected curves for Mn(III)-decorated MnO (red), Co-Pi film (pink), MnO<sub>x</sub> film (brown), fully oxidized MnO (green) and as-prepared MnO nanoparticles (blue).

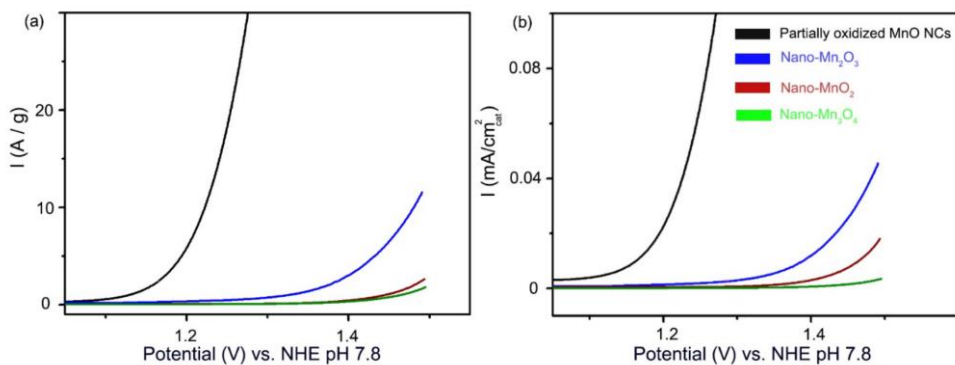


**Figure 3.12.** Polarization corrected curves of partially oxidized MnO NCs (black) and conventional Mn-oxide nano-compounds,  $Mn_2O_3$  (blue),  $MnO_2$  (brown), and  $Mn_3O_4$  (green). Catalytic current value is normalized based on the (a) loading amount and (b) surface area of each catalysts. Surface area of each catalysts was obtained by BET analysis. (partially oxidized MnO NCs:  $28.08 \text{ m}^2/\text{g}$ , nano  $Mn_2O_3$ :  $25.43 \text{ m}^2/\text{g}$ , nano  $Mn_3O_4$ :  $52.76 \text{ m}^2/\text{g}$  and  $MnO_2$ :  $14.61 \text{ m}^2/\text{g}$ )

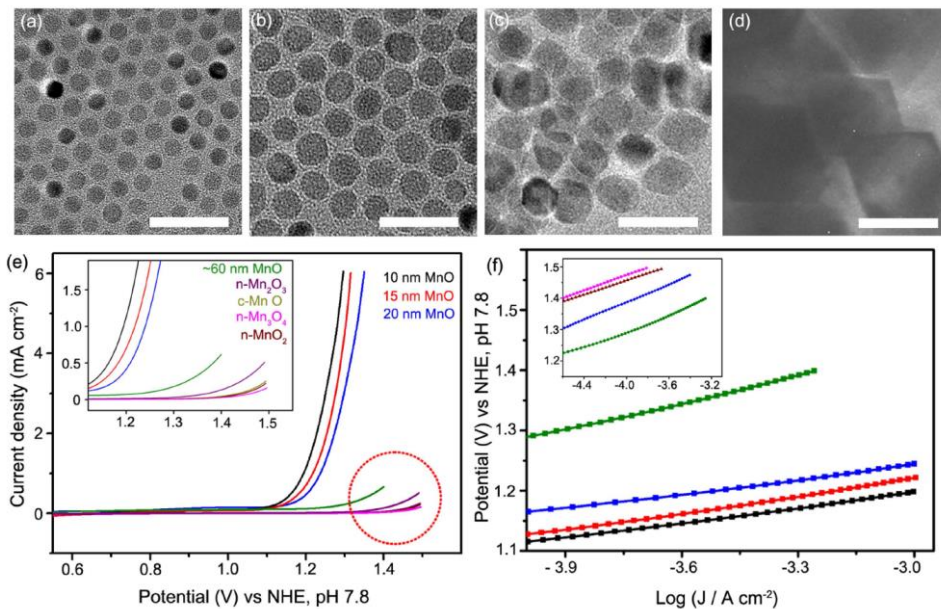


**Figure 3.13.** TEM images of various sized MnO NCs; a. 10 nm, b. 15 nm, c. 20 nm and d. ~60-80 nm MnO NCs. (scale bar : 50 nm) e. CV curves for various sized partially oxidized MnO NCs (10 nm (black), 15 nm (red), 20 nm (blue), ~60-80 nm (green)) and other conventional Mn-Oxide nano compounds (Mn<sub>2</sub>O<sub>3</sub> (purple), commercial bulk MnO (gray), MnO<sub>2</sub>(brown), and Mn<sub>3</sub>O<sub>4</sub>(pink)). f. Tafel plots of various sized partially oxidized MnO NCs and other conventional Mn-oxide nano compounds.

OER Catalyst	Preparation condition	Overpotential at Neutral pH	Notes
Partially oxidized MnO NCS	Spin coating	530 mV (@ 5 mAcm <sup>-2</sup> )	This work
Co-Pi	Electro-deposition	570 mV (@ 5 mAcm <sup>-2</sup> )	Reproduced with the previous method (ref 10)
MnO <sub>x</sub>	Electro-deposition	600 mV (@ 1 mAcm <sup>-2</sup> )	Reproduced with the previous method (ref 25)
Mn <sub>3</sub> O <sub>4</sub>	Spin coating	650 mV (@ 40 μAcm <sup>-2</sup> )	Fails to reach 5 mA/cm <sup>2</sup>
Mn <sub>2</sub> O <sub>3</sub>	Spin coating	490 mV (@ 40 μAcm <sup>-2</sup> )	Fails to reach 5 mA/cm <sup>2</sup>
MnO <sub>2</sub>	Spin coating	630 mV (@ 40 μAcm <sup>-2</sup> )	Fails to reach 5 mA/cm <sup>2</sup>
IrO <sub>x</sub>	Electro-deposition	310 mV (@ 5 mAcm <sup>-2</sup> )	Extrapolation from ref 12

**Table 3.2.** Comparison of OER activity for various water oxidation catalysts.

Faradaic efficiency experiments were performed to examine the origin of the observed current. The faradaic efficiency of partially oxidized MnO NCs was measured by a fluorescence-based O<sub>2</sub> sensor. Electrolysis was performed at the applied potential of 1.3 V vs NHE. Before bulk electrolysis, the designed electrochemical cell was purged with inert gas (99.999% Ar) for 1 h, and the fluorescence sensor was located in the upper part of the cell. The trace for the amount of evolved oxygen measured by the sensor was plotted in Fig. 3.14a (red line). A total 95 μ mol of oxygen molecules was evolved after 7900 s of electrolysis. The theoretical yield of oxygen during electrolysis was calculated from the total charge passed during the electrolysis (blue line). The faradaic efficiency of partially oxidized MnO NCs was approximately 91.95%, indicating that the current measured by cyclic voltammetry was mainly originated from the oxygen evolution reaction. Turnover frequency partially oxidized MnO NCs for at 1.18 V (η : 410 mV) was also obtained based on the electrochemical data and faradaic efficiency. Detailed calculation method was described in the supporting information materials. We would like to note that the TOF value of partially oxidized MnO NCs is calculated per Mn mol which is a lower-limit value, since the number of active sites for OER may be fewer than the number of total Mn ions in the crystals. Comparison of TOF values with other previous solid state catalysts were summarized in Table 3.

To further verify the catalytic stability of the partially oxidized MnO NCs during OER, we performed cyclic voltammetry. We continuously cycled between the potentials 0 V and 1.3 V (vs NHE). As shown in Figure 3.15, the cyclic voltammetry

currents of partially oxidized MnO NCs remained unchanged after 20 cycles, which indicates their catalytic durability. Moreover, a nearly constant current was maintained @ 1.1V vs. Ag/AgCl for 2h.

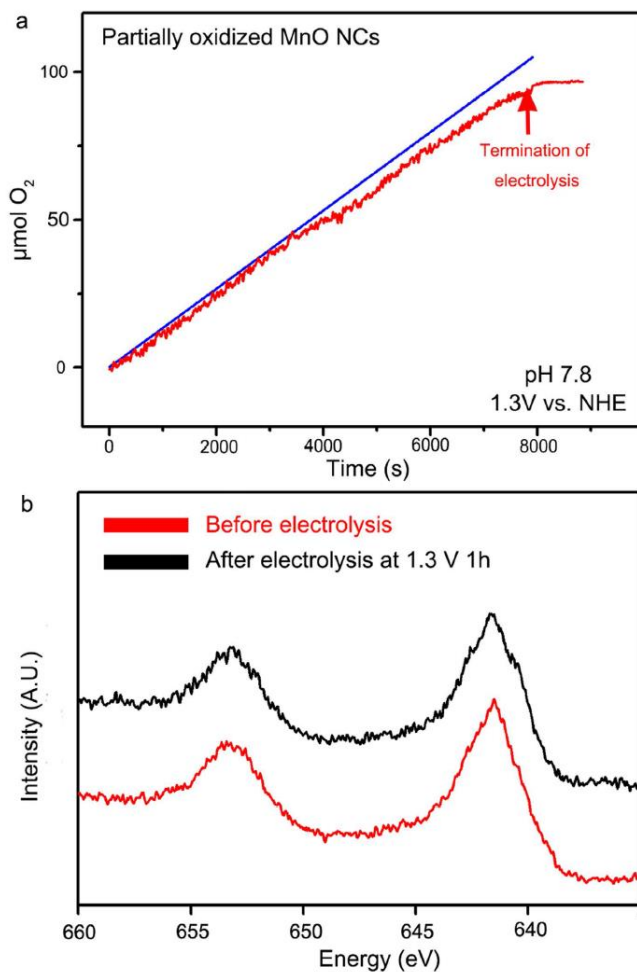


**Figure 3.14.** Measurement of evolved O<sub>2</sub> molecules and catalytic stability test. a. The amount of evolved O<sub>2</sub> molecules measured by experimental amount (red line) and the theoretical amount of evolved O<sub>2</sub> (blue line) during bulk electrolysis. The theoretical amount of O<sub>2</sub> molecules was plotted assuming a Faradaic efficiency of 100%. b. XPS analysis of partially oxidized MnO NCs. even after 1 h of electrolysis, there was no peak shift in Mn 2p region, which indicates the high stability of partially oxidized MnO NCs.

Catalyst	TOF (s <sup>-1</sup> )	Experimental Condition
<b>Partially oxidized MnO NCs<sup>[S1]</sup></b>	<b>0.012</b>	<b>Electrochemical pH 7.8 (<math>\eta</math> : 410mV)</b>
Co-Pi <sup>[S2]</sup>	>0.0007	Electrochemical pH 7 ( $\eta$ : 410mV)
$\alpha$ - MnO <sub>2</sub> nanowire <sup>[S3]</sup>	5.9*10 <sup>-4</sup>	Photochemical Ru(bpy) <sub>3</sub> Cl <sub>2</sub> - Na <sub>2</sub> S <sub>2</sub> O <sub>8</sub> , No buffer, pH 7
CO <sub>3</sub> O <sub>4</sub> <sup>[S4]</sup>	> 0.0025	Photochemical Na <sub>2</sub> SO <sub>4</sub> electrolyte, pH 7 ( $\eta$ : 350mV)
Mn <sub>2</sub> O <sub>3</sub> <sup>[S4]</sup>	0.055	Photochemical KOH electrolyte ( $\eta$ : 325mV)
MnO <sub>2</sub> <sup>[S5]</sup>	0.013	Electrochemical Phosphate buffer, pH 7 ( $\eta$ : 440mV)
IrO <sub>2</sub> <sup>[S6]</sup>	7	Electrochemical pH 5.3 ( $\eta$ : 570mV)
Ru-red/Pt-black <sup>[S6]</sup>	0.417	Electrochemical pH 5.3 ( $\eta$ : 570mV)

**Table 3.3.** The TOF values of the various manganese oxide catalysts that have been reported by others and of our catalyst, partially oxidized MnO NCs. The detailed experimental conditions for photo and electrochemical catalysis are summarized in the third column.

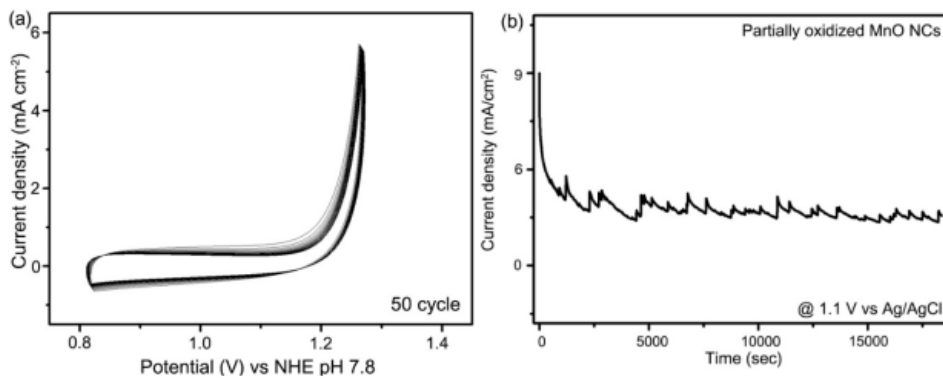


**Figure 3.15.** (a) OER polarization curves of partially oxidized MnO NCs on FTO under 50 cycles of accelerated stability test. (b) Chronoamperometry analysis of partially oxidized MnO NCs.

### 3.3.3. Spectroscopic analysis: Inspection of Mn valency

We believe the exceptional catalytic activity of partially oxidized MnO nanoparticles might originate from the combined effects of its nanometer size and unique electronic structure. X-ray absorption spectroscopy (XAS) and electron paramagnetic resonance (EPR) were conducted to identify the detailed electronic structure of the partially oxidized MnO nanoparticles. We analyzed four reference Mn-oxide compounds; MnO, Mn<sub>3</sub>O<sub>4</sub>, Mn<sub>2</sub>O<sub>3</sub>, and MnO<sub>2</sub>, which are known to have Mn (II), Mn (II/III), Mn (III), and Mn (IV) oxidation states, respectively. XAS provides detailed information on the oxidation state and coordination environment of metal ions. The Mn K-edge spectra for each Mn compounds were recorded at room temperature, and the energy was calibrated and normalized using a glitch in the  $I_0$  relative to the absorption edge of Mn foil. Figure 3.16a shows typical Mn pre-edge features detected near 6540 eV for all of the catalysts. A sequential shift in the XANES peak to higher energy was observed with increasing Mn oxidation state, which agrees with previous literature. As shown in Figure 3.16a, the partially oxidized MnO nanoparticles exhibited higher energy than the MnO particles. Because the edge-rise energy position indicates the mean oxidation state of the manganese, we could estimate the average Mn oxidation state in partially oxidized MnO nanoparticles. As shown in the inset for Figure 3.16b, the extrapolated oxidation state of the partially oxidized MnO nanoparticles was 2.21, which was also well matched with XPS results, and that of the fully oxidized nano-MnO was 2.663,

which was similar to  $\text{Mn}_3\text{O}_4$ . Interestingly, the as-prepared nano-MnO also had a slightly higher oxidation state than bulk MnO, which was likely due to defects generated by the intrinsic nonstoichiometric nature of the Mn oxide surface.

EPR spectroscopy was performed to directly measure the Mn oxidation state. The continuous-wave EPR (CW-EPR) spectra are shown in Figure 3.16c. In both the as-prepared and partially oxidized MnO nanoparticles, a characteristic  $S = 5/2$ , Mn (II) signal at  $g \sim 2$  with six-line  $^{55}\text{Mn}$  ( $I = 5/2$ , 100 % abundant) hyperfine splitting was observed (Figure 3.15c, inset). However, the broad EPR signal near an effective  $g$  value of  $\sim 5.7$ , which is characteristic of  $S = 3/2$ , Mn (IV), was not detected in either sample. We then tried to detect another species, Mn (III), expected to be generated on the MnO nanoparticles surface. The integer spin, known to be  $S = 2$ , Mn (III) is hard to observe via conventional perpendicular mode X-band EPR due to its large zero-field splitting. However, using parallel mode X-band EPR,  $S = 2$ , Mn (III) ions can be observed when the zero-field splitting is in an appropriate regime as observed for other manganese complexes.

Moreover, to detect rapidly decaying Mn (III) species, we prepared the EPR samples in a pyrophosphate solution, which has been shown to effectively ligate Mn (III) ions. As shown in Figure 3.16c, the well-resolved six-line hyperfine splitting with  $A \sim 42$  G and centered at  $g_{\text{eff}} \sim 8.2$  appeared in the Mn(III)-decorated nano MnO particles, which indicates that  $\text{Mn}^{\text{III}}$  ions were generated as speculated. In contrast, the parallel mode CW-EPR spectra of the as-prepared MnO nanoparticles consisted

of broad background signals, most likely from oxygen, with a very weak Mn (III) feature.

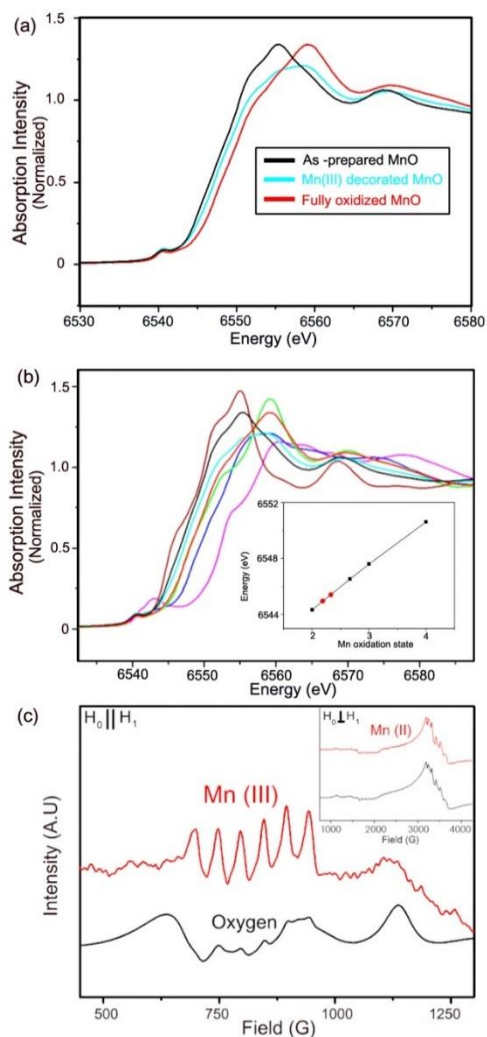


**Figure 3.16.** Change in the Mn oxidation state during surface treatment (a, b). Comparison of the XANES data collected from the as-prepared (black), Mn(III)-decorated (Light blue) and fully oxidized MnO (red) with other Mn-oxide compounds. (c) Parallel mode X-band CW-EPR spectra (Inset: perpendicular mode CW-EPR spectra) demonstrating Mn<sup>II</sup> oxidation to a higher oxidation state, Mn<sup>III</sup>, which results in a mixed valency.

### 3.3.4. Electrokinetic study of MnO NPs

To evaluate the detailed water oxidation mechanism of partially oxidized MnO nanoparticles, we conducted electrochemical study. First, we evaluated pH dependency under neutral condition. For this, we prepared various phosphate buffer solutions varying pH 7 to pH 8.5, which is stable pH range for phosphate buffer and investigated OER activity. As clearly shown in Figure 3.17, onset potential is shifted toward anodic direction as pH increased, 75mV/pH. According to the previous literature, Tafel slope is closely related with pH dependency in galvanic experiment as following equation.

$$\left(\frac{\partial E}{\partial pH}\right)_j = -\left(\frac{\partial E}{\partial \log j}\right)_{pH} \left(\frac{\partial \log j}{\partial pH}\right)_E$$

Combined with Tafel slope (78mV/dec), we could know that Mn(III)-decorated MnO nanoparticles have a first order dependency of log(j) on pH. And typically, 60~80mV/dec Tafel slope indicates during oxygen evolution, one-electron transfer is involved prior to rate determining step. As a result, we obtain following electrochemical law for Mn(III)-decorated MnO nanoparticles.

$$j = k_0(a_{H^+})^{-1} \exp\left[\frac{FE}{RT}\right]$$

Where  $k_0$ ,  $a_{H^+}$ ,  $F$  are potential-independent constant, proton-activity, Faraday constant, respectively. Although we could not identify the whole oxygen

evolution reaction process for now, above equations successfully reveal that one proton and one electron are involved prior to rate determining step in OER.

Taken together, we concluded that the Mn(III)-decorated MnO nanoparticles have two important characters for efficient water oxidation. First, Mn (III) species exist on the MnO particle surface. The *ex-situ* X-ray photoelectron spectroscopy (XPS) analysis indicated the Mn (III) species on the Mn(III)-decorated MnO surfaces were stable after 1 h of bulk electrolysis at 1.3 V. Mn (III) is reportedly the intermediate state in the oxygen evolution reaction. The d-orbital in the Mn (III) state intrinsically has a  $t_{2g}^3 e_g^1$  high spin configuration, which is spontaneously subjected to a Jahn-Teller(J-T) distortion. Unless the structural flexibility is fully guaranteed, large inner stress builds up; therefore, the J-T process is inhibited but charge disproportionation (CD) occurs. Nakamura group revealed that, in case of MnO<sub>2</sub> nanocatalysts, typical water oxidation Mn based catalysts, show inferior catalytic activity under neutral condition because of dominant CD reaction, while exhibit moderate performance under basic condition. Recently, our group also reported that higher Mn (III) content in the initial compound (LiMnP<sub>2</sub>O<sub>7</sub>) can improve the catalytic activity of Mn based compounds. In this study we revealed that Mn(III) can be successfully stabilized with structural flexibility in LiMnP<sub>2</sub>O<sub>7</sub> compounds. In this regard, we believe that generated Mn(III) species via surface treatment are stably maintained on the surface of Mn(III)-decorated MnO nanoparticles, which could drastically enhance the catalytic performance.

Second, we observed the size dependency of the water oxidation catalysis. As shown in Figure 3.13a, 8 nm particles exhibited higher catalytic activity than 15 and 100 nm MnO nanoparticles. Considering the onset potential is normally determined by intrinsic material properties, it can be inferred that a change in surface structure of the MnO particles occurred depending on their size, which affects the Mn redox reaction. The effects of particle size on the critical electro-kinetic steps uncovered in this study are under investigation.

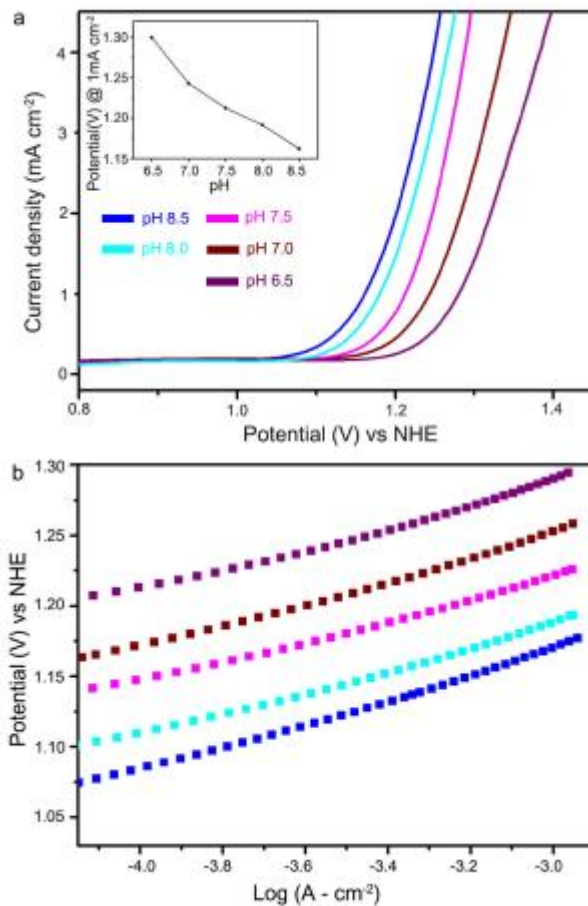


Figure 3.17. a. Cyclic voltammetry curves and b. Tafel plot of partially oxidized MnO NCs under neutral pH conditions, Inset figure indicates that partially oxidized MnO NCs follows Nernst behavior under near neutral condition.

### 3.4. Concluding Remarks

In conclusion, we reported a newly developed partially oxidized Mn(III) – decorated MnO nanocatalysts for the first time and evaluated its superior water oxidation catalytic activity under near neutral conditions. Its OER activity ( $\eta$ : 530 mV @ 5 mAcm<sup>-2</sup>) is the highest among the first row transition metal-based catalysts. Facile post-surface treatment with NH<sub>4</sub>OH solution created a mixed Mn valency (II/III) on the surface of MnO nanoparticles. A size dependency was observed for the catalytic performance. Moreover, because an assembled MnO nanoparticles monolayer works as an efficient water oxidation catalyst (Figure S8 in the supporting information), our system is expected to minimize the light absorption lost to the substrate, which can be essential property for photoelectrochemical (PEC) application.

# **Chapter 4. Mechanistic Investigation of Electrocatalytic Water Oxidation by Uniform 10 nm sized MnO Nanoparticles**

## **4.1. Introduction**

Electrochemical water splitting to produce hydrogen and oxygen molecules is promising resolution for contemporary energy crisis. Hydrogen energy is an attractive alternative resources due to its high energy density and environmentally friendly characteristics. Compared to conventional gas reforming process, electrochemical water splitting is more efficient pathway to produce hydrogen gas without any undesired byproducts. Tardy reaction kinetics in anodic water oxidation process has been regarded as major bottleneck for overall reaction process. Extraction of four electrons and four protons is required to proceed the water oxidation reaction and generally results in considerably high overpotential values. Historically noble metal catalysts, such as  $\text{IrO}_x$ ,  $\text{RuO}_2$  have been practically adopted for its high activity in spite of cost issue. For the practical application, recently, development of first-row transition metal based catalysts have been widely

investigated. Specifically, cobalt, iron, nickel, and manganese based oxide and sulfide compounds exhibit good catalytic activity at basic condition.

In nature, there is water oxidation complex(WOC),  $Mn_4Ca$  cluster which is consist of only manganese and calcium elements. Interestingly, the WOC operates Kok cycle, oxygen evolving reaction under neutral condition(pH 6.5) with exceptionally high turnover frequency and low overpotential, which have never been achieved by any synthetic catalysts.

Inspired by biological WOC, a number of research efforts have been dedicated to develop Mn based catalysts. Nevertheless, still, there exist severe activity discrepancy between synthetic catalysts and the WOC in PS II. Normally at neutral pH, 6~700mV of overpotential is needed to proceed the water oxidation reaction by synthetic Mn catalysts. Such an activity degradation in Mn based catalysts has long been unresolved problems over the decades. To settle this issues, fundamental challenge is to understand the mechanisms underlying OER activity.

Previously claimed activity determinants for Mn catalysts are mainly structural parameters related to the binding of reactant absorbate. For instance, Mn-Mn / Mn-O local distance is known to affect binding strength between surface metal site and anionic reaction intermediates, -OOH or -OH species. Indeed,  $Mn_2O_3$  and  $Mn_3O_4$  which are composed of moderate bonding length of Mn-Mn/O exhibit higher catalytic performance than other Mn oxide compounds. Electronic configuration of 3d orbital is considered as activity descriptor as well. Because  $e_g$  orbital participates in sigma bonding with anionic absorbate, the occupancy in  $e_g$  orbital directly

determines the binding energy of reactant species and thus makes volcano shaped activity trend. For the water oxidation reaction,  $e_g^1$  possession is suggested as optimal electronic configuration for transition metal based catalysts.

It is essentially required to understand the detailed catalytic mechanism, to design catalyst and optimize the performance. Specifically, sequential  $4e^-/4H^+$  transfer happens in water oxidation, which is concomitantly coupled with metal redox process. Therefore, fundamental issue is how to obtain and interpret the kinetic profiles of the catalyst. Electrode kinetics of electrocatalysts can be divided into two independent pathways: i) surface catalytic reaction and ii) electron transport from electrode/electrolyte to electric circuit. In this regard, Savéant group particularly adopted proton-electron hopping mechanism to interpret the reaction kinetics on electrode, theoretically. From the modified Fick's law, current response was predicted and calculated into several rate controlling factors. The analysis enables to predict current-potential relationship and optimal thickness of the catalyst film.

Electro-kinetic study has been conducted to get experimental evidence and insight of electrode kinetics during catalysis. From the combined Tafel slope, pH and buffer strength dependency measurement, electrochemical rate law for each catalyst can be derived. For instance, Nocera group investigated amorphized NiOx and CoOx catalysts and verified that, proton coupled electron transfer pathway exist as quasi-equilibrium step, followed by chemical RDS.

Moreover, *in-situ* observation of reaction intermediates is another important research direction to construct overall water oxidizing mechanism. Several

spectroscopic investigation have been adopted to monitor the change of metal surface status and capture the fast decaying intermediate species. Frei group demonstrated the formation of three-electron oxidative intermediates, superoxide species (Co-OO-Co), that is hydrogen bonded to adjacent Co(III)-OH and identified fast and slow catalytic active sites in Co<sub>3</sub>O<sub>4</sub> nanocatalysts by isotope experiment and time resolved FT-IR spectroscopy. Taken together, the whole OER cycle in Co based catalyst is suggested.

Here, we conducted the in-situ spectroscopic analysis during OER catalysis, mediated by monodisperse manganese oxide nanoparticles(NPs). Manganese is intriguing element among first row transition metals, because not only it serves as main component of oxygen evolving complex (OEC, Mn<sub>4</sub>CaO<sub>5</sub> cluster) in photosystem II (PS II), but also it possess redox active characteristics. (Mn<sub>4</sub>CaO<sub>5</sub> cluster has outstanding efficiency for water oxidation in neutral condition.) Although plenty of efforts have been dedicated to discover the efficient Mn based catalyst inspired by OEC, unfortunately, most of the catalysts exhibit poor catalytic performance. Recently, Shannon group summarized the activity of representative Mn based catalysts, which still display the relatively high overpotential values compared to previously reported Co and Ni based ones.

Several groups have pointed out that the instability of surface Mn(III) species and high symmetric features are primitive reasons for the suppressed redox capability in neutral condition. Competitive redox process, Jahn-Teller distortion and charge disproportionation exist exclusively in Mn(III) ( $t_{2g}^3e_g^1$ ) involved

electrocatalytic reaction. Norscov group and Cao group also emphasized eg1 configuration which is related with the formation of  $\sigma$  bonds with anionic adsorbates. In order to address the outlined issue, several strategy have been suggested. Amorphous manganese oxide materials have gained intense attention due to structural uniqueness, relatively long Mn-Mn, Mn-O distance which gives flexibility. Furthermore, synergistic gold effect was studied to improve the activity. Generation of asymmetric geometry on Mn surface by adopting amine containing molecules is another research direction to improve the activity.

Under neutral condition, undesired restriction additionally exist in Mn based catalysts. According to recently published benchmarking paper, most of the manganese oxide compounds showed inferior activity at pH 7, with no exception. Several groups have pointed out that the instability of surface Mn(III) species and symmetric oxide structure are primitive reasons for the suppressed redox capability in Mn catalysts. Competitive reactions, Jahn-Teller (J-T) distortion and charge disproportionation, exclusively operate in Mn(III) ( $t_{2g}^3e_g^1$ ) involved electrocatalytic reaction. Unfortunately, J-T distortion which requires concomitant elongation / compression in  $MnO_6$  octahedra is considerably prohibited by rigid oxide framework. To address this issue, deliberate generation of asymmetry in the catalyst have been tried to obtain enough flexibility by amorphorization of manganese oxide, adopting organic molecules, synergistic effect with noble metal substrate, and so forth.

We previously demonstrated that if structural flexibility is sufficiently granted, intermediate Mn(III) species can be stabilized. Phosphor derived manganese catalysts with asymmetric Mn geometry display superior performance to oxide compounds. Applied inner pressure and local pair distribution function at Mn(III) state are proposed as new standard to gauge the activity. Interestingly, computation analysis revealed that although high inner pressure required, J-T distortion happened freely at Mn(III) in MnO structure. Inspired from the fact, we recently developed highly active manganese oxide nano-catalysts. Sub-10 nm sized partially oxidized manganese oxide nanoparticles (MnO NPs) exhibit high activity under neutral pH, which is even better than well-known catalysts, Co-Pi amorphous films. Additionally, we observed that there exist clear size dependency on onset potentials and activity of nanosized manganese oxide compounds always overwhelm the bulk counterparts.

Here, as an effort to understand the nano-size effect and unveil the oxygen evolving mechanism, we conducted the *in-situ* spectroscopic analysis during water oxidation catalysis, mediated by monodisperse manganese oxide nanoparticles (NPs). More importantly, from the electrokinetic study and spectroscopic studies, namely, EPR, *in-situ* XAS and *in-situ* UV-vis analysis, we successfully demonstrated new catalytic cycle, which is exclusively applied on our manganese oxide nanoparticle system.

## 4.2. Results and Discussions

### 4.2.1. Thickness dependent activity of MnO nanoparticles

Synthesis of MnO NPs and electrode preparation were performed from the previously reported method. As shown in Figure 4.1a and 4.1b, monodisperse 10 nm sized MnO NPs were successfully synthesized and loaded on FTO substrate. Thickness of the MnO NPs film was precisely controlled from 70 nm to 600 nm via spin coating condition.

Electrochemical analysis was performed to understand detailed electrode kinetics of water oxidation by MnO NPs. Thickness dependent water oxidizing activities were evaluated by cyclic voltammetry (CV) in 0.5 M phosphate buffer at pH 7. In order to minimize the non-faradaic current contribution, all the CV curves were displayed after polarization correction process. As shown in figure 4.2a, the overpotential reaching 5 mA/cm<sup>2</sup> were 610, 560, 530 and 550 mV for 70, 150, 300 and 600 nm film thickness, respectively. We found that 300 nm thickness exhibited the highest water oxidation performance and, over 300 nm thickness, catalytic activity has suddenly taken a turn for the worse. It is originated from the fact that over the optimal thickness charge transport limitation factors dominates over the effect of active site increase, which results in the saturation of the catalytic current.

Tafel plots of each thickness were obtained from the polarization-corrected CV curves. As shown in figure 4.2b, the Tafel slopes of 70, 150, 300 and 600 nm thickness were measured to 82.6, 75.5, 70.1 and 78.2 mV/dec, respectively. For the

electrochemical water oxidation reaction, current –potential relation is described as equation 1, where  $i_0$ ,  $\alpha$ ,  $F$ ,  $E^0$  and  $b$  are exchange current density, transfer coefficient, Faraday constant, thermodynamic potential and Tafel slope, respectively. Additionally, Tafel slope can be expressed by inverse relationship with transfer coefficient.

$$i = i_0 \cdot \exp\left(-\frac{\alpha(E-E^0)F}{RT}\right) \quad (1) \quad b = \left(\frac{\partial E}{\partial \log i}\right) = \frac{2.3 RT}{\alpha F} \quad (2)$$

Therefore, in case of our MnO NPs film, 70~80 mV/dec Tafel slopes is corresponding to  $2.3RT/F$ , which indicates that transfer coefficient is 1. This results imply that a reversible one-electron transfer process exists prior to rate determining step (RDS).

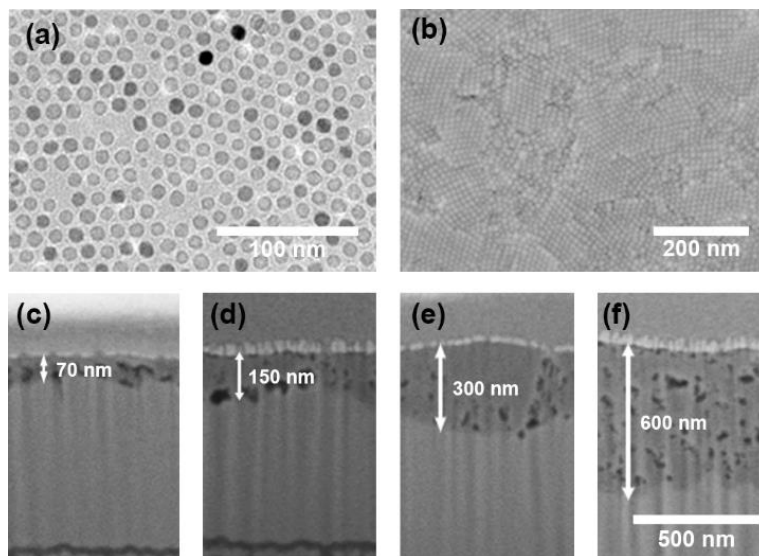


**Figure 4.1.** Characterization of MnO NPs film. (a) TEM image of synthesized MnO NPs and Plane (b) and cross sectional (c~e) SEM image of MnO NPs films on FTO substrate.

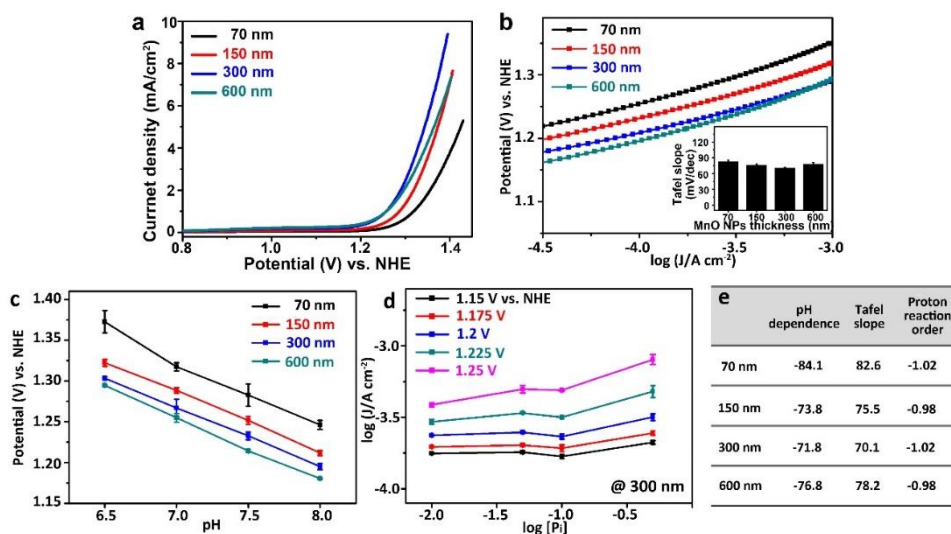
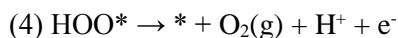
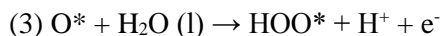
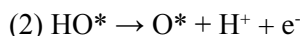
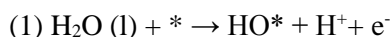


**Figure 4.2.** Electrochemical analysis of MnO NPs films. Polarization corrected cyclic voltammograms (a), Tafel plot near the onset potentials (b), pH dependency at neutral pH range (c), buffer concentration dependency (d), and summary table for resultant reaction order (e) of various thickness MnO NPs film.

## 4.2.2 Theory of Oxygen Evolution reaction (OER) Mechanism

Generally, mechanism for the OER at the surface of the metal oxides has been known as the following four electron involved reaction paths :



Where \* is regarded as the active sites for OER catalysis. Many researches have suggested several theories for general description of OER. In 1984, Rasiyah proposed that when redox potential of the catalysis close to the thermodynamic potential for OER, the catalysts should have high activity. Trasatti proposed that the strength of metal-oxygen bonds onto the surface can be a good descriptor for predicting the catalytic activity. Otagawa group suggested that 3d electron numbers in the transition metal at the bulk structures can be related to the catalytic activity. Recently, Shao-horn Yang group found that  $e_g$  occupancy in surface transition metals can be related to OER mechanism. They take some assumptions that  $e_g$  orbital at the surface of the catalyst can make the  $\sigma$ -bonding with the anion adsorbates onto the surface. Therefore, the occupancy of  $e_g$  orbital can affect on the binding of oxygen-containing intermediate species during the OER. Comparing the various

perovskite materials which contains different  $e_g$  occupancy, they experimentally found that catalysts that have  $e_g$  value of 1.2 shows the highest catalytic activity. Norskov and Rossmeisl group theoretically understand the activity of the OER electrocatalysts using DFT calculations in case of metal oxide OER catalysts. They found the free energy of the rate limiting step in the overall OER reaction and the overpotential value for the OER. These two values can be written by following equations:

$$G_{\text{OER}} = \max [\Delta G_1^\circ, \Delta G_2^\circ, \Delta G_3^\circ, \Delta G_4^\circ] \quad (14)$$

$$\eta (\text{overpotential}) = (G_{\text{OER}}/e) - 1.23 \quad (15)$$

They found that the difference between the binding energy of  $\text{HOO}^*$  and  $\text{OH}^*$  is nearly constant onto the various types of metal oxides surfaces. This difference between two energy can be defined as the theoretically lowest overpotential for OER catalysis. However, only a few catalysts can operate with this lowest overpotential. Instead, they suggested that the difference between the binding energy of  $\text{O}^*$  and  $\text{OH}^*$  could be a origin for the overpotential for the most of the OER electrocatalysts. Moreover, they found that this assumption could be applied to the experimental results studied in the previous reports well. As briefly mentioned above, since water oxidation reaction comprises multi step reactions, identification of the change of current along with the applied potential offers a convincing definition of determining the Tafel slope of an electrochemical reaction and helps to

reveal detailed mechanism. It is generally known that from the Tafel analysis, not only comparison of catalytic activity, but basic analysis of catalytic cycle is possible. For example, the discharge of water molecules or hydroxyl ions to oxidize the active sites onto the surface of the catalysts results in Tafel slope value of 120 mV/dec.<sup>[128]</sup> Further chemical conversion into stable chemical species onto the active sites yields Tafel slope value of 60 mV/dec.

Typically, electrochemical rate law with single step mechanism can be defined with a turnover-limiting electron transfer from the resting state,



Substituting the other key factors such as turnover velocity and surface concentration of active sites into the above relationship, the electrochemical rate law for a reaction can be lead as,

$$j = 4Fk^{\circ}ET \exp(\beta\eta F/RT) \quad (17)$$

where F is faraday constant (96485.3sA/mol) and  $\beta$  is transfer coefficient. This relationship will lead to a Tafel slope ( $\frac{\delta\eta}{\delta\log j}$ ), which can be simplified to  $2.3 \times RT/\beta F$ . In single step,  $\beta$  is close to 0.5 ( $\pm 0.1$ ) which gives out the Tafel slope value around 120 mV/dec at 298K.

After verifying its major mechanism prior to current density activation, it is also needed to evaluate in addition to the dependence of activity on pH. It was necessary to establish the dependence of the reaction rate along with proton involved and buffer strength.

$$j = k_0(a_{\text{buffer}})^n(a_{\text{proton}})^m \exp(\beta EF/RT) \quad (18)$$

where  $a_{\text{buffer}}$  is buffer activity which depends on the buffer strength,  $a_{\text{proton}}$  is proton activity determined by pH dependence. To achieve the proton activity dependency of the mechanism, partial differential equation was applied on the relationship of potential over pH.

$$\left(\frac{\partial E}{\partial \text{pH}}\right)_j = -\left(\frac{\partial \log j}{\partial \text{pH}}\right)_E \left(\frac{\partial E}{\partial \log j}\right)_{\text{pH}} \quad (19)$$

Substituting the obtained experimental results of the Tafel slope and measured pH dependency, it yields a reaction order in proton activity  $a_{\text{proton}}$ . While demonstrating the proton association during the mechanism, finding the number of electron involved during OER which also defined as transfer coefficient ( $\beta$ ) has to be calculated. It can be written as following equation by eliminating all the given constants from equation 1.

$$\beta = \frac{2.3RT}{bF} \quad (20)$$

After substituting all constants with  $b$  is the Tafel slope, it yields a reaction order in electron activity. Taken all the considerations of proton and electron involve during OER, the possible proposed pathway of each electrocatalyst as water oxidation can be explained. For instance, Nocera group successfully established the detailed water oxidation mechanism of newly developed Co-Pi, Ni-Bi catalysts, using electrokinetic study, as described above.

### 4.2.3. Electrokinetics in MnO Nanoparticles

pH dependence of MnO NPs was further examined at neutral condition. Potentials reached at 1 mA/cm<sup>2</sup> were measured at each pH and film thickness. As shown in figure 4.2c, linearity in relation between pH and the measured potentials was observed from pH 6.5 to 8.0. The slopes were calculated as -84.1, -73.8, -71.8 and -76.8 mV/pH for each thickness. Again, the slopes show similar value around 70~80 mV/pH regardless of thickness, like in Tafel slope. In electrochemical rate law, proton reaction order is defined as  $-(\partial \log j / \partial \text{pH})_{E,T,p}$ . Thus, using the values of Tafel slope and pH-dependent potential change, proton reaction order can be derived from the following partial differential equation.

$$\left(\frac{\partial E}{\partial \text{pH}}\right)_{j,T,p} = -\left(\frac{\partial E}{\partial \log j}\right)_{pH,T,p} \left(\frac{\partial \log j}{\partial \text{pH}}\right)_{E,T,p} \quad (3)$$

As shown in figure 4.2e, proton reaction order for each thickness was maintained as -1, which indicates that an inverse first order dependence on the proton activity. Moreover, dependence of current density on phosphate concentration was evaluated at various water oxidizing potentials. A zeroth order dependence on phosphate concentration was observed at each potentials (Figure 4.2d). Combining the results of electrokinetic study, overall electrochemical rate law for catalysis by MnO NPs can be derived, assuming Langmuir condition.

$$j = k_0(a_{H^+})^{-1} \exp\left[\frac{FE}{RT}\right] \quad (4)$$

Equation 4 is consistent with a mechanistic sequence involving a reversible  $1e^-/1H^+$  transfer quasi-equilibrium step followed by a rate determining step. It should be noted that the electrochemical behavior of MnO NPs is entirely different from the previous Mn catalysts. Most of previously reported manganese based compounds consistently exhibit similar Tafel slope, 100~120mV/dec value at neutral pH. Commercially available micron sized manganese oxide compounds,  $MnO_2$ ,  $Mn_2O_3$ , and  $Mn_3O_4$  show 120 mV/dec with no pH dependency. Similar electrochemical data was obtained in phosphor containing materials. Recently reported  $Mn_3(PO_4)_2 \cdot 3H_2O$  and  $Li_2MnP_2O_7$  derivative compounds both exhibit ~120mV/dec. Moreover, even in amorphized manganese oxide, Tafel slope is maintained as 120mV/dec.

Theoretically, 120 mV/dec of Tafel slope means that transfer coefficient( $\alpha$ ) in Tafel equation is 1/2. It is expected that one electron oxidation is rate determining step with no quasi equilibrium step. Indeed, from the *in-situ* spectroscopic analysis, detailed RDS was experimentally identified as  $Mn(II) \rightarrow Mn(III)$  redox process. Therefore it is plausible to think that distinctive electrokinetic behavior is attributed to superior OER activity of MnO NPs to previously reported Mn catalysts. In addition, notably, the various electrokinetic data in our study do not change as film thickness increases, which indicates that the established electrochemical law can be commonly applied to reaction kinetic of MnO NPs irrespective of film thickness. Therefore, it is reasonable to focus on 300 nm thickness for the further mechanistic study.

Regarding redox characteristics of MnO NPs, unique features of MnO NPs was observed in cyclic voltammetry curves. Two distinct redox waves were displayed at 0.68 and 1.07 V vs. NHE. Both peaks showed pH dependence at pH 7~8. The change of peak position from pH 7 to 8 were measured as -107 and -117 mV/pH for 1<sup>st</sup> and 2<sup>nd</sup> redox waves, respectively. Clear pH dependency indicates that proton is coupled with both redox process of MnO NPs. On the other hand, there was no observable redox waves in conventional bulk manganese oxides, MnO and Mn<sub>3</sub>O<sub>4</sub>. Sequential proton coupled redox reactions are inherent characteristic for MnO NPs, which are related to Mn valence change during catalysis.

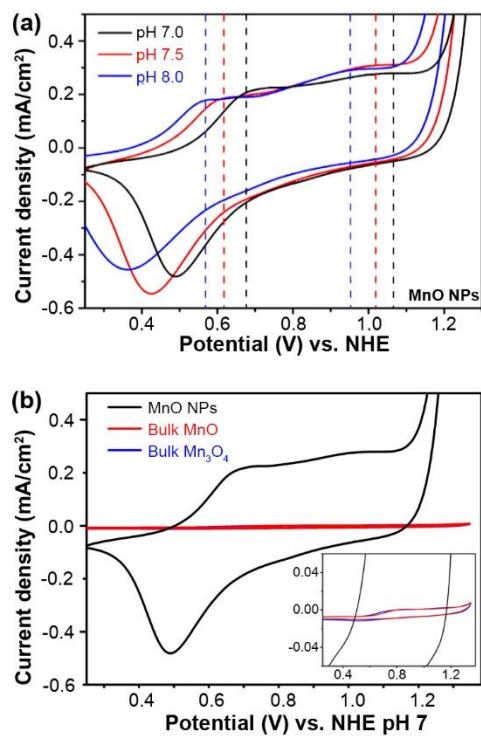


**Figure 4.3.** Comparison of redox characteristics for MnO NPs and bulk manganese oxide compounds. (a) pH dependent redox peak shift of MnO NPs and (b) comparison of redox behaviour between bulk Mn<sub>3</sub>O<sub>4</sub> and MnO compounds and MnO NPs

#### 4.2.4. *In-situ* spectroscopy analysis

To shed light on redox chemistry of MnO NPs, we performed numerous spectroscopic studies to detect reaction intermediates. The continuous wave electron paramagnetic resonance (CW- EPR) spectroscopy was utilized to monitor the manganese oxidation state of the MnO NPs. In this work, four potentials (0.4 V, 0.75 V, 1.1V and 1.3 V vs. NHE @ pH 7) were selected to investigate change of the manganese oxidation state. The perpendicular and parallel mode EPR spectra of MnO NPs at four different applied potentials are displayed in Figure 4.4. The EPR spectrum of as-prepared MnO NPs exhibits a characteristic Mn(II) ( $S = 5/2$ ,  $g_{\text{eff}} \sim 2$ ) and Mn(III) ( $S = 2$ ,  $g_{\text{eff}} \sim 8.2$ ) signal with a six-line  $^{55}\text{Mn}$  ( $I = 5/2$ , 100%\_abundance) hyperfine splitting at perpendicular and parallel mode, respectively.

Then we tried to quantitatively compare the intensity of Mn(II)/Mn(III) spectra on MnO NPs before/after Mn redox potentials. At around 1<sup>st</sup> redox wave, Mn(II) signal continuously decreased while Mn(III) signals was enhanced. The spectral change and electrochemical data implies that the 1<sup>st</sup> redox is corresponding to  $\text{Mn(II)-H}_2\text{O} \rightarrow \text{Mn(III)-OH}$ . Over 2<sup>nd</sup> redox potential, Mn(II) spectra is no longer detected and concomitant slight decrease of Mn(III) is observed. According to previous EPR study on Mn complex, Mn(V) species can be detected at  $g \sim 8.5$  at parallel mode which was not detected in this study. In addition, although Mn(IV) species display EPR signal at  $g \sim 4.3$  in perpendicular mode, it is difficult to directly capture Mn(IV) species due to the large zero field splitting value and fast decaying

nature of reaction intermediates. Thus, this results indirectly support that higher Mn valency is generated during catalysis.

The existence of Mn(IV) or Mn(V) species can be further supported by *in-situ* XAS analysis. For the *in-situ* analysis, pre-electrolysis step were conducted at designed potentials in order to achieve steady state of the catalysts. As expected, clear positive line shift was observed in Mn K-edge spectra with increase of applied potentials. Average Mn oxidation state was calculated using the spectra of the reference manganese oxide compounds. (Figure 4.4d inset) The average oxidation states before Mn redox have the values around 2.5, which means the existence of mixed valency, Mn(II)/Mn(III). Interestingly, at 0.4 V vs. NHE, average oxidation state was slightly reduced. This decline was attributed to partial Mn reduction on the surface, in accordance with the negative current at 0.4 V vs. NHE in cyclic voltammetry curves. (Figure 4.3a) Over the open circuit potential, positive line shift was observed in Mn K-edge spectra. Mn oxidation states were evaluated as 2.96 and 3.20 at 1.1 V and 1.3 V vs. NHE, respectively.

We could specify the generated reaction intermediates by *in-situ* UV-Vis analysis. Spectral changes of MnO NPs electrodes caused by catalytic reaction are examined at neutral pH. The spectra were monitored from 0.8 V to 1.3 V vs. NHE with 0.1 V increment. In order to clearly check the surface status, we additionally obtained difference spectrum at each potential by subtraction from the spectra at 0.8V. As shown in Figure 5a, upon stepping applied potentials with 0.1V increments, two distinct absorption bands around 400 nm ( $\Delta\text{Abs}_{400}$ ) and 600 nm ( $\Delta\text{Abs}_{600}$ ) were

identified. Notably, while peaks around 400 nm showed relatively sharp feature, broad and wide absorption band was observed at around 600 nm.

Based on the characteristics of the peaks and previous literature, we could assign the origin of those peaks. As reported by the researchers, Mn(III) in Mn<sub>3</sub>O<sub>4</sub> nanoparticles exhibit O<sup>2-</sup> Mn<sup>2+</sup> (210–250 nm) and O<sup>2-</sup> Mn<sup>3+</sup> (350–390 nm) charge transfer transitions and d–d crystal field transitions in the range of 550–700 nm corresponding to <sup>3</sup>E<sub>g</sub>(G) ←<sup>3</sup>T<sub>1g</sub>, <sup>3</sup>A<sub>2g</sub>(F) ←<sup>3</sup>T<sub>1g</sub>, <sup>3</sup>A<sub>2g</sub>(G)←<sup>3</sup>T<sub>1g</sub>, <sup>3</sup>T<sub>2g</sub>(H) ←<sup>3</sup>T<sub>1g</sub>, <sup>3</sup>T<sub>1g</sub>(H) ←<sup>3</sup>T<sub>1g</sub>, and <sup>3</sup>E<sub>g</sub>(H)←<sup>3</sup>T<sub>1g</sub> of octahedral Mn<sup>3+</sup> species. On the other hand, Mn(IV) species in MnO<sub>2</sub> exhibit a characteristic broad peak in the region of 400 nm along with shoulder peaks in the region of 575 and 700 nm. The *in-situ* UV-Visible spectral changes showing the continuous peak in the range between 350–500 nm and broad shoulder in the range of 500–700 nm are analogues to those observed for the Mn(IV) species in MnO<sub>2</sub> nanocrystals as reported previously. Also, most of the Mn(V) species reported in the literature exhibit two distinct peaks in the range of 350 nm and 520 nm. Therefore, we could assign the peak around 400 nm and the shoulder around 600 nm possibly to Mn(IV) species rather than Mn(III) or Mn(V) species.

The formation of Mn(IV) species is also further supported by XANES and EPR spectral studies. Notably, upon increment of applied potentials the absorption bands around 400 nm ( $\Delta\text{Abs}_{400}$ ) was slowly shifted from high-energy to low-energy region due to stepwise proton coupled electron transfer. Also, as verified from cyclic voltammetry initially the MnO nano particle undergoes one electron oxidation and

converted into Mn(III) species, which is further supported by EPR. Significantly, after 1.0V the decrease in signal intensity of the Mn(III) and the disappearance of signal corresponds to Mn(II) proved by EPR, revealing that the band observed around 400 nm is possibly assigned to Mn(IV)=O species rather than Mn(III) or Mn(II). Also we can safely discard the possibility of involvement of Mn(V)-oxo species as the XANES analysis showed that the rising edge energy increased slightly across the series consistent with the increasing effective nuclear charge on the manganese and the average Mn oxidation state is 3.2 during OER.

Thus all the above observation from the literature as well as from XANES and EPR studies  $\Delta\text{Abs}_{400}$  is corresponding to the ligand to metal charge transfer band of Mn(IV) species. Furthermore,  $\Delta\text{Abs}_{600}$  can be assigned to d-d transition band of Mn(IV). In case of Mn(IV)-O species, because d-d transition of octahedral system is both Laporte and spin-forbidden according to the selection rule, it intrinsically exhibit broad characters with low intensity.

Then, we displayed  $\Delta\text{Abs}_{400}$  and  $\Delta\text{Abs}_{600}$  against applied potentials with typical J-V curves of MnO NPs. As shown in figure 4.5c,d the intensity of two absorption peaks showed strong correlation with onset of water oxidation. Moreover, reversibility of the Mn species is also successfully demonstrated that gradual decline of peak intensity was detected as potential applied reversely.

On the other hand, in case of bulk MnO compounds, there were no potential dependent spectrum change at same potential range. (Figure 4.6) Moreover, when same *in-situ* experiments are conducted in organic electrolyte, (TBA)ClO<sub>4</sub> no peak

change was observed as well. Therefore, it is considered that the spectral changes observed in figure 4.5 were the consequence of manganese redox chemistry, formation of Mn(IV)=O species, in the presence of water.

Unique Mn redox change from Mn(II) to Mn(IV) is also verified in in-situ Raman spectroscopy. Raman spectra of MnO NPs electrodes recorded during bulk electrolysis was shown in Figure 4.7. At the initial state, characteristic Mn(II) –O stretching vibration ( $A_g$ ) and Mn(III)-O stretching mode ( $E_g$ ) modes are observed as broad shoulder bands around  $640\text{ cm}^{-1}$ ,  $575\text{ cm}^{-1}$ , respectively. Then as applied potential increased up to 1.05V where oxygen evolution initiates, new Raman peaks are evolved around  $555\text{ cm}^{-1}$ ,  $480\text{ cm}^{-1}$  with decrease of Mn(III) related bands. The frequencies and relative intensities of these generated peaks are well matched with stretching vibration of Mn(IV)-O species. Again reversibility of Raman spectra is confirmed. Therefore, these observations demonstrate the sequential redox change of MnO NPs to form active Mn(IV) species.

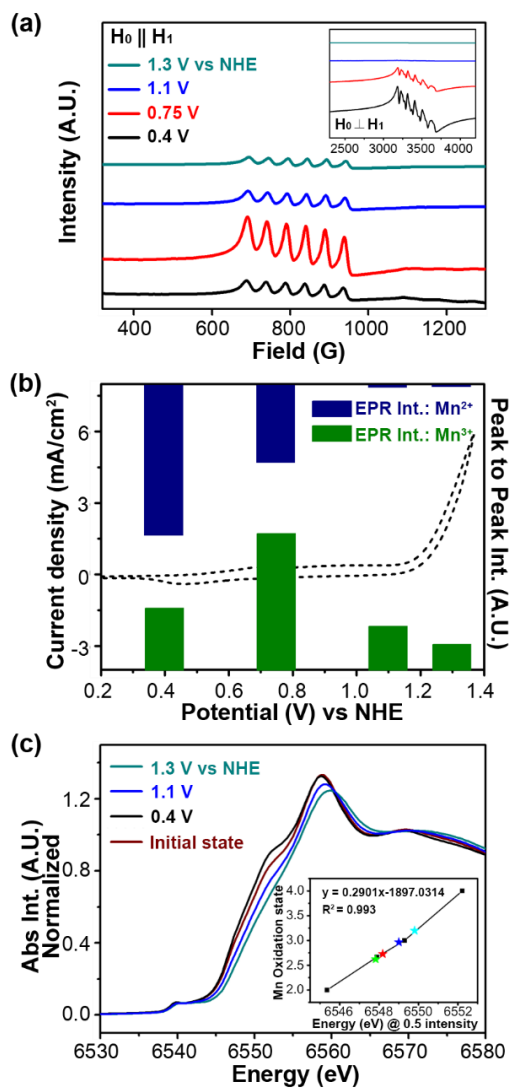


**Figure 4.4.** Mn valency change during water oxidation catalysis. Parallel mode X-band CW-EPR spectra (a) (Inset: perpendicular mode CW-EPR spectra), and peak to peak EPR intensity (b). Mn K-edge XANES spectra (c) and average Mn oxidation state demonstrating electro-oxidation of manganese to higher valency : Initial state (red), 0.4 V (green), 1.1 V (blue), 1.3 V (cyan) vs. NHE

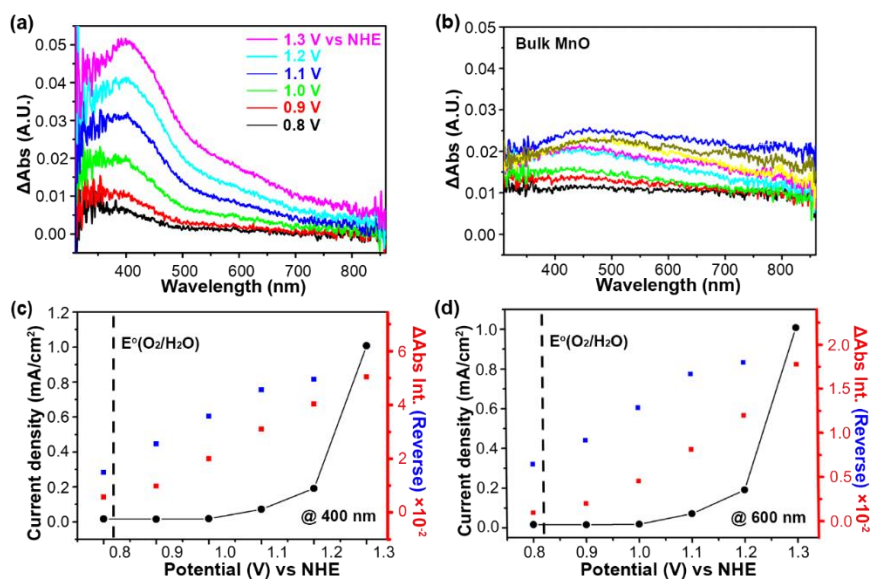


**Figure 4.5.** *In-situ* UV-Vis spectra of MnO NPs. (a) difference spectra depending on applied potentials. (b) difference spectra of bulk MnO (c, d) Potential dependences of the current density (solid line) and difference absorbance at 400 and 600 nm for MnO NPs.

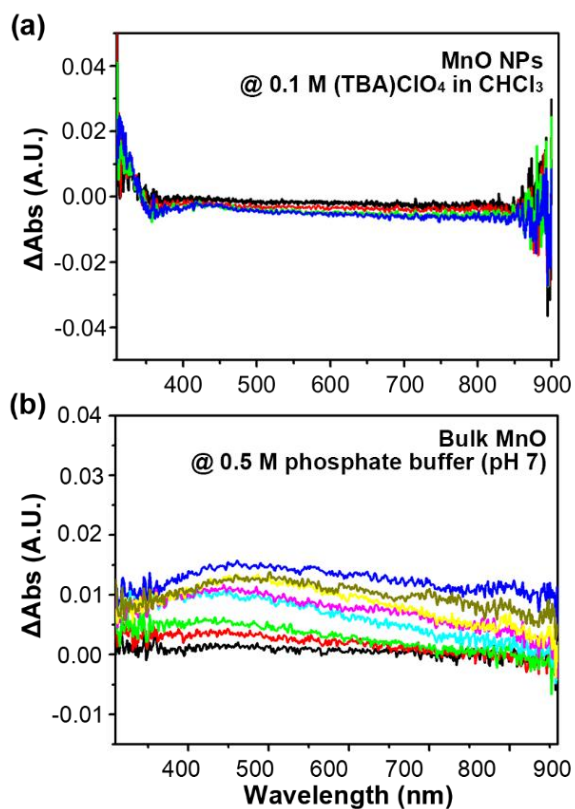


**Figure 4.6.** *In-situ* UV-Vis spectra. Difference spectra of (a) MnO NPs in organic electrolytes at various applied potentials: 0.8 V (black), 0.9 V (red), 1.0 V (green), 1.1 V (blue) vs NHE and (b) bulk MnO compounds in phosphate on applied potential: 0.8 V (black), 0.9 V (red), 1.0 V (green), 1.1V (cyan), 1.2V (magenta), 1.3 V (yellow), 1.4 V (dark yellow), 1.5 V (blue) vs NHE

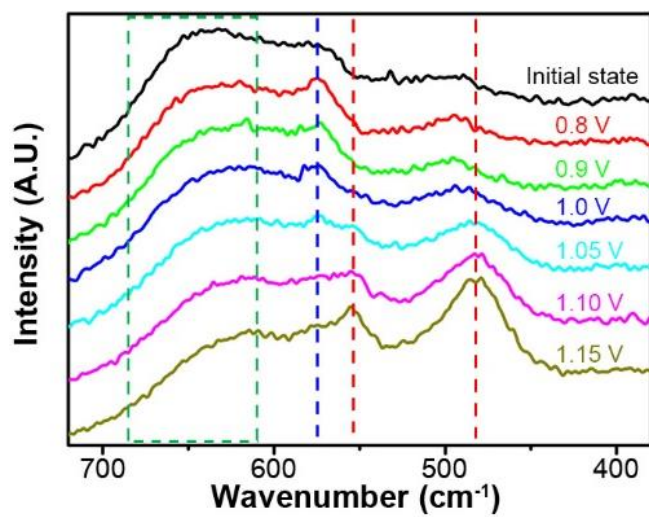


**Figure 4.7.** *In-situ* Raman spectra of MnO NPs. All the potential dependent spectra are collected during bulk electrolysis at designed potentials

#### 4.2.5. Proposed Water Oxidation Mechanism

Taken together with electrochemical and spectroscopic data, we could construct overall redox process of Mn species of MnO NPs during water oxidation. Firstly, redox behavior, pH dependent J-V curve shift, and EPR results suggest that Mn(II)-H<sub>2</sub>O surface species are oxidized to Mn(III)-OH at 1<sup>st</sup> redox wave. Secondly, electrokinetic and *in-situ* UV-Vis data revealed that concerted one proton and one electron involved oxidation reaction, Mn(III)-OH → Mn(IV)=O exist as quasi-equilibrium step before RDS.

We compared mechanistic scheme for our MnO NPs and conventional Mn catalysts.(Figure 4.8) As stated above, it has been well documented that RDS for conventional Mn catalyst is one electron oxidation, Mn(II)-H<sub>2</sub>O → Mn(III)-H<sub>2</sub>O and no quasi-equilibrium step exists. Experimental data of zeroth proton reaction order and 1/2 transfer coefficient value also support this claim. Due to the pK<sub>a</sub> value, it is expected that proton transfer occurs and =O formation is sequentially proceeded. On the other hand, in case of our 10 nm sized MnO NPs, formation of Mn(III) species is no longer rate determining process, instead, concerted electron and proton transfer exists as quasi-equilibrium step to produce Mn(IV)=O intermediates. In proposed mechanism, we adopt rate determining step as O-O bond formation, based on the theoretical study and previous *in-situ* FT-IR experiments. Mechanistic details of how the O-O bond forms and the precise nature of the rate determining step remain to be determined.

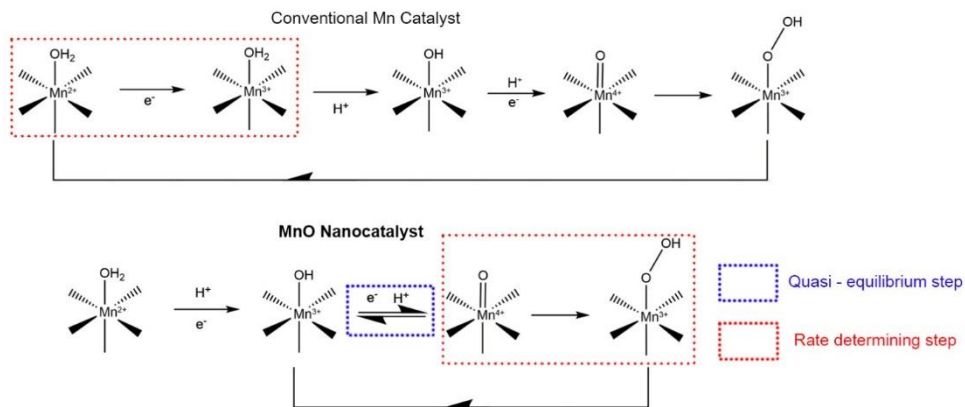


**Figure 4.8.** Proposed water oxidation mechanism of conventional Mn catalyst (top) and monodisperse 10 nm sized MnO nano-catalyst. (bottom) Blue and red dotted rectangle indicates quasi-equilibrium and rate determining step, respectively.

### 4.3. Concluding Remarks

In conclusion, we investigated electrochemical water oxidizing mechanism, mediated by MnO nanocatalyst, exhibiting exceptional high catalytic activity in neutral condition. Comprehensive analysis unveiled the mechanistic uniqueness of nanosized manganese oxide electrocatalysts compared to conventional Mn catalysts. Concerted one proton and one electron transfer step exists as quasi-equilibrium, followed by chemical RDS. The sequential oxidation, Mn(II,III,IV) and generation of Mn(IV)=O species were characterized by combination of various spectroscopic analysis, such as EPR, *in-situ* XANES, and UV-vis spectroscopy. We believe that unique water oxidizing mechanism of MnO NPs, apart from the bulk sized Mn catalysts, is attributed to outstanding activity for water oxidation under neutral pH.

# Chapter 5. Ni-hybridized Manganese Oxide Nanoparticles

## 5.1. Introduction

Inspired from nature, first row transition metal based catalysts have been widely studied for the decades. Various metal valency and its earth-abundant reserves are attractive points as candidates for OER catalysts. Indeed, amorphous metal oxide catalysts have been reported under neutral and alkali condition. For instance, Nocera group developed  $\text{CoO}_x / \text{NiO}_x$  film, synthesized by electro-deposition, operating in neutral condition. Moreover, Berlinguette group succeeded to synthesize amorphous metal oxide compounds, using photodecomposition method.

On the other hand, as another approach, our group recently reported crystalline manganese oxide nanoparticles (NPs) as OER catalysts, operating under neutral condition. Surface treated monodisperse sub 10 nm sized  $\text{MnO}$  NPs have exhibited superb OER performance compared to previous reported Mn based catalysts. In this study, we have tried to combine well-known nickel oxide catalysts with manganese oxide nanoparticles. Manganese oxide nanoparticles were loaded on the  $\text{NiO}_x$  films in form of bi-layers, and enhanced catalytic activity was

investigated under neutral and alkali condition.

Synergistic effect in adjacent metal atoms have been studied in water oxidation field. Bond strength between metal and hydroxide atom (M-OH) is known to govern the OER activity trends. In layered double hydroxide (LDH) catalysts which is well-known OER catalysts under basic condition, this phenomena was observed. Zhou group reported that properties of LDH catalysts was achieved by nickel and iron combination, due to the fact that partial charge transfer occurred from iron to nickel active site. In addition, difference of electronegativity could derive nucleophilic character of active metal site, which facilitates water oxidation reaction. Indeed, Bell group reported that Co species in  $\text{Co}_3\text{O}_4$  compounds becomes more oxidized via more electronegative substrate, such as gold, platinum, and palladium. They observed that OER activity is proportional to difference of electronegativity. In this study, we investigated collaboration effect using all earth-abundant metal based catalysts, and discovered that activity of manganese oxide could be enhanced in help of amorphous nickel oxide substrate.

Modulation of Mn valency is key factor to improve the efficiency because water oxidation catalysis proceeded at the same time as change of surface Mn site. Generally, high metal valency could possess more electrophilic nature and larger oxidizing power which lead to enhanced catalytic activity. In this regard, formation of high valency in the crystal structure were extensively studied. In addition, because Mn (III) state is unstable under catalytic cycle, stabilization of that species is believed as main issue for Mn based OER catalysis. Mn (III) electronic structure,

$t_{2g}^3$ ,  $t_{2g}^1$  accompanies with non-preferred Jahn-Teller distortion that results in disproportionation reaction. Inferior activity of conventional Mn oxide compounds is explained in accordance with the above context. Here, we intentionally generate electrophilic Mn valency with synergistic help of amorphous nickel oxide films. Relatively electronegative  $\text{NiO}_x$  films induce partial oxidation of Mn oxide nanoparticles. Coupling effect between  $\text{Mn}_3\text{O}_4$  nanoparticles and  $\text{NiO}_x$  films was verified with *ex-situ* XPS and XANES analysis. Newly developed  $\text{Mn}_3\text{O}_4/\text{NiO}_x$  vertical hetrostructure showed greatly improved OER performance and, more importantly, have outstanding stability both in near neutral and basic condition.

## 5.2. Materials and Synthesis procedure

### 5.2.1. Synthesis of Manganese (II) Oxide Nanoparticles

$\text{Mn}(\text{CH}_3\text{COO})_3 \cdot 2\text{H}_2\text{O}$  (99%), 1-Octadecene (90%), Myristic acid (99%), and Decanol ( $\text{CH}_3(\text{CH}_2)_9\text{OH}$ ) were purchased from Sigma Aldrich and used without additional treatment. The manganese oxides nanoparticles were synthesized via hot injection method to obtain ~10 nm mono-disperse sphere nanocrystals.<sup>47</sup> 1mmol of manganese acetate dehydrate ( $\text{Mn}(\text{CH}_3\text{COO})_3 \cdot 2\text{H}_2\text{O}$ ), 2mmol of myristic acid, and 20 ml of octadecane were mixed and heated up to 110 °C under continuous degassing for 90 min. 3 mmol of decanol was mixed with 1 mL of octadecene to form a solution and this solution was heated at 110 °C under degassing for 2 hours with vigorous stirring at another glass pot. After 90 min, the temperature of manganese precursor was raised to 295 °C under Ar atmosphere and then the mixture of decanol was injected rapidly for the fast nucleation. The color of the solution changed into dark brown from brown at 110 °C and pale yellow at 295 °C after hot injection. The temperature of the mixed solution was maintained at 295 °C for 1 hour and sequentially the mixture was cooled down to room temperature. The as-prepared MnO nanoparticles were washed with acetone and toluene by 2 fold the amount of the nanoparticles solution each with centrifugation at 13500 RPM for 2 min. The washing process was conducted 3 times.

### 5.2.2. Fabrication of NiO<sub>x</sub>/Mn<sub>3</sub>O<sub>4</sub>

Substrate materials, amorphous nickel oxide films were fabricated by electro-deposition method. To determine the deposition condition, first we measured CV curves in NiCl<sub>2</sub> (320 mM) solution. Nickel redox peaks was observed at the ~ -1.0 V vs Ag/AgCl. Based on the results, electrolysis potential was set to -1.1 V. Since the charge passed during the depositions is proportional to the deposition amount, we controlled the film thickness with electrolysis time. With cathodic electrolysis at -1.1V 60 sec, porous 2 ~ 300 nm NiO<sub>x</sub> films were formed on the FTO glass substrate. This results are consistent with previous reports. Then, 10 nm sized MnO nanoparticles were spin-coated on NiO<sub>x</sub> films. Sub 10 nm sized MnO nanoparticles were synthesized via hot injection method. Synthetic procedure of MnO nanoparticles and spin-coating method were referenced from previous paper (see the supporting information for the experimental details). Because spin coated MnO nanoparticles have highly hydrophobic properties and arrayed in form of island shape, MnO nanoparticles were barely penetrated in to NiO<sub>x</sub> films. The Mn<sub>3</sub>O<sub>4</sub>/NiO<sub>x</sub> films were rinsed thoroughly with deionized water and dried under air at 353 K oven. Subsequently, further heating at 573 K for 5 hours under air atmosphere was performed to enhance crystallinity of materials and adhesion to the substrate. As shown in Figure 5.1, roughly 10 layers of MnO nanoparticles were formed on the NiO<sub>x</sub> films. Energy selective backscattered (ESB) analysis clearly indicated that distinct Mn<sub>3</sub>O<sub>4</sub>/NiO<sub>x</sub> heterostructure were vertically arrayed as expected.

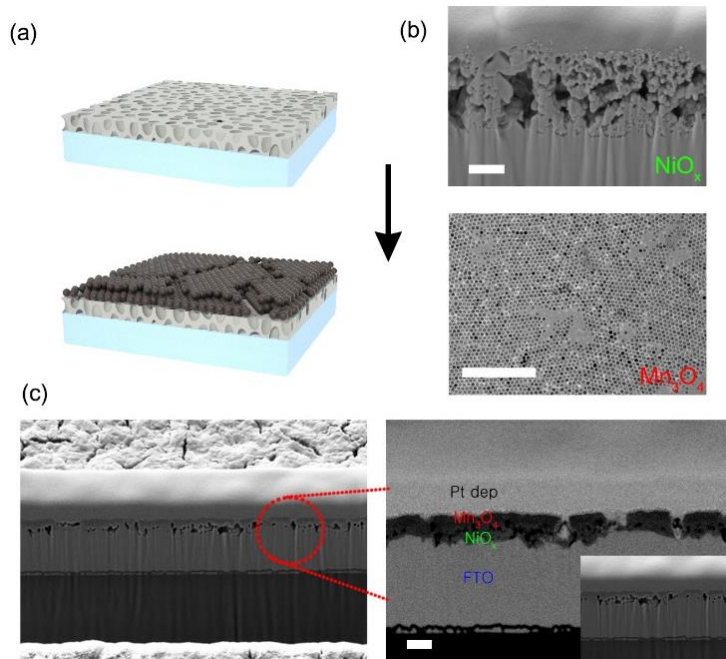


**Figure 5.1** (a) Schematic illustration of  $\text{Mn}_3\text{O}_4/\text{NiO}_x$  structure. (b, c) Morphology of  $\text{NiO}_x$  and  $\text{Mn}_3\text{O}_4$  nanoparticles. (d) ESB/SEM cross images of  $\text{Mn}_3\text{O}_4/\text{NiO}_x$ , which shows that  $\text{Mn}_3\text{O}_4$  and  $\text{NiO}_x$  catalysts are stacked in form of bi-layer structure.

## 5.3. Results and Discussions

### 5.3.1. Structural Characterization

In order to analyze the status of  $\text{Mn}_3\text{O}_4$  NPs in  $\text{Mn}_3\text{O}_4/\text{NiO}$ , HR-TEM EELS line scan were performed from the Mn/Ni interface to surface region. Fig. 5.2.c described around 100nm thickness was successfully formed on top of NiO films. We found that the bimetallic local geometries were built on the surface of the NPs through our unique process. EELS line-scans (Fig. 5.2f) show that Ni ions were diffused into the  $\text{Mn}_3\text{O}_4$  NPs. Further, we piled Mn oxide NPs up to 600nm on the Ni oxide film as a model system (Fig. 5.1g). Surprisingly, Ni peaks always appears even in the surface region of the model system. It indicates that Ni ions were diffused over the whole  $\text{Mn}_3\text{O}_4$  NPs surface. Although the exact configuration of the Ni-Mn local geometry cannot be figured out due to the detection limit of TEM imaging resolution(Fig. 5.2a), what we can estimate is that Ni ions would form single-atom poison or nano-cluster without crystallinity. We thought that the formation of Ni-Mn bimetallic local geometries resulted from the nanoparticle effects. The diffusions of Ni ions would not be possible if the film was a bulk material. Ni ions could be readily spread out over the whole area of the catalyst since there were lots of the diffusion paths along the surface of NPs. Also, the unstable surfaces inherently appear in the 10nm-scale NPs. These instabilities would act as a source to make the bimetallic local geometry.

In order to get the insight of electronic property of Ni-Mn<sub>3</sub>O<sub>4</sub>/NiO system, we compared the electronic structure of Ni-Mn<sub>3</sub>O<sub>4</sub> NPs with those of bare Mn<sub>3</sub>O<sub>4</sub> NPs (Fig. 5.3). The peak I was increased in the EEL O K-edge spectra of Ni- Mn<sub>3</sub>O<sub>4</sub> NPs (Fig. 5.3c), which indicates that charge transfer occurred from surface Mn ions to Ni ions, since EEL O K-edge spectra reflect the unoccupied density of states (DOS) (Fig. 5.3f). Also, it is the direct evidence that Ni ions are chemically bonded with the surface Mn atoms. Furthermore, Ni ions affected the surface stoichiometry of Mn<sub>3</sub>O<sub>4</sub> nanoparticle. The ratio between peak IV and V became smaller in the EEL Mn L<sub>2,3</sub>-edge spectra of Ni- Mn<sub>3</sub>O<sub>4</sub> NPs (Fig. 5.3d), where peak IV and V corresponded to Mn(II) and Mn(III) ions, respectively. This measurement indicates that the average oxidation state became larger at the Ni-hybridized surface. It also coincided with the macroscopic XAS experiments (Fig. 5.3). Ni ions located on the surface of Mn<sub>3</sub>O<sub>4</sub> nanoparticle were small changes in terms of structural aspect, but these changes would induce the electronic reconstruction at the surface of the correlated oxide NPs and tailor the catalytic properties of them. We measured EEL spectra for more than 100 sites and averaged to represent the electronic structure of each system. The procedures to make bare Mn<sub>3</sub>O<sub>4</sub> NPs are exactly same without the existence of nickel oxide underlayer.

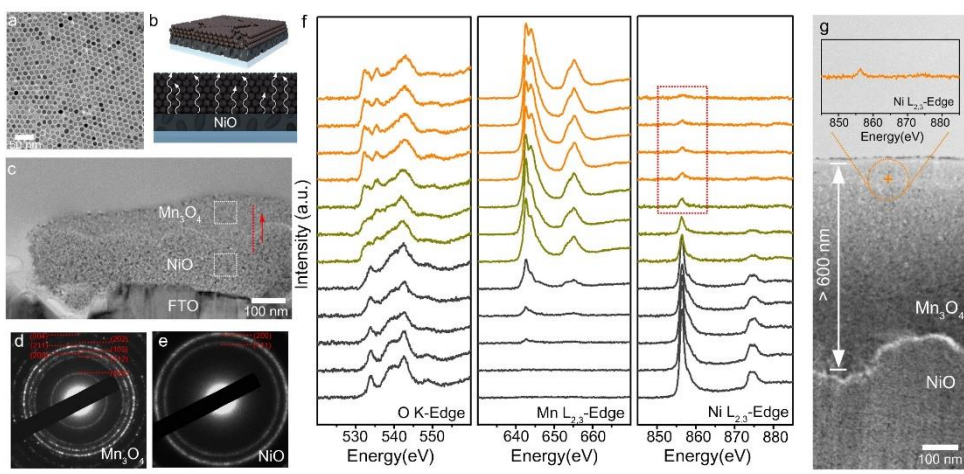


**Figure 5.2.** Structural characterization: a. Mn<sub>3</sub>O<sub>4</sub> Nanoparticles, b. scheme for fabrication c. Cross-sectional TEM image, d.e. Select area electron diffraction image f.g. O K-edge, Mn and Ni L<sub>2,3</sub> edge EELS spectra of Ni-Mn<sub>3</sub>O<sub>4</sub>/NiO structure

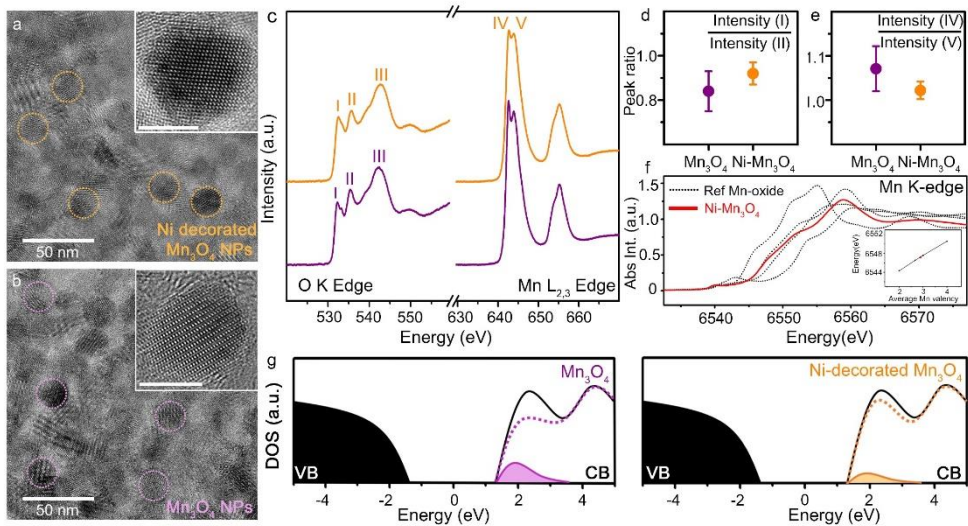


**Figure 5.3.** TEM images of (a) Ni-decorated Mn<sub>3</sub>O<sub>4</sub> nanoparticles and (b) pristine Mn<sub>3</sub>O<sub>4</sub> nanoparticles. EELS spectra (c) and relative EELS intensity comparison(d,e), XAS spectra, and proposed electronic structure of Ni-decorated Mn<sub>3</sub>O<sub>4</sub> nanoparticles and pristine Mn<sub>3</sub>O<sub>4</sub> nanoparticles

### 5.3.2. Electrochemical characterization

Electrochemical study was performed with cyclic voltammetry (CV) method. To evaluate the water oxidation activity of newly developed Mn<sub>3</sub>O<sub>4</sub>/NiO materials, films were prepared on the FTO glass substrate and appraised in both neutral and basic electrolyte. First, Figure 5.4 displayed OER performance of the Mn<sub>3</sub>O<sub>4</sub>/NiO films under near neutral condition. For comparison, we also measured activity of bare Mn<sub>3</sub>O<sub>4</sub> and NiO materials. Surprisingly, activity of hybrid Mn<sub>3</sub>O<sub>4</sub>/NiO films was more than twice as good as that of Mn<sub>3</sub>O<sub>4</sub> and NiO. Overpotential reached at 5mA/cm<sup>2</sup> requires 490 mV which means better activity compared to well-known OER catalysts based on the geometric current density criteria. Tafel analysis was performed with the polarization-corrected CV data to understand electro-kinetics of Mn<sub>3</sub>O<sub>4</sub>/NiO catalysts. Tafel slope of the Mn<sub>3</sub>O<sub>4</sub>/NiO is ~68 mV/dec which is akin to that of previously reported partially oxidized MnO nanoparticles. In addition, exchange current density value is 3.23\*10<sup>-4</sup> mA/cm<sup>2</sup>, which is higher than that of the reference materials. Similar phenomena was observed in basic condition. OER current reached at 10 mA/cm<sup>2</sup> value with 350 mV of overpotentials in case of Mn<sub>3</sub>O<sub>4</sub>/NiO. As shown in Figure 5.4b, Tafel slope was 53mV/dec and this value is comparable with that of iridium oxide and amorphous metal oxide materials. We have summarized OER activity of various catalysts in Table 5.1.

Besides of its superior activity, sustainable stability was verified. We proved durability of  $\text{Mn}_3\text{O}_4/\text{NiO}$  catalysts in various ways. To begin with, we conducted subsequent potential cycling in neutral and basic electrolyte. As shown in Figure 5.5 inset, even after 50th cycles, OER activity was remain unchanged in both condition. In order to check the long term durability of  $\text{Mn}_3\text{O}_4/\text{NiO}$ , chronoamperometry analysis was further performed. Electrolysis potential was set at the point where OER catalysis operated actively; 1.23 V (@ neutral) and 0.6 V (@ basic condition). During the total 40,000 sec of electrolysis, nearly constant current was observed, indicating high stability under OER condition.(Figure 5.5) Moreover, spectroscopic analysis, ex-situ XPS analysis was performed. After 40,000 sec of electrolysis, we compared the Mn 2p spectra of  $\text{Mn}_3\text{O}_4/\text{NiO}$  film with the one of before measurement. As expected, there was no noticeable change in its spectra.

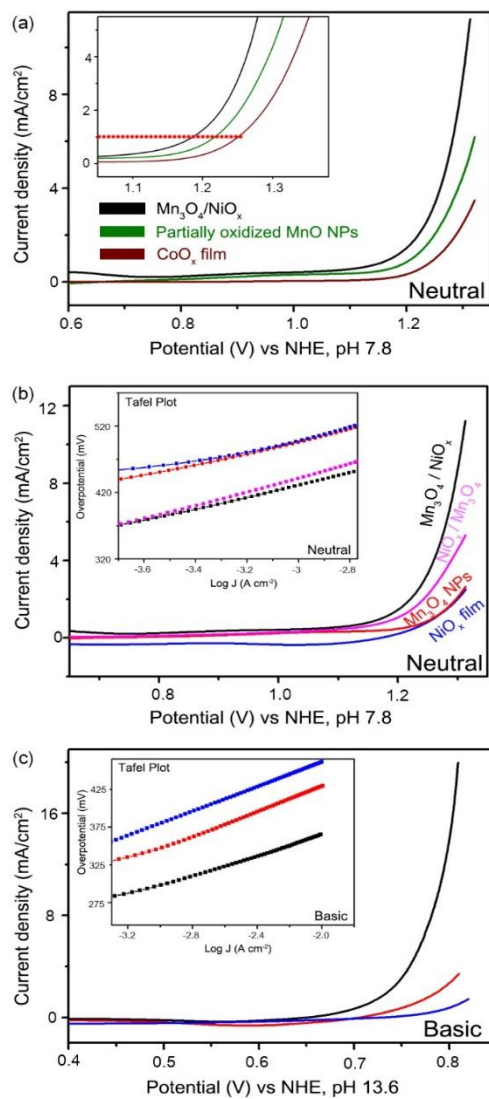


**Figure 5.4.** Electrochemical characterization. (a) Polarization-corrected curves for Mn<sub>3</sub>O<sub>4</sub>/NiO, partially oxidized MnO NPs (green), CoO<sub>x</sub> film (brown), (b) NiO/Mn<sub>3</sub>O<sub>4</sub>, Mn<sub>3</sub>O<sub>4</sub> NPs (red), and NiO<sub>x</sub> films (blue) under near neutral (c) and basic condition. Inset shows Tafel plot of Mn<sub>3</sub>O<sub>4</sub>/NiO, Mn<sub>3</sub>O<sub>4</sub> NPs and NiO<sub>x</sub> films.

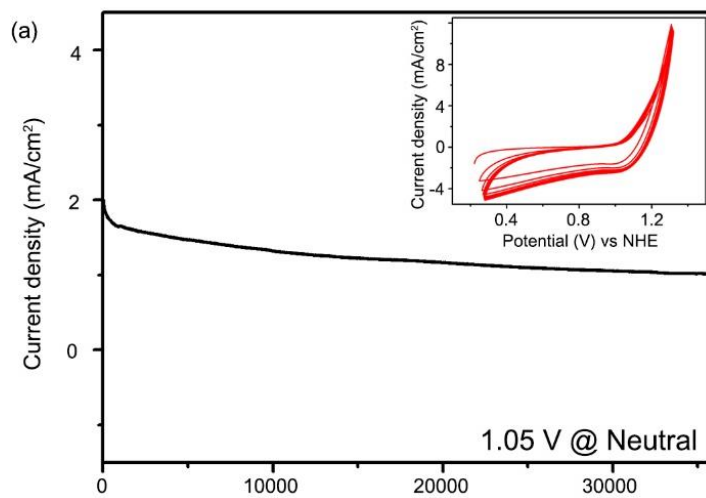
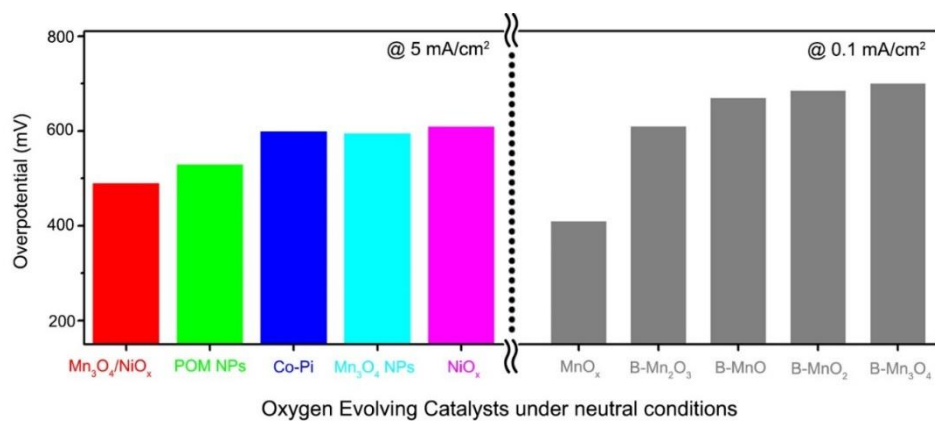


**Figure 5.5.** Sustainability test for OER electrocatalysts in neutral condition. Controlled – potential was held constant for 40,000 sec. Continuous potential cycling test was also performed (inset).

**Table 5.1.** Water oxidation efficiency comparison of various OER catalysts



### 5.3.3. Electronic structure analysis : Resting state

Further analysis of the metal valency was performed to understand the enhanced activity. First, X-ray photoelectron spectroscopy was conducted to investigate the surface state of  $\text{Mn}_3\text{O}_4/\text{NiO}$ . For comparison, commercial  $\text{Mn}_2\text{O}_3$ ,  $\text{Mn}_3\text{O}_4$  compounds was measured as reference. Figure 5.6 displayed Mn 2p spectra of each compounds. It is clearly revealed that spectra of  $\text{Mn}_3\text{O}_4/\text{NiO}$  is positively shifted compared to that of reference  $\text{Mn}_3\text{O}_4$  materials, which indicates the oxidation of Mn species certain extent. To check the formation of any secondary phase on the surface during catalysis, *ex-situ* XPS analysis was performed. As shown in Figure 5.6c, there is no observable peak shifts even after bulk electrolysis (40,000 sec).

X-ray absorption spectroscopy (XAS) analysis was performed to quantitatively evaluate the bulk oxidation state in  $\text{Mn}_3\text{O}_4/\text{NiO}$  structure. Detailed experimental procedure for XAS analysis was referenced from the our previous study. To determine average oxidation states, it was needed to analyze the standard Mn oxide materials ( $\text{MnO}$ ,  $\text{Mn}_3\text{O}_4$ ,  $\text{Mn}_2\text{O}_3$ ,  $\text{MnO}_2$ ). As shown in Figure 5.6 b,c, average Mn oxidation state could be calculated by linear combination method. XANES results were consistent with the trend observed with XPS characterization. Surprisingly, although it is confirmed that Mn phase in our system is  $\text{Mn}_3\text{O}_4$ , the average Mn valency was turned out to be 2.895 which value is higher than conventional  $\text{Mn}_3\text{O}_4$ . Provided there exists only Mn(II), Mn(III) in  $\text{Mn}_3\text{O}_4/\text{NiO}_x$  structure, Mn(III) valency

occupy in portion of 89.5%, while only 66.7% in the conventional  $\text{Mn}_3\text{O}_4$  compounds.

We have observed that OER activity of  $\text{Mn}_3\text{O}_4/\text{NiO}_x$  film is greatly enhanced compared to same thickness of Mn oxide materials in neutral or basic condition. Based on the above data, we could deduce that there exists certain synergistic effect in Mn oxide / amorphous nickel oxide system, probably regarding Mn valency, because it is safe to assume that oxygen evolution reaction preferentially occurred on the Mn oxide surface in our system.

In the preceding studies, the interaction between Mn based water oxidation catalysts and substrate metal electrodes have been investigated. Since high valency, specifically Mn(III) is beneficial to OER catalysis as outlined above, generation of Mn(III) have been tried with conventional Mn oxide system. Incorporation of gold nanoparticles into  $\text{MnO}_x$  film was revealed to act as electron acceptor from the manganese. Moreover, besides from that, there are other previously reported methods to intentionally form Mn high valency, such as chemical oxidation, chemical coupling, ligand functionalization, and so on. In most cases, final products tend to have amorphous characteristics compared to starting materials, and cannot maintain original shape and size.

In this study, we suggest another approach to make more oxidized Mn valency in the crystal structure. Via  $\text{Mn}_3\text{O}_4/\text{NiO}_x$  system, we succeeded to realize synergistic effect on water oxidation catalysis. We think that increased portion of Mn(III) species in  $\text{Mn}_3\text{O}_4/\text{NiO}_x$  catalysts is important character to elucidate its improved

performance. Supporting porous NiO<sub>x</sub> film is expected to lead the partial oxidation of Mn<sub>3</sub>O<sub>4</sub> species, forming more oxidized Mn(III) species in the structure. *Ex-situ* XANES and XPS results inferred that this unordinary phenomena is probably due to the electron transfer from manganese to nickel. Such an electron donation naturally makes exposed surface manganese more electrophilic species, and also nucleophilic OH<sup>-</sup> or H<sub>2</sub>O reactant can easily access the active Mn sites. In the previous reports, we reported that nanosized MnO NPs exhibit outperforming catalytic activity because of its defective nature, and observed Mn(III) species could stably exist during OER process. In this regard, we believe that increased Mn (III) valency in Mn<sub>3</sub>O<sub>4</sub>/NiO<sub>x</sub> structure could solely contribute the water oxidizing activity without any unexpected reaction, such as charge disproportionation process.

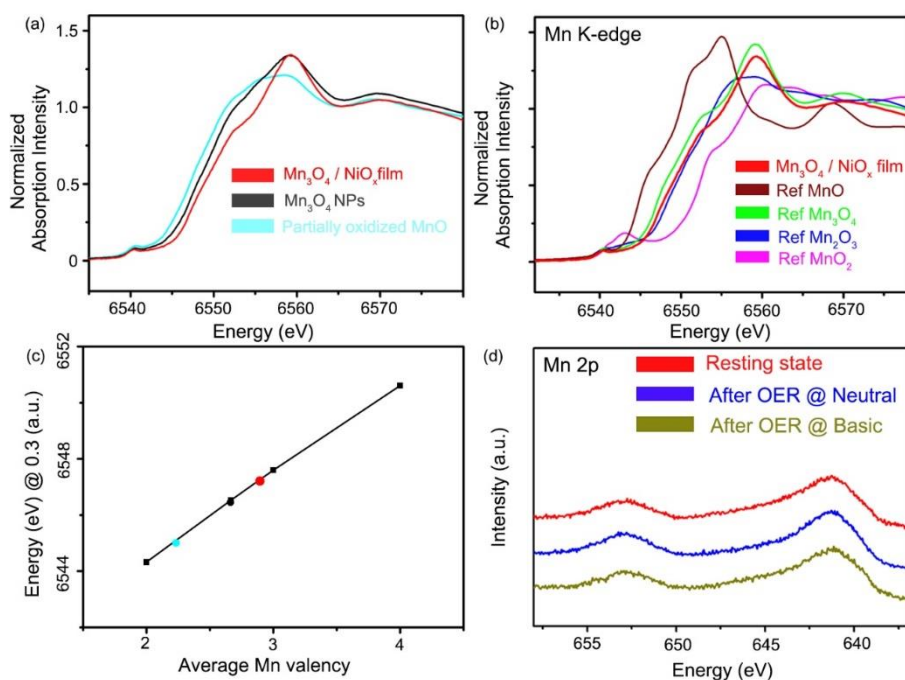


**Figure 5.6.** a,b) *Ex-situ* XANES Mn K-edge spectra and (c) Average Mn oxidation state of  $\text{Mn}_3\text{O}_4/\text{NiO}$ ,  $\text{Mn}_3\text{O}_4$  NPs, partially oxidized MnO NPs, and reference Mn oxide compounds. (d) Comparison of XPS spectra ( $\text{Mn}_3\text{O}_4/\text{NiO}$ ) for resting state and after OER test in neutral and basic conditions.

### **5.3.3. Electronic structure analysis: During Water Oxidation Catalysis**

#### **5.3.3.1. *In-situ* XANES & UV-Vis analysis**

*In-situ* XANES and UV-vis analysis of Ni-Mn<sub>3</sub>O<sub>4</sub>/NiO were conducted to track and directly monitor the change of Mn valency during the OER using an in-situ electrochemical cell. The Mn K-edge spectra of Ni-Mn<sub>3</sub>O<sub>4</sub>/NiO was recorded on an electrode during electrolysis at 1.3 V versus NHE. As shown in Fig 5.6, average Mn valency was 3.354, indicating the existence of high Mn oxidation state. Similar behavior obtained with in-situ UV-Vis experiment. Unlike MnO nanoparticle case, Ni-Mn<sub>3</sub>O<sub>4</sub>/NiO has absorption peak around 730 nm as potential increased, which can be assigned to d-d transition for Mn(IV) or Mn(V) species. In addition, more importantly, pre-edge splitting and intensity increase occurred during catalysis. Such an abnormal increase of pre-edge region indicates the geometric distortion in Ni-Mn<sub>3</sub>O<sub>4</sub>/NiO structure. We think that in Ni-Mn<sub>3</sub>O<sub>4</sub>/NiO system, largely distorted high valent Mn species are generated during catalysis.

#### **5.3.3.2. EPR analysis.**

As next step, we thoroughly investigated electronic structure of reaction intermediates in Ni-Mn<sub>3</sub>O<sub>4</sub>/NiO system. In order to observe the existing manganese species during the water electrolysis, the X-band continuous wave EPR measurements were performed according to the varying applied potentials. While

the initial Mn(II) EPR signal demonstrated typical 6-hyperfine splitting of 90 G at  $g \sim 2$ , the Mn(II) signal disappeared at 1.11 V vs. RHE and Mn(III) signal of  $A \sim 50$  G at  $g \sim 8.18$  emerged at the parallel mode. The increase in hyperfine splitting of Mn(III) from 40 to 50 G signifies the increase in the Jahn-Teller distortion within the structure. Moreover, during the oxygen evolving reaction, 6-line hyperfine splitting of  $A \sim 134$  G, width  $\sim 744$  G appeared at  $g \sim 1.85$  G together with Mn(III) signal at the parallel mode. (Fig. 5.7)

The distinctive position at  $g \sim 1.85$  has never been reported before in Mn based inorganic compounds. First of all, we checked signal decaying phenomena and found that signal at  $g \sim 1.85$  completely disappeared within 30 min after termination of electrolysis, which means that signal at  $g \sim 1.85$  comes from the reaction intermediates. In order to identify the origin of Mn status, multi-frequency EPR measurements were additionally performed. Interestingly, two separate signals at  $g \sim 2$  and  $g \sim 1.83$  were observed from the Q-band field sweep and small Mn(II) and radical signal at  $g \sim 2$  with no signal at  $g \sim 1.83$  from the W- band continuous wave and field sweep measurements. (Fig.5.7)

It should be noted that EPR signal at  $g \sim 1.85$  was realized only in 10 nm sized  $\text{Mn}_3\text{O}_4/\text{NiO}$  system. While similar behavior were observed in 5 nm  $\text{Mn}_3\text{O}_4$  NPs, only Mn(III) signal was detected in 60 nm sized or bulk one and ferromagnetic feature was observed in  $\text{Mn}_3\text{O}_4/\text{NiO}$  which is annealed at 873K.

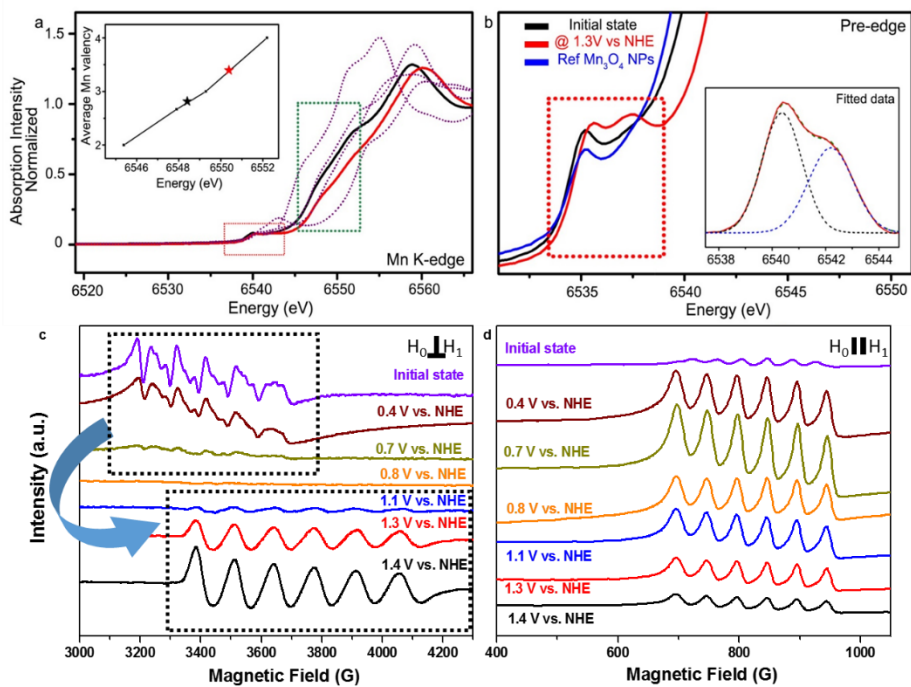


**Figure 5.7.** *In-situ* XAS spectra (a) and enlarged pre-edge region (b) of Ni-decorated  $\text{Mn}_3\text{O}_4$  nanoparticles. Potential dependent perpendicular (c) and parallel mode (d) EPR spectra of Ni-decorated  $\text{Mn}_3\text{O}_4$  nanoparticles

### 5.3.3.3. Interpretation of EPR results

To computationally determine the electronic structure of Mn species, computation study was conducted via EASYSPIN (<http://www.easyspin.org/>) method for initial state of Ni-decorated Mn<sub>3</sub>O<sub>4</sub> nanoparticles and the intermediate during OER. As shown in Fig.xx in the initial state, a characteristic S=5/2, high spin Mn(II) species were observed at g ~2 including six-line hyperfine splitting pattern of I=5/2, <sup>55</sup>Mn, which can be assigned to  $| 5/2; \pm 1/2 \rightarrow 5/2; \mp 1/2 |$ ,  $| 3/2; \pm 1/2 \rightarrow 3/2; \mp 1/2 |$ , and  $| 1/2; \pm 1/2 \rightarrow 1/2; \mp 1/2 |$ . (S=5/2, (g<sub>xx</sub>, g<sub>yy</sub>, g<sub>zz</sub>) = (2.0004 2.0007 2.0007), (A<sub>xx</sub>, A<sub>yy</sub>, A<sub>zz</sub>) = (96.8 G, 98 G, 95.5 G), D = 0.016cm<sup>-1</sup>, E/D=0.3) The integer spin S=2, Mn(III) was detected in the initial condition of Ni-Mn<sub>3</sub>O<sub>4</sub> sample in the parallel mode X-band EPR with help of pyrophosphate as Mn(III)-capturing agent (S=2, (g<sub>xx</sub>, g<sub>yy</sub>, g<sub>zz</sub>) = (2 2 1.98), A<sub>iso</sub>= 40.7 G, D = 2 cm<sup>-1</sup>, E = 0.21 cm<sup>-1</sup>, E/D=0.105).

The intermediate species of Ni-Mn<sub>3</sub>O<sub>4</sub> nanoparticles during OER are interpreted to have high spin S=2, Mn(III) with only marginal difference in hyperfine splitting (S=2, g<sub>iso</sub>= 2, A<sub>iso</sub>= 49.3 G, D = 2 cm<sup>-1</sup>, E = 0.21 cm<sup>-1</sup>, E/D=0.105). Under the expectation that the six-line new signal at g~1.85 comes from low spin S=1/2 Mn(IV) as suggested above, fitting was performed in the perpendicular mode. A calculation with parameters written as below showed very good agreement with the experimental result: S=1/2; (g<sub>xx</sub>, g<sub>yy</sub>, g<sub>zz</sub>) = (1.85 1.84 1.815); (A<sub>xx</sub>, A<sub>yy</sub>, A<sub>zz</sub>) = (121.1 G 124.3 G 127.5 G). (Figure 5.8)

As an effort to acquire the structural information of the intermediate Mn species, we further focused on the interpretation of the observed unconventional g value. Electron angular momentum has two contributions namely, spin and orbital angular momentum that are coupled by spin-orbit coupling phenomenon. It has been well documented that strong spin-orbit coupling results in the deviation of g value, according to the following equation.

$$g_{ij} = g_e \delta_{ij} + 2\lambda \sum_{m=0} \frac{\langle m | l_i | n \rangle \langle n | l_j | m \rangle}{E_n - E_m} \dots\dots\dots (1)$$

It can be simplified in one unpaired electron system.

$$g = g_0 \pm 2 \frac{n\lambda}{\Delta E} \dots\dots\dots (2)$$

Where ij are the molecular coordinate axes,  $\lambda$  is spin-orbit coupling constant,  $E_n$  is the energy of the SOMO, m is the filled and empty orbitals with energy  $E_m$  and  $l_i$  is the component of the orbital angular momentum operator.

Moreover, from so called magic pentagon diagram, values of n can be obtained for each crystal field direction. (the horizontal connections apply to  $L_z$  and the vertical connections apply to  $L_x$  and  $L_y$ ) In this regard, unexpected g value shift should be related to unique electronic structure of Mn (IV) species generated during water oxidation catalysis.

From the electrochemical study, it can be expected that before rate determining step (RDS), one electron and one proton involved proton concerted electron transfer pathway is progressed, which indicates formation of the Mn(IV)=O species from the oxidation of Mn(III)-OH. According to the previous study, when

metal oxo (M=O) bond is formed, z-axis compressed  $C_4$  crystal field is constructed. Replacing of single bond (M-O) in  $ML_6$  octahedral geometry into double bond (M=O) configuration makes shorten bonding distance which destabilize the  $a_1(d_{z^2})$  and  $e(d_{xz}, d_{yz})$  orbital and consequently distorts overall octahedral d-orbital structure. Counteractive spin pairing energy and energy gap between respective d-orbital determine the electron configuration. More importantly via the outlined equation for  $\Delta_g$ , extent of d-orbital splitting can be calculated, as follows. (Figure 5.9)

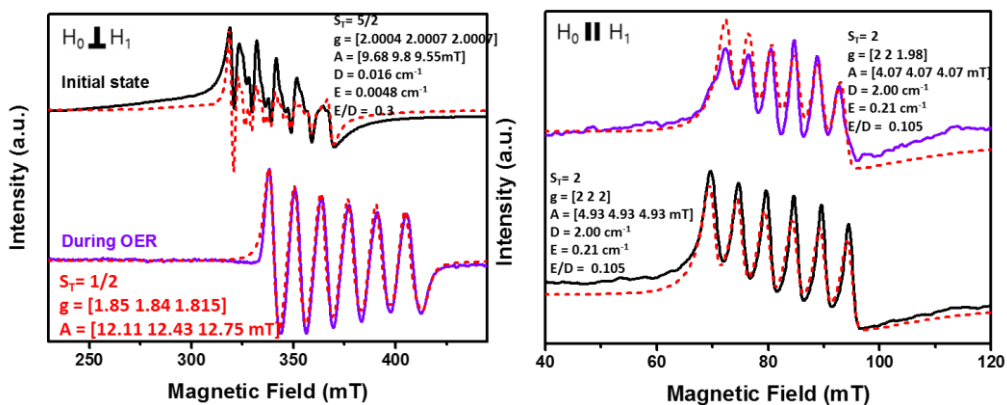


**Figure 5.8.** Simulation of EPR data (perpendicular mode :left, parallel mode: right) of initial state and catalytic active state of Ni-decorated  $\text{Mn}_3\text{O}_4$  nanoparticles. Inset displays the calculated EPR simulation parameters.

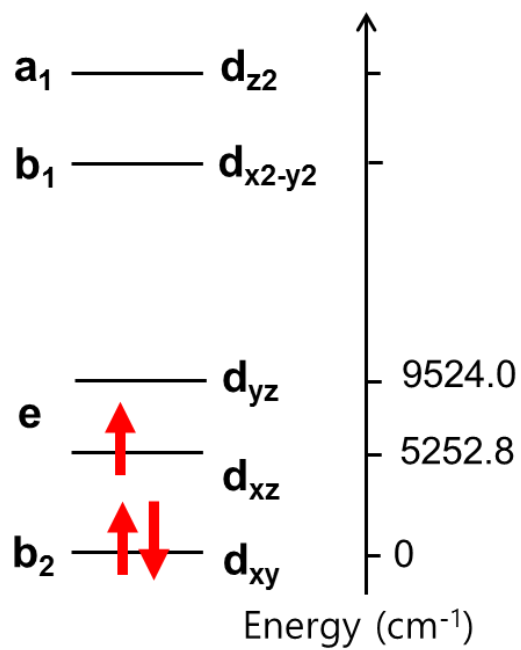


**Figure 5.9.** Proposed electronic structure for catalytic active state of Ni-decorated Mn<sub>3</sub>O<sub>4</sub> nanoparticles

## 5.4. Concluding Remarks

In conclusion, heterostructure,  $\text{Mn}_3\text{O}_4/\text{NiO}_x$  films were synthesized and its oxygen evolving activity was evaluated. Combination of electrodeposited amorphous  $\text{NiO}_x$  films and  $\text{Mn}_3\text{O}_4$  nanoparticles was first reported for OER catalysis. Sub 10 nm sized  $\text{Mn}_3\text{O}_4$  nanoparticles were monodispersed on the porous  $\text{NiO}_x$  films. Densely packed  $\text{Mn}_3\text{O}_4$  nanoparticles exhibited enhanced performance under neutral and basic condition. This earth-abundant and carbon free OER catalysts reported 10  $\text{mA}/\text{cm}^2$  with only 350mV overpotentials. Furthermore, various stability tests revealed its good catalytic durability.

More importantly, we verified that during catalytic reaction, new manganese status was realized in Ni-decorated  $\text{Mn}_3\text{O}_4$  nanoparticles. For the first time, low spin Mn(IV) species was characterized by combined spectroscopic analysis. Our results of synergistic coupling between amorphous metal oxide and crystalline metal oxide particles suggest promising design rules for effective water oxidation catalysts.

## Chapter 6. Conclusion

In Chapter 2, we have presented a new crystalline phase,  $\text{Mn}_3(\text{PO}_4)_2 \cdot 3\text{H}_2\text{O}$ , that acts as an efficient OER catalyst. We found that Mn atoms have an asymmetric geometry in the crystal and display a distorted crystal field with phosphate groups and water molecules.  $\text{Mn}_3(\text{PO}_4)_2 \cdot 3\text{H}_2\text{O}$  exhibits superior catalytic performance compared to MnO and  $\text{MnO}_2$  catalysts under neutral pH. Moreover, EPR analysis revealed the formation of  $\text{Mn}^{\text{III}}$  during catalytic cycle. DFT theoretical calculations verified the experimental observation that  $\text{Mn}^{\text{II}}$  atoms can be easily oxidized into  $\text{Mn}^{\text{III}}$  species through J-T distortion which is stabilized by its structural nature, the distorted and flexible crystal field around the Mn atoms. We expect that the discovery of this new  $\text{Mn}_3(\text{PO}_4)_2 \cdot 3\text{H}_2\text{O}$  crystal and the relationship between its structural features and catalytic performance will provide insights useful for the development of divalent Mn-based catalysts.

In Chapter 3, our studies demonstrate the possibility of a new pyrophosphate-based Mn crystal,  $\text{Li}_2\text{MnP}_2\text{O}_7$ , as an efficient water oxidation catalyst under neutral conditions for the first time. By tuning the manganese valency in  $\text{Li}_2\text{MnP}_2\text{O}_7$ , we can observe the effect of the Mn(III) state itself on water oxidation catalysis with minimal crystallographic change.  $\text{Li}_{2-x}\text{MnP}_2\text{O}_7$  compounds show catalytic stability up to 1.5 V vs NHE without additional delithiation or phase transformation ensuring us for understanding the effect of oxidation state of

manganese on water oxidation catalysis based on their catalytic activities. A higher Mn(III) content in the catalyst can boost catalytic activity by increasing the degree of distortion in local Mn environment both at the surface and the bulk  $\text{Li}_{2-x}\text{MnP}_2\text{O}_7$ . We expect that the results highlight the understanding of the effect of the Mn oxidation state on the oxygen evolution reaction and can provide valuable insight for developing a new Mn-based water oxidation catalyst. Moreover, our approach can be applied to construct the design rule for other transition metal (Co, Ni, Fe, Cu)-based water oxidation catalysts.

## References

- [1] A. Kudo, Y. Miseki, *Chemical Society Reviews* **2009**, 38, 253-278.
- [2] aD. G. Nocera, *Daedalus* **2006**, 135, 112-115; bN. S. Lewis, D. G. Nocera, *Proceedings of the National Academy of Sciences* **2006**, 103, 15729-15735; cA. J. Esswein, D. G. Nocera, *Chemical reviews* **2007**, 107, 4022-4047.
- [3] U. S. E. I. Administration., **2013**.
- [4] aP. M. Cox, R. A. Betts, C. D. Jones, S. A. Spall, I. J. Totterdell, *Nature* **2000**, 408, 184-187; bJ. R. Petit, J. Jouzel, D. Raynaud, N. I. Barkov, J. M. Barnola, I. Basile, M. Bender, J. Chappellaz, M. Davis, G. Delaygue, M. Delmotte, V. M. Kotlyakov, M. Legrand, V. Y. Lipenkov, C. Lorius, L. Pepin, C. Ritz, E. Saltzman, M. Stievenard, *Nature* **1999**, 399, 429-436; cJ. L. Sarmiento, C. Le Quéré, *Science* **1996**, 274, 1346-1350; dS. Solomon, G.-K. Plattner, R. Knutti, P. Friedlingstein, *Proceedings of the National Academy of Sciences* **2009**, 106, 1704-1709; eK. Caldeira, M. R. Rampino, *Geophysical Research Letters* **1991**, 18, 987-990.
- [5] C. Ronneau, *Energie, pollution de l'air et developpement durable*, **2004**.
- [6] L. M. Gandia, G. Arzamedi, P. M. Diéguez, *Renewable Hydrogen Technologies: Production, Purification, Storage, Applications and Safety*, Newnes, **2013**.
- [7] A. Ursua, L. M. Gandia, P. Sanchis, *Proceedings of the IEEE* **2012**, 100, 410-426.
- [8] aJ. Ivy, National Renewable Energy Lab., Golden, CO (US), **2004**; bA. Roy, Loughborough University **2006**.
- [9] R. J. Gilliam, J. W. Graydon, D. W. Kirk, S. J. Thorpe, *International Journal of Hydrogen Energy* **2007**, 32, 359-364.
- [10] J. Larminie, A. Dicks, M. S. McDonald, *Fuel cell systems explained, Vol.*

- 2, Wiley New York, **2003**.
- [11] H. Wolfschmidt, O. Paschos, U. Stimming, in *Fuel Cell Science*, John Wiley & Sons, Inc., **2010**, pp. 1-70.
- [12] B. E. Conway, G. Jerkiewicz, *Electrochimica Acta* **2000**, *45*, 4075-4083.
- [13] J. K. Nørskov, T. Bligaard, A. Logadottir, J. R. Kitchin, J. G. Chen, S. Pandelov, U. Stimming, *Journal of The Electrochemical Society* **2005**, *152*, J23-J26.
- [14] L. R. F. Allen J. Bard, *John Wiley & Sons, Inc.* **2001**, 864.
- [15] J. Tafel, *Z. phys. Chem* **1905**, *50*, 641.
- [16] B. E. Conway, B. V. Tilak, *Electrochimica Acta* **2002**, *47*, 3571-3594.
- [17] S. W. Boettcher, E. L. Warren, M. C. Putnam, E. A. Santori, D. Turner-Evans, M. D. Kelzenberg, M. G. Walter, J. R. McKone, B. S. Brunschwig, H. A. Atwater, N. S. Lewis, *Journal of the American Chemical Society* **2011**, *133*, 1216-1219.
- [18] J. R. McKone, E. L. Warren, M. J. Bierman, S. W. Boettcher, B. S. Brunschwig, N. S. Lewis, H. B. Gray, *Energy & Environmental Science* **2011**, *4*, 3573-3583.
- [19] C. Chen, Y. Kang, Z. Huo, Z. Zhu, W. Huang, H. L. Xin, J. D. Snyder, D. Li, J. A. Herron, M. Mavrikakis, M. Chi, K. L. More, Y. Li, N. M. Markovic, G. A. Somorjai, P. Yang, V. R. Stamenkovic, *Science* **2014**, *343*, 1339-1343.
- [20] L. I. K. V. I. Bystrov, *Elektrokhimiya* **1967**, *3*, 1499.
- [21] L. I. K. V. I. Bystrov, *Elektrokhimiya* **1967**, *3*, 1345.
- [22] A. L. R. A. B. Kijimnik, *Elektrokhimiya* **1970**, *6*, 330.
- [23] F. M. K. Gossner, *Z. Phys. Chem. Frankf. A.M.* **1968**, *58*, 24.
- [24] J. O. M. Bockris, I. A. Ammar, A. K. M. S. Huq, *The Journal of Physical Chemistry* **1957**, *61*, 879-886.
- [25] B. E. Conway, J. O. Bockris, apos, M., *The Journal of Chemical Physics* **1957**, *26*, 532-541.

- [26] A. K. Vijh, *The Journal of Physical Chemistry* **1968**, 72, 1148-1156.
- [27] R. J. Mannan, *Ph.D. Thesis, University of Pennsylvania* **1967**.
- [28] N. Pentland, J. O. M. Bockris, E. Sheldon, *Journal of The Electrochemical Society* **1957**, 104, 182-194.
- [29] D. J. G. Ives, S. Swaroopa, *Journal of the Chemical Society (Resumed)* **1955**, 3489-3497.
- [30] V. E. P. U. V. Palm, *Zh. Fiz. Khim.* **1964**, 38, 773.
- [31] A. L. R. A. B. Kilimnik, *Elektrokhimiya* **1969**, 5, 1235.
- [32] V. A. S. T. T. Tenno, U. V. Palm, *Proceedings 2nd Symposium on Double Layer and Adsorption on Solid Electrodes, Tartu* **1970**, 361.
- [33] A. L. V. L. P. Bicelli, M. Graziano, *Wadd Tech. Rp.* **1961**, 61.
- [34] A. B. A. L. Rotinyan, Kilimnik, E. D. Levin, *Proceedings 2nd Symposium on Double Layer and Adsorption on Solid Electrodes, Tartu.* **1970**, 321.
- [35] J. O. M. Bockris, S. Srinivasan, *Electrochimica Acta* **1964**, 9, 31-44.
- [36] W. P.-M. Z. A. Iofa, *Zh. Fiz. Khim.* **1963**, 37, 2300.
- [37] E. S. B. I.V. Kudryashov, V. L. Kirlis, *Elektrokhimiya* **1970**, 5, 737.
- [38] V. V. S. A. G. Pecherskaya, *Zh. PriM. Khim.* **1946**, 19, 1303.
- [39] B. E. Wilde, F. G. Hodge, *Electrochimica Acta* **1969**, 14, 619-627.
- [40] N. D. V. Kho Ngok Ba, *Elektrokhimiya* **1968**, 4, 990.
- [41] U. P. M. Magi, V. Past, *Uch. Zap. Tartu. Gos. Univ.* **1966**, 193, 96.
- [42] Z. A. I. S. Ya. Lanina, *Elektrokhimiya* **1969**, 5, 359.
- [43] E. J. Kelly, *Journal of The Electrochemical Society* **1965**, 112, 124-131.
- [44] M. P. U. Palm, *Uch. Zap. Tartu. Gos. Univ.* **1970**, 265, 34.
- [45] H. H. H. F. Fischer, *Z. Elektrochem.* **1956**, 54, 187.
- [46] I. A. B. A. M. Morozov, E. A. Preis, *Elektrokhimiya* **1969**, 5, 40.
- [47] L. A. S. Raicheva, *C. R. Aca. Bulg. Sci.* **1965**, 18, 1023.
- [48] J. N. Butler, M. L. Meehan, *Transactions of the Faraday Society* **1966**, 62, 3524-3534.
- [49] B. G. Dekker, M. Sluyters-Rehbach, J. H. Sluyters, *Journal of*

- Electroanalytical Chemistry and Interfacial Electrochemistry* **1969**, *21*, 137-147.
- [50] A. N. F. B. N. Kabanov, *Zh. Fiz. Khim.* **1934**, *5*, 418.
- [51] K. P. M. Z. A. Iofa, *Zh. Fiz. Khim.* **1944**, *18*, 137.
- [52] J. O. M. Bockris, R. Parsons, *Transactions of the Faraday Society* **1949**, *45*, 916-928.
- [53] D. B. Matthews, *Ph. D. Thesis, University of Pennsylvania* **1965**.
- [54] J. N. Butler, A. C. Makrides, *Transactions of the Faraday Society* **1964**, *60*, 1664-1676.
- [55] E. D. L. A. L. Rotinyan, *Elektrokhimiya* **1970**, *6*, 328.
- [56] J. N. Butler, M. Dienst, *Journal of The Electrochemical Society* **1965**, *112*, 226-232.
- [57] A. T. Petrenko, *Elektrokhimiya* **1965**, *1*, 839.
- [58] V. V. S. I. V. Gamali, *Zh. Prikl. Khim* **1962**, *35*, 127.
- [59] A. L. R. N. M. Kozhevnikova, *Elektrokhimiya* **1965**, *1*, 664.
- [60] Z. A. I. E. I. Mikhailova, *Elektrokhimiya* **1965**, *1*, 107.
- [61] A. K. M. S. Huq, A. J. Rosenberg, *Journal of The Electrochemical Society* **1964**, *111*, 270-278.
- [62] A. T. Kuhn, P. M. Wright, *Journal of Electroanalytical Chemistry and Interfacial Electrochemistry* **1970**, *27*, 319-323.
- [63] G. V. A. D. K. Avdeyev, Y. V. Durin, *Proceedings 2nd Symposium on Double Layer and Adsorption on Solid Electrodes, Tartu* **1970**, *58*.
- [64] H. Shiratori, *Denki Kagaku* **1961**, *27*.
- [65] B. E. Conway, *Proceedings of the Royal Society of London. Series A. Mathematical and Physical Sciences* **1960**, *256*, 128-144.
- [66] V. V. S. A. G. Pecherskaya, *Zh. Fiz. Khim.* **1950**, *24*, 856.
- [67] V. P. K. Punning, *Uch. Zap. Tartu. Gos. Univ.* **1969**, *235*, 35.
- [68] P. Rüetschi, B. D. Cahan, *Journal of The Electrochemical Society* **1957**, *104*, 406-413.

- [69] J. P. Hoare, S. Schuldiner, *The Journal of Chemical Physics* **1956**, 25, 786-787.
- [70] D. Galizzioli, *Thesis, University of Milan* **1969**.
- [71] A. T. Petrenko, *Zh. Fiz. Khim.* **1962**, 36, 1527.
- [72] N. T. Thomas, K. Nobe, *Journal of The Electrochemical Society* **1970**, 117, 622-626.
- [73] N. Hackerman, C. D. Hall, *Journal of The Electrochemical Society* **1954**, 101, 321-327.
- [74] A. N. D. O. L. Kabanova, *Elektrokhimiya* **1970**, 6, 222.
- [75] L. A. M. Ya. M. Kolotyркиn, *Zh. Fiz. Khim.* **1951**, 25, 1365.
- [76] J. O. M. Bockris, R. Parsons, *Transactions of the Faraday Society* **1948**, 44, 860-872.
- [77] N. P. F. A. L. Rotinyan, Li Un Sok, *Zh. Fiz. Khim.* **1957**, 31, 1295.
- [78] B. S. K. V. L. Kheifets, A. L. Rotinyan, *Elektrokhimiya* **1970**, 6, 1959.
- [79] A. N. Frumkin, *Advances in Electrochemistry and Electrochemical Engineering* **1969**, 3.
- [80] K. Gossner, *Z. Phys. Chem. Frankf. A.M.* **1963**, 36, 392.
- [81] S. Schuldiner, *Journal of The Electrochemical Society* **1952**, 99, 488-494.
- [82] S. Schuldiner, *Journal of The Electrochemical Society* **1954**, 101, 426-432.
- [83] S. Schuldiner, *Journal of The Electrochemical Society* **1959**, 106, 891-895.
- [84] R. K. Shervedani, A. Lasia, *Journal of The Electrochemical Society* **1998**, 145, 2219-2225.
- [85] J. Choi, Y. Qu, M. Hoffmann, *Journal of Nanoparticle Research* **2012**, 14, 1-12.
- [86] I. M. Kodintsev, S. Trasatti, *Electrochimica Acta* **1994**, 39, 1803-1808.
- [87] J. Kibsgaard, T. F. Jaramillo, F. Besenbacher, *Nat Chem* **2014**, 6, 248-253.
- [88] D. Voiry, M. Salehi, R. Silva, T. Fujita, M. Chen, T. Asefa, V. B. Shenoy, G. Eda, M. Chhowalla, *Nano Letters* **2013**, 13, 6222-6227.
- [89] V. Damien, Y. Hisato, L. Junwen, S. Rafael, C. B. A. Diego, F. Takeshi, C.

- Mingwei, A. Tewodros, B. S. Vivek, E. Goki, C. Manish, *Nature Materials* **2013**, *12*, 850-855.
- [90] F. Harnisch, G. Sievers, U. Schröder, *Applied Catalysis B: Environmental* **2009**, *89*, 455-458.
- [91] D. Kong, H. Wang, Z. Lu, Y. Cui, *Journal of the American Chemical Society* **2014**, *136*, 4897-4900.
- [92] B. Cao, G. M. Veith, J. C. Neufeind, R. R. Adzic, P. G. Khalifah, *Journal of the American Chemical Society* **2013**, *135*, 19186-19192.
- [93] Y. Sun, C. Liu, D. C. Grauer, J. Yano, J. R. Long, P. Yang, C. J. Chang, *Journal of the American Chemical Society* **2013**, *135*, 17699-17702.
- [94] Z. Wu, B. Fang, Z. Wang, C. Wang, Z. Liu, F. Liu, W. Wang, A. Alfantazi, D. Wang, D. P. Wilkinson, *ACS Catalysis* **2013**, *3*, 2101-2107.
- [95] B. Seger, A. B. Laursen, P. C. K. Vesborg, T. Pedersen, O. Hansen, S. Dahl, I. Chorkendorff, *Angewandte Chemie International Edition* **2012**, *51*, 9128-9131.
- [96] J. D. Benck, Z. Chen, L. Y. Kuritzky, A. J. Forman, T. F. Jaramillo, *ACS Catalysis* **2012**, *2*, 1916-1923.
- [97] D. H. Youn, S. Han, J. Y. Kim, J. Y. Kim, H. Park, S. H. Choi, J. S. Lee, *ACS Nano* **2014**, *8*, 5164-5173.
- [98] W. F. Chen, C. H. Wang, K. Sasaki, N. Marinkovic, W. Xu, J. T. Muckerman, Y. Zhu, R. R. Adzic, *Energy & Environmental Science* **2013**, *6*, 943-951.
- [99] A. B. Laursen, T. Pedersen, P. Malacrida, B. Seger, O. Hansen, P. C. K. Vesborg, I. Chorkendorff, *Physical Chemistry Chemical Physics* **2013**, *15*, 20000-20004.
- [100] A. B. Laursen, P. C. K. Vesborg, I. Chorkendorff, *Chemical Communications* **2013**, *49*, 4965-4967.
- [101] H. Vrubel, D. Merki, X. Hu, *Energy & Environmental Science* **2012**, *5*, 6136-6144.

- [102] D. Merki, S. Fierro, H. Vrubel, X. Hu, *Chemical Science* **2011**, *2*, 1262-1267.
- [103] T. F. Jaramillo, K. P. Jørgensen, J. Bonde, J. H. Nielsen, S. Horch, I. Chorkendorff, *Science* **2007**, *317*, 100-102.
- [104] M. A. Lukowski, A. S. Daniel, F. Meng, A. Forticaux, L. Li, S. Jin, *Journal of the American Chemical Society* **2013**, *135*, 10274-10277.
- [105] T. F. Jaramillo, J. Bonde, J. Zhang, B.-L. Ooi, K. Andersson, J. Ulstrup, I. Chorkendorff, *The Journal of Physical Chemistry C* **2008**, *112*, 17492-17498.
- [106] Y. Li, H. Wang, L. Xie, Y. Liang, G. Hong, H. Dai, *Journal of the American Chemical Society* **2011**, *133*, 7296-7299.
- [107] X. Ge, L. Chen, L. Zhang, Y. Wen, A. Hirata, M. Chen, *Advanced Materials* **2014**, *26*, 3100-3104.
- [108] Z. Chen, D. Cummins, B. N. Reinecke, E. Clark, M. K. Sunkara, T. F. Jaramillo, *Nano Letters* **2011**, *11*, 4168-4175.
- [109] J. Kibsgaard, Z. Chen, B. N. Reinecke, T. F. Jaramillo, *Nat Mater* **2012**, *11*, 963-969.
- [110] W.-F. Chen, K. Sasaki, C. Ma, A. I. Frenkel, N. Marinkovic, J. T. Muckerman, Y. Zhu, R. R. Adzic, *Angewandte Chemie International Edition* **2012**, *51*, 6131-6135.
- [111] H. Wang, Z. Lu, D. Kong, J. Sun, T. M. Hymel, Y. Cui, *ACS Nano* **2014**, *8*, 4940-4947.
- [112] K. Novoselov, A. K. Geim, S. Morozov, D. Jiang, M. K. I. Grigorieva, S. Dubonos, A. Firsov, *Nature* **2005**, *438*, 197-200.
- [113] aY. Liang, Y. Li, H. Wang, J. Zhou, J. Wang, T. Regier, H. Dai, *Nature Mater.* **2011**, *10*, 780-786; bJ.-D. Qiu, G.-C. Wang, R.-P. Liang, X.-H. Xia, H.-W. Yu, *J. Phys. Chem. C* **2011**, *115*, 15639-15645; cQ. Xiang, J. Yu, M. Jaroniec, *Chem. Soc. Rev.* **2012**, *41*, 782-796.
- [114] U. Sim, T.-Y. Yang, J. Moon, J. An, J. Hwang, J.-H. Seo, J. Lee, K. Y.

- Kim, J. Lee, S. Han, B. H. Hong, K. T. Nam, *Energy Environ. Sci.* **2013**, *6*, 3658-3664.
- [115] Y. Zheng, Y. Jiao, L. H. Li, T. Xing, Y. Chen, M. Jaroniec, S. Z. Qiao, *ACS Nano* **2014**.
- [116] Y. Zheng, Y. Jiao, L. H. Li, T. Xing, Y. Chen, M. Jaroniec, S. Z. Qiao, *ACS Nano* **2014**, *8*, 5290-5296.
- [117] Y. Zheng, Y. Jiao, Y. Zhu, L. H. Li, Y. Han, Y. Chen, A. Du, M. Jaroniec, S. Z. Qiao, *Nat Commun* **2014**, *5*.
- [118] A. J. Bard, L. R. Faulkner, *Electrochemical methods: fundamentals and applications, Vol. 2*, Wiley New York, **1980**.
- [119] H. E. Zittel, F. J. Miller, *Analytical Chemistry* **1965**, *37*, 200-203.
- [120] aM. G. Walter, E. L. Warren, J. R. McKone, S. W. Boettcher, Q. Mi, E. A. Santori, N. S. Lewis, *Chemical Reviews* **2010**, *110*, 6446-6473; bA. J. Bard, M. A. Fox, *Accounts of Chemical Research* **1995**, *28*, 141-145; cD. Gust, T. A. Moore, A. L. Moore, *Accounts of Chemical Research* **2009**, *42*, 1890-1898; dJ. R. Swierk, T. E. Mallouk, *Chemical Society Reviews* **2013**, *42*, 2357-2387; eM. Gratzel, *Nature* **2001**, *414*, 338-344; fT. J. Meyer, *Accounts of Chemical Research* **1989**, *22*, 163-170; gJ. Barber, *Chemical Society Reviews* **2009**, *38*, 185-196; hT. A. Faunce, W. Lubitz, A. W. Rutherford, D. MacFarlane, G. F. Moore, P. Yang, D. G. Nocera, T. A. Moore, D. H. Gregory, S. Fukuzumi, K. B. Yoon, F. A. Armstrong, M. R. Wasielewski, S. Styring, *Energy & Environmental Science* **2013**, *6*, 695-698.
- [121] aB. Loll, J. Kern, W. Saenger, A. Zouni, J. Biesiadka, *Nature* **2005**, *438*, 1040-1044; bJ. Yano, J. Kern, K. Sauer, M. J. Latimer, Y. Pushkar, J. Biesiadka, B. Loll, W. Saenger, J. Messinger, A. Zouni, V. K. Yachandra, *Science* **2006**, *314*, 821-825; cK. N. Ferreira, T. M. Iverson, K. Maghlaoui, J. Barber, S. Iwata, *Science* **2004**, *303*, 1831-1838; dY. Umena, K. Kawakami, J.-R. Shen, N. Kamiya, *Nature* **2011**, *473*, 55-60; eT. A.

- Roelofs, W. Liang, M. J. Latimer, R. M. Cinco, A. Rompel, J. C. Andrews, K. Sauer, V. K. Yachandra, M. P. Klein, *Proceedings of the National Academy of Sciences* **1996**, *93*, 3335-3340; fH. Dau, L. Iuzzolino, J. Dittmer, *Biochimica et Biophysica Acta (BBA) - Bioenergetics* **2001**, *1503*, 24-39.
- [122] Y. Tachibana, L. Vayssieres, J. R. Durrant, *Nat Photon* **2012**, *6*, 511-518.
- [123] aM. W. Kanan, D. G. Nocera, *Science* **2008**, *321*, 1072-1075; bT. A. Betley, Q. Wu, T. Van Voorhis, D. G. Nocera, *Inorganic Chemistry* **2008**, *47*, 1849-1861.
- [124] A. Fujishima, K. Honda, *Nature* **1972**, *238*, 37-38.
- [125] I. C. Man, H.-Y. Su, F. Calle-Vallejo, H. A. Hansen, J. I. Martínez, N. G. Inoglu, J. Kitchin, T. F. Jaramillo, J. K. Nørskov, J. Rossmeisl, *ChemCatChem* **2011**, *3*, 1159-1165.
- [126] aP. Rasiyah, A. C. C. Tseung, *Journal of The Electrochemical Society* **1984**, *131*, 803-808; bS. Trasatti, *Electrochimica Acta* **1984**, *29*, 1503-1512; cJ. O. Bockris, T. Otagawa, *The Journal of Physical Chemistry* **1983**, *87*, 2960-2971; dJ. Suntivich, K. J. May, H. A. Gasteiger, J. B. Goodenough, Y. Shao-Horn, *Science* **2011**, *334*, 1383-1385.
- [127] R. D. L. Smith, M. S. Prévot, R. D. Fagan, Z. Zhang, P. A. Sedach, M. K. J. Siu, S. Trudel, C. P. Berlinguette, *Science* **2013**, *340*, 60-63.
- [128] E. Gileadi, *Electrode Kinetics for Chemists, Chemical Engineers, and Materials Scientists*, wiley, **1993**.
- [129] S.-Y. Huang, P. Ganesan, W. S. Jung, N. Cadirov, B. N. Popov, *ECS Transactions* **2010**, *33*, 1979-1987.
- [130] Y. Matsumoto, E. Sato, *Materials Chemistry and Physics* **1986**, *14*, 397-426.
- [131] aW. J. Youngblood, S.-H. A. Lee, Y. Kobayashi, E. A. Hernandez-Pagan, P. G. Hoertz, T. A. Moore, A. L. Moore, D. Gust, T. E. Mallouk, *Journal of the American Chemical Society* **2009**, *131*, 926-927; bF. Liu, J. J.

- Concepcion, J. W. Jurss, T. Cardolaccia, J. L. Templeton, T. J. Meyer, *Inorganic Chemistry* **2008**, *47*, 1727-1752; cL. Duan, F. Bozoglian, S. Mandal, B. Stewart, T. Privalov, A. Llobet, L. Sun, *Nat Chem* **2012**, *4*, 418-423; dY. Zhao, J. R. Swierk, J. D. Megiatto, B. Sherman, W. J. Youngblood, D. Qin, D. M. Lentz, A. L. Moore, T. A. Moore, D. Gust, T. E. Mallouk, *Proceedings of the National Academy of Sciences* **2012**, *109*, 15612-15616; eM. W. Kanan, J. Yano, Y. Surendranath, M. Dincă, V. K. Yachandra, D. G. Nocera, *Journal of the American Chemical Society* **2010**, *132*, 13692-13701.
- [132] aM. Gong, Y. Li, H. Wang, Y. Liang, J. Z. Wu, J. Zhou, J. Wang, T. Regier, F. Wei, H. Dai, *Journal of the American Chemical Society* **2013**, *135*, 8452-8455; bC. C. L. McCrory, S. Jung, J. C. Peters, T. F. Jaramillo, *Journal of the American Chemical Society* **2013**, *135*, 16977-16987; cM. Yagi, M. Kaneko, *Chemical Reviews* **2000**, *101*, 21-36; dM.-T. Zhang, Z. Chen, P. Kang, T. J. Meyer, *Journal of the American Chemical Society* **2013**, *135*, 2048-2051; eD. K. Zhong, M. Cornuz, K. Sivula, M. Gratzel, D. R. Gamelin, *Energy & Environmental Science* **2011**, *4*, 1759-1764; fD. K. Zhong, S. Choi, D. R. Gamelin, *Journal of the American Chemical Society* **2011**, *133*, 18370-18377; gC. Du, X. Yang, M. T. Mayer, H. Hoyt, J. Xie, G. McMahon, G. Bischooping, D. Wang, *Angewandte Chemie International Edition* **2013**, *52*, 12692-12695.
- [133] Z. Chen, T. J. Meyer, *Angewandte Chemie International Edition* **2013**, *52*, 700-703.
- [134] M. Dincă, Y. Surendranath, D. G. Nocera, *Proceedings of the National Academy of Sciences* **2010**, *107*, 10337-10341.
- [135] J. A. Seabold, K.-S. Choi, *Journal of the American Chemical Society* **2012**, *134*, 2186-2192.
- [136] aR. K. Hocking, R. Brimblecombe, L.-Y. Chang, A. Singh, M. H. Cheah, C. Glover, W. H. Casey, L. Spiccia, *Nat Chem* **2011**, *3*, 461-466; bW. F.

- Ruettinger, D. M. Ho, G. C. Dismukes, *Inorganic Chemistry* **1999**, *38*, 1036-1037; cJ. S. Kanady, E. Y. Tsui, M. W. Day, T. Agapie, *Science* **2011**, *333*, 733-736; dE. Y. Tsui, R. Tran, J. Yano, T. Agapie, *Nat Chem* **2013**, *5*, 293-299; eM. M. Najafpour, T. Ehrenberg, M. Wiechen, P. Kurz, *Angewandte Chemie International Edition* **2010**, *49*, 2233-2237; fR. Brimblecombe, D. R. J. Kolling, A. M. Bond, G. C. Dismukes, G. F. Swiegers, L. Spiccia, *Inorganic Chemistry* **2009**, *48*, 7269-7279.
- [137] aM. Fekete, R. K. Hocking, S. L. Y. Chang, C. Italiano, A. F. Patti, F. Arena, L. Spiccia, *Energy & Environmental Science* **2013**, *6*, 2222-2232; bF. Jiao, H. Frei, *Chemical Communications* **2010**, *46*, 2920-2922; cY. Gorlin, T. F. Jaramillo, *Journal of the American Chemical Society* **2010**, *132*, 13612-13614; dI. Zaharieva, P. Chernev, M. Risch, K. Klingan, M. Kohlhoff, A. Fischer, H. Dau, *Energy & Environmental Science* **2012**, *5*, 7081-7089.
- [138] D. M. Robinson, Y. B. Go, M. Greenblatt, G. C. Dismukes, *Journal of the American Chemical Society* **2010**, *132*, 11467-11469.
- [139] A. Indra, P. W. Menezes, I. Zaharieva, E. Baktash, J. Pfrommer, M. Schwarze, H. Dau, M. Driess, *Angewandte Chemie International Edition* **2013**, *52*, 13206-13210.
- [140] T. Takashima, K. Hashimoto, R. Nakamura, *Journal of the American Chemical Society* **2012**, *134*, 18153-18156.
- [141] D. M. Robinson, Y. B. Go, M. Mui, G. Gardner, Z. Zhang, D. Mastrogiovanni, E. Garfunkel, J. Li, M. Greenblatt, G. C. Dismukes, *Journal of the American Chemical Society* **2013**, *135*, 3494-3501.
- [142] N. Birkner, S. Nayeri, B. Pashaei, M. M. Najafpour, W. H. Casey, A. Navrotsky, *Proceedings of the National Academy of Sciences* **2013**, *110*, 8801-8806.
- [143] E. Tsuji, A. Imanishi, K.-i. Fukui, Y. Nakato, *Electrochimica Acta* **2011**, *56*, 2009-2016.

- [144] L. Ouattara, S. Fierro, O. Frey, M. Koudelka, C. Comninellis, *J Appl Electrochem* **2009**, *39*, 1361-1367.
- [145] S. Trasatti, *Electrodes of conductive metallic oxides*, Elsevier, Amsterdam [etc.], **1981**.
- [146] C. Iwakura, A. Honji, H. Tamura, *Electrochimica Acta* **1981**, *26*, 1319-1326.
- [147] B. Cui, H. Lin, J.-B. Li, X. Li, J. Yang, J. Tao, *Advanced Functional Materials* **2008**, *18*, 1440-1447.
- [148] M.-R. Gao, Y.-F. Xu, J. Jiang, Y.-R. Zheng, S.-H. Yu, *Journal of the American Chemical Society* **2012**, *134*, 2930-2933.
- [149] H. B. Suffredini, J. L. Cerne, F. C. Crnkovic, S. A. S. Machado, L. A. Avaca, *International Journal of Hydrogen Energy* **2000**, *25*, 415-423.
- [150] K. Jin, J. Park, J. Lee, K. D. Yang, G. K. Pradhan, U. Sim, D. Jeong, H. L. Jang, S. Park, D. Kim, N.-E. Sung, S. H. Kim, S. Han, K. T. Nam, *Journal of the American Chemical Society* **2014**, *136*, 7435-7443.
- [151] J. Park, H. Kim, K. Jin, B. J. Lee, Y.-S. Park, H. Kim, I. Park, K. D. Yang, H.-Y. Jeong, J. Kim, K. T. Hong, H. W. Jang, K. Kang, K. T. Nam, *Journal of the American Chemical Society* **2014**, *136*, 4201-4211.
- [152] Y. Surendranath, M. W. Kanan, D. G. Nocera, *Journal of the American Chemical Society* **2010**, *132*, 16501-16509.
- [153] R. D. L. Smith, M. S. Prévot, R. D. Fagan, S. Trudel, C. P. Berlinguette, *Journal of the American Chemical Society* **2013**, *135*, 11580-11586.
- [154] A. C. Tavares, M. A. M. Cartaxo, M. I. da Silva Pereira, F. M. Costa, *J Solid State Electrochem* **2001**, *5*, 57-67.
- [155] Z. Chen, T. F. Jaramillo, T. G. Deutsch, A. Kleiman-Shwarsstein, A. J. Forman, N. Gaillard, R. Garland, K. Takanabe, C. Heske, M. Sunkara, *Journal of Materials Research* **2010**, *25*, 3-16.
- [156] A. J. Nozik, R. Memming, *The Journal of Physical Chemistry* **1996**, *100*, 13061-13078.

- [157] L. C. Seitz, Z. Chen, A. J. Forman, B. A. Pinaud, J. D. Benck, T. F. Jaramillo, *ChemSusChem* **2014**, *7*, 1372-1385.
- [158] J. Oh, T. G. Deutsch, H.-C. Yuan, H. M. Branz, *Energy & Environmental Science* **2011**, *4*, 1690-1694.
- [159] Y. Hou, B. L. Abrams, P. C. Vesborg, M. E. Björketun, K. Herbst, L. Bech, A. M. Setti, C. D. Damsgaard, T. Pedersen, O. Hansen, *Nature materials* **2011**, *10*, 434-438.
- [160] A. Heller, *Accounts of Chemical Research* **1981**, *14*, 154-162.
- [161] O. Khaselev, J. A. Turner, *Science* **1998**, *280*, 425-427.
- [162] M. H. Lee, K. Takei, J. Zhang, R. Kapadia, M. Zheng, Y. Z. Chen, J. Nah, T. S. Matthews, Y. L. Chueh, J. W. Ager, *Angewandte Chemie* **2012**, *124*, 10918-10922.
- [163] D. Yokoyama, T. Minegishi, K. Maeda, M. Katayama, J. Kubota, A. Yamada, M. Konagai, K. Domen, *Electrochemistry Communications* **2010**, *12*, 851-853.
- [164] D. Yokoyama, T. Minegishi, K. Jimbo, T. Hisatomi, G. Ma, M. Katayama, J. Kubota, H. Katagiri, K. Domen, *Applied physics express* **2010**, *3*, 101202.
- [165] G. Ma, T. Minegishi, D. Yokoyama, J. Kubota, K. Domen, *Chemical Physics Letters* **2011**, *501*, 619-622.
- [166] J. Kim, T. Minegishi, J. Kobota, K. Domen, *Energy Environ. Sci.* **2012**, *5*, 6368-6374.
- [167] A. Paracchino, V. Laporte, K. Sivula, M. Grätzel, E. Thimsen, *Nature Mater.* **2011**, *10*, 456-461.
- [168] C. G. Morales-Guio, S. D. Tilley, H. Vrubel, M. Grätzel, X. Hu, *Nature communications* **2014**, *5*.
- [169] F. F. Abdi, L. Han, A. H. Smets, M. Zeman, B. Dam, R. van de Krol, *Nature communications* **2013**, *4*.
- [170] A. Fujishima, *nature* **1972**, *238*, 37-38.

- [171] Q. Peng, B. Kalanyan, P. G. Hoertz, A. Miller, D. H. Kim, K. Hanson, L. Alibabaei, J. Liu, T. J. Meyer, G. N. Parsons, *Nano letters* **2013**, *13*, 1481-1488.
- [172] X. Liu, F. Wang, Q. Wang, *Physical Chemistry Chemical Physics* **2012**, *14*, 7894-7911.
- [173] J. Su, L. Guo, S. Yoriya, C. A. Grimes, *Crystal Growth & Design* **2009**, *10*, 856-861.
- [174] S. D. Tilley, M. Cornuz, K. Sivula, M. Grätzel, *Angewandte Chemie* **2010**, *122*, 6549-6552.
- [175] C. Janáky, K. Rajeshwar, N. De Tacconi, W. Chanmanee, M. Huda, *Catalysis Today* **2013**, *199*, 53-64.
- [176] Y. Park, K. J. McDonald, K.-S. Choi, *Chemical Society Reviews* **2013**, *42*, 2321-2337.
- [177] K. Sivula, F. Le Formal, M. Grätzel, *ChemSusChem* **2011**, *4*, 432-449.
- [178] D. K. Zhong, S. Choi, D. R. Gamelin, *Journal of the American Chemical Society* **2011**, *133*, 18370-18377.
- [179] W. Luo, Z. Li, T. Yu, Z. Zou, *The Journal of Physical Chemistry C* **2012**, *116*, 5076-5081.
- [180] S. P. Berglund, A. J. Rettie, S. Hoang, C. B. Mullins, *Physical Chemistry Chemical Physics* **2012**, *14*, 7065-7075.
- [181] T. W. Kim, K.-S. Choi, *Science* **2014**, *343*, 990-994.
- [182] I. Cesar, A. Kay, J. A. Gonzalez Martinez, M. Grätzel, *Journal of the American Chemical Society* **2006**, *128*, 4582-4583.
- [183] Y.-S. Hu, A. Kleiman-Shwarsctein, A. J. Forman, D. Hazen, J.-N. Park, E. W. McFarland, *Chemistry of Materials* **2008**, *20*, 3803-3805.
- [184] A. Kleiman-Shwarsctein, Y.-S. Hu, A. J. Forman, G. D. Stucky, E. W. McFarland, *The Journal of Physical Chemistry C* **2008**, *112*, 15900-15907.
- [185] A. Kleiman-Shwarsctein, M. N. Huda, A. Walsh, Y. Yan, G. D. Stucky, Y.-S. Hu, M. M. Al-Jassim, E. W. McFarland, *Chemistry of Materials*

**2009**, 22, 510-517.

- [186] J. Y. Kim, G. Magesh, D. H. Youn, J.-W. Jang, J. Kubota, K. Domen, J. S. Lee, *Scientific reports* **2013**, 3.
- [187] Y. W. Chen, J. D. Prange, S. Dühnen, Y. Park, M. Gunji, C. E. Chidsey, P. C. McIntyre, *Nature Mater.* **2011**, 10, 539-544.
- [188] M. J. Kenney, M. Gong, Y. Li, J. Z. Wu, J. Feng, M. Lanza, H. Dai, *Science* **2013**, 342, 836-840.
- [189] G. Lin, M. Kapur, R. Kainthla, J. M. Bockris, *Applied Physics Letters* **1989**, 55, 386-387.
- [190] S. Y. Reece, J. A. Hamel, K. Sung, T. D. Jarvi, A. J. Esswein, J. J. Pijpers, D. G. Nocera, *Science* **2011**, 334, 645-648.

## 국 문 초 록

현대 사회는 화석연료의 고갈과 에너지 소비의 급증으로 인해 에너지 위기시대에 봉착하였다. 여러가지 대체 에너지 자원에 대한 연구가 활발히 진행되는 가운데, 수소 에너지는 에너지원의 환경친화적 특성과 높은 에너지 효율로 인해 최근 각광을 받고 있다. 특히, 기존 가스 개질방법을 통한 수소 생산 방식에서 벗어난, 전기화학적으로 수소를 생산하는 방법은 진정한 의미의 친환경적 에너지 생산방법론이라 할 수 있다. 전체 물 분해 반응 중, 음극에서 일어나는 물 산화를 통한 산소발생반응은 전체 반응의 속도 결정단계로 작용한다. 따라서 음극에 적용할 수 있는 값싸고 효율 좋은 촉매 개발의 필요성이 대두되고 있다.

한편, 자연계 식물 안, 광계에는 칼슘과 망간만으로 이루어진, 물 산화 촉매 유기물이 존재한다. 놀랍게도 자연계 촉매는 현재까지 보고된 어떠한 합성 촉매보다도 높은 특성을 지니고 있다. 이에 영감을 받아, 수많은 연구진들이 이 자연계 시스템을 모방한 산소발생 촉매 개발에 초점을 맞추고 있다. 하지만 예상과는 다르게 자연계 시스템의 주요 성분인 망간으로 구성된 합성 촉매는 특성이 좋지 못하며 특히 중성에서의 특성 악화가 지속적으로 보고되고 있다. 본 연구에서는 망간 기반 촉매의 오랜 기간 동안 풀리지 않는 문제를 극복하고자 다양한 망간 기반의 새로운 촉매를 개발하였다.

Chapter 2에서는 자연계 시스템을 모방하여 플렉서블한 구조를 지니고 있는  $\text{Mn}_3(\text{PO}_4)_2 \cdot 3\text{H}_2\text{O}$  촉매를 개발하였다. Triclinic 구조를 지니고 있는  $\text{Mn}_3(\text{PO}_4)_2 \cdot 3\text{H}_2\text{O}$  촉매는 기존 망간 산화물 기반 촉매보다 높은 특성을 보인다. 계산 과학을 통해 기존 촉매와는 달리 본 연구진이 개발한  $\text{Mn}_3(\text{PO}_4)_2 \cdot 3\text{H}_2\text{O}$  구조 안에 망간 3+ 반응 중간체가 안정화 될 수 있음을 알 수 있었다.

Chapter 3에서는 나노사이즈의 망간 산화물을 개발하고, 중성에서 높은 특성을 보이는 것을 확인하였다. Hot injection 이라는 thermal decomposition 방법을 통해 균일한 나노 입자를 합성하고 이의

촉매 특성을 평가하였다. 특히 본 연구진이 개발한 부분 산화된 망간 산화물의 경우 다른 전이금속 기반 촉매인 코발트 포스페이트 물질이나 비정질 망간 산화물보다 더 높은 특성을 보이는 것을 알 수 있었다.

Chapter 4에서는 Chapter 3에서 개발한 부분 산화된 망간 산화물의 실제 물분해 작동 기작을 상세히 분석하였다. 다양한 실시간 분석 기법과 전기화학 측정 및 분석을 통해 기존의 벌크 크기의 망간 촉매와는 다른 메커니즘을 규명하였다. 특히 Proton coupled electron transfer 기작이 본 연구진이 개발한 나노 크기의 망간 산화물에서 작동하는 것을 최초로 밝히고, 이를 통해  $Mn(IV)=O$  반응 중간체가 새로이 물 산화 기작에 참여함을 증명하였다.

Chapter 5에서는 더 나아가 망간 산화물 위에 니켈 클러스터를 표면에 특이적으로 도핑하여 물 분해 효율 향상의 극대화를 꾀하였다. 전기 음성도 차이를 이용하여, 표면에 확산된 니켈 금속입자가 망간을 부분적으로 더 산화시키고, 촉매 특성의 향상을 야기하였다. 놀랍게도 본 연구진이 개발한 니켈이 도핑된 망간 산화물의 경우 물 분해 중 세계 최초로 특히 망간 상태가 구현되는 것을 확인할 수 있었다. 이는 무기 화합물에서 기존에 발견되지 않았던 low spin  $Mn(IV)$  물질이 본 연구진이 개발한 촉매에 구현된 것이다. 이는 EPR 분석 및 계산 과학을 통해 증명되었다.

종합적으로 본 연구에서는 다양한 망간 기반 촉매의 개발을 통해 망간 기반 촉매의 효율을 극대화시켰다. 이는 자연계를 모방한 구조의 구현 및 나노사이즈가 가지는 독특한 표면 상태, 그리고 표면에 특이적으로 확산된 이종금속 원자에 의해 이루어졌다. 본 연구은 이번 연구를 통해 발견된 디자인 원리를 바탕으로 자연계 칼슘 망간 클러스터가 가지는 놀라운 촉매 특성을 구현할 수 있을 것으로 기대한다.

**주요어:** 물 산화, 수소 생산, 산소 발생 촉매, 망간 포스페이트, 나노 촉매, 망간 산화물, 반응 중간체 분석, 전기화학 분석,

**학 번:** 2010 - 22773